Control of Hybrid-excited Permanent Magnet Machines

Nattapong Pothi

A thesis submitted for the degree of Doctor of Philosophy

Department of Electronic and Electrical Engineering

University of Sheffield

Mappin Street, Sheffield, S1 3JD, UK

August 2016

ABSTRACT

This thesis focuses on the control of hybrid-excited permanent magnet machines (HEPMMs) in both flux-enhancing and flux-weakening operations, taking due account of both efficiency improvement and fault protection.

High torque at low speed and wide operating speed range can be achieved by the proposed control strategy for the hybrid-excited switched-flux permanent magnet machine (HESFPMM) with iron flux-bridge. The torque can be enhanced by utilising the positive field excitation current. In the flux-weakening region, the field excitation current is controlled towards zero rather than negative, while the *d*-axis current is also utilised. The efficiency can thus be significantly improved. Also, three flux-weakening control methods for the HEPMMs, namely using field excitation current alone, using armature current alone, and the optimisation method, are compared and experimentally verified. All three methods can achieve the same torque in the constant-torque region due to the field excitation currents being kept the same, whilst the optimisation method provides the highest torque and efficiency in the flux-weakening region compared to other methods.

Maximum efficiency can be achieved by applying an appropriate field excitation current according to the given torque and speed conditions rather than fixing it at the maximum value. Two control strategies, optimisation and maximum efficiency tracking (MET), are proposed in order to improve the efficiency of HEPMMs. These methods have demonstrated experimentally the enhanced performance under dynamic conditions, in which the load torque is changed, compared with the method which utilises the maximum field excitation current for all operating regions.

Finally, since the PM-flux of the prototype HEPMM is inherently short-circuited when the field excitation current is not fed into the excitation windings, the open-circuit back-emf is almost zero. As a result, the machine has an inherent fault protection capability which can be utilised to prevent dangerous excess voltage issues from uncontrolled generator faults (UCGF) at high speed operation. An original method of fault protection for the HEPMM is therefore proposed and experimentally verified based on the utilisation of field excitation current control.

ACKNOWLEDGEMENTS

I would like to express my greatest gratitude to all those who have supported me throughout my research, as without their help I would not have been able to accomplish this thesis. I am deeply indebted to my supervisor, Professor Zi-Qiang-Zhu, who has been a pillar of support and wisdom. I have benefited from his guidance, constant support, and inspiring suggestions in both research and English skills.

Furthermore, I would like to thank all members of the Electrical Machines and Drives Research Group (EMD) of the University of Sheffield, for their assistance and helpful discussions. In particular, my warm thanks to Mr. Beomseok Lee, who always supports others' research efforts, Dr. Ren Yuan and Mr. Xu Peilin, who have supported my publications, Mr. Atheer A. Habash and Mr. Ali Almarhoon, who always share their experiences, and my Thai friends for all their friendship and encouragement, especially for making my time in the UK great and memorable. I would like to thank the Royal Thai Government, Office of Education Affairs in London, and the University of Phayao, which provided me the great opportunity for study abroad.

Especially, I would like to give my special thanks and deepest gratitude to my parents, my parents-in-law, my wife and our sons, who have stayed behind me and have been through all of these experiences together during my research time. Their great love and support has encouraged me to keep things in perspective throughout my time in the UK.

Finally, I am very proud to say that "I can do it"!

CONTENTS

LIST OF SYMBOLS

Symbol	Explanation	Unit
A_p	static gain of voltage loss of inverter	V
d, q	direct and quadrature axes in rotor reference frame	
I_a	amplitude of armature current	A
i_f	field excitation current	A
$i_{f,\max}$	maximum field excitation current	A
$i_{f,\max}^{en}$	maximum enhancing field excitation current	A
$i_{f,opt}$	optimised field excitation current	A
i_d, i_q	*d*-axis and *q*-axis armature currents	A
i_a, i_b, i_c	phase-a, phase-b, and phase-c currents	A
I_{m}	maximum current	A
L_d, L_q	*d*-axis and *q*-axis inductances	H
L_f	self-inductance of field winding	
L_{mf}	mutual inductance between the armature and field windings	H
L_s	armature inductance	H
k_p, k_i	proportional and integral controller gains	
m	modulation index	
N_f, N_s	turn numbers of field and armature windings	turns
P	number of pole pairs	
P_{in}, P_{out}	input power and output power	W

Symbol	Explanation	Unit
R_f, R_s	field winding and armature winding resistances	Ω
r_{ce}, r_d	resistances of switching power device and diode	Ω
T_a, T_b, T_c	phase-a, phase-b, and phase-c switching times	s
T_e	electromagnetic torque	Nm
T_m	measured torque	Nm
T_{on}, T_{off}	on-state and off-state time durations	s
T_p	time interval	s
T_s	switching period	s
V_{ce}, V_{ceo}	voltage drop and threshold of switching power devices	V
V_d, V_{do}	voltage drop and threshold of diode	V
V_{dc}	DC-link voltage	V
$V_{dc,con}$	DC supply voltage of converter	V
$V_{dc,\max}$	pre-set maximum DC-link voltage	V
V_{m}	maximum voltage	V
V_s	main DC supply voltage	V
v_d, v_q	*d*-axis and *q*-axis armature voltages	V
v_{d_dec}, v_{q_dec}	*d*-axis and *q*-axis decoupling voltages	V
v_{dm}, v_{qm}	*d*-axis and *q*-axis over-modulated voltages	V
v_f	field excitation voltage	V
$v_{\alpha m}, v_{\beta m}$	α-axis and β-axis over-modulated voltages	V
ψ_d, ψ_q	*d*-axis and *q*-axis stator flux-linkages	Wb

Symbol	Explanation	Unit
ψ_{pm}	permanent magnet flux-linkage	Wb
ω_c	bandwidth of the low-pass filter	rad/s
ω_e	electrical rotor angular velocity	rad/s
ω_m	mechanical rotor angular velocity	rpm
ω_{rated}	rated speed	rpm
ω_{rated}^{en}	rated speed of the enhancing torque	rpm
ω_{rated}^{fw}	rated speed of the weakening torque	rpm
Δi_d	modified *d*-axis current	A
Δi_f	modified field excitation current	A
Δi_q	modified *q*-axis current	A
Δ_v	voltage error regulation current	A
$\Delta V_d^{nonlinear}$	estimated *d*-axis nonlinear voltage loss of inverter	V
$\Delta V_q^{nonlinear}$	estimated *q*-axis nonlinear voltage loss of inverter	V
θ_e	electrical rotor position	rad
θ_i	current angle	rad
θ_{MTPA}	optimal current angle of the MTPA	rad
η_{avg}	average efficiency	
η	efficiency	
*	reference value	

LIST OF ABBREVIATIONS

AC	Alternating Current
DC	Direct Current
emf	Electromotive Force
HEPMM	Hybrid Excited Permanent Magnet Machine
HESFPMM	Hybrid Excited Switched Flux Permanent Magnet Machine
IGBT	Insulated Gate Bipolar Transistor
IPM	Interior Permanent magnet
LPF	Low Pass Filter
MET	Maximum Efficiency Tracking
MMEOM	Minimum Magnitude Error Over Modulation
MMF	Magnetomotive Force
MTPA	Maximum Torque Per Ampere
MTPV	Maximum Torque Per Voltage
PI	Proportional Integral
PM	Permanent Magnet
PWM	Pulse Width Modulation
rpm	Revolution per minute
SFPM	Switched Flux Permanent Magnet
SPM	Surface-mounted Permanent Magnet
SVPWM	Space Vector Pulse Width Modulation
UCGF	Uncontrolled Generation Fault
VSI	Voltage Source Inverter

CHAPTER 1

GENERAL INTRODUCTION

1.1. Introduction

The objective of an electric drive system is the controlled conversion of electrical energy to mechanical energy, or vice versa. Electrical drive systems are widely used for industrial and domestic applications, e.g. pumps, fans, compressors, robotics, elevators, electric vehicles, aerospace, etc. Recently, there has been increased interest in the application of the permanent magnet synchronous machine (PMSM) drives due to its high efficiency, high power density, small size, low weight, good reliability, simple mechanical construction, and easy maintenance. Indeed, those advantages have relied upon for the dramatic growth and development of products such as permanent magnet (PM) materials, power electronic devices, digital signal processors, sensors, programming technology, and high performance control strategies. Unless the flux weakening technique is employed, however, the PMSMs are non-adjustable in terms of excitation flux-linkage, which depends only on the PM-flux source, whereas rare-earth PM materials are expensive. Hybrid-excited permanent magnet machines (HEPMMs) have been developed to incorporate the adjustable flux-linkage feature utilising both PM and field winding as excitation sources.

Since HEPMMs offer three controllable currents (i.e. *d*-axis, *q*-axis, and field excitation currents), there is an additional control flexibility which makes them more attractive in both research and industrial applications. In order to achieve the expected performance of such machines in terms of high efficiency and wide operating speed range, however, especially in flux-weakening operations, the appropriate set of these currents should be determined. The control strategy for hybrid-excited PM machines will thus be the research subject for this thesis.

1.2. Permanent Magnet Synchronous Machines

1.2.1. Conventional PMSM machines

PM synchronous machines (PMSMs), which are also known as PM brushless AC machines, have been utilised in many applications, such as servo drives, the aerospace and automotive industries, etc., due to characteristics such as high torque density and high efficiency [CHE11], [CHU14], [RAH80], [TUR16], [WU15], [ZHU07], [ZHU12a]. Since the PM is utilised instead of field winding on the rotor side, as in wound field synchronous machines, there is no need for an extra DC power supply or field windings to provide rotor excitation. Consequently, the weight of the rotor can be reduced and field copper loss is also eliminated [HON80], [MER54]. In case of induction machines, the PM is most widely used in industrial drives as a prime-mover because of its ruggedness, reliability, simplicity, and low price. However, the induction machine is less efficient compared to PMSMs due to the slip power loss and low power factor. PMSMs are able to overcome the low efficiency limitations of both the wound field synchronous machines and induction machines.

PMSMs can be classified into three categories based on the arrangements of the PMs in the rotor: (1) surface mounted type (SPM), where the PMs are mounted on the surface of the rotor; (2) interior type (IPM), where the PMs are buried within the rotor core; and (3) inset type, where the PMs are inset into the rotor core from the air gap. Cross sections of SPM, IPM, and inset PMSMs are shown in Figs.1.1(a)-(c), respectively.

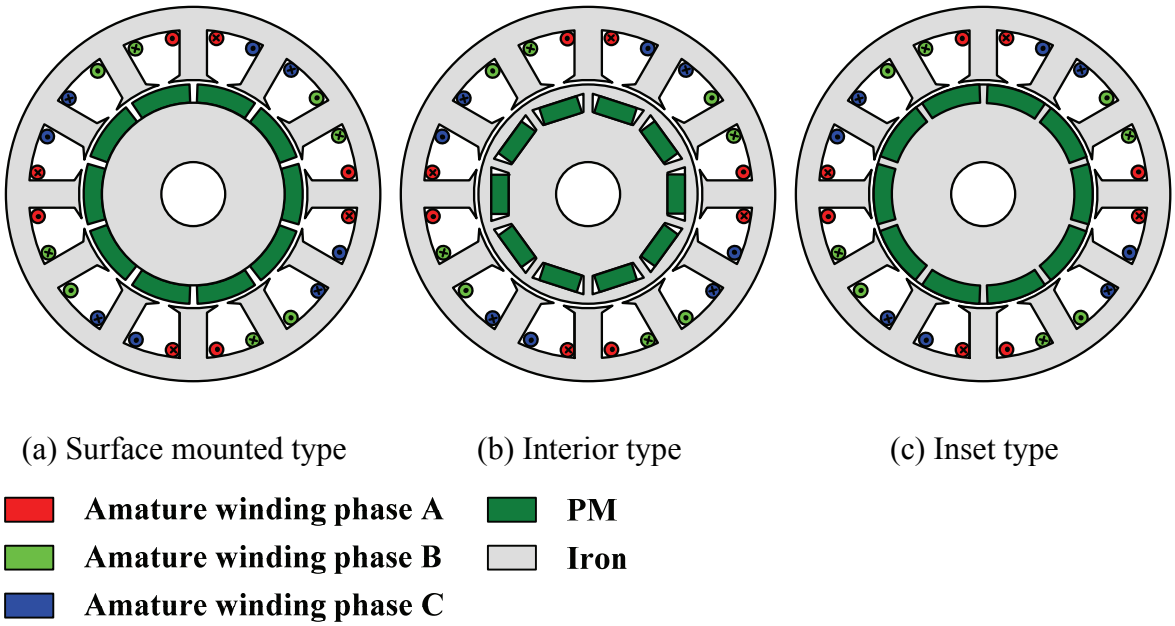

Fig. 1.1. Cross sections of the conventional PMSM topologies.

1) Surface mounted permanent magnet (SPM) machines

As shown above in Fig.1.1(a) the arrangement of the PMs in the rotor of the SPM machines produces high air-gap flux density because the PMs are mounted on the surface of the rotor, where there is less leakage. In addition, since the reluctances of both *d*-axis and *q*-axis of the SPM machine are almost equal, the *d*-axis inductance is approximately the same as the *q*-axis inductance. Only the PM torque is thus produced. Since the PMs are held on the surface of the rotor surface, however, the rotor structure is less robust as it would be easily affected by the centrifugal force. Consequently, PMs need retaining in such machines for high speed applications [RAH87], [REF05].

2) Interior permanent magnet (IPM) machines

As shown in Fig.1.1(b), the PMs of the IPM machine are buried in the rotor, making it mechanically robust and therefore suitable for high-speed applications. The IPM machines are also more attractive than the SPM machines in terms of the flux weakening and the PM eddy current loss, especially at high operation speeds [KUR04], [HON82]. Based on the reluctance of the rotor structure, the *q*-axis inductance is larger than the *d*-axis inductance. The output torque of such machines would be higher than the SPM machines for the same amount of PMs due to the reluctance torque. Furthermore, the IPM machines also exhibit a good flux-weakening capability.

3) Inset permanent magnet machines

Fig.1.1(c) shows the inset type of the conventional PMSM, in which the PMs are inset into the rotor surface. This arrangement is much more mechanically robust compared to the SPM machines, and as the *q*-axis inductance is also greater than the *d*-axis, both PM and the reluctance torques are produced [INA00], [SEB86].

1.2.2. Switched-flux permanent magnet machines

Switched-flux permanent magnet (SFPM) machines have been of interest in research and industrial applications due to their essential merits, for example, high torque and power density, high efficiency, and inherently sinusoidal PM flux-linkage, which is suitable for brushless AC drives. Moreover, the SFPM machine exhibits a robust rotor structure, since both the PM and the armature winding are located in the stator. Consequently, any temperature rise in such machines would be more easily managed and the risk of demagnetization would also be reduced. The SFPM machine is hence suitable for high speed operations [CHE11], [HUA15], [LEE14], [ZHU07], [ZHU08]. The conventional, multi-tooth, E-core and C-core SFPM machines were developed as an attempt to reduce the PM usage and improve the flux-weakening performance, as illustrated in the cross-sections of these machines shown in Figs.1.2.(a)-(d), respectively.

Fig.1.2(a) shows the 12 stator/10 rotor poles conventional SFPM machine [HOA97], [ZHU05], [HUA08], which has been investigated in several studies. Each salient stator pole consists of adjacent sides of two U-shaped laminated segments connected in parallel with the PM. In Fig.1.2(b), the electromagnetic performance of the 24 stator/19 rotor poles multi-tooth SFPM machine was discussed and compared to the conventional SFPM machine [CHE08], [ZHU08]. The multi-tooth SFPM machine can provide higher torque than the conventional version. In addition, almost half of the PM volume can be reduced [ZHU12].

The reason for the development of the E-core and C-core SFPM machines was to reduce the amount of PM usage. Only half of PM volume of those machines is consumed compared to that of the conventional SFPM machine. As a result, for the C-core SFPM machine, the stator slot area can be increased twice. The electromagnetic performances of four machine topologies, i.e. conventional, multi-tooth, E-core, and C-core SFPM machines, have been investigated in [ZHU12], [LEE14]. Compared with the conventional SFPM machine, the E-core SFPM machine provides the highest average torque, while the

best flux-weakening capability is observed in the C-core SFPM machines. The multi-tooth SFPM machine offers the lowest cogging torque. It is noted that since phase windings of the E-core SFPM machine cannot physically contact with each other, such a machine topology provides the potential for fault-tolerant capability [CHE11].

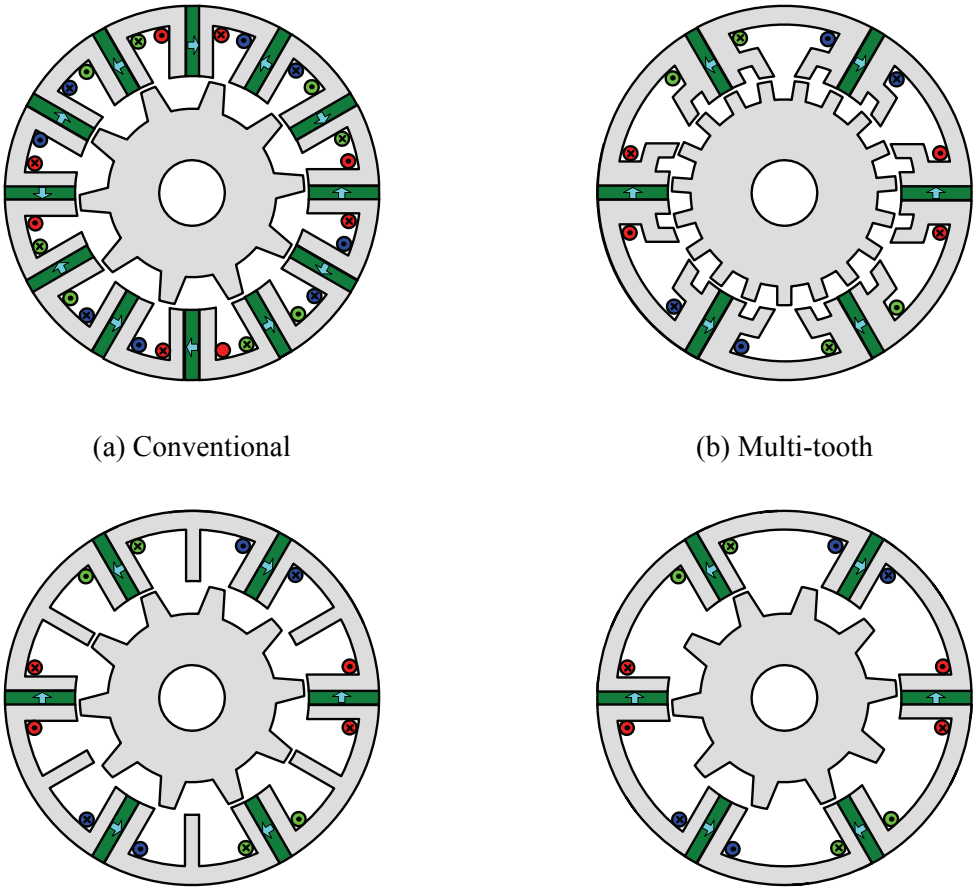

(a) Conventional (b) Multi-tooth

(c) E-core (d) C-core

Fig. 1.2. Cross-sections of alternate SFPM machine topologies.

1.3. Hybrid-excited Permanent Magnet Machines

Hybrid-excited permanent magnet machines (HEPMMs) consist of two excitation sources, i.e. PMs and field windings, such machines provide the capability to adjust the flux-linkage through the field excitation current in both enhancing and weakening operations. Consequently, a high transient starting torque and wide operating speed range can be provided [CHE11a], [WAN12], [YAM10], [ZHA16]. Since the windings and PMs are located on the stator, these machines also benefit from a good cooling capability and robust rotor structure [AMA09], [CHE11a], [OWE10], [ZHA10]. Furthermore, HEPMMs provide more optional currents (i.e. *d*-axis, *q*-axis, and field excitation currents), which can be utilised to improve the control performance of drive systems in some specific conditions compared to the conventional PMSMs. A large amount of hybrid-excited switched-flux permanent magnet machines (HESFPMMs) have been developed, such as conventional HESFPMM, HESFPMM with field-coils in PM slots, E-core HESFPMM, HESFPM with field-coils in stator back-iron, HESFPMM with iron-bridge, and stator slot HEPMM, as illustrated in Figs.1.3. (a)-(f) respectively.

Fig.1.3 (a) shows the 12 stator/10 rotor poles conventional HESFPMM. The topology is mainly the same as the conventional SFPM machine in which only the field-coils are wound on each of the salient stator poles and are connected in series. In Fig.1.3 (b), the HESFPMM with field-coils in the PM slots is developed and investigated [WEI09], [WEI11]. Based on this machine topology, the PM usage can be significantly reduced. In [CHE11a], the E-core HESFPMM is developed by placing the field-coils on the middle teeth of the E-core shaped stator lamination, as shown in Fig.1.3 (c). Since the armature and field windings are separately wound on the stator, it is simple to manufacture. In Fig.1.3 (d), the HESFPMM with field-coils in the stator back-iron is introduced and investigated [GAU14], [HOA07]. The topology of this machine shows that a good flux-regulation capability can be provided. With the utilisation of iron-flux bridges in the HESFPMM [OWE10], as shown in Fig.1.3 (e), the flux-linkage adjusting capability can be improved by leveraging the field excitation current. In Fig.1.3 (f), the stator slot HEPMM is developed by [AFI15], in which the PMs are inserted on the slot opening between two adjacent stator poles. Since the back-emf of such a machine can be almost zero when there is no field excitation current used, this provides fault protection capability.

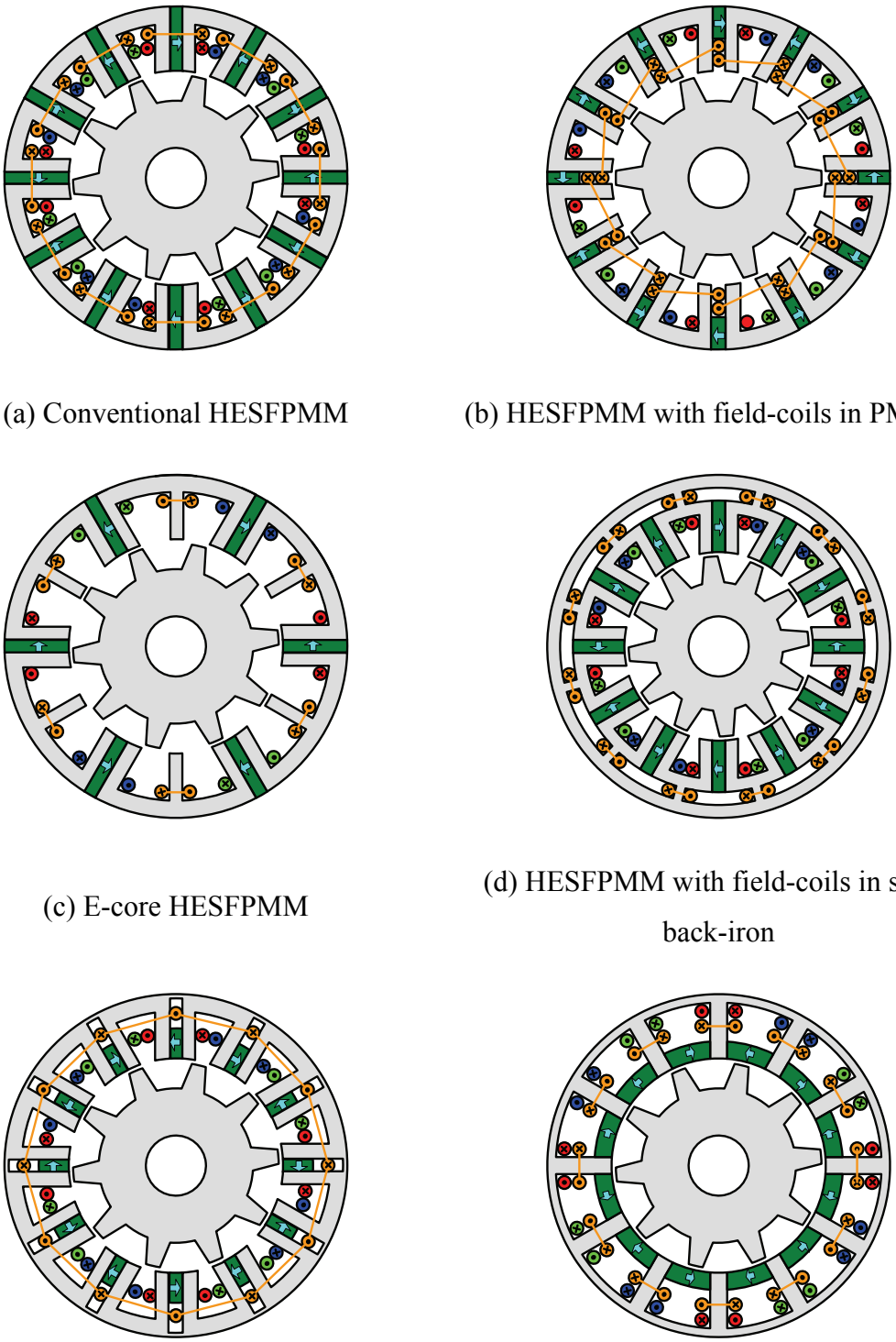

Fig. 1.3. Cross-sections of hybrid-excited PM machine topologies.

1.4. Control Strategies for the PMSMs

The operation of PMSMs according to current and voltage limitations can be mainly classified into two operating regions: constant-torque region and flux-weakening region, which sometimes is also defined as the constant-power region.

1.4.1. Constant-torque operation

In the constant-torque region, where the machine is operated below the rated speed, the maximum torque per ampere (MTPA) is widely employed to achieve the optimal efficiency [KIM97], [MOR94], [SUN15]. For the PMSMs with saliency ratio (L_q>L_d) such as the IPM machines, the MTPA condition results in a negative d-axis current for utilising the reluctance torque, as shown in Fig.1.4. Meanwhile, in the SPM machines (L_q=L_d), the MTPA condition is achieved with zero d-axis current (i_d = 0). These operating modes are given by (1.1) [MOR94]. Additionally, the optimal condition of the MTPA has been demonstrated in Appendix A.

$$i_d^{MTPA} = \begin{cases} 0 & ; \text{nonsaliency} \quad (L_d = L_q) \\ \dfrac{\psi_{pm}}{2\left(L_q - L_d\right)} - \sqrt{\dfrac{\psi_{pm}^2}{4\left(L_q - L_d\right)} + i_q^2} & ; \text{with saliency } (L_d < L_q) \end{cases} \tag{1.1}$$

where ψ_{pm} is the PM flux-linkage, L_d and L_q are the d-axis and q-axis inductances, and i_q denotes the q-axis current.

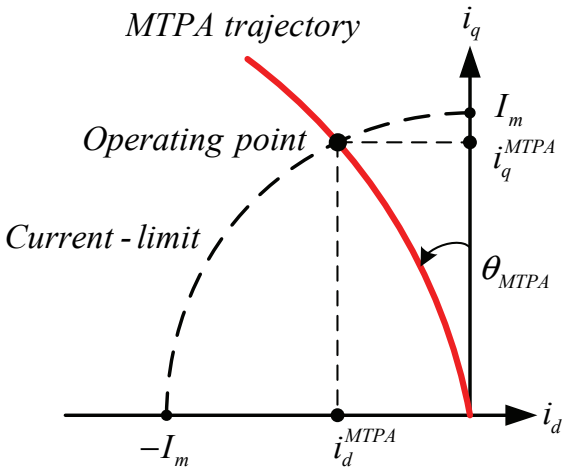

Fig. 1.4. MTPA trajectory of the IPM machine.

1.4.2. Flux-weakening operation

As mentioned in the previous section, PMSMs have been widely considered for many applications due to their advantages, including high torque density, high efficiency, and also wide operating speed range. In order to achieve the maximum torque in the constant-torque region, the *d*-axis and *q*-axis currents are controlled, tracking the MTPA trajectory [CHE10], [CON10]. They have, however, been widely used as motor drives, particularly for variable speed and variable load-torque applications where a wider operating speed range is required, for example in spindle drives, automotive vehicles, and electrical propulsion [KWO06], [KWO07], [LIN12], [LIU12], [MOR90], [PAN05]. When the machine is operated beyond the rated speed at which the armature current reaches its limit, the voltage cannot be further increased to achieve a higher speed due to the voltage limitation of the inverter. In order to extend the operating speed range from the constant-torque region to the constant-power region under the current and voltage constraints, the flux-weakening control method is thus required. Several flux-weakening control strategies have been presented [KWO06], [KWO07], [LIN12], [LIU12], [MOR90], [PAN05], [YOO08], [ZHU00].

Generally, PMSM drive systems can be classified as finite-speed and infinite-speed operations, as shown in Figs.1.5. and 1.6, respectively [KWO07], [SUL11]. These operations are divided corresponding to the centre of the voltage limit, as indicated at point C, depending on whether it is outside or inside the circle of the current limit. Fig.1.5. (a) shows the finite-speed operation of the non-saliency SPM machine in which the *d*-axis and *q*-axis inductances are equal ($L_d = L_q$). Starting from point O to A, up to rated speed ω_1, the current is controlled following the MTPA trajectory with zero *d*-axis current, as mentioned in (1.1). When in operation above the speed ω_1, the current is controlled on the current limit cycle, as illustrated by the curve AB, until it reaches the maximum speed ω_2 at point B.

Fig.1.5. (b) shows the finite-speed operation of the non-saliency IPM machine ($L_d < L_q$). In the constant torque region, the negative *d*-axis current is utilised to achieve MTPA, while the current trajectory above the rated speed is still the same as the non-saliency SPM machine. In case of infinite-speed operation where the centre of the voltage limit is inside the current limit circle, the machine can be ideally operated up to the speed ω_3 at point C, without the influence of current and voltage constraints. Meanwhile, only

mechanical issues, such as centrifugal forces and bearing friction, can affect the speed limit [SUL11]. The infinite-speed operations of both SPM and IPM machines are shown in Figs.1.6. (a) and (b), respectively.

For maximising the output torque within the whole operating speed range of the PMSM drive, which covers both the SPM and IPM machines, three operating regions are summarised in the following section [LIU12], [MOR90], [SOO94]:

Region-I: ($\omega_m \leq \omega_1$)

This region corresponds to the constant-torque operation in which the phase current is utilised at its maximum value ($I = I_m$), while the voltage is lower than its limit ($V < V_m$), where ω_m is the machine speed, I and V are the magnitudes of phase current and voltage, I_m and V_m denote the maximum current and voltage. The current is controlled following the curve "OA", as illustrated in Figs.1.5 and 1.6, based on the MTPA trajectory.

Region-II: ($\omega_1 < \omega_m \leq \omega_2$)

This region corresponds to the flux weakening operation in which the phase current and voltage are at their maximum values ($I = I_m$ and $V = V_m$). The operating speed can be extended by utilising the negative d-axis current in order to weaken the PM flux-linkage. The current is controlled following the curve "AB" which is the current limit cycle.

Region-III: ($\omega_2 < \omega_m \leq \omega_3$)

This region corresponds to the flux weakening operation in which the phase current is lower than its maximum value ($I < I_m$), while the voltage reaches its limit ($V = V_m$). The current is controlled following the curve "BC" in which the machine can be ideally extended to infinite speed, as illustrated in Fig. 1.6.

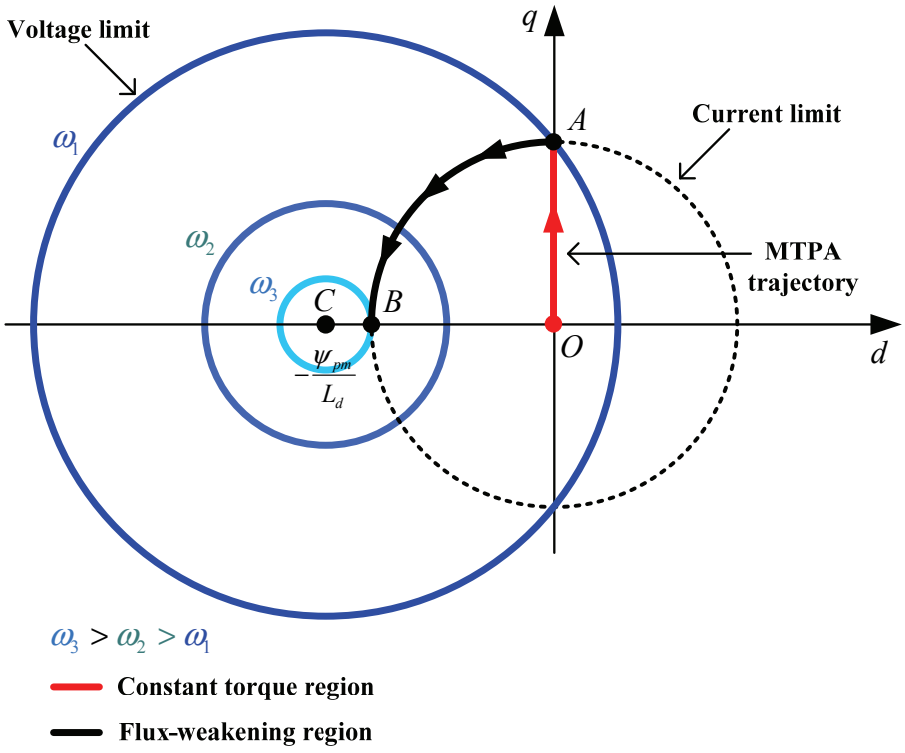

(a) Non-saliency ($L_d = L_q$)

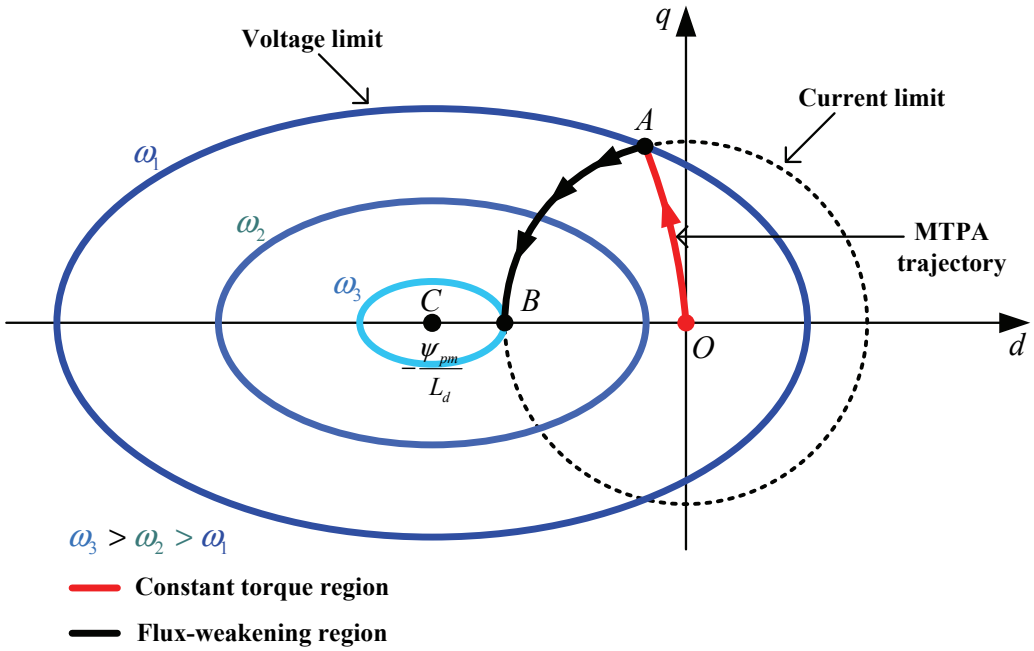

(b) With saliency ($L_d < L_q$)

Fig. 1.5 Finite-speed operation of the PMSMs.

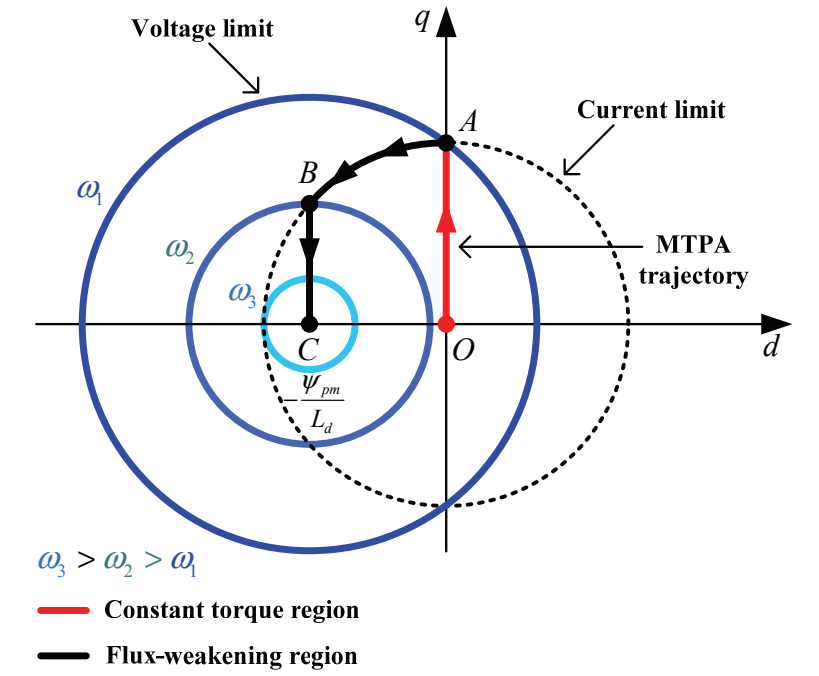

(a) Non-saliency ($L_d = L_q$)

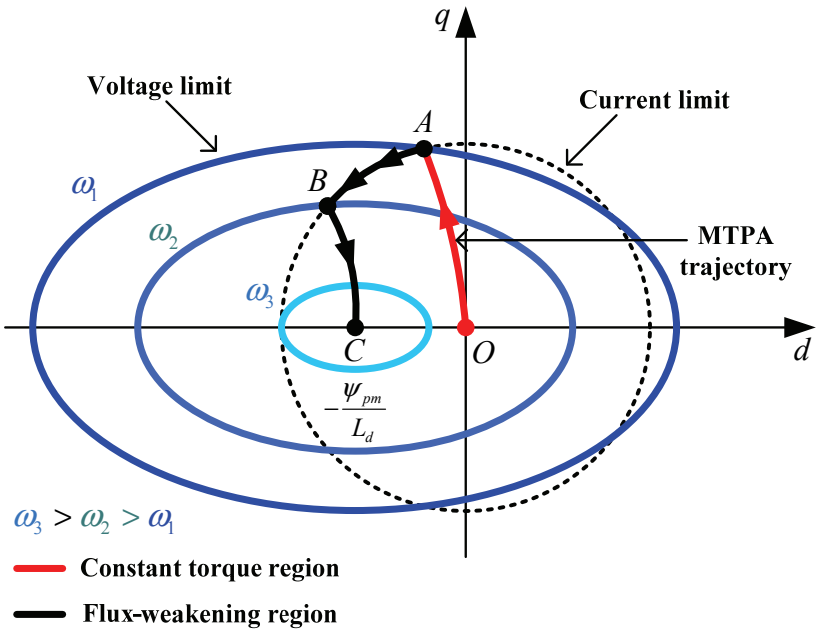

(a) With saliency ($L_d < L_q$)

Fig. 1.6. Infinite-speed operation of the PMSMs.

1.4.2.1. Feed-forward flux-weakening control

To extend the operating speed of the PMSMs, several feed-forward flux-weakening control strategies are presented [DHA90], [MAC91], [MOR94], [TUR10]. These methods utilise an analytical model to determine the operating reference currents under steady-state conditions. In the constant torque region, the reference currents are commonly controlled by tracking the MTPA trajectory. Meanwhile, in the flux-weakening region, the *d*-axis reference current is calculated by utilising the machine parameters operating under the current and voltage constraints. The *q*-axis reference current is generally determined from the torque command or speed control loop. Fig.1.7. shows the feed-forward flux-weakening control for IPM machines [MOR94]. The *d*-axis reference currents of both constant torque and flux-weakening regions are given in (1.2.) and (1.3.) respectively. Although feed forward flux-weakening control exhibits good stability and is simple to implement, the drive performance would be degraded if there was any variation of the machine parameters [LIU12], [SUL11].

Constant torque region:

$$i_d^* = \frac{\psi_{pm}}{2\left(L_q - L_d\right)} - \sqrt{\frac{\psi_{pm}^2}{4\left(L_q - L_d\right)^2} + i_q^2} \tag{1.2.}$$

Flux-weakening region:

$$i_d^* = -\frac{\psi_{pm}}{L_d} + \frac{1}{L_d}\sqrt{\frac{V_m^2}{\omega_e^2} + \left(L_q i_q\right)^2} \tag{1.3.}$$

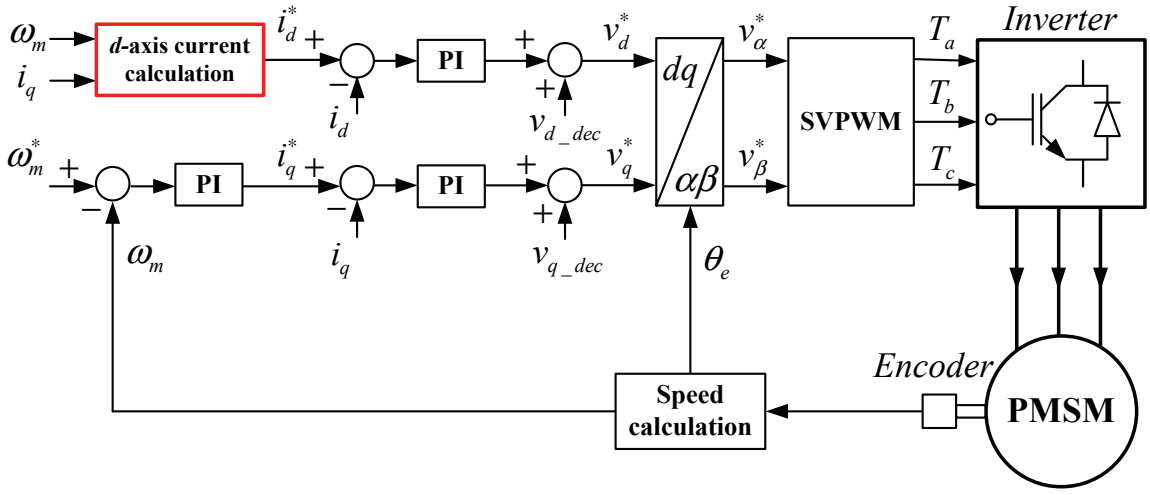

Fig. 1.7. Feed-forward flux-weakening control strategy for IPM machines [MOR94].

1.4.2.2. Feedback flux-weakening control for finite-speed operation

Although feed-forward flux-weakening control methods can provide good stability and fast transient responses, those methods are sensitive to variations in machine parameters, even when all parameters have been carefully measured [CHE99]. Several feedback flux-weakening control strategies, which are robust to the variation of machine parameters, have therefore been proposed [KWO06], [KWO08], [KWO12], [LIN12], [MAR98], [PAN05], [SON96], [YOO07]. The objective of such methods is to maintain the output voltage of the current regulator operating within the voltage constraint while operating in the flux-weakening region, by feeding back the modification current to adjust the *d*-axis reference current. In Fig.1.8, the voltage regulation method is introduced [SON96] and [YOO07a], presenting the operation of SPM and IPM machines respectively. In the constant torque region, the modification part is not activated, since the command voltage is still inside the voltage limit. Meanwhile, in the flux-weakening region, such a method utilises the difference in voltage between the absolute *d*-*q* axis command voltage and the maximum output voltage in the linear range of space vector PWM, which is ($V_{dc}/\sqrt{3}$), to modify the *d*-axis reference current. The modification part is operated with the proportional and integral (PI) regulators, in which the gains should be set by trial and error and the bandwidth should be low enough to avoid any interference with the current control loop [SUL11].

In Fig.1.9, the flux-weakening control strategy, which is referred to as the voltage error method [LIN12], is proposed by [KWO06]. In this method, maximum magnitude error over-modulation (MMEOM) is employed to increase the utilisation of DC-link voltage during the flux-weakening operation, which will be explained in Chapter 2. Consequently, the rated speed of the machine can be increased because the output voltage can be moved closer to the corner of the hexagon in the stationary voltage plane [HAV99], [KWO08]. It is obvious that only the difference voltage of the *q*-axis is utilised, since this method is proposed for finite-speed operation of the SPM machine (in which the flux-linkage can be adjusted by the *d*-axis current) only. Based on the voltage equation of the PMSMs, only the *q*-axis voltage is thus influenced. The low pass filter (LPF) and constant gain (α) are used to improve the transient performance of the flux-weakening control system. Similarly, the voltage error regulation flux-weakening control is shown in Fig.1.10. [KWO08]. Since both *d*-axis and *q*-axis voltages are utilised to determine the *d*-axis reference current, such a method can be applied to the finite speed

operation of both SPM and IMP machines. In addition, the output torque can be increased by 10% compared to the voltage regulation method, as shown in Fig.1.8.

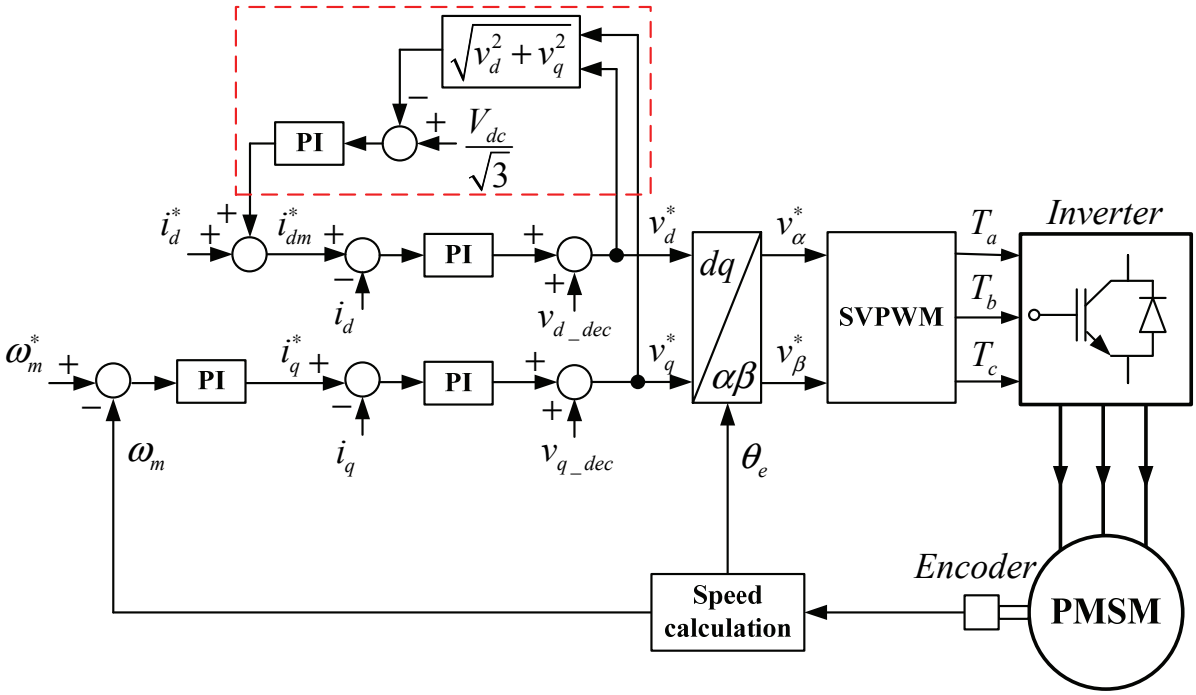

Fig. 1.8 Voltage regulation method [SON96], [YOO07a].

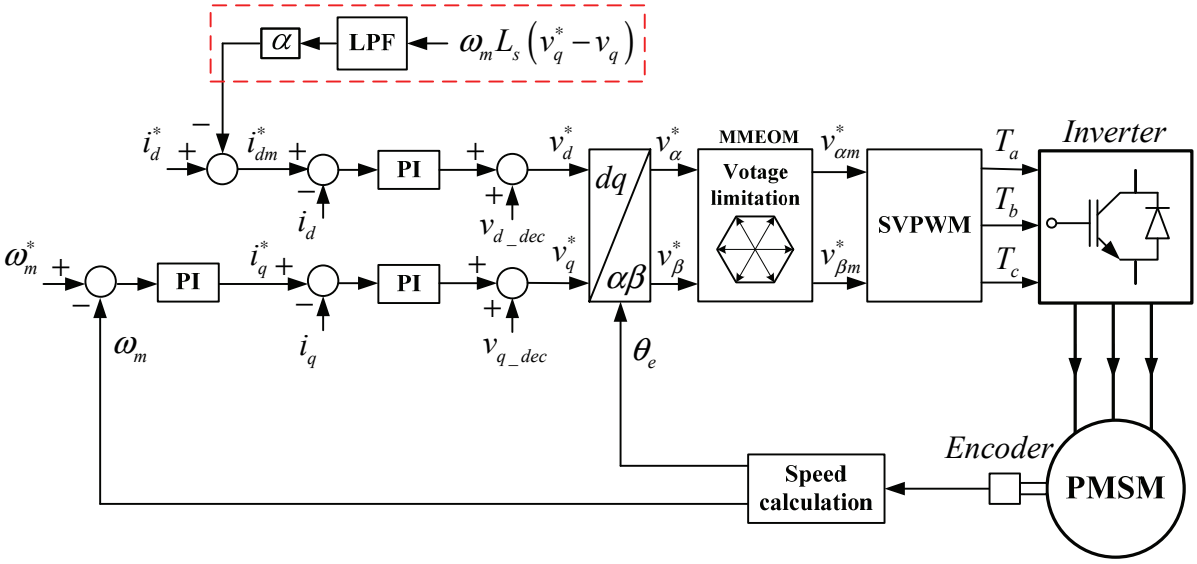

Fig. 1.9. Voltage error method [KWO06].

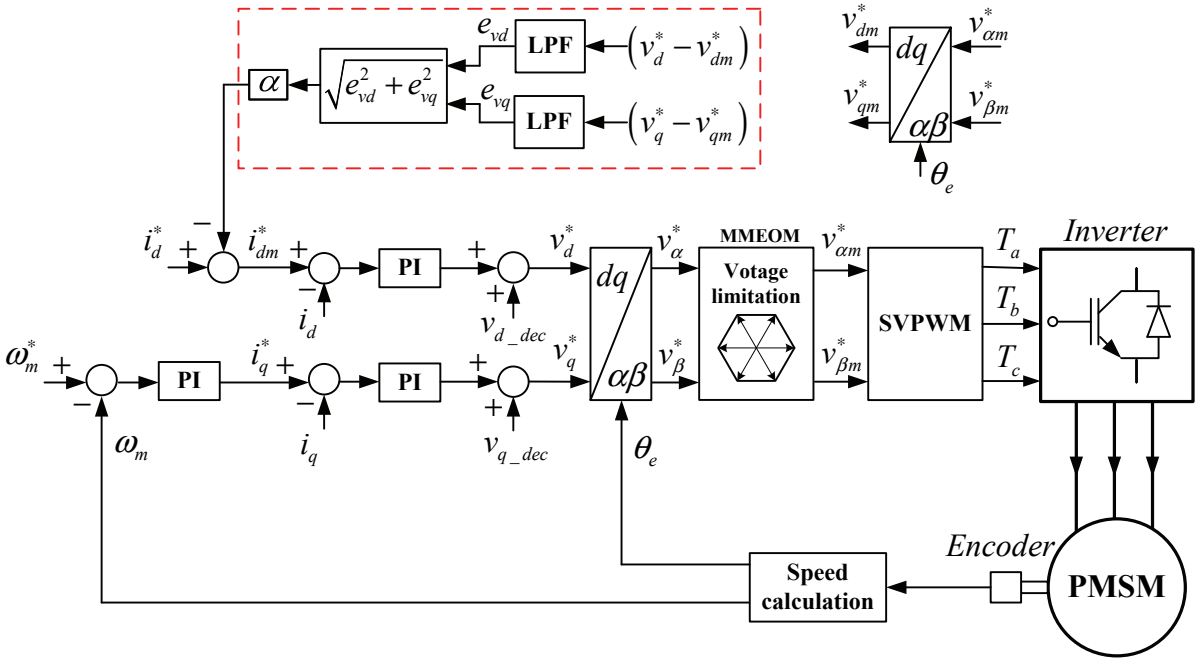

Fig. 1.10. Voltage error regulation method [KWO08].

1.4.2.3. Feedback flux-weakening control for infinite-speed operation

Generally, when the machine is operating in the flux-weakening region under finite speed operation (region-II), the flux-linkage can sufficiently be weakened by utilising only the negative *d*-axis current for extending the speed range. In the case of the infinite speed operation (region-III), however, which corresponds to a constant power speed ratio (CPSR) characteristic with $L_d I_m > \psi_{pm}$ [KWO07], [LUI12], the *q*-axis voltage is controlled towards zero by the negative *d*-axis current. Consequently, a higher speed range cannot be achieved. Under this condition, the *q*-axis current would have to be modified instead of the *d*-axis current, following the maximum torque per voltage (MTPV) trajectory, in order to extend the operating speed range. As a result, the *d*-axis voltage would be controlled, while the *q*-axis voltage would still be maintained at zero. The feedback flux-weakening control methods for infinite speed operation region are introduced by [KWO07] and [LUI12], as shown in Figs.1.11 and 1.12, respectively.

In Fig.1.11, the flux-weakening control strategy for infinite speed consists of two main modification parts, the *d*-axis modification part for region-II and the *q*-axis modification part for region-III. It is observed that in the *d*-axis modification part, it is the same control strategy as the voltage error regulation method as shown in Fig.1.10. When the machine is operating in flux-weakening in region-II, the *d*-axis reference current is

hence modified by Δi_d, which utilises the difference in voltage between the input and output of the MMEOM block, as mentioned in the previous section. Meanwhile, the q-axis reference current is determined by only the speed control loop, where $\Delta i_q = 0$, because the q-axis voltage is still greater than zero in this region. On the other hand, when the machine is operating in region-III, the d-axis reference current is still maintained at the same value as in region-II, while the q-axis reference current is modified by Δi_q following the MTPV trajectory. Indeed, in order to improve the dynamic performance of the flux-weakening control system and the optimised current trajectory, the resistance voltage drop and inverter nonlinearities are considered in the q-axis modification part, as proposed by [LUI12], and the control strategy as illustrated in Fig.1.12. It is obvious that in the q-axis modification part, although the PI with LPF is utilised instead of constant gain (α), both methods are effectively the same, utilising the q-axis voltage to determine the modified current Δi_q.

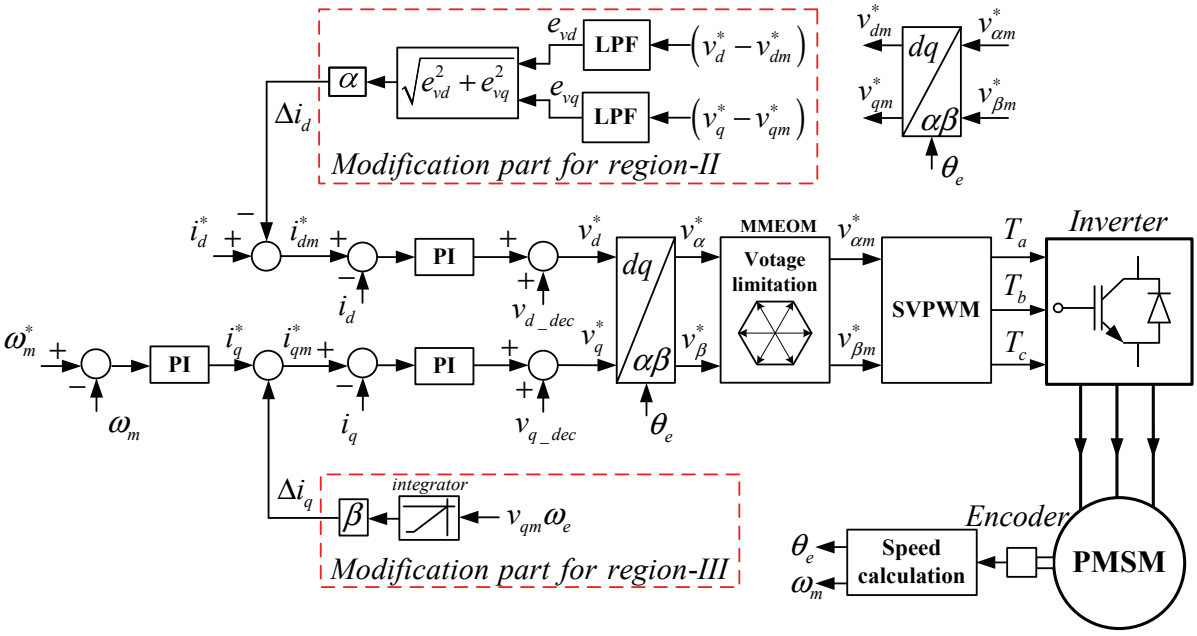

Fig. 1.11. Flux-weakening control for infinite speed [KWO07].

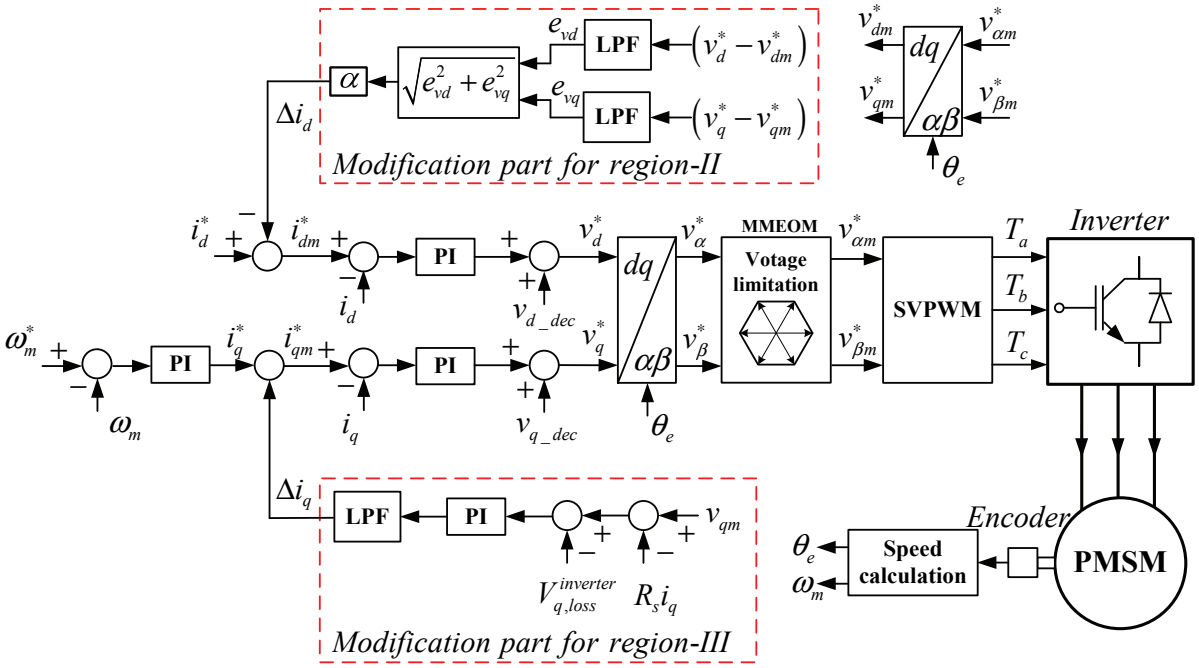

Fig. 1.12. Flux-weakening control considering voltage losses for infinite speed [LUI12].

1.5. Control strategies for the HEPMMs

HESFPMMs combine the synergy of the PMSM and the rotor wound field synchronous machine. The excitation flux of such machines is produced by two different sources, i.e. the PM and the field winding. HEPMMs have the capability to adjust the flux-linkage through the field excitation current. Furthermore, such machines also offer more optional currents, i.e. *d*-axis, *q*-axis, and field excitation currents. However, the appropriate set of those currents for operating in any given torque and speed conditions, especially in flux-weakening region, is still difficult to determine. Several control strategies for the HEPMMs have hence been presented [KEF10], [HUA12], [MBA12], [NGU14], [SHI07], [WAN13].

In [KEF10], the specific value of the field excitation current is utilised to weaken the *d*-axis flux-linkage. A large torque drop is therefore noticeable when the operating region changes between flux-enhancing and flux-weakening. Considering the machine speed and load torque changes, the analytical expressions for the optimal reference currents are proposed based on Extended Lagrange multipliers optimisation [MBA12], as illustrated in Fig.1.13. The optimal armature currents and field excitation current can be defined with respect to the current and voltage constraints, for which both torque and speed are required. A fuzzy control method is applied with particle swarm optimisation in

[HUA12]. Although these methods can determine the optimal field excitation and the armature currents, they are dependent on the machine parameters and involve a heavy computational burden. Furthermore, those methods can be verified by simulation results. The self-optimising field excitation current for achieving the maximum output torque of the HEPMM is shown in Fig.1.14 [WAN13]. The optimised field excitation reference current is determined by utilising the measured speed, field excitation current, and DC-link voltage. The optimisation algorithm consists of three operation regions for all speed ranges in which numerous decision steps are considered. Additionally, in low load-torque conditions, maximum efficiency can only be obtained based on the selection of the specific value of the field excitation current [AMA09]. Copper loss minimisation in the HEPMM has been investigated by [ZHA16] in which the optimised currents are also calculated based on the Extended Lagrange multipliers optimisation. On the other hand, [NGU14] proposes the self-tuning adaptive algorithm for copper loss minimisation. In this method, the current-ratio between field excitation and *d*-axis currents are analysed to determine optimal conditions by comparing the current and previous values of copper losses. However, those optimisation control methods are verified only by simulation.

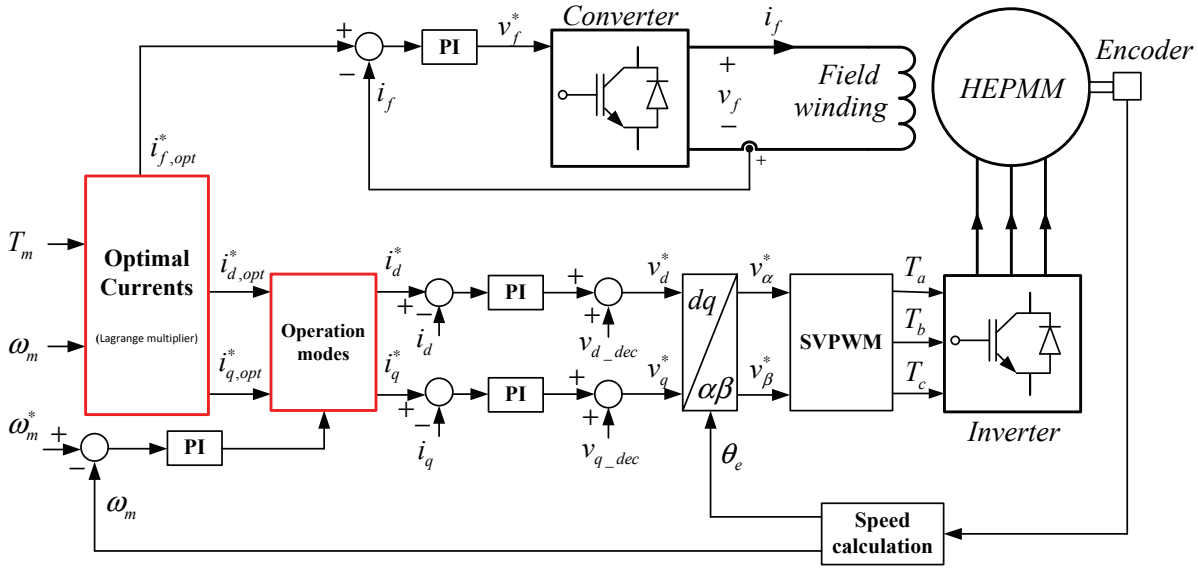

Fig. 1.13. Optimisation control strategy of the HEPMM [MBA12].

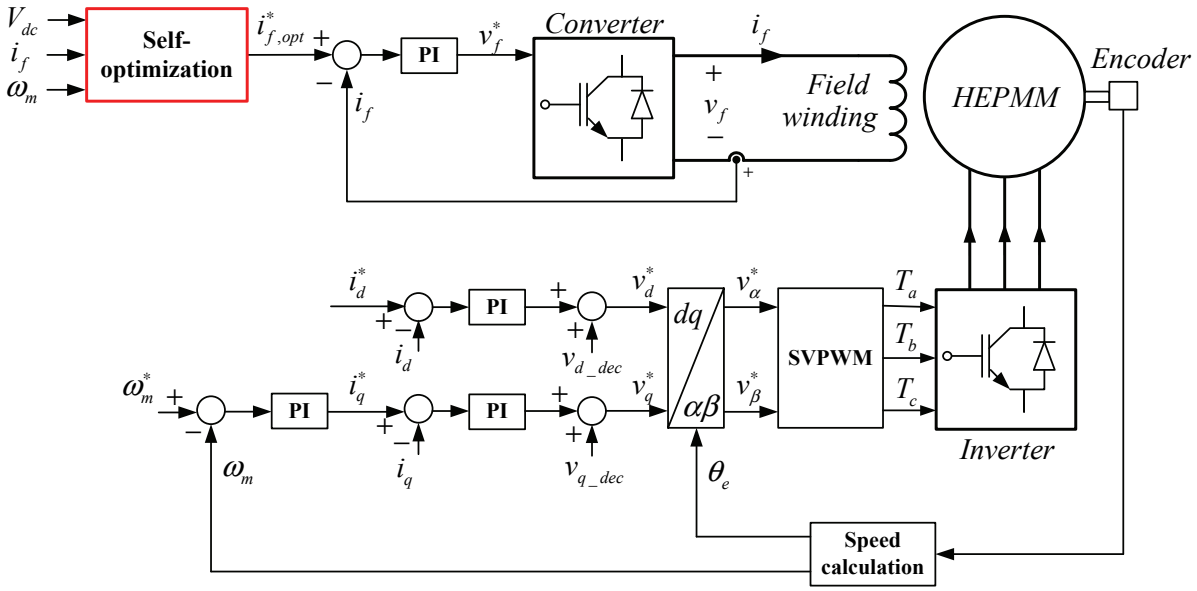

Fig. 1.14. Self-optimisation method of the HEPMM [WAN13].

1.6. Fault tolerance of PMSMs

Since variable speed drives are widely employed for a variety of applications, the reliability, continuous operation, and even safety issues have been considered in the development of advanced PMSM drive systems [KIM11]. PMSM condition monitoring and fault tolerance have been investigated [EIR11]. Several types of faults may occur in PMSMs under different circumstances, which are summarised in Table 1.1 [SUN07]. When one of the motor phases becomes open-circuited, which is defined as a single phase open-circuit fault, all switching gate-signals are commonly removed to protect the machine and drive system. Accordingly, two remaining phases are connected to the DC-link, acting as uncontrolled rectifiers [WEL02]. Likewise, the three-phase short circuit fault is the most serious fault type in PMSMs. When this fault occurs, the current amplitude is related to the ratio of PM-flux to *d*-axis inductance, which is defined as the machine's characteristic current [WEL03].

In high speed operation, especially in the flux-weakening region, the PMSM operates based on the flux-weakening control strategy because the amplitude of line back-emf is still controlled within the voltage constraint, which is referred to the DC-link voltage of the inverter. When all switching gate-signals are suddenly removed, however, even the damage of the processing unit or encoder under the flux-weakening operation, the back-emf in each phase would instantaneously become a large voltage source, which

would deliver the regenerated current back to the DC-link through the free-wheeling diodes of the inverter switches. This would be defined as an uncontrolled generation fault [JAH99], [HUN06], [PEL11]. In addition, it would be serious if the DC-link capacitor cannot absorb the abruptly regenerated energy. Consequently, the explosion of both capacitor and inverter switches might be a consequence of the dangerous excess voltage.

IPM machines exhibit potential in terms of fault tolerance based on the design of the saliency ratio (L_q/L_d) [JAH99], [PEL11], [WEL03]. The higher the saliency ratio of the IPM machine, the lower the machine's characteristic current (ψ_{pm}/L_d) which can be leveraged to reduce the damage caused by faults occurring during high speed operation. On the other hand, the fault tolerance for the PMSM drive could be solved by adding an extra inverter leg of a standard three-phase voltage source inverter [BOL00], [ERR12], [RIB04], [WAL07], in which case there would be an increased cost of implementation.

Table 1.1. Classification of PMSM faults

Cause	Fault classification
On-state failure of both switches on inverter phase leg	Single-phase open circuit fault
Open circuit of one motor phase	
Off-state failure of one switch	Single-phase short circuit fault
Ground of one motor phase	
DC power supply short circuit	Three-phase short circuit fault
Ground of motor phases	
All gate-signals are removed	Uncontrolled generation fault

1.7. Thesis outline and contribution

This thesis focuses on the development of control strategies for the HEPMM in both flux-enhancing and flux-weakening operations, taking due account of both efficiency improvement and fault protection. The machines investigated are the HESFPMM with iron flux-bridge and the HEPMM stator slot, which are defined as Machine-I and Machine-II, respectively. The research structure is briefly illustrated in Fig.1.15 below.

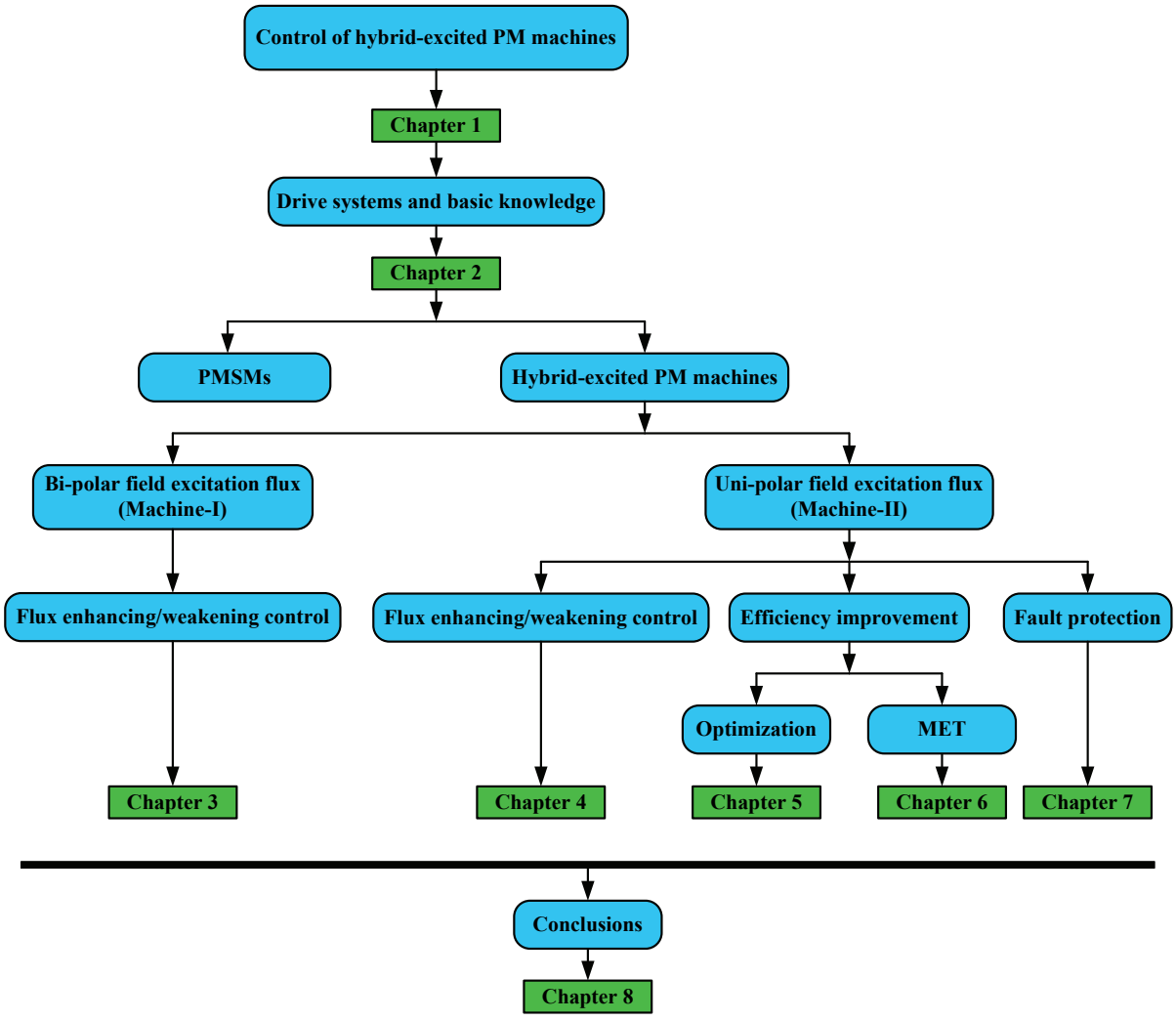

Fig. 1.15. Outline of research

1.7.1. Thesis outline

This thesis is organised as follows:

Chapter 1: A literature review is provided for application of both PMSMs and HEPMMs, including machine topologies, control strategies, and fault protection.

Chapter 2: The drive systems for the HEPMM operation are introduced, together with the specific hardware configurations, and the prototype HEPMM, are briefly presented in this chapter. Meanwhile, the principle of field orientation control, the three-phase transformation method, the space vector modulation technique, the over-modulation technique, and the inverter nonlinearity are presented.

Chapter 3: This chapter proposes a control strategy for the HESFPMM with iron-flux bridge (Machine-I). The proposed method exhibits several advantages, such as highly enhanced torque in the constant torque region, extended speed range, robustness against machine parameters, and higher efficiency in the flux-weakening region. The effectiveness of the proposed method is experimentally validated.

Chapter 4: Three flux-weakening control methods for the stator slot HEPMM (Machine-II), namely utilising field excitation current alone (Method-I), armature current alone (Method-II), and the optimisation method (Method-III), are compared in this chapter. These flux-weakening control methods are verified by experimental results.

Chapter 5: The efficiency improvement for all operating regions, which is based on the optimisation method for the HEPMM as presented in chapter 4, is proposed. Since the optimal field excitation current is determined as a function of *d*-axis and *q*-axis currents regardless of the machine parameter variation, it is simple to implement and robust. The proposed method is experimentally validated.

Chapter 6: The maximum efficiency tracking (MET) method for the HEPMM is proposed. The field excitation current is modified by a small amount of tracking step size over every time interval, while its direction is determined by the comparison of the current and previous efficiency values. The proposed method can therefore be easily applied to other hybrid-excited machines without the requirement for machine parameters, as the turn-ratio between the field winding and the armature winding is required, as discussed in Chapter 5. The effectiveness of the proposed method is verified by experimental results.

Chapter 7: The fault protection capability of the stator slot HEPMM (Machine-II), in which its back-emf is almost zero when the field excitation current is zero, is

examined to prevent the dangerous excess voltage issue from uncontrolled generator faults (UCGF) at high speed operation. Since only the field excitation current is utilised to protect the machine and inverter switches from the UCGF, it is simple to implement. The concept of this proposed control strategy could also be applied to other hybrid-excited PM machines. The proposed control strategy is verified by both simulation and experimental results.

Chapter 8: General conclusions and recommendations for future work are presented in this chapter.

1.7.2. Contributions

- Enhancing the torque at low speed and extending the operating speed range based on the proposed control strategy of the HESFPMM with the iron-flux bridges.
- The optimisation condition with respect to the maximum efficiency of the HEPMM, in which only the turn-ratio between the field winding and the armature winding is required, is verified. The optimised field excitation current is found to be a function of *d*-axis and *q*-axis currents, which is simple to implement and robust in terms of the machine parameter variation. In addition, the optimisation method can be applied to the flux-weakening operation and utilised to improve the efficiency for all operating regions, i.e. low-torque operation, constant-torque, and flux-weakening regions.
- Under any given torque and speed operation, maximum efficiency can be achieved by applying an appropriate field excitation current, which is automatically determined based on the searching method, defined as maximum efficiency tracking (MET). The efficiency can thus be improved by comparing it to the method that utilises the maximum field excitation current.
- A novel method of fault protection of the HEPMM is proposed and verified based on the utilisation of field excitation current control, by which the back-emf can be controlled to zero by $i_f = 0$.

CHAPTER 2

DRIVE SYSTEMS FOR HYBRID-EXCITED PERMANENT MAGNET SYNCHRONOUS MACHINES

2.1 Introduction

The experimental platform, which is employed to demonstrate the effectiveness of all propose control methods presented in this thesis, is shown in Fig.2.1. The dSPACE drive system was developed for the three-phase AC machine drive, and it can also be adapted for the hybrid-excited PM machine. This chapter focuses on the experimental hardware and the fundamental principle which relates to the proposed control strategies, as presented in each chapter. The dSPACE processor board and its accessories for interconnections are firstly introduced. Afterward, the hardware configurations for the hybrid-excited PM machine drive and also the prototype machines are described. Finally, in the fundamental principle part, the field orientation control, three-phase transformations, i.e. Clarke's and Park's transformations, space vector pulse width modulation (SVPWM) and over-modulation technique, and the inverter nonlinearity are covered.

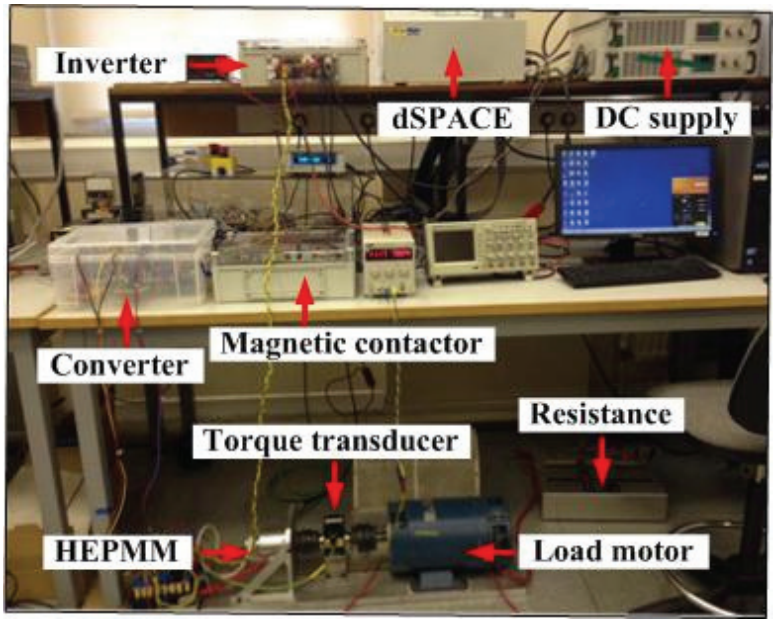

Fig. 2.1. Experimental platform.

2.2 Prototype hybrid-excited permanent magnet machines

2.2.1 HESFPMM (Machine-I)

The hybrid-excited switched-flux permanent magnet machine (HESFPMM) was designed by [OWN10], Fig.2.2. This machine utilises an iron-flux bridge, which connects the adjacent sides of the U-shaped laminated segments in each stator pole, to increase the flux-adjusting capability controlled by the field excitation current in both flux-enhancing and flux-weakening operations. Both positive and negative field excitation currents are utilised for enhancing/weakening the flux-linkage, respectively. The 2D FE model and the prototype HESFPMM are illustrated in Fig.2.2(a) and (b), respectively.

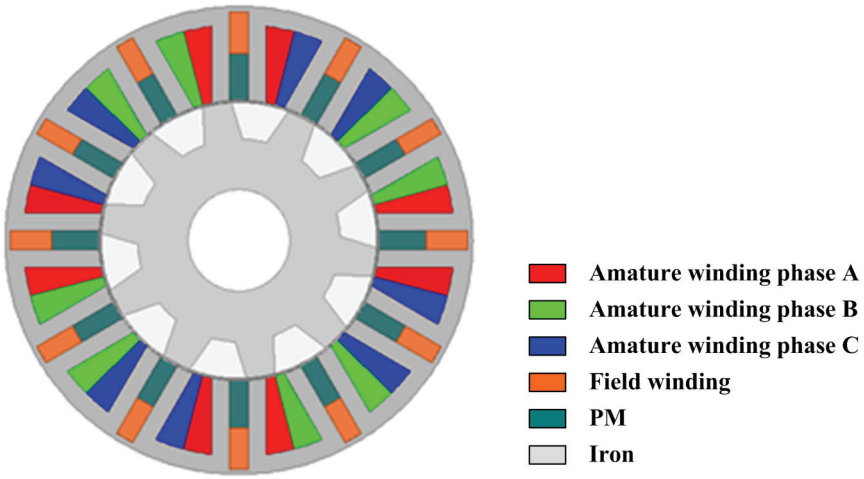

(a) 2D FE model of the HESFPMM.

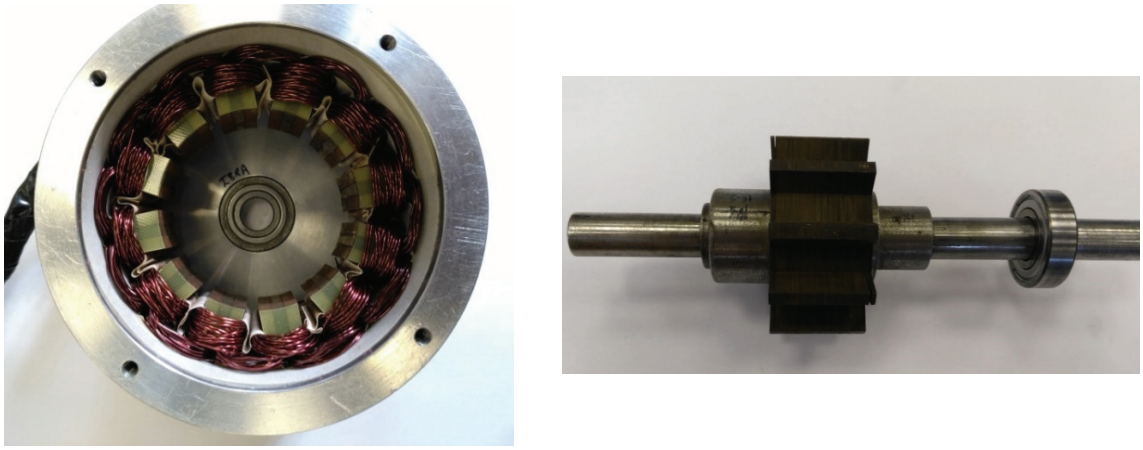

(b) Prototype HESFPMM.

Fig. 2.2. Three-phase 10 rotor/ 12 stator pole HESFPMM.

The stator diameter of the prototype HESFPMM is designed at 90 mm, while the axial length is 25 mm. The stator iron bridge thickness is 1.0 mm. Other machine parameters are given in Table 2.1. Since this machine can be operated without the utilization of field excitation current (PM only), the rated torque is 0.75 Nm, while the armature current is 15A based on the dc-link voltage at 36V. Under this condition, the rated speed is around 1000 rpm. Fig.2.3 shows the flux-linkage and back-emf of the prototype machine obtained from the 2D finite element (FE) analysis and measurement with the speed at 500 rpm. It is obvious that the flux-linkage and back-emf of the prototype machine can be enhanced/weakened by utilising the positive/negative field excitation current.

Table 2.1. Machine parameters of the HESFPMM

Stator outer diameter	90 mm
Axial length	25 mm
Split ratio of stator inner to outer diameter	0.6
Air-gap length	0.5 mm
Rotor pole arc/pitch ratio	0.33
Stator pole arc/pitch ratio	0.25
PM arc/stator pole pitch ratio	0.25
Stator back-iron thickness	3.53 mm
Stator iron bridge thickness	1.0 mm
d-axis and *q*-axis inductances (L_d, L_q)	0.37 mH
Self-inductance of field winding (L_f)	0.208 mH
Armature resistance (R_s)	0.43 Ω
Field winding resistance (R_f)	0.74 Ω
PM flux (ψ_{pm})	5.14 mWb
DC-link voltage (V_{dc})	36 V
Rated current (I_m)	15 A
Rated torque	0.75 Nm
Rated speed (ω_{rated})	1000 rpm
Number of pole pairs (P)	10
Number of turns per phase (N_s)	72
Number of turns per field excitation coil (N_f)	20

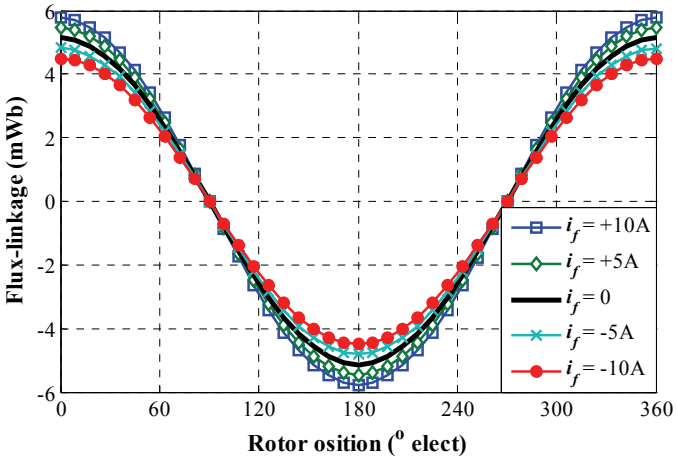

(a) Flux-linkage against rotor position

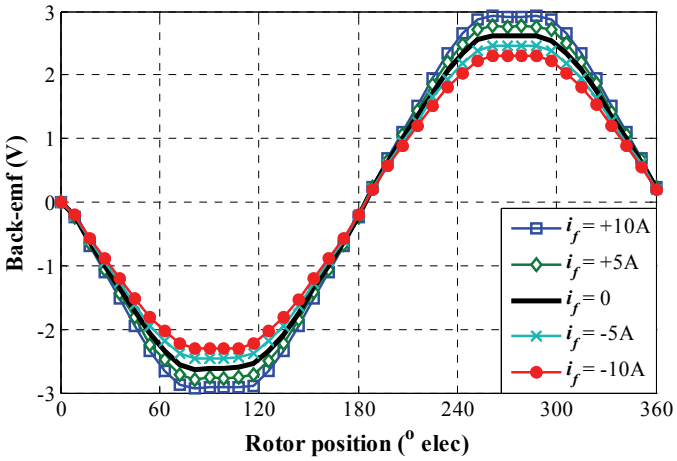

(b) Back-emf against rotor position

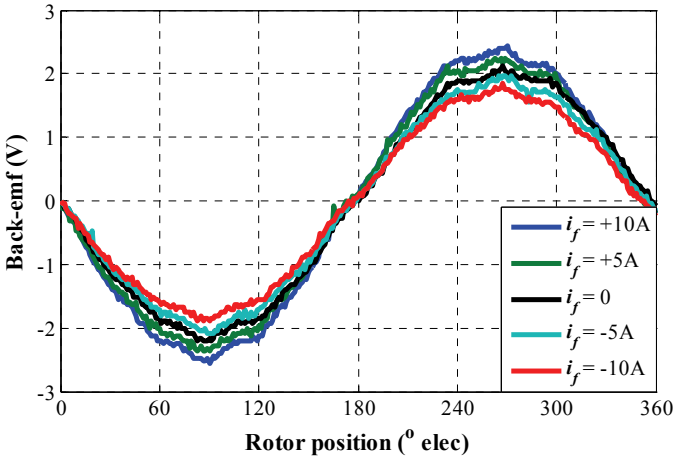

(c) Measured back-emf against rotor position

Fig. 2.3. Open-circuit characteristic of the HESFPMM corresponding to the specific values of field excitation current, 500 rpm.

2.2.2 HEPMM (Machine-II)

The three-phase 10 rotor/12 stator pole hybrid-excited permanent magnet machine (HEPMM) was designed by [AFI15]. The PMs are placed on the slot opening between two adjacent salient stator poles. Indeed, the flux-linkage of this machine is almost zero when the field excitation current is not utilised ($i_f = 0$), and it can be enhanced by the positive field excitation current ($i_f > 0$). As a consequence, this machine utilizes only the positive field excitation current in both flux-enhancing and flux-weakening operation. Figs.2.4(a) and (b) show the 2D FE model and the prototype HEPMM, respectively.

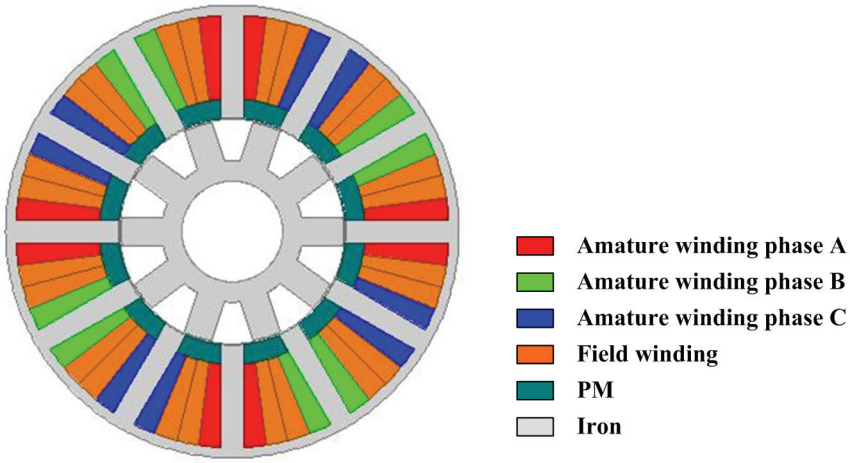

(a) 2D FE model of the HEPMM.

(b) Prototype HEPMM.

Fig. 2.4. Three-phase 10 rotor/ 12 stator pole HEPMM.

The stator diameter of the prototype HEPMM is the same as the HESFPMM in which the stator outer diameter and the axial length are 90 mm and 25 mm, respectively. Other machine parameters are given in Table 2.1. The flux-linkage and back-emf of the prototype HEPMM obtained from the 2D finite element (FE) analysis and measurement are shown in Fig.2.5 (a)-(c), respectively. The flux-linkage and back-emf of the HEPMM can be enhanced/weakened by utilising only the positive field excitation current. It can be clearly seen that, in this machine, when the field excitation current is not employed (i_f = 0), the back-emf is almost zero. Consequently, the prototype HEPMM (Machine-II) exhibits a fault protection capability based on the field excitation current control, as presented in Chapter 7.

Table 2.2. Machine parameters of the HEPMM

Stator outer diameter	90 mm
Axial length	25 mm
Split ratio of stator inner to outer diameter	0.5
Air-gap length	0.5 mm
Stator back-iron thickness	2.0 mm
Permanent magnet flux (ψ_{pm})	0.98 mWb
DC-link voltage (V_{dc})	40 V
Rated torque	0.71 Nm
Rated speed (ω_{rated})	700 rpm
Rated current (I_m)	7.92 A
Maximum field excitation current ($i_{f,max}$)	5.6 A
Number of pole pairs (P)	10
Number of turns per phase of armature winding (N_s)	184
Number of turns of field winding (N_f)	552
Armature winding resistance (R_s)	1 Ω
Field winding resistance (R_f)	3 Ω
d-axis and q-axis inductances (L_d, L_q)	2 mH
Self-inductance of field winding (L_f)	0.5 mH

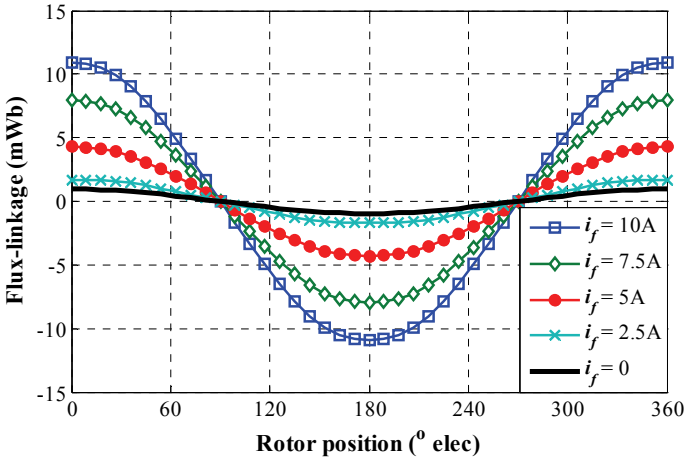

(a) Flux-linkage against rotor position

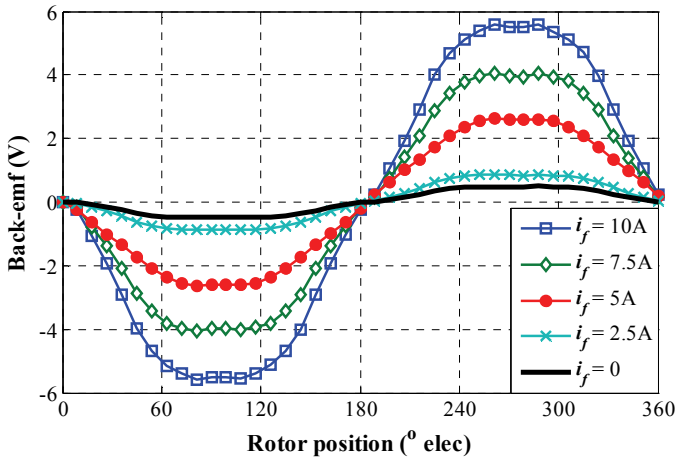

(b) Back-emf against rotor position

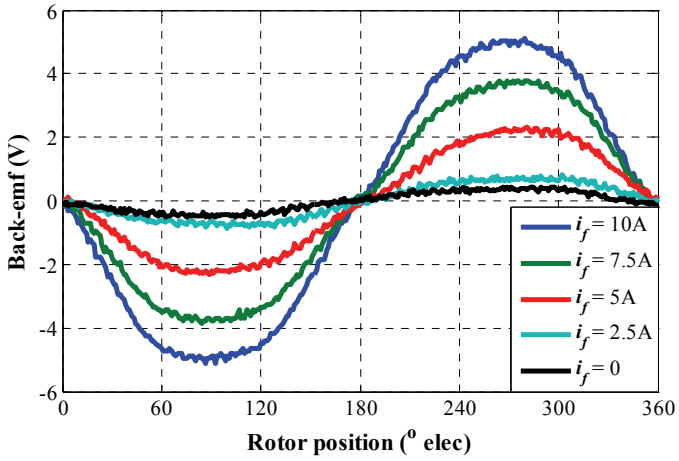

(c) Measured back-emf against rotor position

Fig. 2.5. Open-circuit characteristic of the HEPMM corresponding to the specific values of field excitation current, 500 rpm.

TABLE 2.3. Hybrid-excited PM machines under investigation in each chapter.

Machine	Chapter	Topic
HESFPMM (Machine-I)	3	To investigate the control strategy for the hybrid-excited switched-flux permanent magnet machine with iron flux-bridge including the flux-enhancing and the flux-weakening operations. In this machine, the field excitation current can be utilised in both positive and negative directions for the flux-enhancing and flux-weakening respectively.
HEPMM (Machine-II)	4	To investigate the flux-weakening control strategies of the hybrid-excited PM machine. Only the positive field excitation current is utilised to modify the flux-linkage in both flux-enhancing and flux-weakening operations.
	5	To investigate the efficiency improvement based on the optimisation of field excitation current in whole operating regions, i.e. low-torque operation, constant-torque, and flux-weakening regions.
	6	To investigate the maximum efficiency tracking (MET) of the hybrid-excited PM machine utilising the field excitation current.
	7	To investigate the fault protection capability of the hybrid-excited PM machine utilising the field excitation current control.

2.3 Field orientation control of three-phase PMSM

The control of AC machines can be principally classified into scalar and vector controls. Although the scalar control is simple to implement and it also exhibits good performance in steady-state condition, the dynamic response is low since the transient condition is not considered. Therefore, in order to achieve the fast dynamic response and high reliability, the vector control has been employed [VAS03]. In the AC machine, the torque and flux controls were introduced and named as field orientation control or vector control. Indeed, the aim of field excitation current control is similar to the control of a separate excited DC machine in which the armature current and field current are orthogonal to each other [ONG97]. The torque can be controlled independently to the flux-linkage by adjusting the armature current, while the flux-linkage is controlled by the field current. Therefore, for the field orientation control of the PMSMs, the torque and flux-linkage are separately controlled relying on the control of stator current in the *d*-axis and *q*-axis, respectively [ABU12] [SUL11]. Fig.2.6 shows the vector diagram of PMSM, which is based on the rotor orientation. It is obvious that the armature current needs to be transformed to the synchronous reference frame, in *d*-*q* axis, in which both *d*-axis and *q*-axis currents are naturally held at 90 degrees apart. Indeed, the PM-flux linkage (ψ_{pm}) is on the *d*-axis, while the torque can be controlled by the *q*-axis current. However, since the machine speed is determined by an encoder, the rotor position alignment is required and explained in Appendix-B.

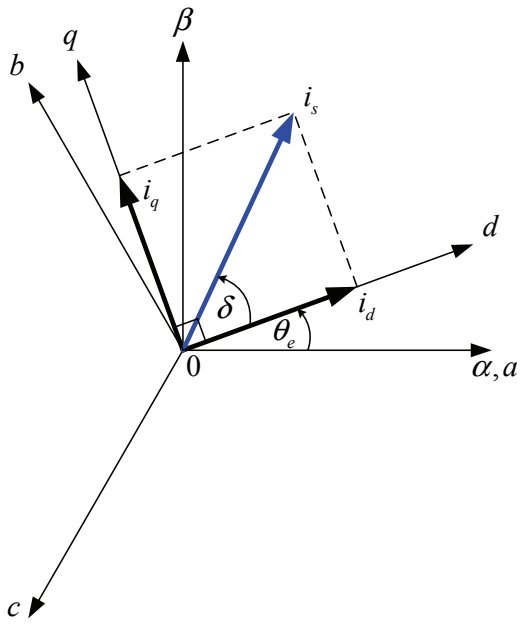

Fig. 2.6. Vector diagram based on the field orientation control of the PMSM.

The torque equation of the PMSM is given as

$$T_e = \frac{3}{2} P\left[\psi_{pm} i_q + (L_d - L_q) i_d i_q\right]. \tag{2.1}$$

where i_d, i_q are *d*-axis and *q*-axis currents, L_d, L_q are *d*-axis and *q*-axis inductances, ψ_{pm} is PM flux-linkage, and *P* is number of pole pairs.

In the SPM, the *d*-axis and *q*-axis inductances are equal ($L_d = L_q$). Hence, the torque can be expressed as

$$T_e = \frac{3}{2} P\left(\psi_{pm} i_q\right) = \frac{3}{2} P\left(\psi_{pm} I \sin\delta\right) \tag{2.2}$$

It should be noted that, the torque can achieve the maximum value when the load torque angle (δ) is equal to 90 degrees at any given the stator current, which corresponds to the vector diagram based on the field orientation control of the PMSM, as shown in Fig.2.6. The general field orientation control block diagram of the PMSM is shown in Fig.2.7, in which the decoupling terms for the *d*-axis and *q*-axis voltages can be given as $v_{d\_dec} = -\omega_e L_q i_q$ and $v_{q\_dec} = \omega_e\left(\psi_{pm} + L_d i_d\right)$, respectively.

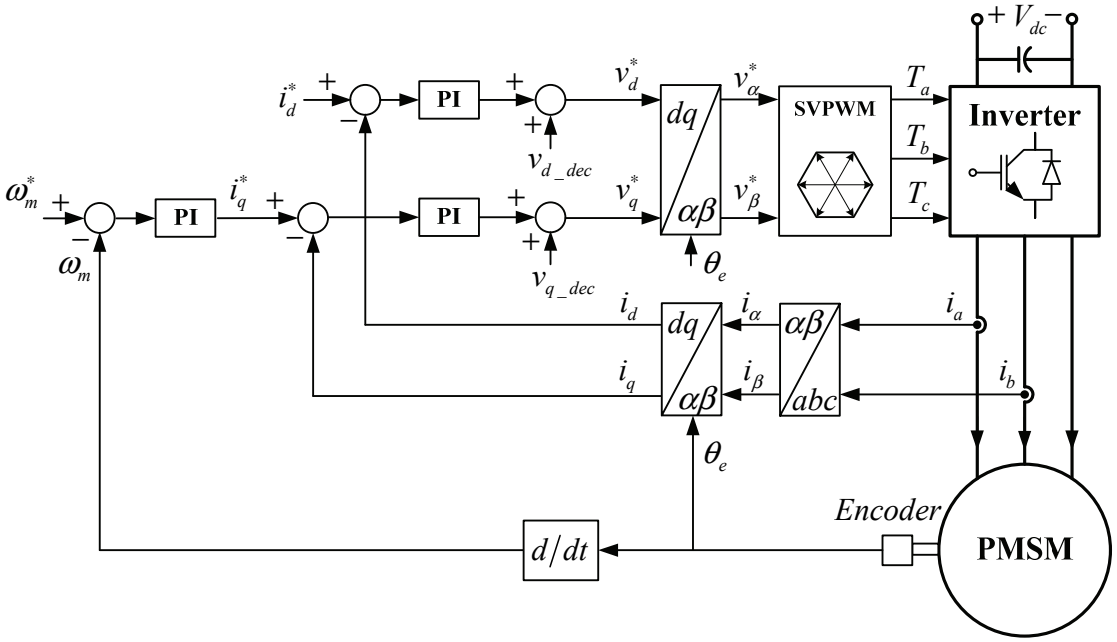

Fig. 2.7. Field orientation control or vector control block diagram of the PMSM.

2.4 Three-phase transformations

Clarke and Park transformations are fundamentally utilised in the vector control in order to transfer the variables, e.g. voltage, current, and also flux-linkage, into another reference axes. This section will briefly explain those transformation methods as follows.

2.4.1 Clarke's transformation

Fig.2.8 shows the Clarke's transformation vectors in which the quantities in three-phase, expressed by current vectors, are transferred from the three-phase reference frame to the stationary reference frame, α-β axis. It can be presented by (2.3) [ABU12].

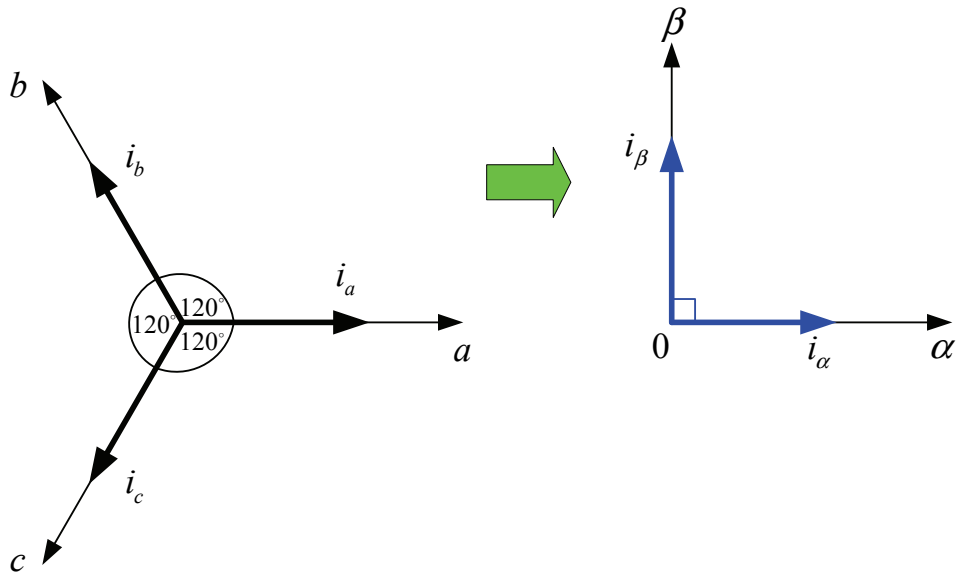

Fig. 2.8. Clarke's transformation vector.

$$\begin{bmatrix} i_\alpha \\ i_\beta \end{bmatrix} = \frac{2}{3}\begin{bmatrix} 1 & -\frac{1}{2} & -\frac{1}{2} \\ 0 & \frac{\sqrt{3}}{2} & -\frac{\sqrt{3}}{2} \end{bmatrix}\begin{bmatrix} i_a \\ i_b \\ i_c \end{bmatrix} \tag{2.3}$$

The inverse Clarke's transformation can be given by (2.4).

$$\begin{bmatrix} i_a \\ i_b \\ i_c \end{bmatrix} = \begin{bmatrix} 1 & 0 \\ -\frac{1}{2} & \frac{\sqrt{3}}{2} \\ -\frac{1}{2} & -\frac{\sqrt{3}}{2} \end{bmatrix}\begin{bmatrix} i_\alpha \\ i_\beta \end{bmatrix}. \tag{2.4}$$

2.4.2 Park's transformation

Fig.2.9 shows the Park's transformation vector in which the quantities in the stationary reference frame, α-β axis, are transferred to the synchronous reference frame, *d-q* axis. The Park's transformation can be expressed in the equation as (2.5) [ABU12].

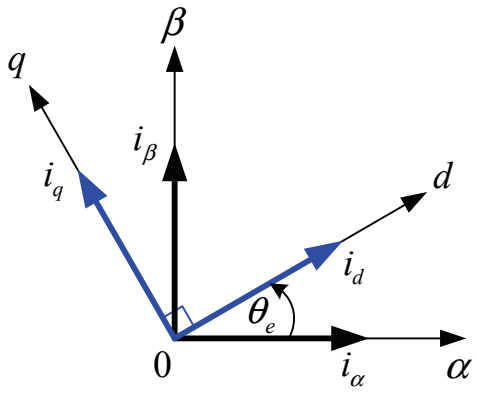

Fig. 2.9. Park's transformation vector.

$$\begin{bmatrix} i_d \\ i_q \end{bmatrix} = \begin{bmatrix} \cos\theta_e & \sin\theta_e \\ -\sin\theta_e & \cos\theta_e \end{bmatrix} \begin{bmatrix} i_\alpha \\ i_\beta \end{bmatrix} \tag{2.5}$$

The inverse Park's transformation can be given by (2.6).

$$\begin{bmatrix} i_\alpha \\ i_\beta \end{bmatrix} = \begin{bmatrix} \cos\theta_e & -\sin\theta_e \\ \sin\theta_e & \cos\theta_e \end{bmatrix} \begin{bmatrix} i_d \\ i_q \end{bmatrix} \tag{2.6}$$

In practice, the Clarke and Park transformation can be combined together in order to convert the currents in the stationary reference frame (*a-b-c* axis) to the synchronous reference frame (*d-q* axis), as given in (2.7)

$$\begin{bmatrix} i_d \\ i_q \end{bmatrix} = \frac{2}{3} \begin{bmatrix} \cos\theta_e & \cos\left(\theta_e - \frac{2\pi}{3}\right) & \cos\left(\theta_e + \frac{2\pi}{3}\right) \\ -\sin\theta_e & -\sin\left(\theta_e - \frac{2\pi}{3}\right) & -\sin\left(\theta_e + \frac{2\pi}{3}\right) \end{bmatrix} \begin{bmatrix} i_a \\ i_b \\ i_c \end{bmatrix} \tag{2.7}$$

2.5 Pulse width modulation strategies

2.5.1 Space vector pulse width modulation

The space vector pulse width modulation (SVPWM) is widely employed in the three-phase AC machine drive, since it exhibits more advantages than the traditional carrier based PWM, i.e. sinusoidal PWM (SPWM), due to a higher dc-link voltage utilization [ABU12], [HOL94], [VAN88]. The peak fundamental phase voltage of the SPWM is $0.5V_{dc}$, while the SVPWM is $(2/\sqrt{3})*V_{dc}$. Based on the principle of SVPWM, there are eight possible switching states for the three-phase VSI, as shown in Fig.2.10. Each phase-leg of the VSI consists of two switches that are basically operated in different switching state. When the upper switch is on-state, the lower switch is controlled to be off-state, and vice versa. The on-state for each switch is denoted by "1", while "0" is for off-state. The inverter is fed by the dc-link voltage (V_{dc}) and its power is transferred to the three-phase load corresponding to the duty ratio, which is the on-state time duration divided by the switching time period (T_{on}/T_s). Therefore, in order to generate the output voltages following the requirement of control system, the on-state time durations for all switches need to be determined.

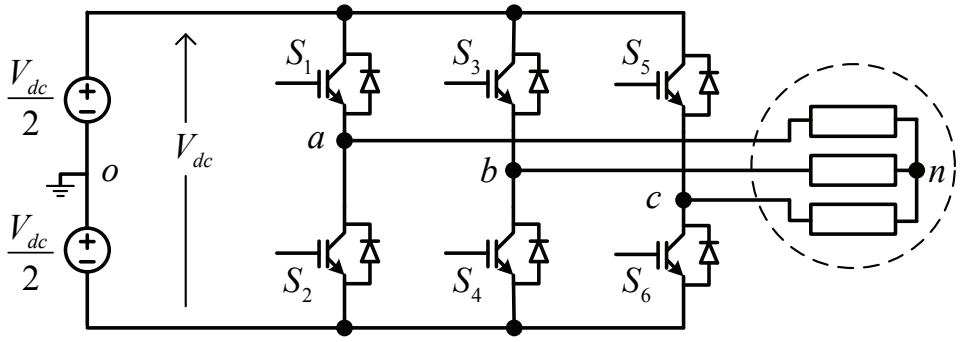

Fig. 2.10. Circuit topology of three-phase voltage source inverter.

The switching pulse generation is originally started based on the ideal three-phase voltage waveform as shown in Fig. 2.11(a). The voltage waveforms of phases A, B, and C are illustrated in red, green, and blue, respectively. It is obvious that there are 6 sectors in a sinusoidal period, which is defined by the interaction points of those voltage waveforms. The maximum voltage of phase A is considered to be a starting point, where it has been set as sector 1. Based on the SVPWM technique, the voltage vector can be presented in the switching state vector, which is suitable to transfer from the three-phase quantities into the stationary reference frame, α-β axis, as shown in Fig. 2.11.

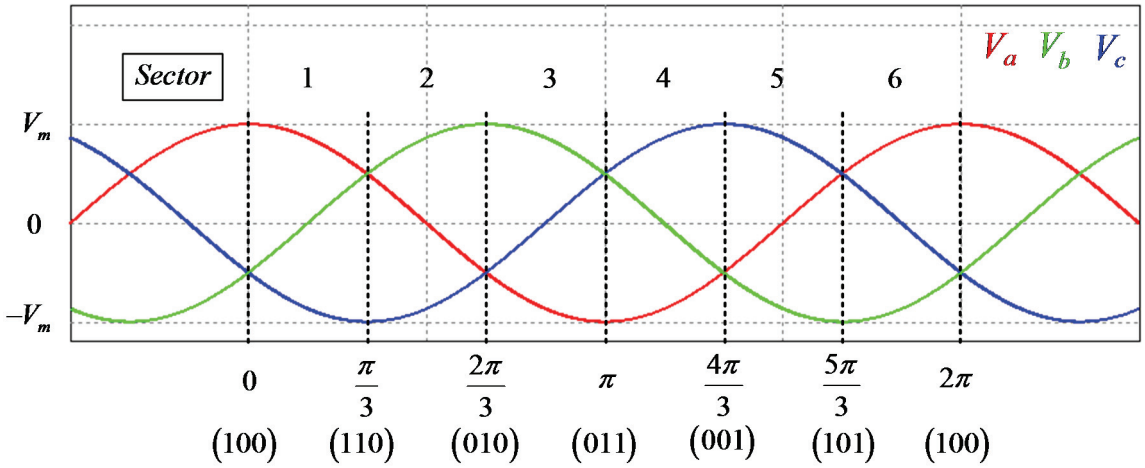

(a) Sector definition

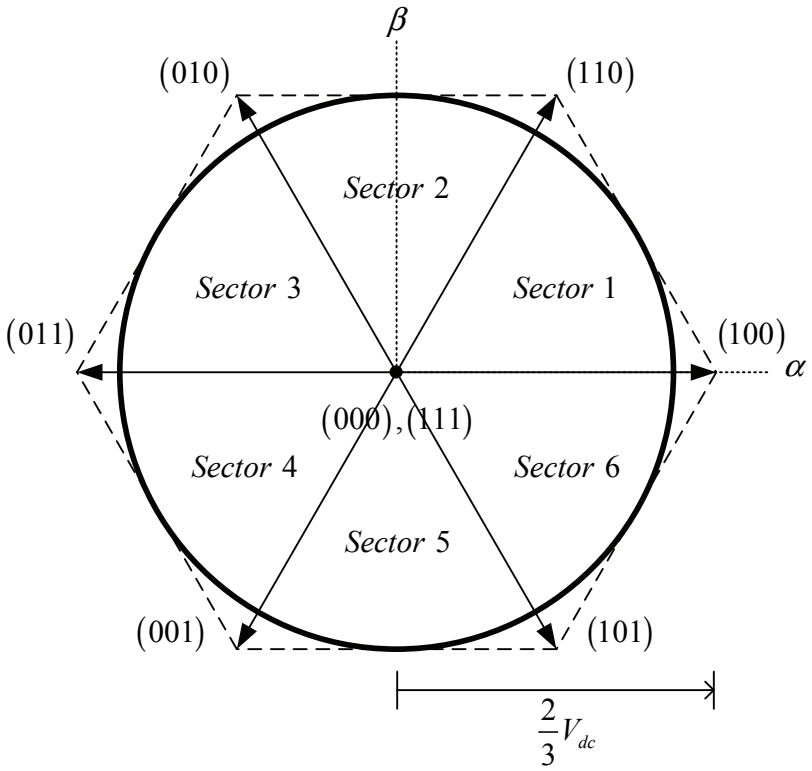

(b) Switching state vector.

Fig. 2.11. Switching state of the SVPWM.

Eight possible logical states are defined, including six-active states, sectors 1-6, and two zero-states in which all switches are either in on-state or off-state. In the switching state (100) condition, the upper switch of phase A is on-state, while phases B and C are off-states. Other conditions as (110), (010), (011), (001) and (101) are indicated for the switching state of sector 2 to sector 6, respectively.

Fig. 2.12 shows the switching operation based on the SVPWM of sector 1, which is (100) switching state. It is assumed that the inverter is operated under an ideal switching condition without the influence of long tail current due to nonlinear load which causes the current to be not reduced to zero instantaneously after the switch is at off-state. In Fig.2.12(a), based on the (100) switching state, S_1 is at on-state, while S_3 and S_5 are at off-state. Undoubtedly, S_2, S_4, S_6, the lower leg switches of phases A, B, and C respectively, are different from their upper switches. Therefore, the current of phase A flows from the dc power supply to the load, which is defined as positive direction. Meanwhile, the currents of phases B and C flow though their lower switches, as shown in Fig.2.12(a). Consequently, the phase voltages can be determined by the voltage division, as shown in Fig.2.12(b). The phase and line-line voltages in any switching sector based on the SVPWM can be presented in a function of DC-link voltage (V_{dc}), as shown in Table 2.4.

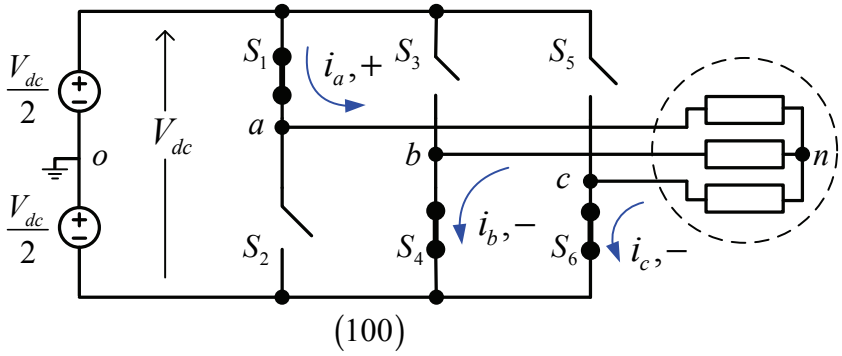

(a) Current direction.

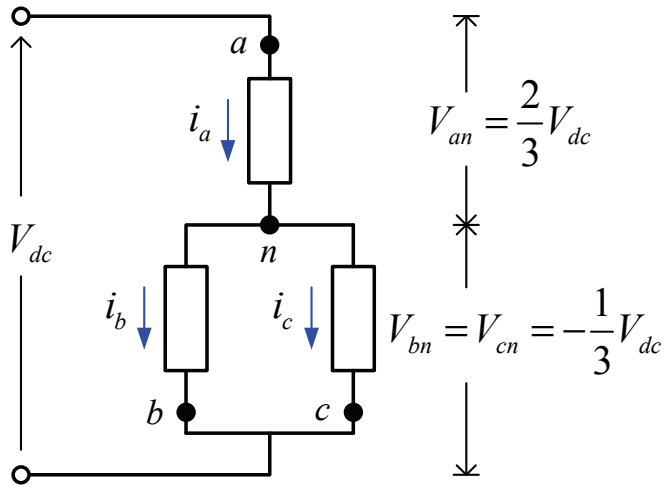

(b) Voltage division.

Fig. 2.12. Switching state in (100) condition, sector 1.

TABLE 2.4. Voltages of three-phase inverter based on SVPWM.

Vector	V_{an}	V_{bn}	V_{cn}	V_{ab}	V_{bc}	V_{ca}
1 (100)	$\frac{2}{3}V_{dc}$	$-\frac{1}{3}V_{dc}$	$-\frac{1}{3}V_{dc}$	V_{dc}	0	$-V_{dc}$
2 (110)	$-\frac{1}{3}V_{dc}$	$\frac{2}{3}V_{dc}$	$-\frac{1}{3}V_{dc}$	$-V_{dc}$	V_{dc}	0
3 (010)	$\frac{1}{3}V_{dc}$	$\frac{1}{3}V_{dc}$	$-\frac{2}{3}V_{dc}$	0	V_{dc}	$-V_{dc}$
4 (011)	$-\frac{1}{3}V_{dc}$	$-\frac{1}{3}V_{dc}$	$\frac{2}{3}V_{dc}$	0	$-V_{dc}$	V_{dc}
5 (001)	$\frac{1}{3}V_{dc}$	$-\frac{2}{3}V_{dc}$	$\frac{1}{3}V_{dc}$	V_{dc}	$-V_{dc}$	0
6 (101)	$-\frac{2}{3}V_{dc}$	$\frac{1}{3}V_{dc}$	$\frac{1}{3}V_{dc}$	$-V_{dc}$	0	V_{dc}
Null vector (000) (111)	0	0	0	0	0	0

Based on the three-phase VSI topology and the star-connection of three-phase load, the relationship between the terminal voltages (V_{ao}, V_{bo}, V_{co}), the phase voltages (V_{an}, V_{bn}, V_{cn}), and the line voltages (V_{ab}, V_{bc}, V_{ca}) can be summarized in matrix form as,

$$\begin{bmatrix} V_{an} \\ V_{bn} \\ V_{cn} \end{bmatrix} = \frac{1}{3}\begin{bmatrix} 2 & -1 & -1 \\ -1 & 2 & -1 \\ -1 & -1 & 2 \end{bmatrix}\begin{bmatrix} V_{ao} \\ V_{bo} \\ V_{co} \end{bmatrix} \tag{2.8}$$

and

$$\begin{bmatrix} V_{ab} \\ V_{bc} \\ V_{ca} \end{bmatrix} = \begin{bmatrix} 1 & -1 & 0 \\ 0 & 1 & -1 \\ -1 & 0 & 1 \end{bmatrix}\begin{bmatrix} V_{ao} \\ V_{bo} \\ V_{co} \end{bmatrix}. \tag{2.9}$$

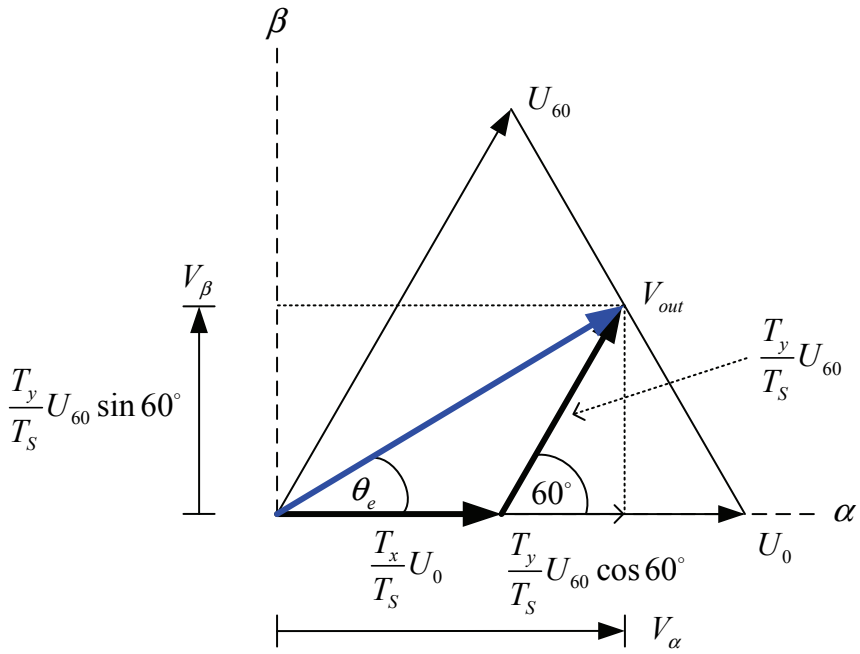

Fig. 2.13. An arbitrary voltage vector in sector 1 [TIE98].

Since the voltage generation based on the SVPWM is considered in the linear range, the modulation index can be determined by the ratio of maximum magnitude of voltage space vector to the maximum output voltage in linear range, as given in (2.10).

$$m = |U_0| = |U_{60}| = \frac{\frac{2}{3}V_{dc}}{\left(\frac{2}{3}V_{dc}\cos 30^\circ\right)} = \frac{2}{\sqrt{3}} = 1.155 \tag{2.10}$$

In Fig.2.13, based on the switching time period, the active and inactive time durations are presented as given in (2.11). The summation of them could not exceed the switching period (T_s). The output voltage can be presented in form of voltage space vector and the ratio between the active time duration and the switching time period, as given in (2.12).

$$T_s = T_x + T_y + T_z \tag{2.11}$$

$$V_{out} \approx \frac{T_x}{T_s}U_0 + \frac{T_y}{T_s}U_{60} \tag{2.12}$$

where T_s, T_x and T_y are switching time period, active time duration of the voltage space vector of U_0 and U_{60}, respectively, and T_z is time duration of a null vector, V_{out} is the output voltage.

Therefore, the output voltage can be expressed in the time modulation as,

$$V_{out} = t_1 U_0 + t_2 U_{60} \tag{2.13}$$

where

$$t_1 = \frac{T_x}{T_S}, \quad t_2 = \frac{T_y}{T_S}. \tag{2.14}$$

Therefore, the voltage space vector is expressed in the α-β axis as,

$$V_\alpha = V_S \cos\theta_e = t_1 |U_0| + t_2 |U_{60}| \cos 60^\circ \tag{2.15}$$

$$V_\beta = V_S \sin\theta_e = t_2 |U_{60}| \sin 60^\circ \tag{2.16}$$

By instituting of (2.14) into (2.15) and (2.16), the voltage space vector in α-β axis can be represented in terms of active time modulation as given in (2.17) and (2.18). Consequently, the active time durations for 6 sectors can be determined in function of α-β axis voltage vectors as shown in Table 2.5.

$$V_\alpha = \frac{2}{\sqrt{3}} t_1 + \frac{1}{\sqrt{3}} t_2 \tag{2.17}$$

$$V_\beta = t_2 \tag{2.18}$$

TABLE 2.5. Time modulation of the SVPWM.

Sector	t_1	t_2
1	$\frac{\sqrt{3}}{2}V_\alpha - \frac{1}{2}V_\beta$	V_β
2	$-\frac{\sqrt{3}}{2}V_\alpha + \frac{1}{2}V_\beta$	$\frac{\sqrt{3}}{2}V_\alpha + \frac{1}{2}V_\beta$
3	V_β	$-\frac{\sqrt{3}}{2}V_\alpha - \frac{1}{2}V_\beta$
4	$-V_\beta$	$-\frac{\sqrt{3}}{2}V_\alpha + \frac{1}{2}V_\beta$
5	$-\frac{\sqrt{3}}{2}V_\alpha - \frac{1}{2}V_\beta$	$\frac{\sqrt{3}}{2}V_\alpha - \frac{1}{2}V_\beta$
6	$\frac{\sqrt{3}}{2}V_\alpha + \frac{1}{2}V_\beta$	$-V_\beta$

Finally, the variables (t_{aon}, t_{bon}, t_{con}) are defined as (2.19), which is called as duty cycle, in order to calculate the switching functions (T_a, T_b, T_c). The switching functions in each sector are defined in function of the duty cycles for a practical PWM generation, as shown in Table 2.6. The switching pattern of sector 1 can be presented in Fig. 2.14. In addition, the switching patterns of all sectors based on the SVPWM technique are shown in Fig. 2.15.

$$t_{aon} = \frac{T_s - t_1 - t_2}{2}$$
$$t_{bon} = t_{aon} + t_1 \tag{2.19}$$
$$t_{con} = t_{bon} + t_2$$

TABLE 2.6. PWM patterns.

Sector	1	2	3	4	5	6
T_a	t_{aon}	t_{bon}	t_{con}	t_{con}	t_{bon}	t_{aon}
T_b	t_{bon}	t_{aon}	t_{aon}	t_{bon}	t_{con}	t_{con}
T_c	t_{con}	t_{con}	t_{bon}	t_{aon}	t_{aon}	t_{bon}

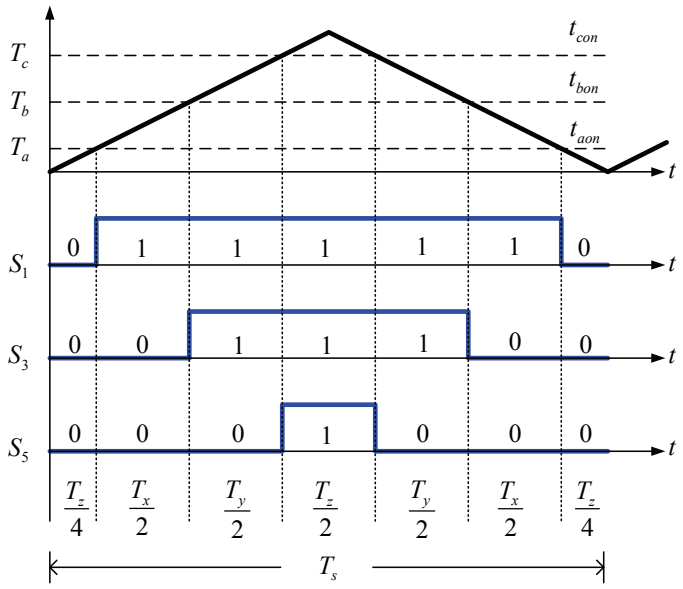

Fig. 2.14. PWM patterns in sector 1.

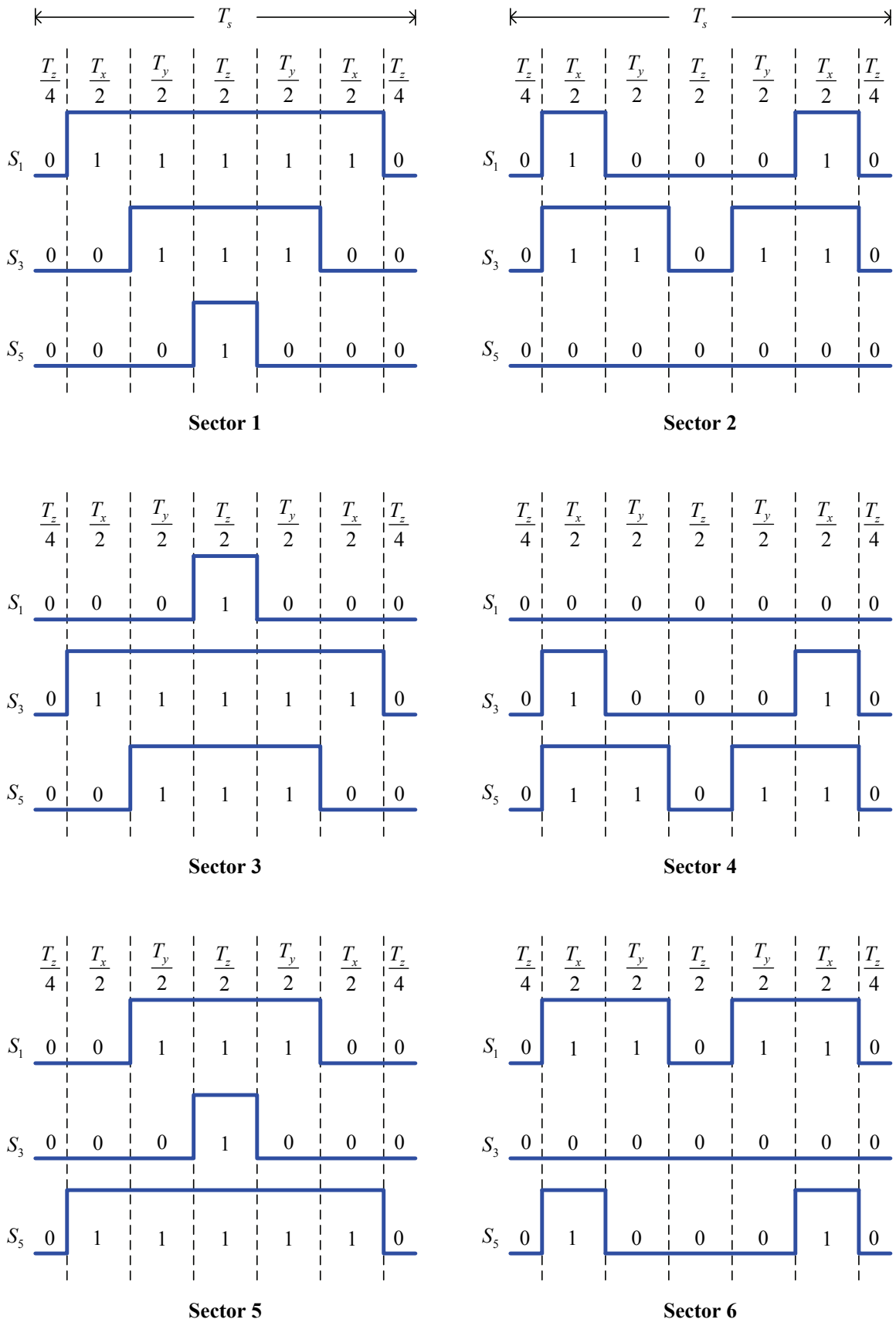

Fig. 2.15. SVPWM switching patterns for all sectors.

2.5.2 Minimum magnitude error over-modulation

The minimum magnitude error over-modulation (MMEOM) [HAV99], [MOC91] is one of the over-modulation techniques that can be used to improve the utilization of DC-link voltage in flux-weakening region, where the requirement of machine voltage tends to exceed the voltage boundary provided by the actual inverter system. The magnitude of the original voltage vector will be modified and it is limited within the hexagon surface [SEO98], as illustrated by the bold-lines shown in Fig.2.16. Therefore, in flux-weakening region, the higher output voltage can be provided compared with the SVPWM, as aforementioned in the previous section. The generated voltage can be divided into 6 sectors in α-β axes, which has been described the same as the SVPWM in the previous section. Since it might be easier to explain the modified reference voltage principle in each sector, the per-unit is considered for the MMEOM, in which the base-voltage is the maximum voltage of the SVPWM ($2/\sqrt{3}$). Consequently, the maximum output of modified reference voltage in α-β axis can be 1.154 and 1.0 per-units (p.u.), respectively.

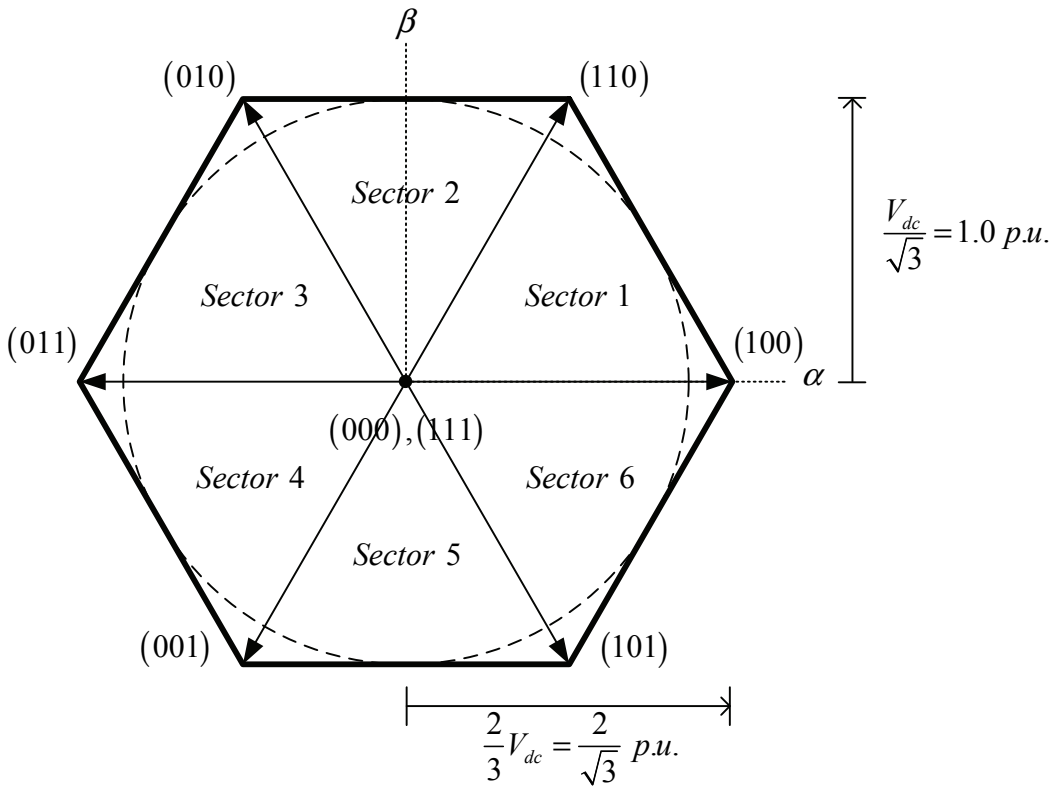

Fig. 2.16. Switching states of the MMEOM.

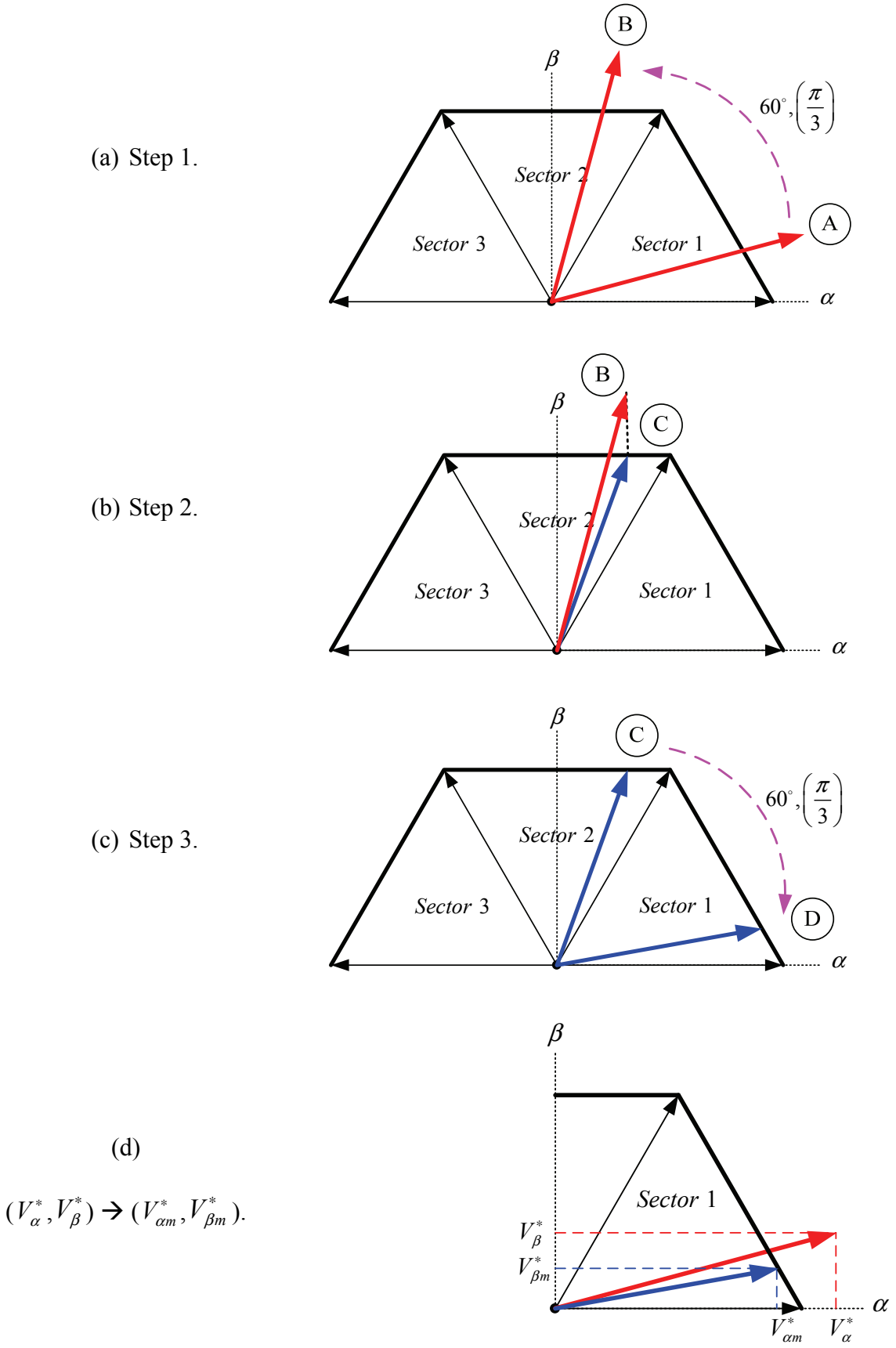

Fig. 2.17. MMEOM technique in sector 1.

In sector 1, the modified reference voltage can be clearly explained in Fig. 2.17 by utilising the arrow symbol. The red arrow represents the reference voltage vector, while the blue is the modified reference voltage vector. In this sector, it can be mainly arranged into 3 steps as follows.

Calculation voltage for sector 1:

Step 1:

$$\begin{bmatrix} V_{\alpha}^{'} \\ V_{\beta}^{'} \end{bmatrix} = \begin{bmatrix} \cos\left(\frac{\pi}{3}\right) & -\sin\left(\frac{\pi}{3}\right) \\ \sin\left(\frac{\pi}{3}\right) & \cos\left(\frac{\pi}{3}\right) \end{bmatrix} \begin{bmatrix} V_{\alpha}^{*} \\ V_{\beta}^{*} \end{bmatrix} = \begin{bmatrix} \frac{1}{2}V_{\alpha}^{*} - \frac{\sqrt{3}}{2}V_{\beta}^{*} \\ \frac{\sqrt{3}}{2}V_{\alpha}^{*} + \frac{1}{2}V_{\beta}^{*} \end{bmatrix} \tag{2.20}$$

Step 2:

$$\begin{bmatrix} V_{\alpha}^{'} \\ V_{\beta}^{'} \end{bmatrix} = \begin{bmatrix} \frac{1}{2}V_{\alpha}^{*} - \frac{\sqrt{3}}{2}V_{\beta}^{*} \\ 1 \end{bmatrix} \tag{2.21}$$

Step 3:

$$\begin{bmatrix} V_{\alpha m}^{*} \\ V_{\beta m}^{*} \end{bmatrix} = \begin{bmatrix} \cos\left(\frac{\pi}{3}\right) & \sin\left(\frac{\pi}{3}\right) \\ -\sin\left(\frac{\pi}{3}\right) & \cos\left(\frac{\pi}{3}\right) \end{bmatrix} \begin{bmatrix} V_{\alpha}^{'} \\ V_{\beta}^{'} \end{bmatrix} = \begin{bmatrix} \frac{1}{4}V_{\alpha}^{*} - \frac{\sqrt{3}}{4}V_{\beta}^{*} + \frac{\sqrt{3}}{2} \\ -\frac{\sqrt{3}}{4}V_{\alpha}^{*} + \frac{3}{4}V_{\beta}^{*} + \frac{1}{2} \end{bmatrix} \tag{2.22}$$

In the step 1, the reference voltage vector $(V_{\alpha\beta}^{*})$ is allocated in sector 1, at point A in Fig.2.17(a), by 60 degrees or π/3 radians in the counter clockwise (CCW) to the sector 2, as shown in point B. The transferred voltage $(V_{\alpha\beta}^{'})$ for this step is given in (2.20). Then, in the step 2, since the transferred voltage vector exceeds the voltage limit of inverter, it will be projected from point B to C, where it is the hexagon, as shown in Fig.2.17(b). As a result, the transferred voltage vector in the β-axis will be set at 1.0 p.u., while the transferred voltage vector in the α-axis is remained the same value, as shown in the equation (2.21). In the step 3, the transferred reference voltage is allocated from point C backward to point D in the sector 1 by 60 degrees, as shown in Fig.2.17(c). Therefore, the modified reference voltages $(V_{\alpha m}^{*}, V_{\beta m}^{*})$, in per-unit, for the sector 1 can be determined as expressed in the equation (2.22), and those reference voltages can be obviously compared as shown in Fig.2.17(d).

(a) Step 1.

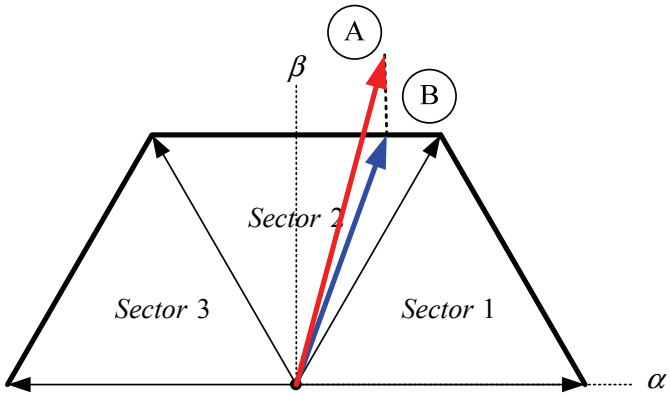

(b)

$(V_\alpha^*, V_\beta^*) \rightarrow (V_{\alpha m}^*, V_{\beta m}^*)$.

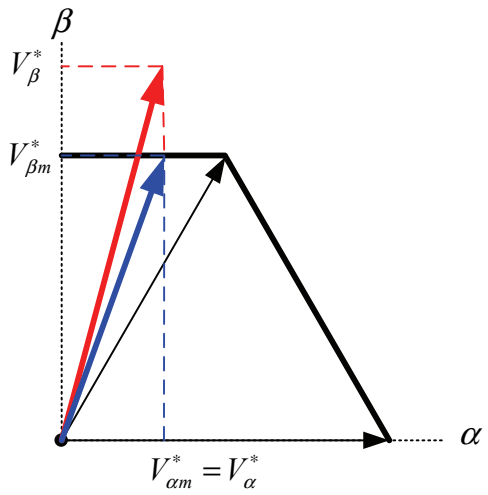

Fig. 2.18. MMEOM technique in sector 2.

Calculation voltage for sector 2:

$$\begin{bmatrix} V_{\alpha m}^* \\ V_{\beta m}^* \end{bmatrix} = \begin{bmatrix} V_\alpha^* \\ 1 \end{bmatrix} \tag{2.23}$$

Fig.2.18 shows the operation of the MMEOM in sector 2. The reference voltage, which is expressed in red, is out of the voltage limit of inverter as shown in bold line of hexagon. Hence, the reference voltage vector will be projected from point A into point B, where it is the edge of hexagon, as shown in Fig.2.18(a). Accordingly, the modified voltage vector can be determined as given in equation (2.23). Undoubtedly, the modified voltage vector can be clearly illustrated in Fig.2.18(b).

(a) Step 1.

(b) Step 2.

(c) Step 3.

(d)

$(V_\alpha^*, V_\beta^*) \rightarrow (V_{\alpha m}^*, V_{\beta m}^*)$.

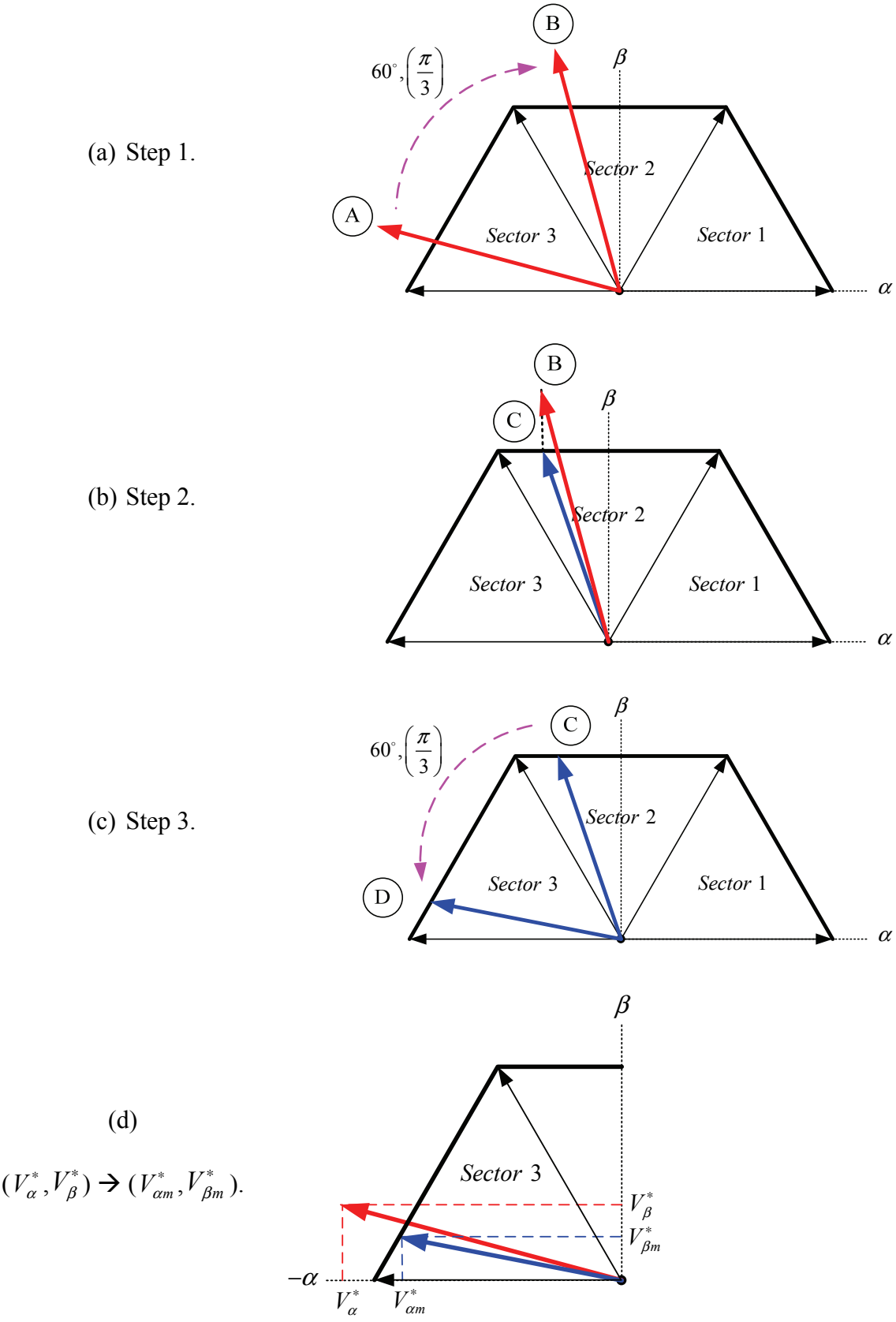

Fig. 2.19. MMEOM technique in sector 3.

Calculation voltage for sector 3:

Step 1:

$$\begin{bmatrix} V_{\alpha}^{'} \\ V_{\beta}^{'} \end{bmatrix} = \begin{bmatrix} \cos\left(\frac{\pi}{3}\right) & \sin\left(\frac{\pi}{3}\right) \\ -\sin\left(\frac{\pi}{3}\right) & \cos\left(\frac{\pi}{3}\right) \end{bmatrix} \begin{bmatrix} V_{\alpha}^{*} \\ V_{\beta}^{*} \end{bmatrix} = \begin{bmatrix} \frac{1}{2}V_{\alpha}^{*} + \frac{\sqrt{3}}{2}V_{\beta}^{*} \\ -\frac{\sqrt{3}}{2}V_{\alpha}^{*} + \frac{1}{2}V_{\beta}^{*} \end{bmatrix} \tag{2.24}$$

Step 2:

$$\begin{bmatrix} V_{\alpha}^{'} \\ V_{\beta}^{'} \end{bmatrix} = \begin{bmatrix} \frac{1}{2}V_{\alpha}^{*} + \frac{\sqrt{3}}{2}V_{\beta}^{*} \\ 1 \end{bmatrix} \tag{2.25}$$

Step 3:

$$\begin{bmatrix} V_{\alpha m}^{*} \\ V_{\beta m}^{*} \end{bmatrix} = \begin{bmatrix} \cos\left(\frac{\pi}{3}\right) & -\sin\left(\frac{\pi}{3}\right) \\ \sin\left(\frac{\pi}{3}\right) & \cos\left(\frac{\pi}{3}\right) \end{bmatrix} \begin{bmatrix} V_{\alpha}^{'} \\ V_{\beta}^{'} \end{bmatrix} = \begin{bmatrix} \frac{1}{4}V_{\alpha}^{*} + \frac{\sqrt{3}}{4}V_{\beta}^{*} - \frac{\sqrt{3}}{2} \\ \frac{\sqrt{3}}{4}V_{\alpha}^{*} + \frac{3}{4}V_{\beta}^{*} + \frac{1}{2} \end{bmatrix} \tag{2.26}$$

In sector 3, the modified voltage vector can be determined the same as in sector 1, which is only the transformation angle, is in the clockwise (CW) by 60 degrees ($\pi/3$ radians) as shown in Fig.2.19. The calculation in this sector can be shown in (2.24) – (2.26). However, the voltage vectors in sectors 4, 5, and 6 are absolutely the same as in sectors 1, 2, and 3, respectively. Therefore, the modified reference voltages for all sectors can be given in Table 2.7, which are expressed in per-unit.

TABLE 2.7. Modified α-β reference voltages based on the MMEOM (in p.u.).

Sector	$V_{\alpha m}^{*}$	$V_{\beta m}^{*}$
1	$\frac{1}{4}V_{\alpha}^{*} - \frac{\sqrt{3}}{4}V_{\beta}^{*} + \frac{\sqrt{3}}{2}$	$-\frac{\sqrt{3}}{4}V_{\alpha}^{*} + \frac{3}{4}V_{\beta}^{*} + \frac{1}{2}$
2	V_{α}^{*}	1
3	$\frac{1}{4}V_{\alpha}^{*} + \frac{\sqrt{3}}{4}V_{\beta}^{*} - \frac{\sqrt{3}}{2}$	$\frac{\sqrt{3}}{4}V_{\alpha}^{*} + \frac{3}{4}V_{\beta}^{*} + \frac{1}{2}$
4	$\frac{1}{4}V_{\alpha}^{*} - \frac{\sqrt{3}}{4}V_{\beta}^{*} - \frac{\sqrt{3}}{2}$	$-\frac{\sqrt{3}}{4}V_{\alpha}^{*} + \frac{3}{4}V_{\beta}^{*} - \frac{1}{2}$
5	V_{α}^{*}	-1
6	$\frac{1}{4}V_{\alpha}^{*} + \frac{\sqrt{3}}{4}V_{\beta}^{*} + \frac{\sqrt{3}}{2}$	$\frac{\sqrt{3}}{4}V_{\alpha}^{*} + \frac{3}{4}V_{\beta}^{*} - \frac{1}{2}$

2.6 Inverter nonlinearity

The inverter nonlinearity voltage results in the difference between the real voltage and the command voltage, which is provided by the control system. Furthermore, it also degrades the control performance of drive system, especially in the flux-weakening operation. The nonlinearity voltage is caused by the dead-time, the dc-link voltage error between the real and measured values, and the non-ideal characteristic of switching devices [KIM06]. However, since the compensation of the dc-link voltage error is not necessarily required for all proposed control strategies, which is considered in this thesis. The dead-time and voltage drop caused by non-ideal characteristic of switching devices are explained as follows.

2.6.1 Dead-time

Since the motor can be considered as a resistance and inductance load, the dead-time or the blanking time, which can be programed by the drive processor, is normally considered to prevent the short circuit of the phase-leg switch of inverter during the commutation. The dead-time is usually defined between 2-5 µs, which it is set at 2 µs in this thesis which larger than switching time delay (on/off state) of the inverter switches. Fig.2.20 compares the switching between the ideal case and the actual operation with dead-time in both upper and lower switches, where S_1 and S_2 are expressed as the switching signals for phase A.

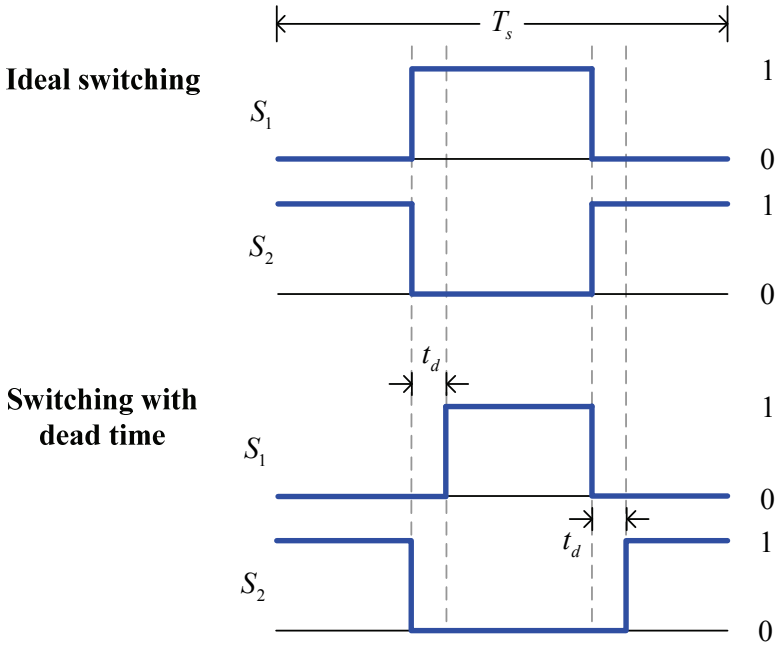

Fig. 2.20. Switching signal with dead-time.

2.6.2 Inverter nonlinearity voltage estimation

Fig.2.21 shows the active power devices operation, which is based on the phase current direction, for one leg of the three-phase VSI. In an ideal switching, the upper and lower switches in each phase leg, e.g. S_1 and S_2 of phase A, are assumed to be changing their states at the same time. When $i_a \geq 0$, S_1 is turned on ($S_1 = 1$), and S_2 will be at off-state ($S_2 = 0$), the terminal voltage (V_{ao}) is equal to $V_{dc}/2 - V_{ce}$, as shown in Fig.2.21(a), where V_{ce} is the saturation voltage of the on-state switch. Meanwhile, when S_1 is at off-state, the phase current will flow through the free-wheeling diode of the lower switch, S_2. Therefore, $V_{ao} = -V_{dc}/2 - V_d$, where V_d is the forward voltage of the free-wheeling diode. On the other hand, in case of $i_a < 0$, as shown in Fig.2.21(b), $V_{ao} = V_{dc}/2 + V_d$ when S_1 is at on-state, while $-V_{dc}/2 + V_{ce}$ is at off-state. Hence, the terminal voltage in each phase can be expressed in the form of equation as (2.27) - (2.29) [KIM06].

$$V_{ao} = (V_{dc} - V_{ce} + V_d)(S_1 - 0.5) - \frac{1}{2}(V_{ce} + V_d)\,sign(i_a) \tag{2.27}$$

$$V_{bo} = (V_{dc} - V_{ce} + V_d)(S_3 - 0.5) - \frac{1}{2}(V_{ce} + V_d)\,sign(i_b) \tag{2.28}$$

$$V_{co} = (V_{dc} - V_{ce} + V_d)(S_5 - 0.5) - \frac{1}{2}(V_{ce} + V_d)\,sign(i_c). \tag{2.29}$$

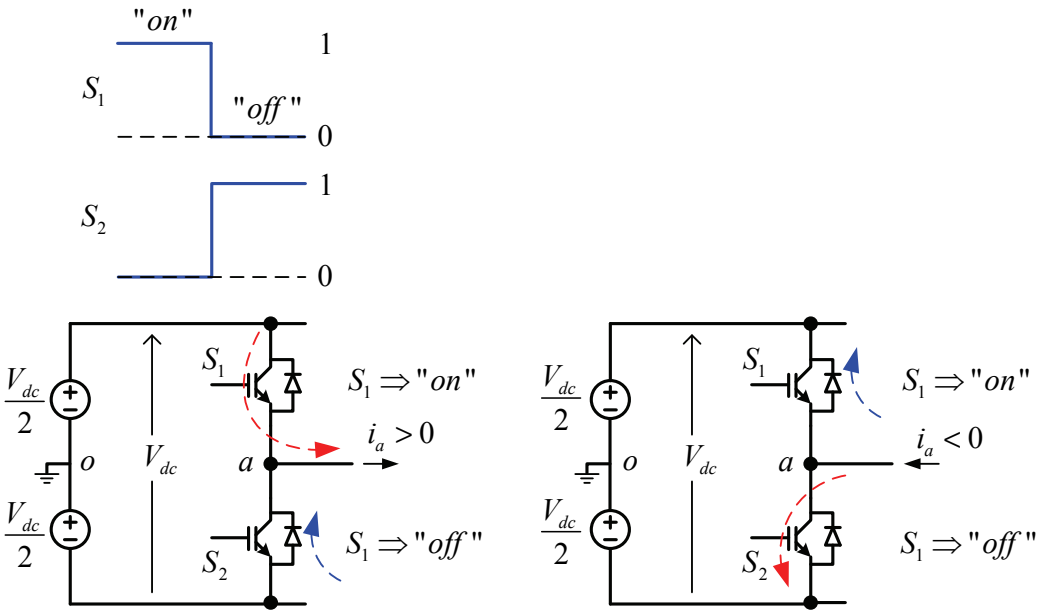

(a) $i_a \geq 0$. (b) $i_a < 0$.

Fig. 2.21. Active power device operation following the current direction of the VSI.

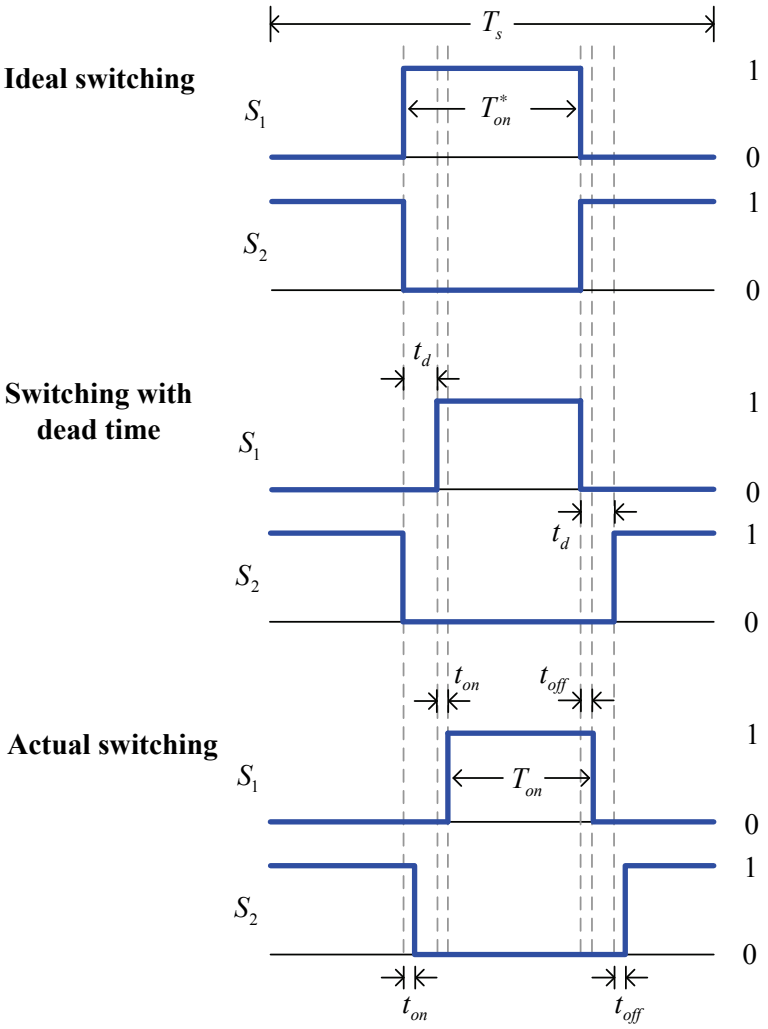

Fig. 2.22. Practical switching signals.

Indeed, the terminal voltage can be represented by duty ratio, e.g. $S_1 = T_{on}/T_s$ [KIM06], in order to estimate the average voltage in a switching period. However, the error of on-state time (T_{on}) will be impacted by the loss time as illustrated in Fig.2.22, where the practical switching signal has considered the influence of dead-time and switching time delay in both on-state (t_{on}) and off-state (t_{off}). Therefore, the loss time in each phase can be determined as given in (2.30) – (2.32).

$$T^*_{on,a} - T_{on,a} = (t_d + t_{on} - t_{off})sign(i_a) \tag{2.30}$$

$$T^*_{on,b} - T_{on,b} = (t_d + t_{on} - t_{off})sign(i_b) \tag{2.31}$$

$$T^*_{on,c} - T_{on,c} = (t_d + t_{on} - t_{off})sign(i_c) \tag{2.32}$$

The voltage drop of switching power devices, which is the IGBT for this thesis, can be represented as,

$$V_{ce} = V_{ceo} + r_{ce}\left|i_a\right|, \quad V_d = V_{do} + r_d\left|i_a\right|. \tag{2.33}$$

where V_{ceo}, V_{do} are the threshold voltages of switching power devices, switch and free-wheeling diode, respectively, and r_{ce}, r_d denote their resistances.

According to the relationship of the terminal voltage and the phase voltage that has been introduced in (2.8), the phase voltage which considers the inverter nonlinearity can be given by (2.34).

$$\begin{aligned} V_{an} = {} & \frac{\left(V_{dc} - V_{ce} + V_d\right)}{3}\left[\frac{2T_{on,a} - T_{on,b} - T_{on,c}}{T_s}\right] \\ & - \frac{\left(2sign(i_a) - sign(i_b) - sign(i_c)\right)\left(V_{ce0} + V_{do}\right)}{6} \\ & - \frac{\left(r_{ce} + r_d\right) i_a}{2} \end{aligned}. \tag{2.34}$$

Meanwhile, the reference phase voltage can be calculated from the ideal on-state time as,

$$V_{an}^* = \frac{V_{dc}}{3}\left[\frac{2T_{on,a}^* - T_{on,b}^* - T_{on,c}^*}{T_s}\right]. \tag{2.35}$$

Therefore, the voltage loss due to the non-ideal characteristic of switching power devices of phase A can be determined by $\Delta V_{an} = V_{an}^* - V_{an}$. It can be summarized as given in (2.36) [KIM06] [LIU12].

$$\begin{bmatrix} \Delta V_{an} \\ \Delta V_{bn} \\ \Delta V_{cn} \end{bmatrix} = A_p \begin{bmatrix} 2 & -1 & -1 \\ -1 & 2 & -1 \\ -1 & -1 & 2 \end{bmatrix} \begin{bmatrix} sign(i_a) \\ sign(i_b) \\ sign(i_c) \end{bmatrix} + \frac{r_{ce} + r_d}{2} \begin{bmatrix} i_a \\ i_b \\ i_c \end{bmatrix}. \tag{2.36}$$

The intermediate parameter (A_p) is provided as,

$$A_p = \frac{\left(V_{dc} - V_{ce} + V_d\right)\left(t_d + t_{on} - t_{off}\right)}{3T_s} + \frac{V_{ceo} + V_{do}}{6}. \tag{2.37}$$

The inverter nonlinearity voltage loss can be expressed in the *d*-*q* axis, by utilising Park's transformation, as given in (2.38).

$$\begin{bmatrix} \Delta V_d^{nonlinear} \\ \Delta V_q^{nonlinear} \end{bmatrix} = 2A_p \begin{bmatrix} \sin\theta_e & \sin\left(\theta_e - \frac{\pi}{3}\right) & \sin\left(\theta_e + \frac{\pi}{3}\right) \\ \cos\theta_e & \cos\left(\theta_e - \frac{\pi}{3}\right) & \cos\left(\theta_e + \frac{\pi}{3}\right) \end{bmatrix} \begin{bmatrix} sign(i_a) \\ sign(i_b) \\ sign(i_c) \end{bmatrix} + \frac{r_{ce} + r_d}{2} \begin{bmatrix} i_d \\ i_q \end{bmatrix}. \quad (2.38)$$

Fig.2.23 shows the inverter nonlinearity voltage drops in both *d*-axis and *q*-axis when the machine is operated in constant-torque region, i.e. i_q = 7.92 A, i_d = 0, with the speed at 500 rpm. Based on the equation (2.38), the measured phase currents and rotor position are required in order to determine the resistance voltage drop of inverter switches and current directions. Meanwhile, the voltage drop due to the non-ideal characteristic of inverter switches (A_p), which has been defined in (2.37), is calculated based on the information of switching devices provided by the manufacturer [INT05]. V_{dc} = 40V, T_s = 0.0001 s (switching frequency is 10 kHz), t_d = 2 µs, t_{on} = 500 ns, t_{off} = 700 ns, V_{ceo} = 1.85 V, V_{do} = 2.2 V, and $r_{ce} = r_d$ = 0.04 Ω.

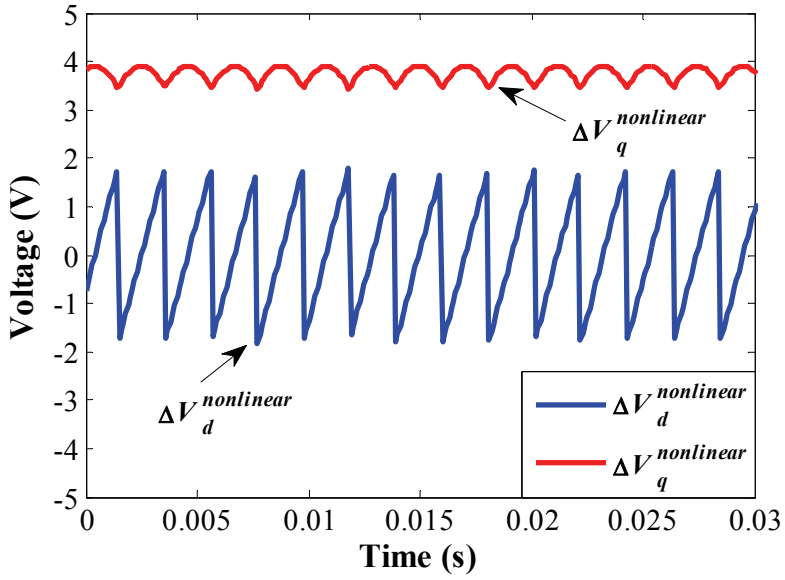

Fig. 2.23. Measured inverter nonlinearity voltage loss.

2.7 Experimental hardware

2.7.1 Three-phase voltage source inverter

The three-phase VSI that is utilised to verify all proposed control methods is illustrated in Fig.2.24. It consists of 6 switching devices, for which the IGBTs are used in this thesis. Consequently, a free-wheeling diode will be provided for each switch in order to protect the switching device from being damaged by the reverse current due to an inductive load, as shown in Fig.2.25. The IRAMY20UP60B intelligent module [INT05], which provides rated current and voltage of 20A and 600V, was selected. Furthermore, since the IGBT module has a built-in integrated gate driver for all gating signals, it does not require any additional hardware for triggering the switches. The PWM signals generated from the DS5101 board provide a voltage level at 5V. Hence, it is compatible to the logic input voltage of the IGBT module, which makes it simple without the requirement of the voltage level shifter board.

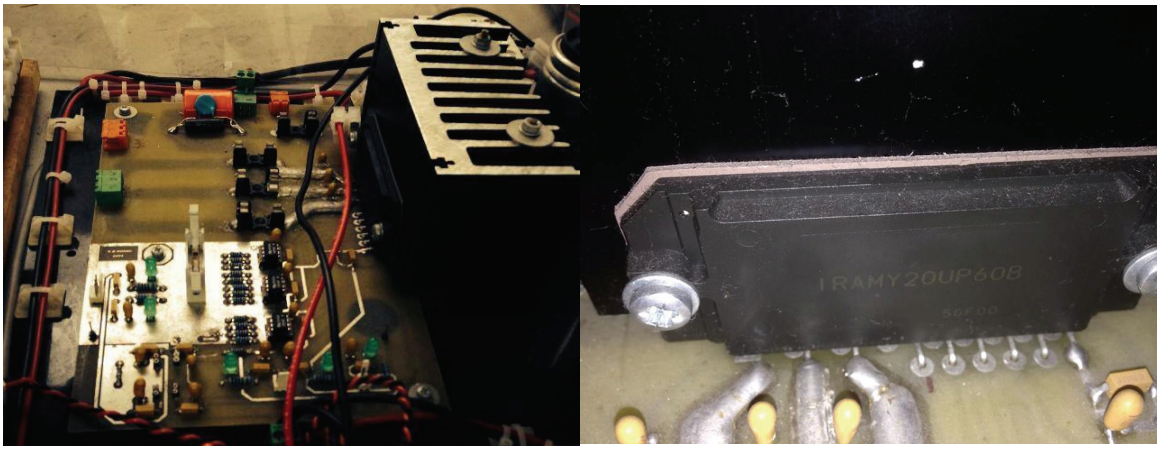

Fig. 2.24. Three-phase voltage source inverter.

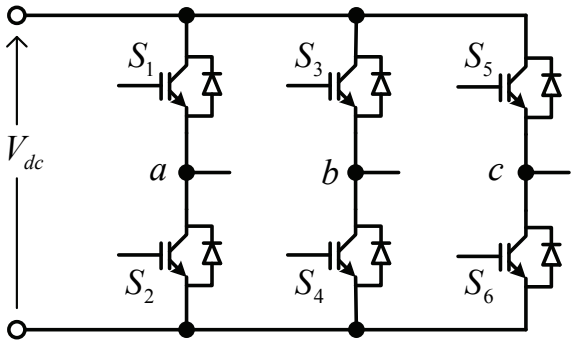

Fig. 2.25. Three-phase voltage source inverter circuit.

2.7.2 DC-DC converter

Since the hybrid-excited PM machines exhibit an outstanding capability to adjust the flux-linkage through the field winding, the DC-DC converter is required in order to regulate the field excitation current. Indeed, the field winding resistance of both prototype machines is low, and hence, a step-down (buck-type) converter is considered, as shown in Fig.2.26. Meanwhile, the field excitation current direction can be easily controlled by an H-bridge, which consists of 4 switching devices. The field voltage (v_f) is automatically adjusted corresponding to the field excitation current feedback control in which the proportional and integral (PI) regulators are utilised in order to improve the tracking accuracy of the field excitation current. The DC-DC converter board, which is employed to control the field excitation current according to its reference value, is shown in Fig.2.27.

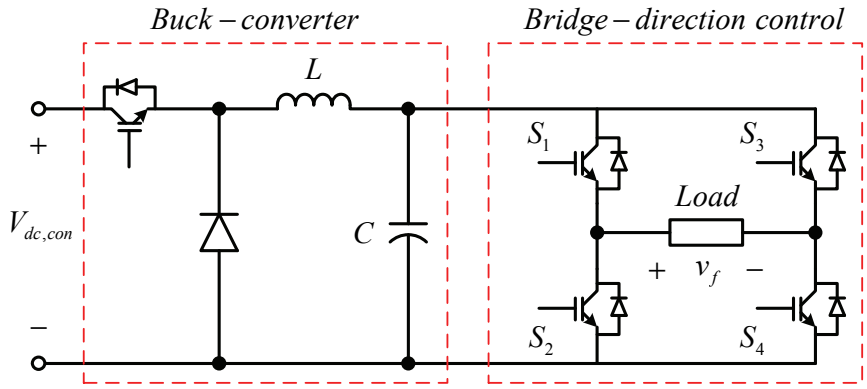

Fig. 2.26. Circuit diagram of the step-down converter with H-bridge.

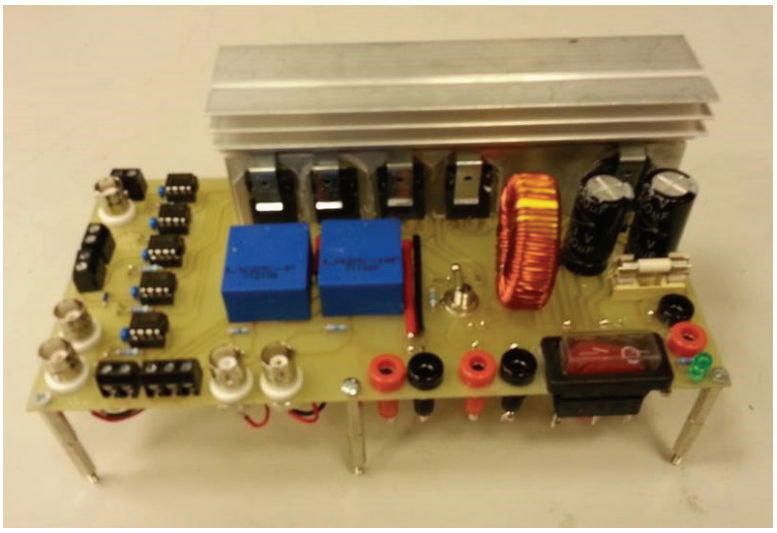

Fig. 2.27. DC-DC converter board.

The inductance and capacitance in Fig.2.27 are 500 mH and 1000 μF, respectively. All switching devices are FGH40N60SMDF's IGBTs, which can provide rated current and voltage of 40A and 600V [FAI13]. Indeed, the gate-drivers and opt-couples are also built-in Fig.2.28 shows the tracking accuracy of the field excitation current control in the specific values of both positive and negative currents (-4A, -2A, 2A, 4A). It is obvious that the field excitation current can track with its reference value in both positive and negative directions. Additionally, the field excitation current control also provides a good dynamic performance as can be seen in the step response shown in Fig.2.29. The rise-time is only 0.0292 s, while the reference current is set at 5.6A.

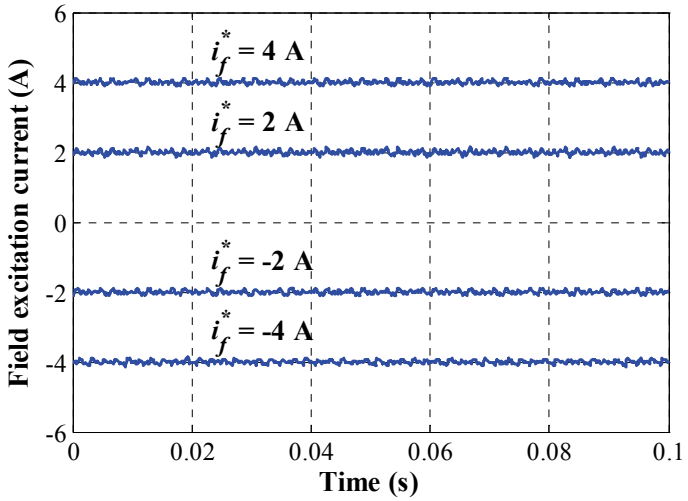

Fig. 2.28. Field excitation current tracking performance.

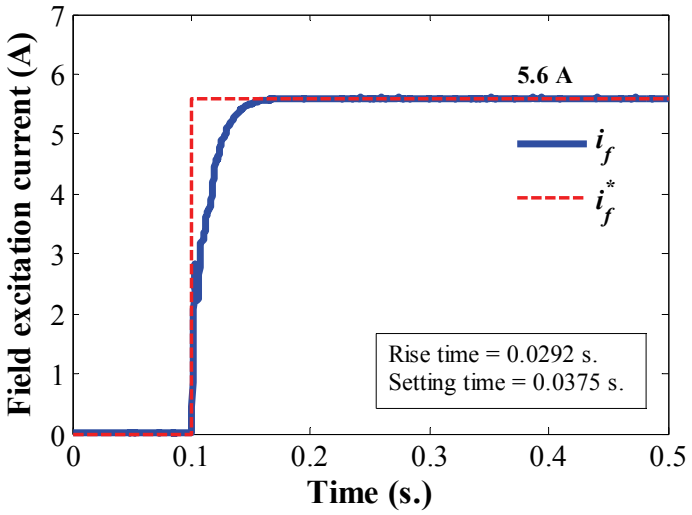

Fig. 2.29. Step response of the field excitation current.

2.7.3 Magnetic contactor

The general purpose magnetic contactor, as shown in Fig.2.30, was designed for employing in high current connection which can operate as a switch. It is utilised in the fault protection in chapter 6, and it can be applied to other application since there are 2 optional connections, i.e. normally close (NC) and normally open (NO), which is based on the product series of Finder series 44.62 as double poles double terminals (DPDT) [FIN13]. The maximum current is available at 16A, while a safety-oriented designs assuring high surge resistance for the voltage level is at 10,000V. Moreover, it can be used in both AC and DC power systems.

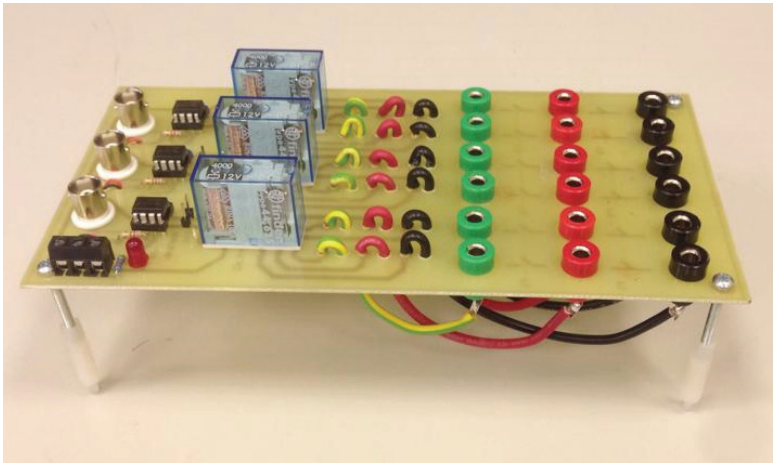

Fig. 2.30. General propose magnetic contactor board.

2.7.4 Current and voltage transducers

The hall-effect current transducer (LA 25-P) [LEM14] is utilised for measuring the instantaneous values of currents including the armature current in each phase and the field excitation current, as shown in Fig.2.31(left) that is only one of the general purpose current transducer board. In the same way, the Hall-effect voltage transducer (LV 25-P) [LEM12] is utilised to measure the DC-link voltage, the phase and line-line voltages, and also the field voltage, as shown in Fig.2.31(right). Fortunately, since the dSPACE platform (DS2004 high speed A/D board) provides a wide range voltage level for analogue input signals in both positive and negative directions, ±10V voltage range is selected in this thesis. Consequently, the additional voltage level shifter board is not required as other processors since it is compatible to connect the output current and voltage signals directly to the dSPACE board.

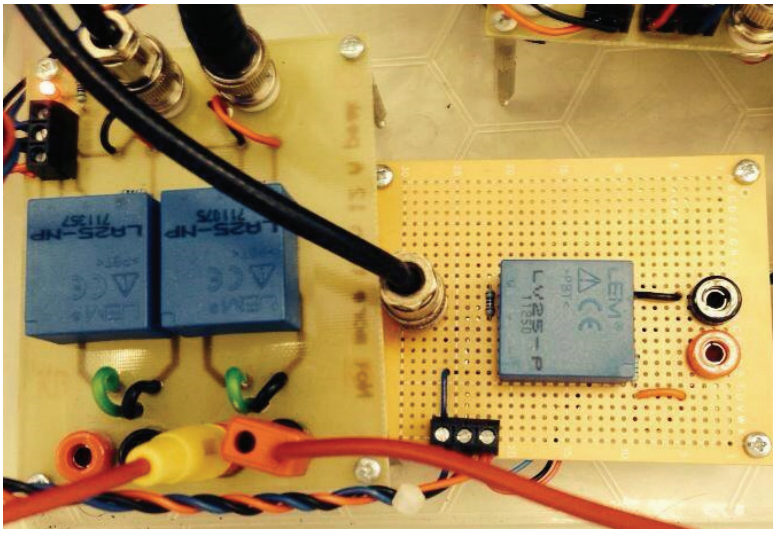

Fig. 2.31. Voltage and current transducer boards.

2.7.5 Incremental encoder

The incremental encoder (Hengstler RI58-D) [HEN10] is employed in order to measure the instantaneous rotor position information, as illustrated in Fig.2.32. The maximum speed is available at 4000 rpm, and it provides high accuracy with 5000 pulses per revolution. This encoder is a through hollow shaft type in which the shaft diameter is 12 mm. Basically, the output signals of this encoder consist of index pulse signal and two quadrature pulse signals, which are commonly defined their symbols as Z, A, and B, respectively. Indeed, the numbers of pulses per revolution of both A and B are the same, but only the pulse waveform of signal A always leads the signal B by 90 electrical degrees. Meanwhile, the pulse signal Z appears in every revolution for determining the initial rotor position, and it is also used to reset the pulse counter.

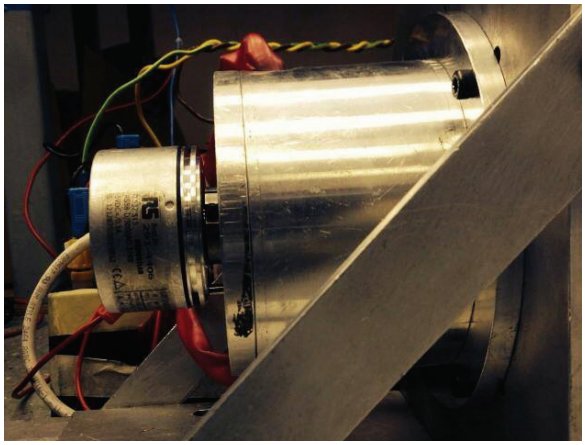

Fig. 2.32. Incremental encoder.

2.7.6 Other equipment

The Megtrol torque transducer (TM307) [MAG14], as shown in Fig.2.33(a), is utilised to measure the instantaneous torque for all application in this thesis. It provides the maximum torque at 10 Nm, and it can also measure the speed where the maximum range is 20,000 rpm. Since both measured torque and speed signals can directly connect to the dSPACE board without the requirement of additional hardware, it is very easy to implement for a drive system. Fig.2.33(b) shows the test-rig which was designed for the AC machine drive. The 1.5 kW wound field type DC motor consists of 4 wires, in which the armature and field windings can be separately controlled. The DC motor is employed to define the load torque, which acts as a generator by utilising the resistance load to dissipate the output power. Therefore, there are 2 options to adjust the load torque, i.e. by verifying the resistance or by controlling the field winding voltage. For that reason, it is especially suitable to be used in the flux-weakening operation.

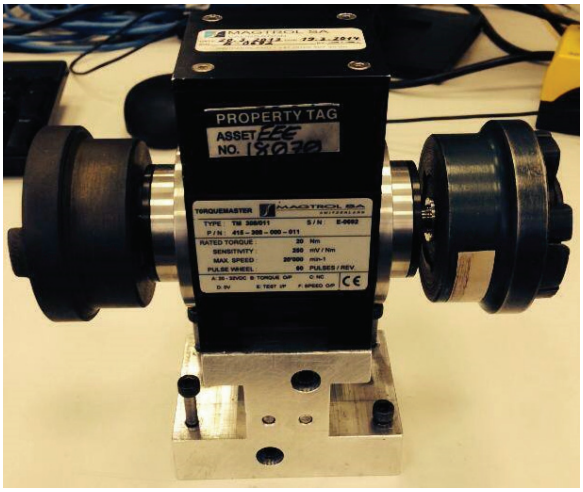

(a) Torque transducer.

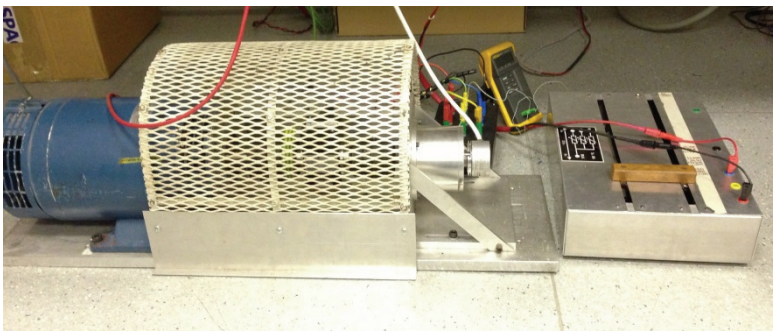

(b) Test-rig.

Fig. 2.33. Torque transducer and test-rig.

2.8 dSPACE-based drive system

Fig.2.34 shows the block diagram of the developed dSPACE-based drive system for the hybrid-excited PM machine. In order to achieve the high performance of the drive system, the field orientation control operating together with the SVPWM technique are considered. The three-phase voltage source inverter (VSI) is employed to drive the three-phase hybrid-excited PM machine, while the step down DC-DC converter is utilised to regulate the field excitation current. The DS5101 board is used to generate switching pulse signals for both the inverter and the DC-DC converter. All measured control variables, i.e. armature currents in phases A and B, field excitation current, dc-link voltage, field voltage, and torque, are sent to the DS2004 board in order to capture their data waveforms. Likewise, the rotor position is determined by the incremental encoder, and its information signals are sent to the dSPACE processor via the DS3001 board. The detail in each part of dSPACE-based drive system will be described in the following sections.

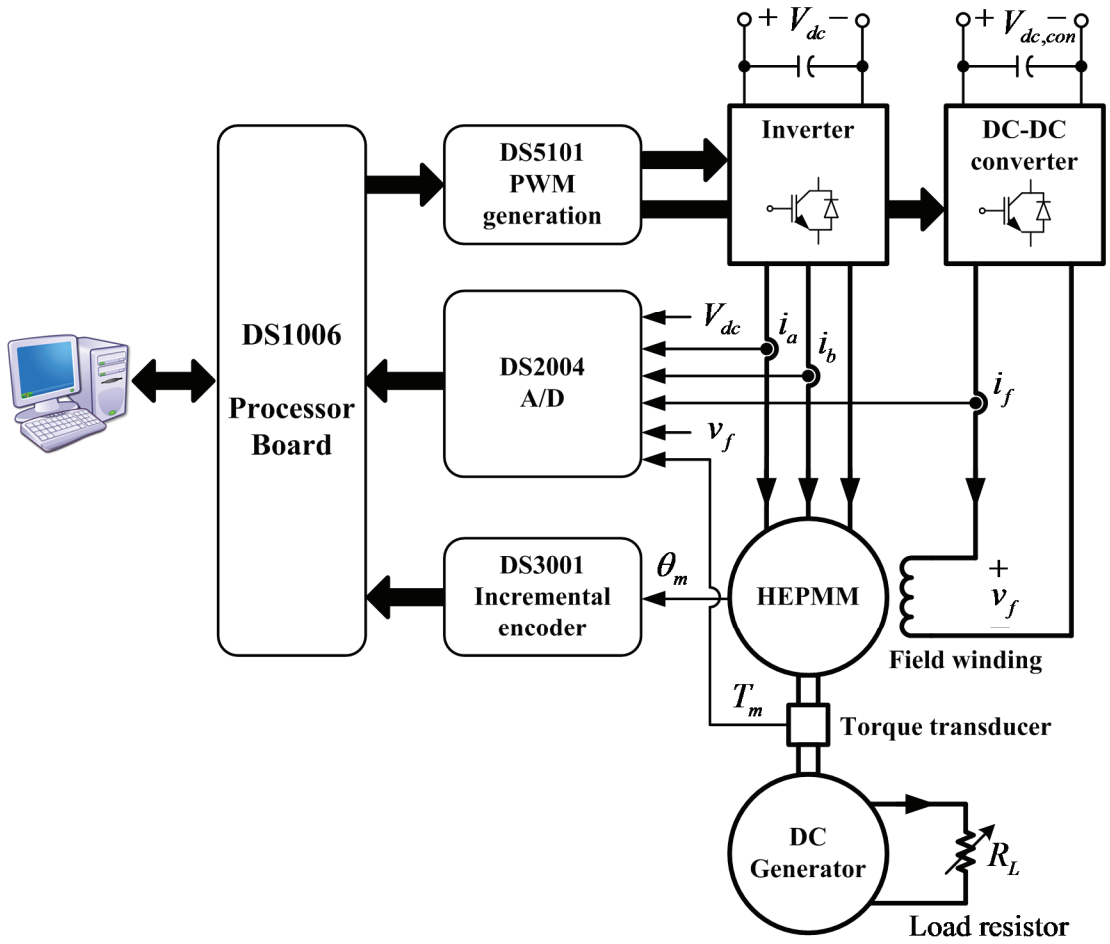

Fig. 2.34. Block diagram of the dSPACE-based drive system.

2.8.1 dSPACE processor

The DS1006 dSPACE processor board is designed for high control performance applications, as shown in Fig. 2.35, which is applied for all proposed control strategies in this thesis. The DS1006 provides a capability to solve the complex computation for the real-time system. It can be directly connected to all dSPACE I/O boards via PHS bus through the DS911 Gigalink module, which is linked by fiber-optic connection. Moreover, it is possible to utilise a multiprocessor system by utilising each individual core. Thus, a parallel computing and high performance data exchange between the cores are provided. Also, based on the RTI-MP, the graphical programming can be easily used to assign the I/O boards.

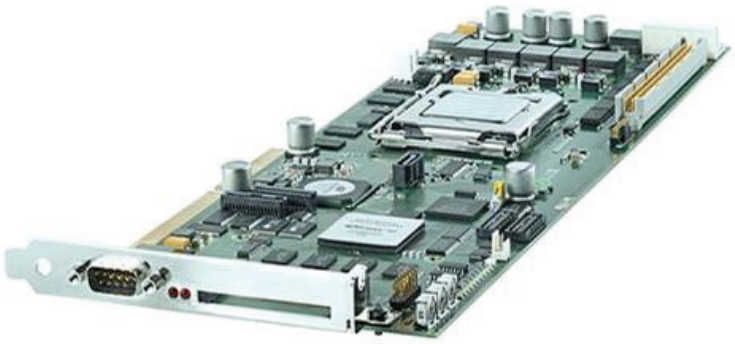

Fig. 2.35. DS1006 dSPACE processor board [DSP10].

The outstanding features are highlighted as follows:

- Quad-core AMD Opteron^{TM} processor running at 2.8 GHz.
- 1 GB DDR2-800 SDRAM local memory for the application and dynamic application data, 4x128 MB DDR2-267 SDRAM global memory for host data exchange, and 2 MB for flash memory.
- 3 general propose timers for each core.
- Interrupt controller for handling 18 different interrupt sources for each core.
- Fast 64-bit access for block transfer function and 32-bit access for single 32-bit data words.
- Interface via eight 16-bit I/O ports (host interface).
- RS232 interface with standard UART (serial interface).
- Ambient temperature is around 0 to 40 degree Celsius.

2.8.2 PWM generation

The DS5101 digital waveform output board, as shown in Fig.2.36, is designed for high speed signal generation and also high revolution in which it can generate a pack of PWM signals at various frequencies. The DS5101 consists of 16 timing I/O channels which can be interrupted by the external signal, and any channel can generate an interrupt that can be performed by software. The maximum output frequency is 2 MHz with 25 ns time resolution. Furthermore, for each channel, the dual-port memory (DPMEM) is available for 128 programme states, and the data memory is offered for 512 delay parameters. In physical connection, the board provides 37-pin female Sub-D output connectors.

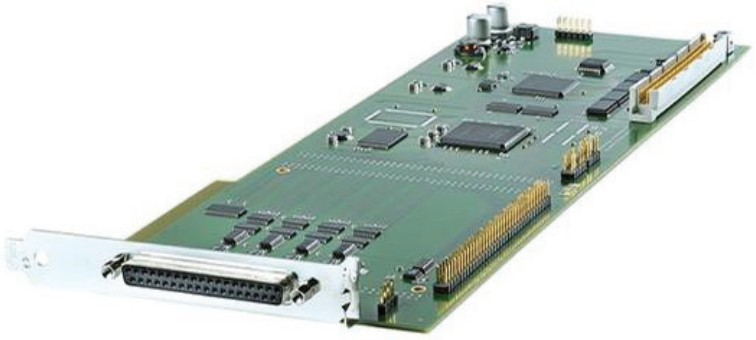

Fig. 2.36. DS5101 digital waveform output board [DSP10].

2.8.3 Incremental encoder interface

The DS3001 incremental encoder interface board, as shown in Fig.2.37, is designed for position control applications. The board consists of five parallel input channels, which is appropriately used to connect the incremental encoder. Each channel has its own 24-bit position counter that can also be used for digital signals. Measuring digital or sinusoidal position signals are available for this board.

Fig. 2.37. DS3001 incremental encoder interface board [DSP10].

Since the range of input encoder lines is defined between 2^{-21} to 2^{21}, the position angle in radian unit can be determined based on the scaled output signal by the DS3001 Matlab/ Simulink model as expressed in (2.39).

$$\theta_m = 2^{21}\left(\frac{2\pi}{encoder\ line}\right)\cdot scaled\ output \tag{2.39}$$

The encoder line of the incremental encoder, which is used in this thesis, is 5000 pulses per revolution as mentioned in section 2.8.5.

2.8.4 High speed A/D

Fig. 2.38 shows the DS2004 high speed A/D board that can be used in the dSPACE system for digitizing analogue input signals with high sample rate. The DS2004 provides 16 A/D differential input channels, and it consists of 16 independent A/D converters with a resolution of 16 bits. The conversion time per channel is only 800 ns. The input signal voltage range is available for both positive and negative sides, i.e. ±5 V and ±10 V, that can be programmable in Matlab/Simulink. Hence, it is easy to connect the output signal from other sensor board such as current and voltage without the additional voltage level shifter board. There are 4 external trigger inputs. In addition, the triggered sample mode of this board can be used to record data within a defined window.

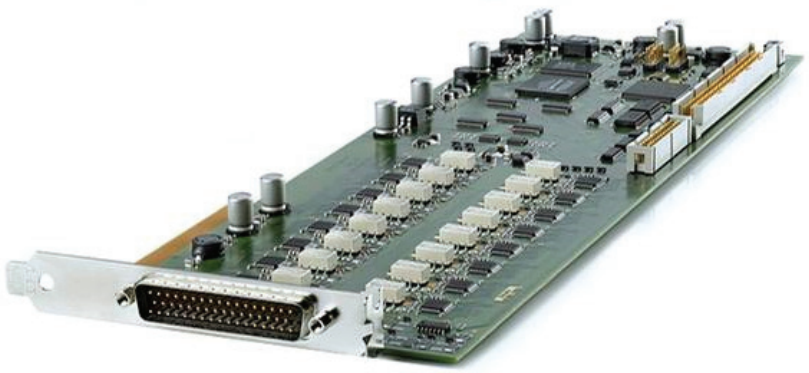

Fig. 2.38. DS2004 high-speed A/D board [DSP10].

2.9 Summary

In this chapter, the drive systems for hybrid-excited permanent magnet synchronous machines have been introduced together with the specific hardware configuration. The prototype hybrid-excited PM machines are briefly presented. The principle of field orientation control, three-phase transformation method, space vector modulation technique, over-modulation technique, and the inverter nonlinearity are also covered. All of them are used for other chapters.

CHAPTER 3

A NEW CONTROL STRATEGY OF HYBRID-EXCITED SWITCHED-FLUX PERMANENT MAGNET MACHINES

This chapter proposes a new control strategy for operating in both flux-enhancing and flux-weakening regions of the hybrid-excited switched-flux permanent magnet machine (HESFPMM). The positive field excitation current is utilised to enhance the torque via flux-linkage, and it is gradually modified when the speed exceeds the rated speed of enhanced torque until the field excitation current is zero. In the flux-weakening region, the *d*-axis current is utilised, while the field excitation current is controlled towards zero rather than negative in the flux-weakening mode. The modification currents are determined by the voltage error regulation method. The special magnetic circuit can effectively reduce the *d*-axis flux-linkage by either partially short-circuiting the PM flux via the iron bridge or removing the field excitation current. The proposed method exhibits advantages, such as highly enhanced torque in the constant torque region, extended speed range, robustness against machine parameters, and higher efficiency in the flux-weakening region. The feasibility of the proposed method is verified by experimental results.

3.1 Introduction

The hybrid-excited switched-flux permanent magnet machines (HESFPMMs), which have two excitation sources, i.e. the PM and the field excitation, have been investigated in [OWE09], [OWE10], [HUA09], [HUA011], [GAU07], [HOA07], [ZHA11]. Such hybrid-excited machines have the potential to improve the machine flux-enhancing and flux-weakening characteristics, due to their adjustable flux-linkage capability. In order to enhance the effectiveness of the field excitation current, the iron flux bridges (IFBs), which mainly introduce a low reluctance path for the field excitation flux, are presented in [OWE10]. Although torque density is slightly sacrificed, the flux-enhancing and flux-weakening performance can be achieved [WAN11], [WAN12].

In hybrid-excited PM machines, the torque-speed characteristics are obtained by calculating the appropriate set of field current, *d*-axis and *q*-axis currents [AMA09],

[HUA12]. In [KEF10], the fixed field excitation current is utilised to weaken the *d*-axis flux-linkage. However, a large torque drop occurs when the operating region changes between flux-enhancing and flux-weakening. Considering the machine speed and load torque changes, the analytical expressions for the optimal reference currents are proposed based on Extended Lagrange multipliers optimisation [MBA12]. As an extended study, the optimal field current controller is proposed which uses the recursive method under a certain voltage limitation in order to achieve a total copper loss minimization [SHI07]. In addition, a fuzzy control method is applied with particle swarm optimisation [HUA12]. Although these methods can determine the optimal field excitation and the armature currents, they are machine parameters dependent and involved a heavy computational burden. Meanwhile, in the high speed region, the enhanced torque is limited by the inverter capacity, mainly the DC-link voltage and the maximum current. As the machine speed approaches the rated speed, the field excitation current should be modified accordingly to prevent the saturation of the current controllers. However, the field excitation current transition in flux enhancing operation is not considered in the previous research.

This chapter proposes a new control strategy for the HESFPMMs with iron flux bridges, Fig.3.1. Initial investigation on the control principle has been introduced in [POT15]. In order to control the field excitation current and *d*-axis current gradually in the proposed method when the machine speed changes, load torque changes or even DC-link voltage drops, the voltage error regulation method is utilised in which the machine parameters are not required. Then, the onset speed of the current modification from the flux-enhancing to the flux-weakening mode can be automatically determined. In flux-enhancing mode, the field excitation current is set to its maximum value for the torque enhancement, while it is controlled towards zero in transition from flux-enhancing to flux-weakening operation. In flux-weakening mode, the negative *d*-axis current is mainly employed, since the negative field excitation current cannot effectively weaken the *d*-axis flux linkage in the HESFPMM. Experimental results are provided to demonstrate the validity of the proposed method.

3.2 Machine Topology and Operating Principle

3.2.1 HESFPMM Topology (Machine-I)

The three-phase, 12-stator/10-rotor pole HESFPMM structure is shown in Fig.3.1, and the machine parameters are given in Table 2.1, as indicated in Chapter 2. Each salient stator pole consists of adjacent sides of two U-shaped laminated segments connected via an iron flux bridge. The slot between the adjacent sides of the U-shaped laminated segments consists of a parallel magnetised PM and a coil side of the field winding. The concentrated armature coils are wound on each of the salient stator poles and are connected in series to form the phases A, B, and C. The salient 10 pole rotor is simple and robust since it has no magnets or excitation coils.

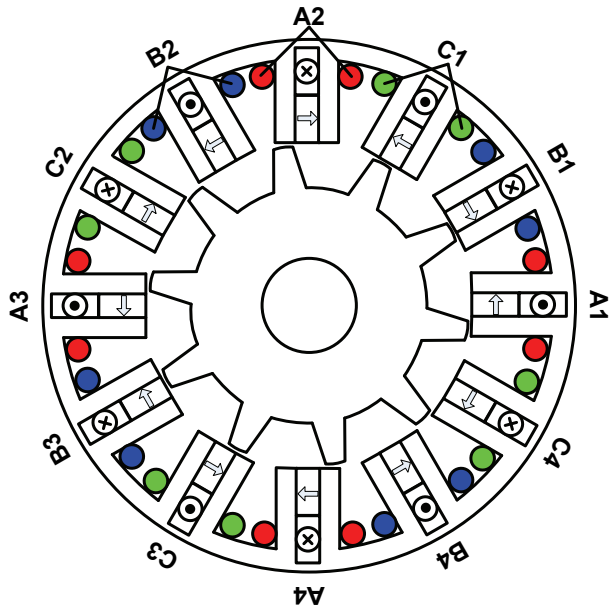

Fig. 3.1. Cross-section of the HESFPMM with iron flux bridges.

3.2.2 Principle of flux modulation

The advantage of the HESFPMMs is its ability to modulate the air-gap flux via the field excitation. The principle of flux modulation is shown in Fig.3.3 and Fig.3.4. On open-circuit with no field excitation current ($i_f = 0$), the PM flux is the only source that excites the air-gap flux, Fig.3.2. However, some of this PM flux also shunts through the

iron-flux bridges and will not contribute to the air-gap flux. Although the iron-flux bridges reduce the open-circuit air-gap flux, they enhance the effectiveness of the field excitation [OWE10].

In the flux enhancing mode, i.e. with positive field excitation currents ($i_f > 0$), the air-gap flux is larger than the open-circuit PM flux, due to the addition of the positive field excitation flux, which is in the same direction as the PM flux in the air-gap, Fig.3.3(a). The net enhanced air-gap flux is shown in Fig.3.3(b). In the flux weakening mode, i.e. with negative field excitation currents ($i_f < 0$), the air-gap flux can be decreased less than the open-circuit PM flux because of the addition of the negative field excitation flux, which is in the opposite direction of the PM flux in the air-gap, Fig.3.4(a). The iron-flux bridges serve as a relatively low reluctance flux path for the field excitation flux which is in parallel to the PM flux path. However, for flux-weakening, the effectiveness of the excitation field is limited by the high reluctance of the PM since some of the excitation flux shunts through the PMs. The net enhanced air-gap flux is shown in Fig.3.4(b).

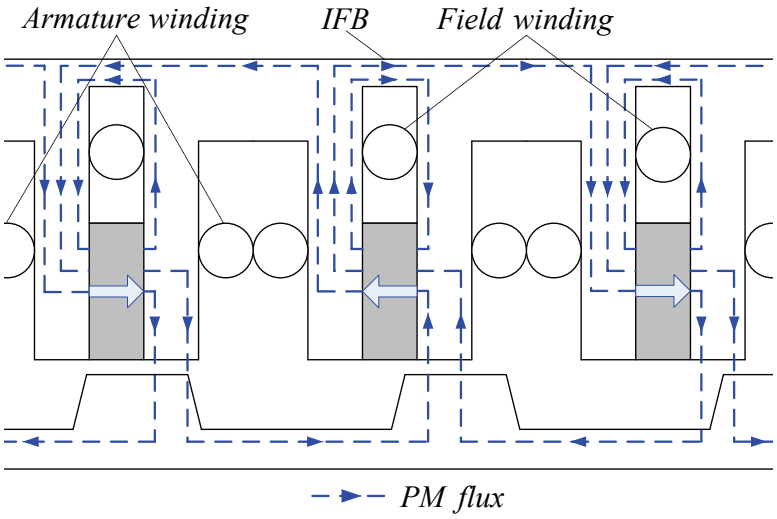

Fig. 3.2. PM flux path in the simplified machine with the rotor at *d*-axis.

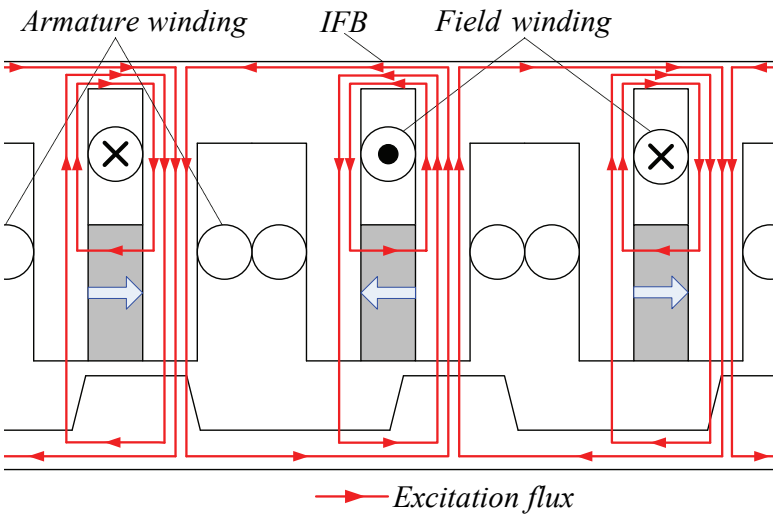

(a) Only positive field excitation current ($i_f > 0$).

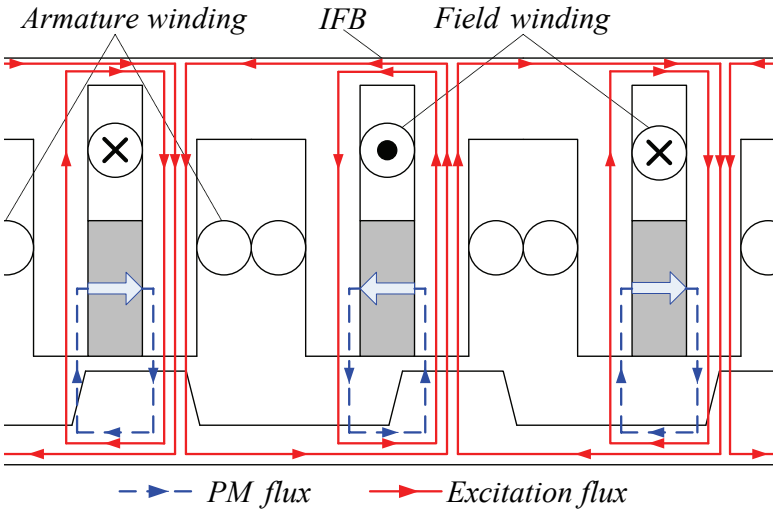

(b) Net flux-enhancing operation (PM and $i_f > 0$).

Fig. 3.3. Flux-enhancing operation in the simplified machine model.

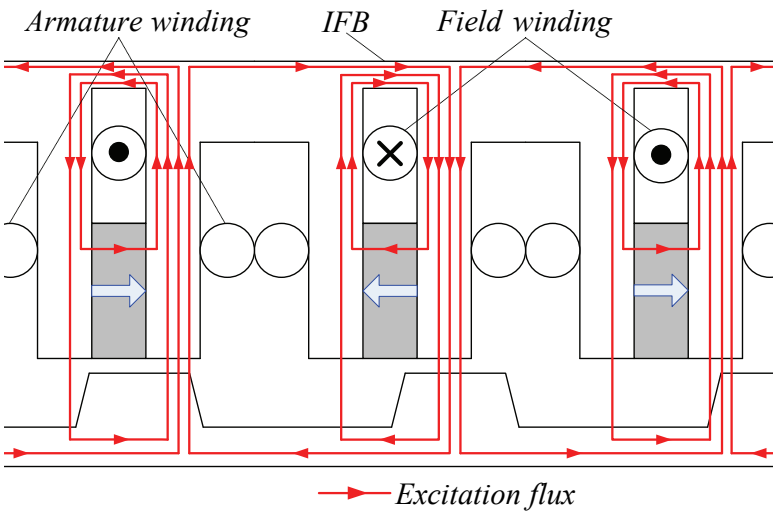

(a) Only negative field excitation current ($i_f < 0$).

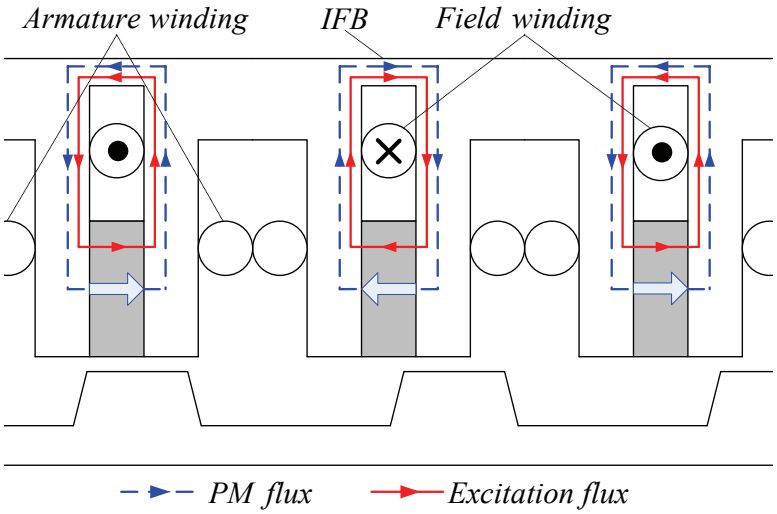

(b) Net flux-weakening operation (PM and $i_f < 0$).

Fig. 3.4. Flux-weakening operation in the simplified machine model.

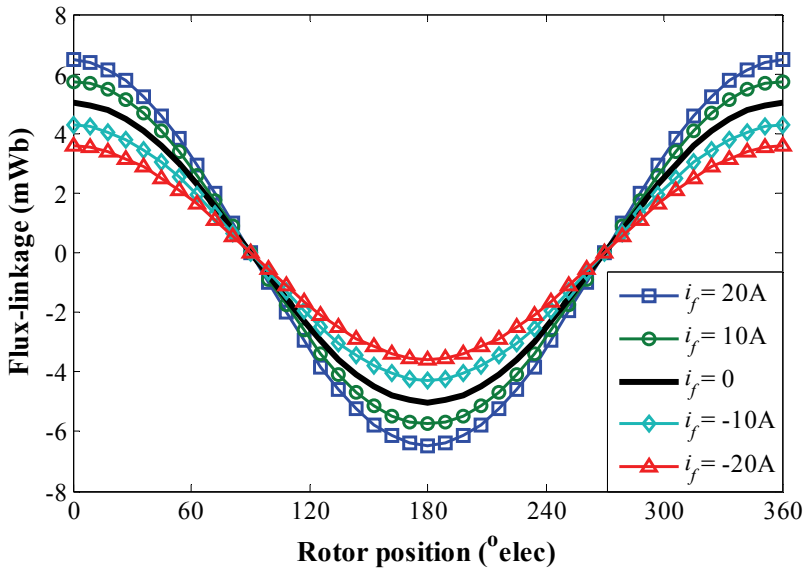

(a) Phase flux-linkage against rotor position.

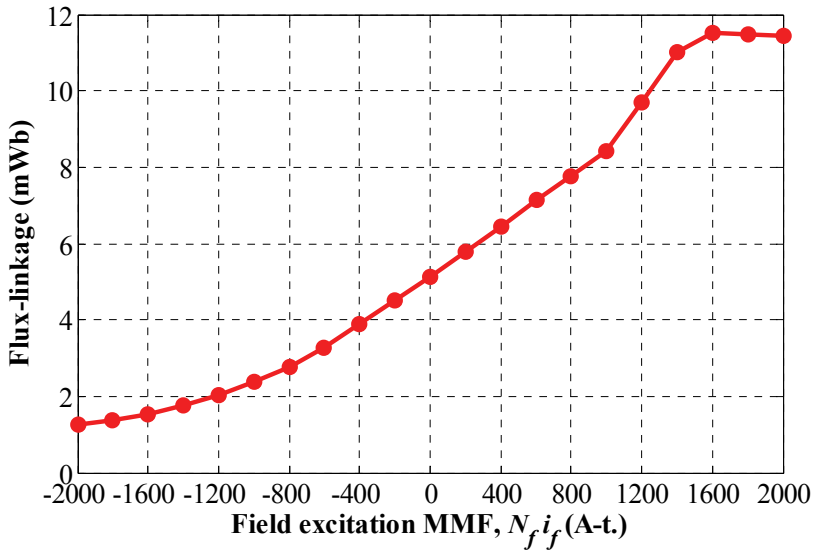

(b) Phase flux-linkage with field excitation MMF.

Fig. 3.5. Flux-linkage adjusting capability of the HESFPMM.

The phase flux-linkages obtained by 2D FE analysis in against either rotor position or excitation MMF are shown in Fig.3.5(a) and (b), respectively. It can be observed that the phase flux-linkage can be either increased or decreased by adjusting the field excitation currents. However, the flux enhancing mode is more effective than the flux weakening operation. This is mainly due to the different directions of the PM flux and the positive field excitation flux in the iron flux bridges. In the flux enhancing mode,

as illustrated in Fig.3.3(a), the PM flux and the excitation flux are in opposite directions, i.e. the iron flux bridge is pre-magnetised with a negative flux. Then, by increasing field excitation current, the net flux is pulled into the air-gap. This is different for the flux weakening operation since the iron flux bridges are pre-magnetised with a positive flux, i.e. both flux sources are in the same direction, as shown in Fig.3.4(a). By increasing flux weakening current, the net flux is increasingly shunted via the saturated iron flux bridges and the high reluctance PM, Fig.3.4(b), thus limiting the ability to further reduce the air-gap flux.

In Fig.3.6 and Fig.3.7, the operating principle of the prototype machine can be also expressed by the flux distributions obtained from the 2D finite element (FE) analysis. On open-circuit without field excitation current ($i_f = 0$), Fig.3.6, the majority of PM flux is naturally short-circuited through the iron-flux bridge. Meanwhile, the flux distributions of both enhancing and weakening operations are shown in Fig.3.7. It is obvious that the flux-linkage can be enhanced/weakened based on the utilisation of the positive/negative field excitation current by utilising Fig.3.2 – Fig.3.4.

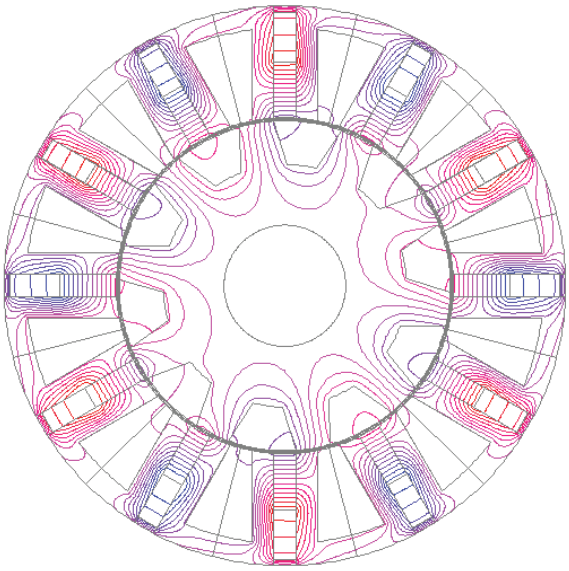

Fig. 3.6. PM flux-distribution with $i_f = 0$.

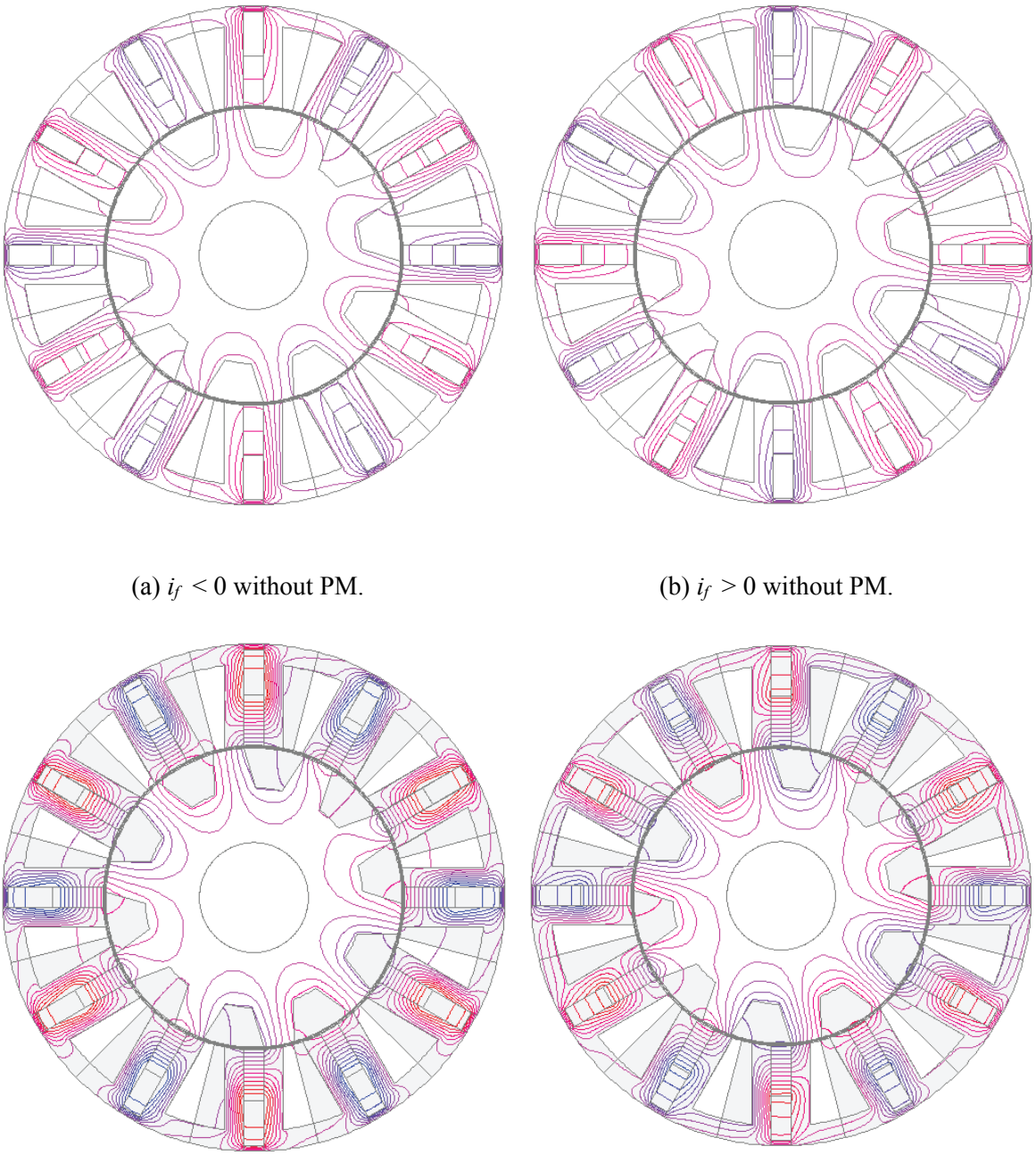

(a) $i_f < 0$ without PM.

(b) $i_f > 0$ without PM.

(c) Net flux- weakening, $i_f < 0$ with PM.

(d) Net flux- enhancing, $i_f > 0$ with PM.

Fig. 3.7. Flux distributions of both enhancing and weakening operations.

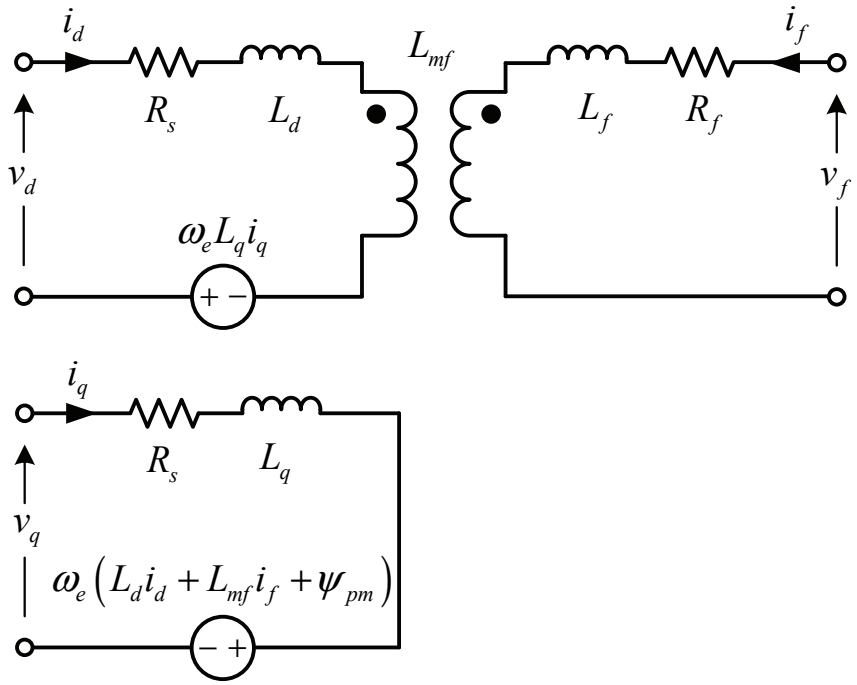

Fig.3.8. Equivalent circuits of the HESFPMM [HUA12].

3.3 Mathematical Model of the HESFPMM

Based on the equivalent circuits expressed in Fig.3.8, the voltage equations of the HESFPM can be given by (3.1) and (3.2) in the rotor reference frame by neglecting magnetic saturation, iron loss and temperature dependences. Since the field excitation current is employed to principally modify the *d*-axis flux-linkage produced by the PMs, the field current model is considered in the *d*-axis equivalent circuit, whilst the influence of the modified *d*-axis flux-linkage is considered on torque generation in *q*-axis circuit. Then, the machine model can be written as

$$v_d = R_s i_d + L_d \frac{di_d}{dt} + L_{mf} \frac{di_f}{dt} - \omega_e L_q i_q \tag{3.1}$$

$$v_q = R_s i_q + L_q \frac{di_q}{dt} + \omega_e \left(L_d i_d + \psi_{pm} + L_{mf} i_f \right) \tag{3.2}$$

$$T_e = \frac{3}{2} P \left[i_q \psi_d - i_d \psi_q \right]. \tag{3.3}$$

Since each axis flux-linkage can be expressed as $\psi_d = \psi_{pm} + L_d i_d + L_{mf} i_f$ and $\psi_q = L_q i_q$.

The electromagnetic torque equation can be rearranged as

$$T_e = \frac{3}{2} P\left[i_q \psi_{pm} + i_d i_q \left(L_d - L_q \right) + L_{mf} i_f i_q \right] \tag{3.4}$$

$$T_e = \frac{3}{2} P\left[i_q \psi_{pm} + L_{mf} i_f i_q \right] \tag{3.5}$$

Therefore, when the saliency of the HESFPMMs is assumed as 1 ($L_d = L_q$), the torque can be generated from two parts, i.e. the interaction between PM flux-linkage and *q*-axis current, and interaction between *q*-axis current, field current and mutual inductance between field and armature windings. Consequently, it can be concluded that the torque can be controlled by both the armature and field excitation currents as discussed in Section 3.2.

Due to the inverter constraints such as the DC-link voltage and current limits, the operating point of the machines is limited. The voltage and current constraints of an inverter can be expressed in the terms of the *d*-axis and *q*-axis voltages and currents as shown in (3.6) and (3.7), respectively.

$$v_d^2 + v_q^2 \le V_{\mathrm{m}}^2 \tag{3.6}$$

$$i_d^2 + i_q^2 \le I_{\mathrm{m}}^2 \tag{3.7}$$

In steady-state, by neglecting the resistance the voltage constraint of the HESFPMMs can be arranged in terms of the *d*- and *q*-axis currents as shown in (3.8).

$$L_d^2 \left(i_d + \frac{\psi_{pm} + L_{mf} i_f}{L_d} \right)^2 + L_q^2 i_q^2 \le \left(\frac{V_m}{\omega_e} \right)^2 \tag{3.8}$$

From the assumption of unity saliency for the HESFPMMs, i.e. $L_d = L_q = L_s$, the constraint can be simply expressed as (3.9)

$$\left(i_d + \frac{\psi_{pm} + L_{mf} i_f}{L_d} \right)^2 + i_q^2 \le \left(\frac{V_m}{L_s \omega_e} \right)^2 \tag{3.9}.$$

In vector control, variables are transferred into the synchronous reference frame, ideally dc quantities. Then, torque and flux-linkage can be separately controlled by *q*-axis current and *d*-axis current, respectively. The gains of both current controllers, commonly proportional and integral (PI), are selected based on the voltage equations, (3.1) and (3.2). Besides, the decoupling control is utilised to improve the dynamic performance of current control loop especially in high speed operation [JUN99], [ZHU10]. The *d*-axis and *q*-axis currents controller in *s*-domain with decoupling terms are given in (3.10) and (3.11), respectively.

$$v_d^* = \left(k_p + \frac{k_i}{s}\right)\left(i_d^* - i_d\right) + v_{d\_dec} \tag{3.10}$$

$$v_q^* = \left(k_p + \frac{k_i}{s}\right)\left(i_q^* - i_q\right) + v_{q\_dec} \tag{3.11}$$

where the decoupling terms of the *d*-axis and *q*-axis can be expressed as $v_{d\_dec} = -\omega_e L_q i_q$ and $v_{q\_dec} = \omega_e \left(\psi_{pm} + L_d i_d + L_{mf} i_f\right)$, respectively.

For the rotor position and speed measurement, an incremental encoder is utilised. The pulses generated from the encoder are digitised within the sampling period of time [OHM82], [ZHA12]. Hence, the rotor position can be measured by the counted pulses, and then the mechanical speed is measured by the differential of the measured rotor position as shown in (3.12).

$$\omega_m = \frac{d\theta_m}{dt} = \frac{\left[\theta_m(k) - \theta_m(k-1)\right]}{\Delta T_s} \tag{3.12}$$

where $\theta_m(k-1)$ and $\theta_m(k)$ are the instantaneous rotor positions with respect to initial and end of the time interval (ΔT_s).

3.4 Proposed Control Strategy

With respect to the different field excitation current levels, the operating regions of the HESFPMM are defined in Fig.3.9(a). In region-I, from point A to B, the enhanced torque can be generated with an aid of the positive field excitation current. The rated speed with enhanced torque, which is defined at point B, is lower than that with zero field current, since the enhanced torque operation requires higher voltage due to the increased flux-linkage. Over the rated speed with enhanced torque operation (ω_{rated}^{en}), the field excitation current should be reduced in order to satisfy the inverter constraints, from points B to C. Above the point C, the operating range can be extended by utilising the negative field excitation current or negative *d*-axis current.

Consequently, the maximum operating point can be obtained by following the envelope of each region, represented by the bold line in Fig.3.9(a). In order to avoid the torque drop during transition in Region-II, the excitation current should be changed gradually while satisfying the operating condition such as voltage and current limitations of the inverter. The proposed flux-enhancing and flux-weakening control method and limitations of the inverter will be discussed in the following section.

The overall block diagram of the proposed control strategy is presented in Fig.3.9(b). The PI controllers are employed for both the speed and current controls. In order to achieve the maximum DC-link voltage utilisation, the minimum magnitude error over-modulation (MMEOM) technique is utilised along with the space vector pulse width modulation (SVPWM), in which the output voltage can be moved closer to the corner of the hexagon in a stationary voltage plane [HAV99], [KWO06], [KWO07], [KWO08]. The field excitation current is controlled by the DC-DC buck-converter via the current feedback control with PI controller.

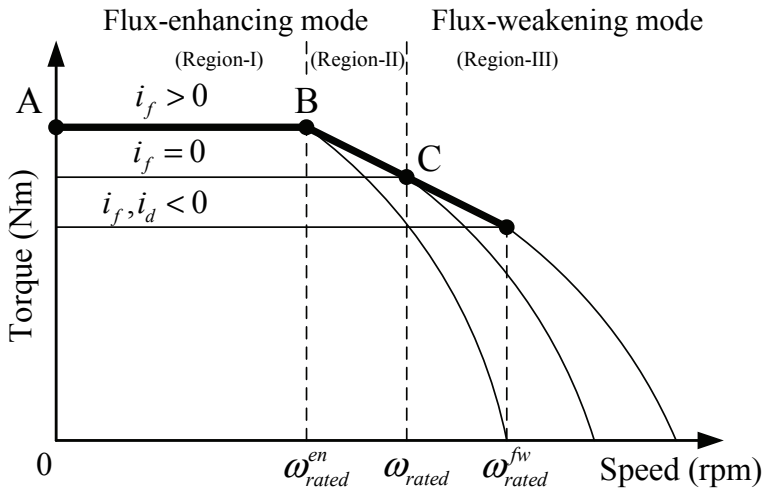

(a) Definition of operating modes.

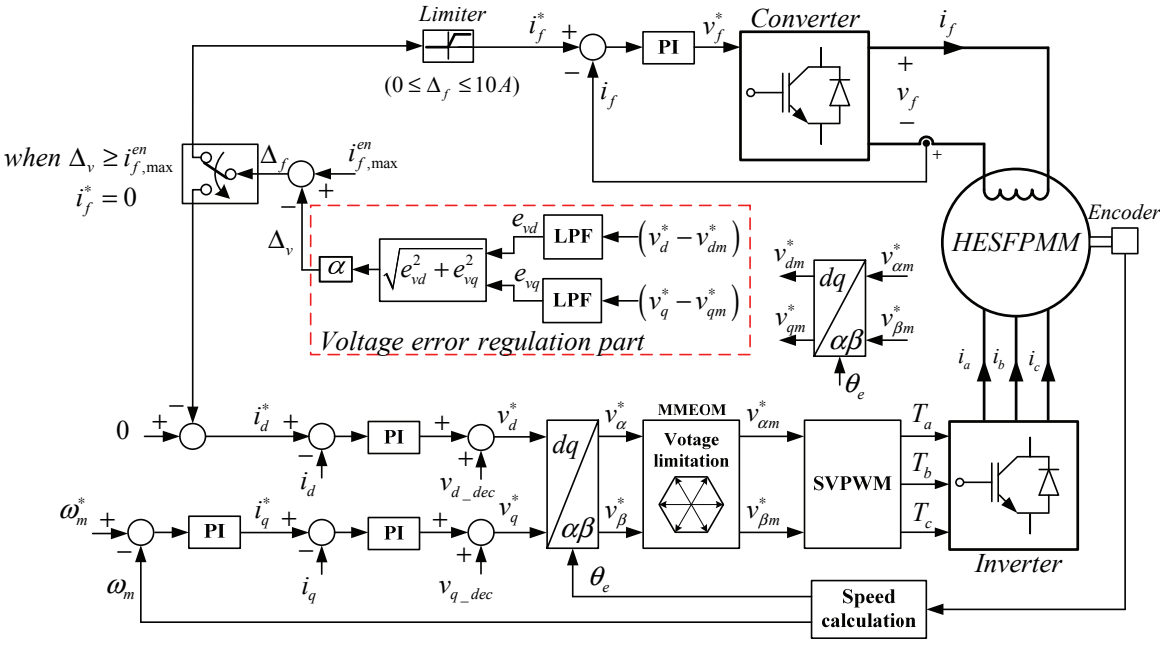

(b) Overall block diagram of the proposed control strategy.

Fig. 3.9. Definition of operating modes and proposed control strategy.

The proposed control strategy is based on the voltage error regulation method, which uses the voltage difference between reference and modulated value of the MMEOM block in the synchronous reference frame. The voltage error regulation loop consists of low-pass filters (LPFs) and a gain α. It should be noted that the transient performance and steady-state torque have trade-off relationship related to the gain, α [KWO06]. The larger gain exhibits better dynamic performance, but the lower torque per ampere ratio (T/A).

When the machine speed approaches the rated speed, the output of the current controller is close to the maximum voltage of the inverter. If the demand voltage exceeds the available voltage of the inverter, the modified component will be produced to reduce the back-EMF of the machine. The operating conditions of the proposed method are presented in Table 3.1.

Table 3.1. Proposed operating conditions

Reference current	Flux-enhancing		Flux-weakening
	Region-I	*Region-II*	*Region-III*
i_f^*	$i_{f,\max}^{en}$	Δ_f	0
i_d^*	0	0	$-\Delta_f$
i_q^*	I_m	I_m	$\sqrt{I_m^2 - i_d^2}$

3.4.1 Flux-enhancing Mode

When the machine operates in Region-I between points A and B, as shown in Fig.3.9(a), the voltage error regulation part is not activated because the voltage saturation of the MMEOM block does not occur. The reference field current is set to the maximum enhancing field excitation current ($i_{f,\max}^{en}$) in order to maximise the torque of the machine. Since the *d*-axis current does not contribute to the torque generation in HESFPMMs when the saliency is assumed as 1, the *d*-axis reference current is set to zero, while the *q*-axis reference current is given by the speed controller.

When the machine operates beyond point B the inverter cannot generate the required reference voltage due to the enhanced flux-linkage. In order to avoid the output saturation of the current controllers, the voltage error regulator is automatically activated and the field excitation current is modified by the voltage error regulation current (Δ_v) in

Region-II from point B to C. As the machine speed increases, the reference excitation current (Δ_f) will be reduced towards zero, then eventually the reference field excitation current will be zero at point C.

3.4.2 Flux-weakening Mode

When the machine operates in Region-III beyond the point C, the flux weakening operation can be achieved by using either the negative field excitation current, the negative *d*-axis current, or the combination of both currents. However, as discussed in the previous section, the PM flux is short-circuited via the low reluctance paths of the iron flux bridges and the magnets in the HESFPMMs, which indicates that the employment of negative field excitation current will result in high copper loss without effectively influencing the flux-weakening performance. Therefore, for the proposed control strategy, only the negative *d*-axis current control is utilised to weaken the flux-linkage produced by PMs, while the field excitation current is set to zero in Region-III. To satisfy the current limitation and voltage constraint of the inverter, the *q*-axis reference current should also be modified with respect to the utilisation of the *d*-axis current shown in Table 3.1. Consequently, by using the voltage error regulation method, a smooth field current transition can be achieved from flux-enhancing operation to flux-weakening operation and vice versa.

3.5 Experimental Verification

3.5.1 Experimental setup

In order to verify the feasibility of the proposed method experimentally, the vector control algorithm is implemented on a dSPACE platform. To generate a load torque, a DC machine, which has the rating values of 1600 rpm and 1.5 kW, is utilised with an external resistance to dissipate the generated power, as mentioned in Chapter 2. The maximum enhancing excitation current is set at 4 A in the flux-enhancing mode. It should be noted that the DC-link voltage is reduced from rated value 36 V to 26 V in order to obtain more expanded region of the flux weakening operation of the HESFPMM, so that it can meet with the speed limitation of test rig, as depicted in Fig.2.18(b), to make it easier to observe the machine performance. SVPWM technique is used with 10 kHz switching frequency, while the DC-DC converter frequency is 5 kHz. The armature current and the maximum field excitation current are set to 10 A. The maximum speed of

the encoder is 4000 rpm which can cover the whole testing speed range. Other experimental setup settings are presented in Table 3.3.

Table 3.3. Experimental setup

Maximum enhancing excitation current	4 A
Maximum motor test speed	1600 rpm
DC-link voltage	26 V
Armature current (peak)	10 A
Switching frequency of the inverter	10 kHz
Converter DC voltage source	30 V
Maximum absolute field excitation current	10 A
Switching frequency of the converter	5 kHz

3.5.2 Experimental results

Fig.3.10(a) and (b) show the measured maximum torque and the maximum output power versus machine speed for the proposed method and the method utilising only the field excitation current control. Both control methods are also compared with the method that neither the flux-enhancing nor flux-weakening are controlled ($i_f = i_d = 0$). From standstill to rated speed with the enhanced torque, the method utilising only the field excitation current control and the proposed method can achieve the same torque and output power due to the same enhanced field excitation currents. As the machine speed increases over around 600 rpm, the field excitation current is modified by the voltage error regulation part in order to operate under the voltage limitation as shown in Fig.3.11(a). In flux-weakening region over around 900 rpm, the proposed method produces more torque compared with the method utilising only the field excitation current control due to the short-circuit of PM flux. Hence, it shows that the proposed method can provide high maximum torque and power at a given speed for all operating regions. In addition, a smooth speed transition between flux-enhancing and flux-weakening mode is also obtained.

The comparison of *d*-axis and *q*-axis currents between the method utilising only the field excitation current control and the proposed method is shown in Fig.3.11(b). In the method utilising only the field excitation current control, the *d*-axis current is set to zero over the entire speed range. Therefore, the *q*-axis current should be maintained at the maximum current (I_m) for all operation modes. However, since the flux-linkage cannot be sufficiently weakened by the negative field excitation current during flux-weakening mode, the voltage demand would exceed the voltage limitation. Hence, the *q*-axis current needs to be reduced when the voltage reaches its limit in order to achieve the reference speed. As for the proposed method, the *d*-axis current is kept zero in the flux-enhancing mode which ensure that the *q*-axis current is maintained at the maximum current, while in the flux-weakening mode the *q*-axis current needs to be reduced since absolute value of *d*-axis current increases.

Fig.3.12(a) presents the comparison of the copper loss of field winding for both methods, i.e. the method utilising only the field excitation current control and the proposed method. It is obvious that in the flux-enhancing mode same copper loss is obtained due to the same field excitation current utilised. However, in the flux-weakening mode, the copper loss in the proposed method can be eliminated with the zero field excitation current, while it is significantly increased by applying the method utilising only the field excitation current control, resulting in reduced machine efficiency and increased winding temperature. Fig.3.12(b) shows the copper loss of armature windings corresponding to the armature currents shown in Fig.3.11(b). By considering both the armature winding and the field winding copper losses, the total copper loss in all operating speed range can be illustrated in Fig.13(a).

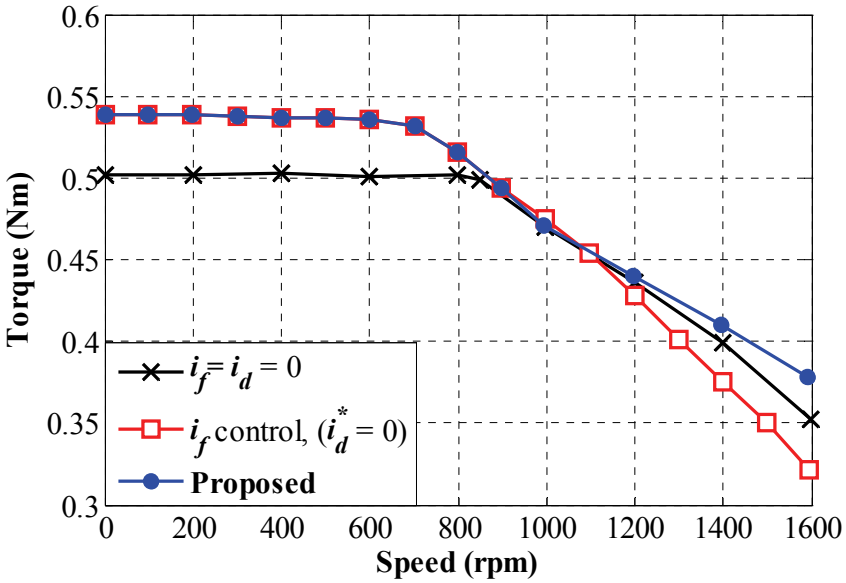

(a) Torque-speed curves.

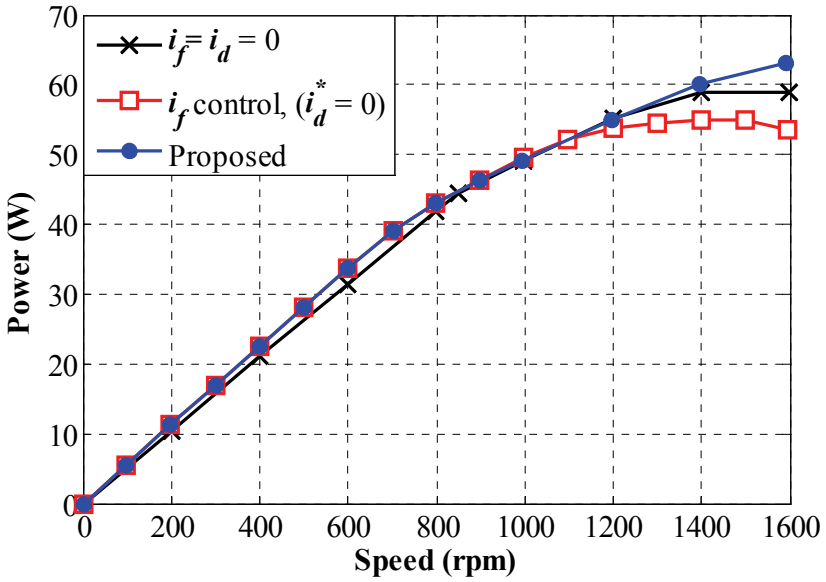

(b) Output power.

Fig. 3.10. Measured torque and output power against speed.

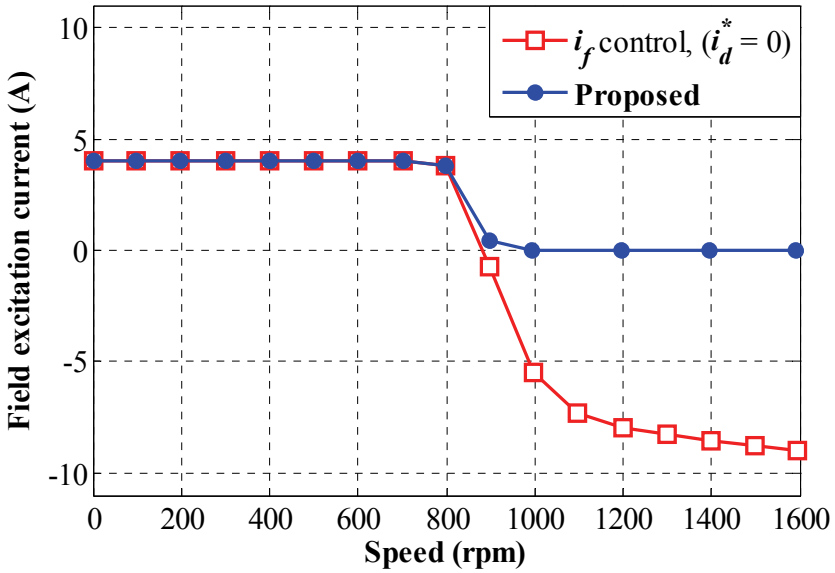

(a) Field excitation current.

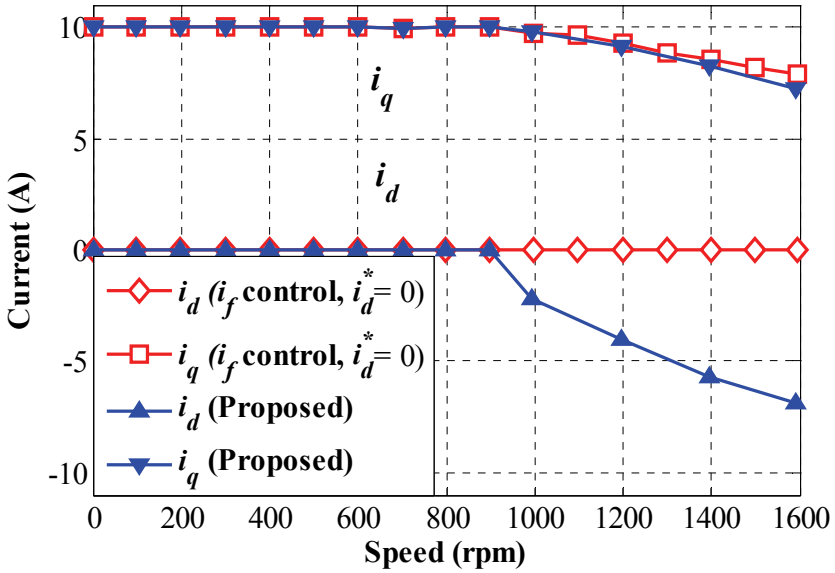

(b) Field excitation current.

Fig. 3.11. Measured torque, power and currents against speed.

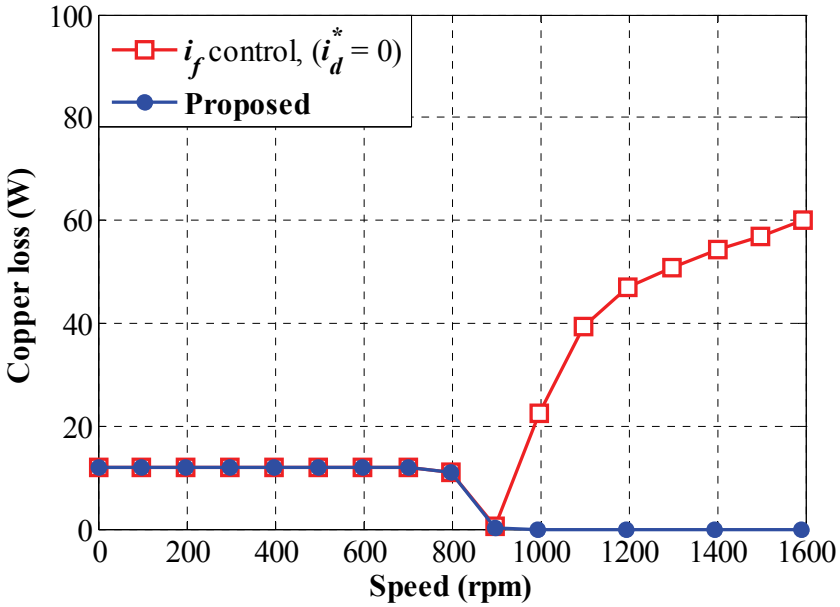

(a) Copper loss of field winding.

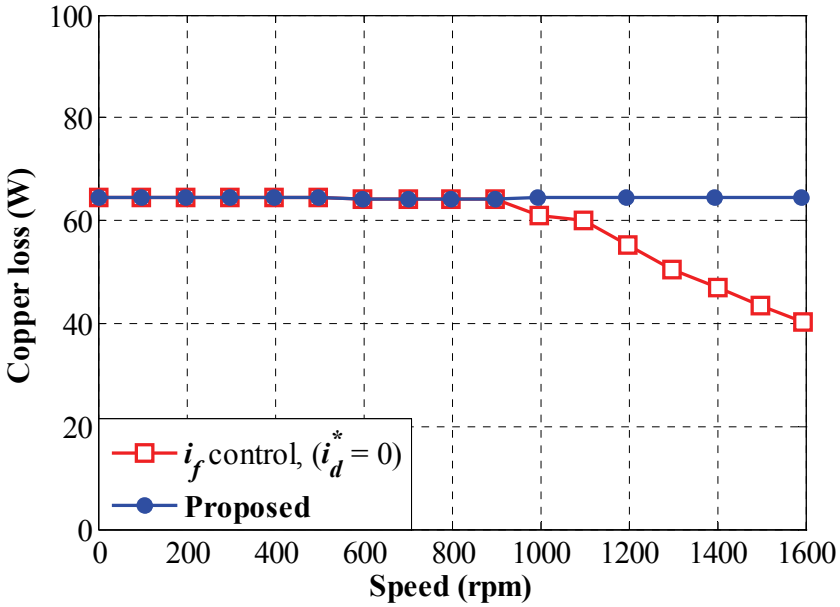

(b) Copper loss of armature winding.

Fig. 3.12. Measured copper loss against speed.

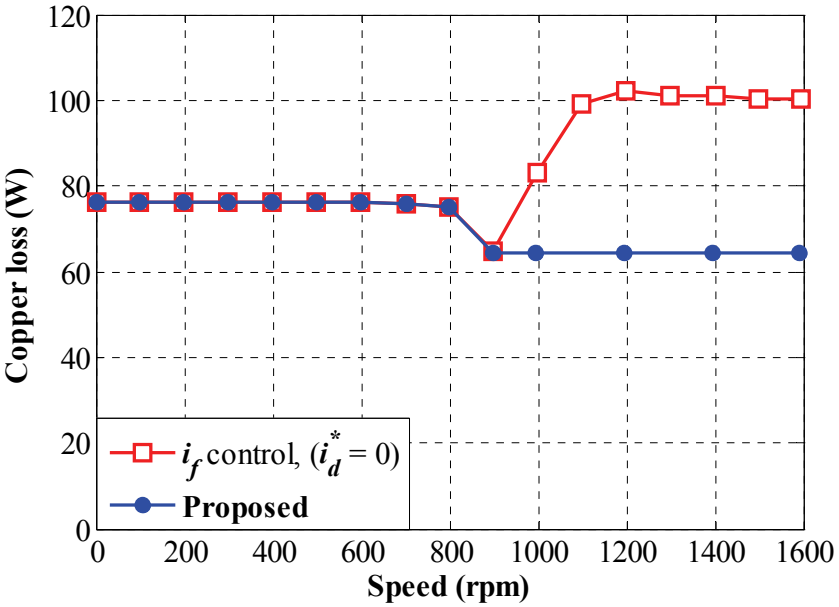

(a) Total copper loss.

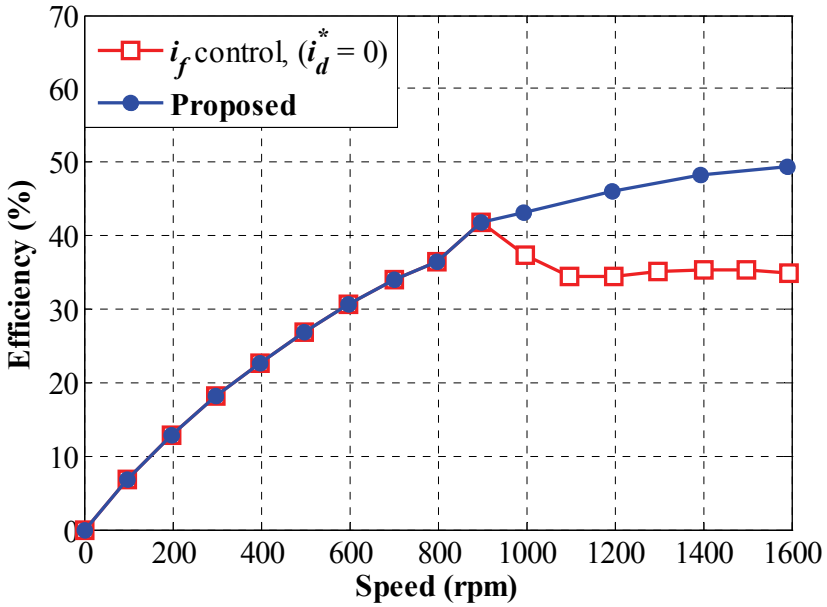

(b) Efficiency.

Fig. 3.13. Measured total copper loss and efficiency against speed.

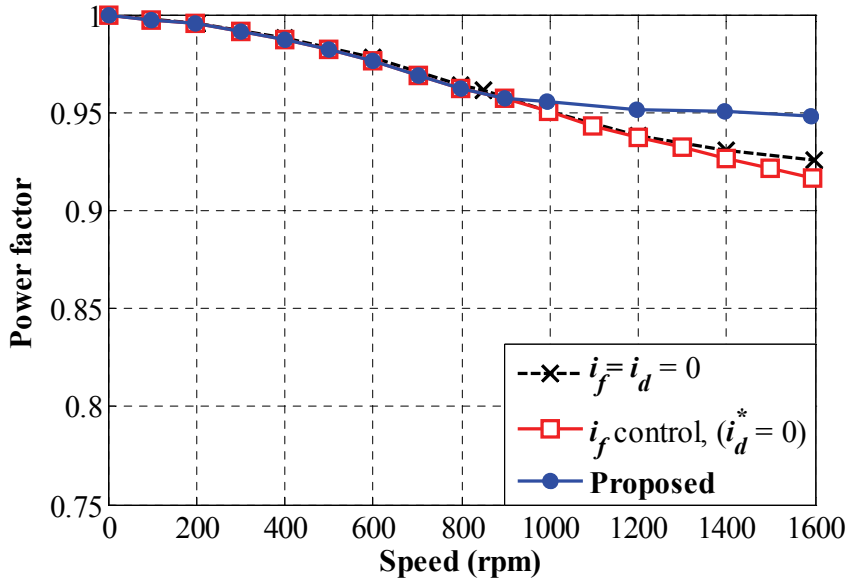

Fig. 3.14. Power factor.

The efficiency of the proposed method is compared with the method utilising only the field excitation current, Fig.3.13(b). The calculation of core loss and copper loss are presented in [ICF14]. However, it should be noted that the core losses and mechanical loss have been considered, since the efficiency (η) is calculated by the measured load torque (T_m) and speed in rad/s (ω_m) and electrical power, as shown in (3.13).

$$\eta = \frac{P_{out}}{P_{in}} = \frac{T_m \omega_m}{1.5\left(i_d v_d + i_q v_q\right) + R_f i_f^2}. \tag{3.13}$$

It can be seen that both methods can provide the same efficiency in the flux-enhancing mode due to the utilisation of the same field enhancing current and q-axis current. However, in the flux-weakening mode, the proposed method has higher efficiency since the copper loss of the field winding can be eliminated by employing the proposed control strategy in Fig.3.12(a). In addition, the proposed method can improve the power factor in flux-weakening region compared with other methods, as illustrated in Fig.3.14.

To further demonstrate the effectiveness of the proposed control method, its dynamic response is compared with the method utilising only the field excitation current, Fig.3.15. For a unit step change, the machine is operated at 0.5 second by setting the speed reference at 1200 rpm. The field excitation current is initially set at its maximum, and it gradually reduces towards zero in region-II corresponding to the steady-state results. In flux-weakening mode utilising only the field excitation current, the modulated voltage cannot meet its demand. This is because the flux-linkage cannot be effectively weakened by the negative field excitation current. Hence, the voltage error regulation current (Δ_v) is further increased. The increase in field excitation current results in excessive copper loss of the field winding, which can be eliminated in the proposed method since the field excitation current is controlled to zero.

In addition, the robustness against machine parameters of the proposed method is investigated. Under this condition, since the variation of *d*-axis inductance directly affects the flux-weakening performance of the proposed method in which the *d*-axis current is utilised, the estimated armature inductance is increased by 50%, as illustrated in Fig. 3.16. It can be seen that the speed can still effectively track its reference value, while the currents and copper losses exhibit similar performance as normal operation, which validates one of the advantages of the proposed method, i.e. robustness against machine parameters.

It is worth noting that although the speed is required in the decoupling terms, which results in slight deterioration of transient response on high speed operation when the sensorless strategies are utilised, on most operating conditions, the PI controllers in the current loop can automatically compensate the effect caused by the inaccuracy decoupling terms values.

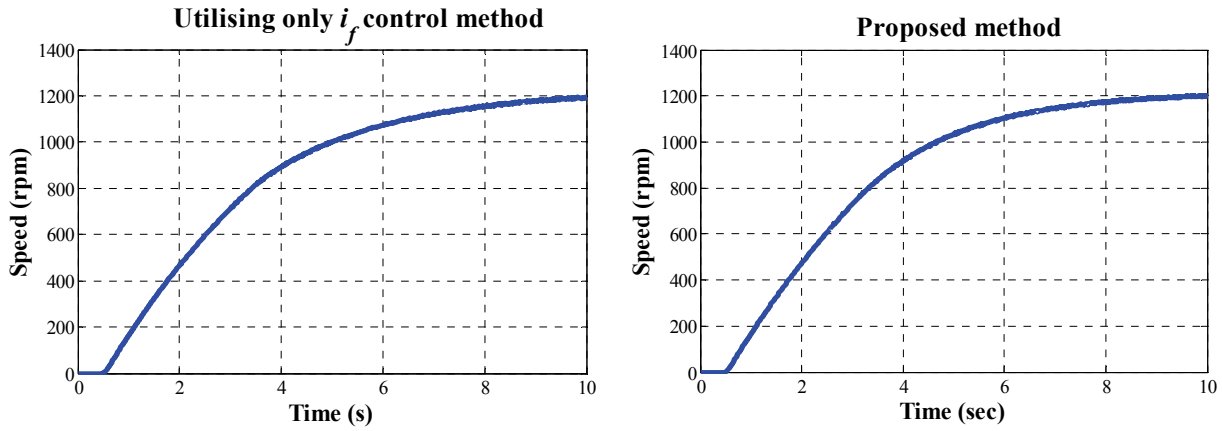

(a) Speed response.

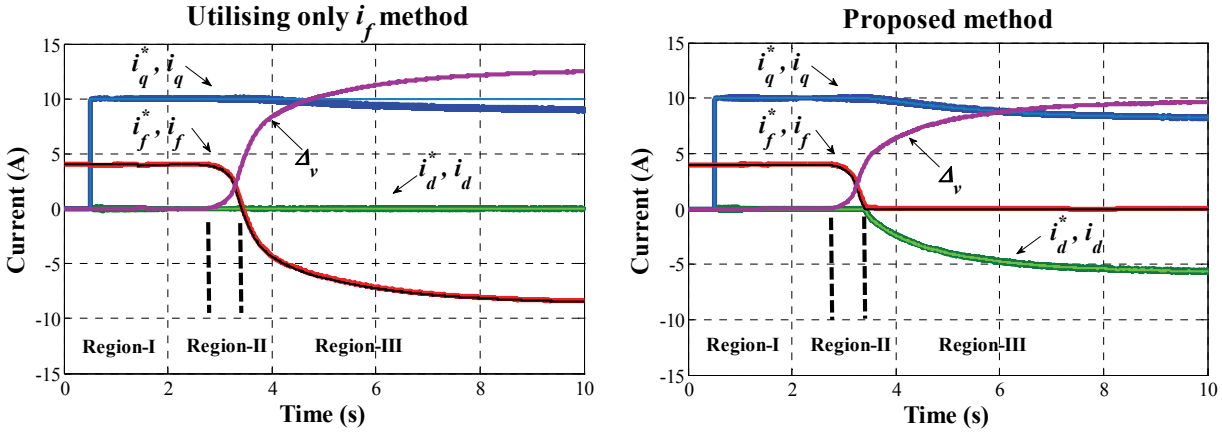

(b) *d*-axis, *q*-axis and field excitation currents.

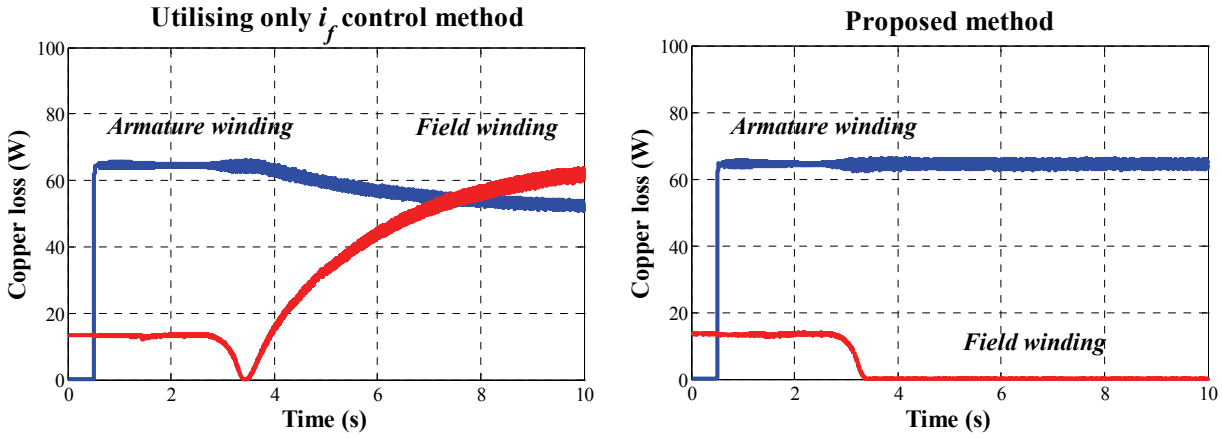

(c) Copper losses.

Fig. 3.15. Dynamic responses of the proposed method.

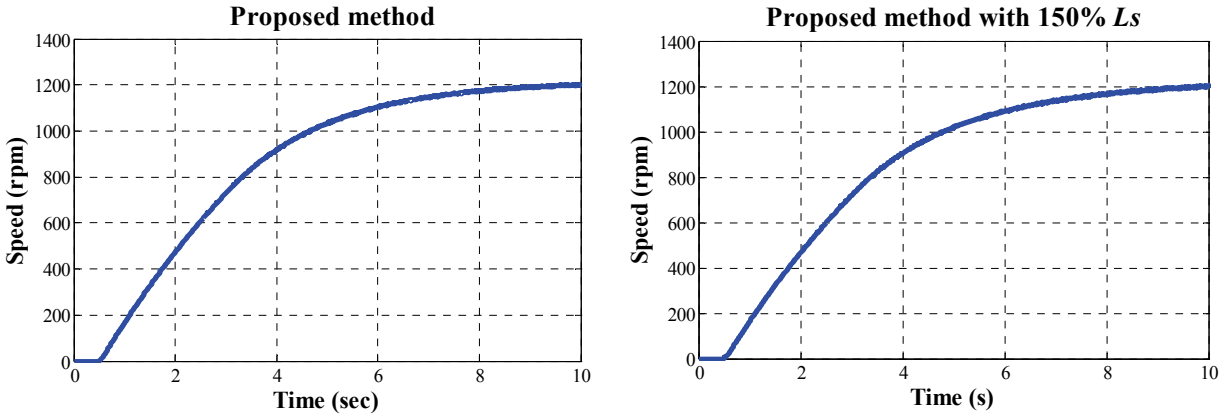

(a) Speed.

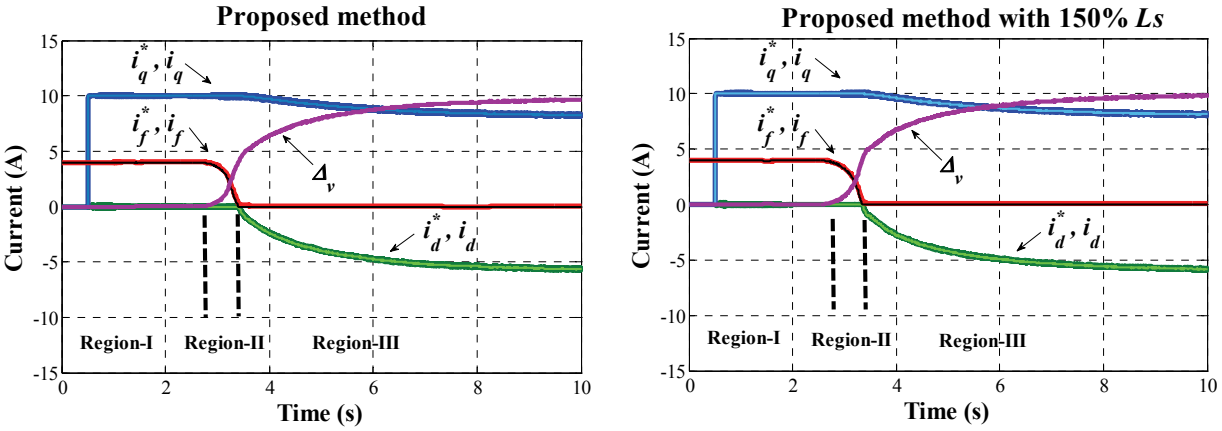

(b) *d*-axis, *q*-axis, field excitation currents.

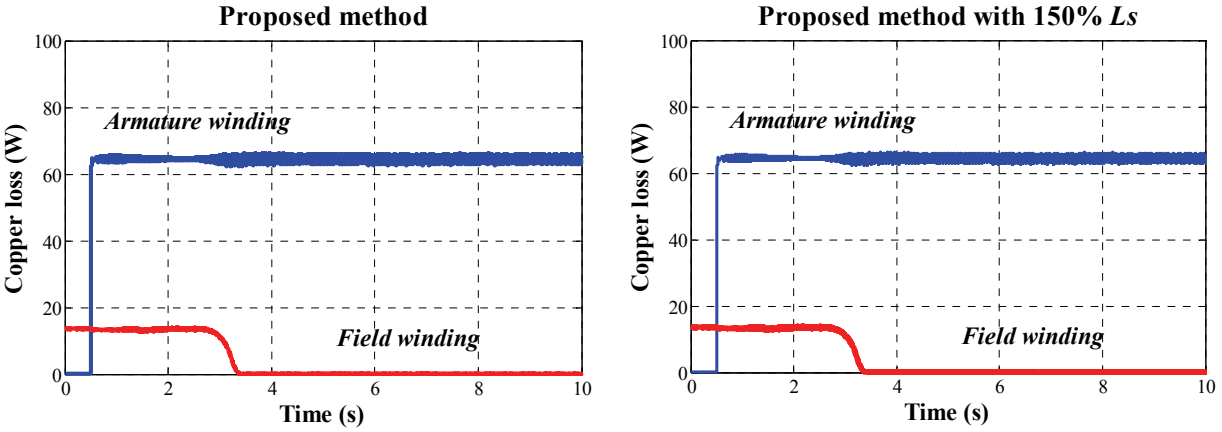

(c) Copper loss.

Fig. 3.16. Robustness verification against machine parameters.

3.6 Efficiency Map

The attractive feature of the HESFPMMs with regard to their capability is not only the possibility of the enhancing torque, but also the potential of extending the speed range. Moreover, the efficiency in flux-weakening operation can be further improved with the proposed method. Additionally, when the machine is operated below the rated torque, the efficiency can also be significantly improved by utilising the field excitation current. In this region, the field excitation current will be set as a constant value since the demand voltage is still inside the voltage limit. The measured efficiency map without/with utilisation of field excitation current are presented in Fig.3.17(a) and (b), respectively.

The maximum efficiency, which has been selected by a specified range of field excitation current, is presented in Fig.3.17(b). Since the *d*-axis flux-linkage can be enhanced by utilising the positive field excitation current, the requirement of *q*-axis current will be reduced during the same torque and speed operation. As a result, the armature copper loss will be decreased as well. However, the field excitation current causes the copper loss of field winding. Therefore, in order to achieve the maximum efficiency, the copper losses need to be minimised. The comparison results of the efficiency map show that the efficiency of HESFPMM can be improved by using a proper field excitation current.

It is worth mentioning that in Fig.3.13(b) and Fig.3.17, the overall efficiency is low since the prototype machine is a low power machine and the DC-link voltage is reduced in order to limit the maximum operating speed which is imposed by the test rig. However, the efficiency improvement of the proposed method is obvious, which, together with Fig.3.10(a) and (b) for the torque and power improvement and the speed extension, has demonstrated the effectiveness of the proposed control method.

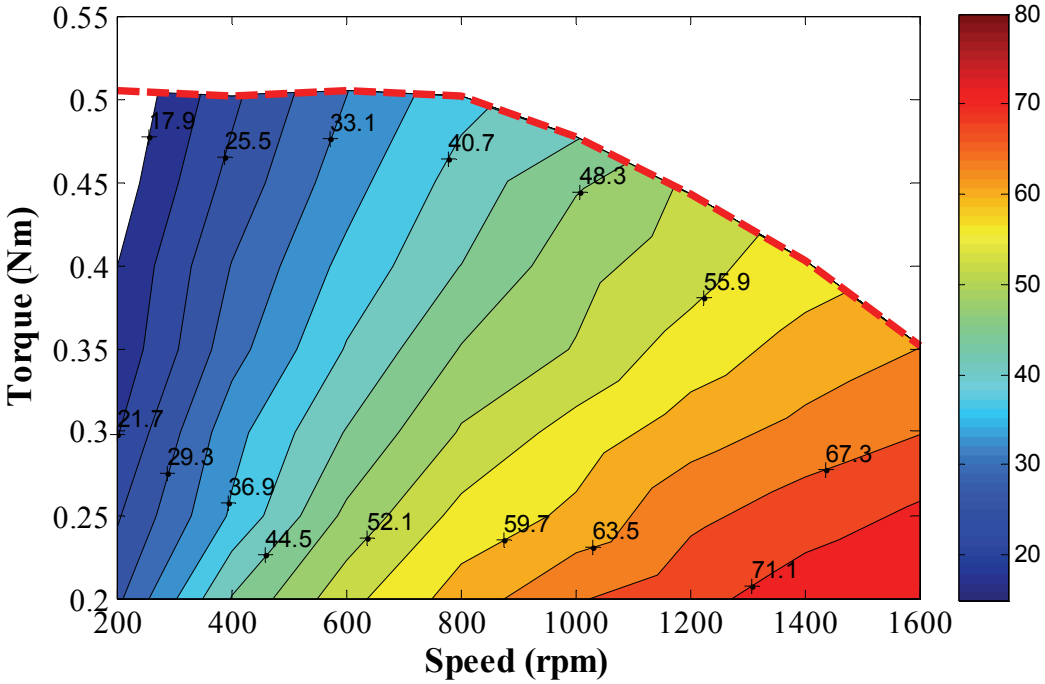

(a) Without the utilisation of field excitation current ($i_f = 0$).

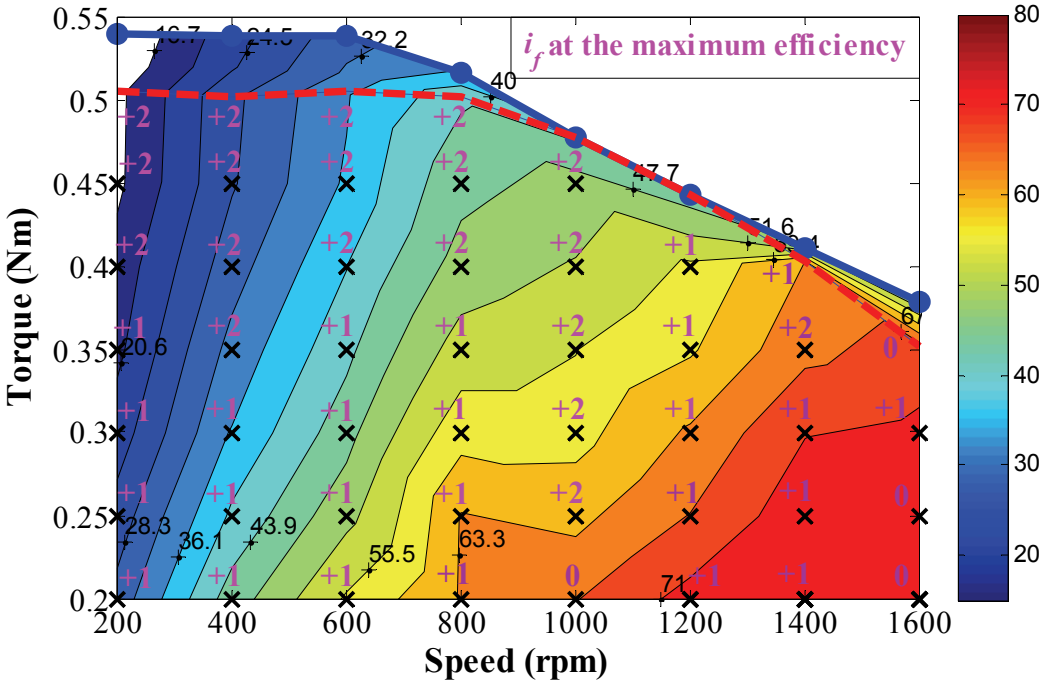

(b) With the utilisation of field excitation current.

Fig. 3.17. Efficiency map versus speed.

3.7 Summary

A new control strategy for the hybrid-excited switched-flux permanent magnet machines has been presented in this chapter. It utilises a novel feature of HESFPMMs, in which the flux produced by the permanent magnets can be inherently short-circuited via the iron flux-bridges. The proposed method utilises the field excitation current to enhance the torque response in the flux-enhancing mode, while in the flux-weakening operation, the field excitation current is controlled toward zero, and the negative *d*-axis current is used for the extended operating range. The references of the field excitation current and *d*-axis current are determined by the voltage error regulation method. The proposed method not only shows robustness against machine parameter changes, but also exhibits a smooth transition between flux-enhancing and flux-weakening operation using the field excitation current control. Furthermore, in the operation below the rated torque, the efficiency can be improved based on the utilisation of field excitation current as has been presented in the efficiency map. The proposed method is applicable to other hybrid-excited machines.

CHAPTER 4

FLUX-WEAKENING CONTROL OF HYBRID-EXCITED PERMANENT MAGNET MACHINES

In this chapter, three flux-weakening control methods, i.e. utilising field excitation current alone (Method-I), utilising armature current alone (Method-II), and optimisation method (Method-III), for the HEPMM are considered. All three methods can achieve the same torque in the constant-torque region due to the same enhanced field excitation currents. In the flux-weakening region, Method-I exhibits low torque and a limited operating speed range since the field excitation current reaches zero. Nevertheless, the operating speed range can be further extended by Method-II and Method-III. In addition, Method-III can provide a higher efficiency in flux-weakening region than Method-II since the copper loss of field winding can be decreased in proportion to the reduction of field excitation current. Those flux-weakening control methods are verified by experimental results.

4.1 Introduction

In order to achieve the maximum torque in the constant-torque region of the PMSM, the *d*-axis and *q*-axis currents are controlled by tracking the maximum torque per ampere (MTPA) trajectory [CHE10], [CON10]. In some specific applications with wide speed range, for instance, automotive vehicles and spindle drives, flux-weakening control is required [KWO06], [KWO07], [LIN12], [LIU12], [MOR90], [PAN05]. Several flux-weakening control methods are presented in [KWO06], [KWO07], [LIN12], [LIU12], [MOR90], [PAN05], [ZHU00]. However, since only the permanent magnet is primarily utilised to generate the excitation flux of such machines, the control variables that can be used to weaken the flux-linkage are limited to only *d*-axis current.

Because the hybrid-excited permanent magnet machines (HEPMMs), as shown in Fig.4.1, consist of two excitation sources, i.e. permanent magnets (PMs) and field windings, such machines provide a capability to adjust the flux-linkage through the field excitation current. Consequently, high torque at low speed and wide operating speed range can be provided [AFI15], [CHE11a], [ZHA10]. Moreover, due to windings and

PMs are located on the stator, high-speed operation and cooling capability are relatively easier for such machines [AFI15], [AMA09], [CHE11a], [OWE10], [ZHA10], as has been introduced in Chapter 1. Accordingly, the HEPMMs are very attractive.

Based on the operating principle of the HEPMM, the field excitation current is a major excitation source compared with the PMs. Therefore, the maximum field excitation current is commonly employed to achieve the highest torque of such machines. However, in flux-weakening operation, the *d*-axis current is utilised to oppose the direction of field excitation flux produced by field excitation current. As a result, the efficiency in this region would be deteriorated due to the excessive copper loss of field winding. Indeed, both of field excitation and *d*-axis currents can be utilised to weaken the flux-linkage for extending the speed range of the HEPMM. Therefore, these currents need to be optimised. In [KEF10], a specific value of field excitation current is utilised in flux-weakening region. A large torque drop is noticeably emerged when the machine speed exceeds its rated speed. The methods based on Extended Lagrange multipliers optimisation have been investigated in [HGU14], [HUA12], [MBA12], [SHI07]. Therefore, the optimal currents can be determined by the analytical expressions. Nevertheless, they are sensitive to the variation of the machine parameters, and also difficult to implement due to high computational burden. The flux-weakening control of the HEPMM is presented in [POT15], which the field excitation current and the *d*-axis current can be automatically modified depending on the operation regions. Although the influence of machine parameters variation can be avoided for such method, the optimisation of weakening currents, i.e. field excitation and *d*-axis currents, relating to the efficiency improvement in flux-weakening region is not considered.

Since there are mainly two currents that HEPMM can be utilised to weaken the flux-linkage in flux-weakening operation, i.e. field excitation current and *d*-axis current, three flux-weakening control methods are proposed: 1) utilising field excitation current only, 2) utilising armature current only, and 3) optimisation method. Those methods are defined as Method-I, Method-II, and Method-III, respectively. A comparison of three flux-weakening control methods of the HEPMMs, in terms of the torque, operating speed range, and efficiency, is presented in this chapter. Since the weakening currents in both Method-I and Method-II, i.e. field excitation and *d*-axis currents, are modified based on the voltage error regulation method [KWO07], the utilisation of DC-link voltage is efficient. In Method-III, the maximum efficiency condition is analyzed based on the

differentiation method in order to determine the optimal field excitation current. In addition, since it is calculated as a function of the *d*-axis and *q*-axis currents without the requirement of the sensitive machine parameters such as resistances, Method-III is simple to implement and robust to the machine parameter variation. All flux-weakening control methods are validated by experimental results.

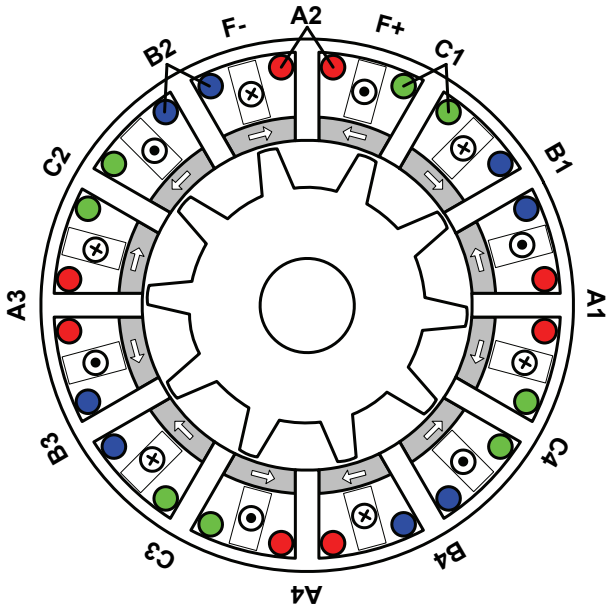

Fig. 4.1. Cross-section of the prototype HEPMM employed for investigation, [AFI15].

4.2 Machine Topology and Operating Principle (Machine-II)

The HEPMM employed for investigation, which consists of 12-stator/10-rotor poles, is shown in Fig.4.1. The armature windings (phase A, B, and C) and the field windings are wound on each of the salient stator poles. Four armature windings in each phase and twelve field windings are separately connected in series. The PMs are located on the slot opening between two adjacent stator poles. The machine parameters are given in Table 2.2, Chapter 2. There has no magnets or excitation coils on the rotor structure, which makes it simple and robust. The phase flux-linkage against the field excitation current obtained by 2D finite element (FE) analysis is shown in Fig.4.2. It is obvious that the phase flux-linkage of the prototype machine can be enhanced/weakened utilising only the positive field excitation current.

The operating principle of the prototype machine can be clearly explained by utilising the simplified model, Fig.4.3. On open circuit ($i_f = 0$), Fig.4.3(a), the PM flux is inherently short-circuited via the stator without the flux-linkage. In Fig.4.3(b), if only the

positive field excitation flux ($i_f > 0$) is excited, the flux-linkage can be enhanced. By considering both flux sources, i.e. the PM flux and the field excitation flux, the net enhanced flux-linkage is shown in Fig.4.3(c). Clearly, when the field excitation current is further increased, the PM flux is pulled into the air-gap.

In Fig.4.4, the operating principle of the prototype machine can also be expressed by the flux distributions obtained from the 2D finite element (FE) analysis. On open-circuit with no field excitation current ($i_f = 0$), Fig.4.4(a), the PM flux is naturally short-circuited through the stator back-iron. As a result, the flux linkage entering into the air-gap is almost invisible. In contrast, in Fig.4.4(b), if only the positive field excitation current ($i_f > 0$) is provided (the PMs are not magnetised), the flux will enter into the airgap and rotor. Then, based on the combined effects of both flux sources, i.e. the PM and field windings, the total enhanced flux-linkage can be shown in Fig.4.4(c), compared to Fig. 4.4(a). It is noted that the PM flux can be entirely pushed into the air-gap if the field excitation current is further increased by utilising the model in Fig.4.3.

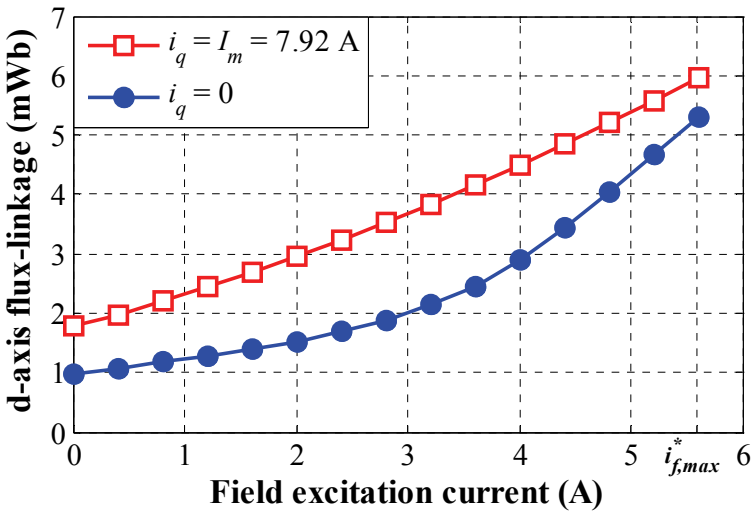

Fig. 4.2. Flux-linkage adjustability of the prototype HEPMM machine, $i_d = 0$.

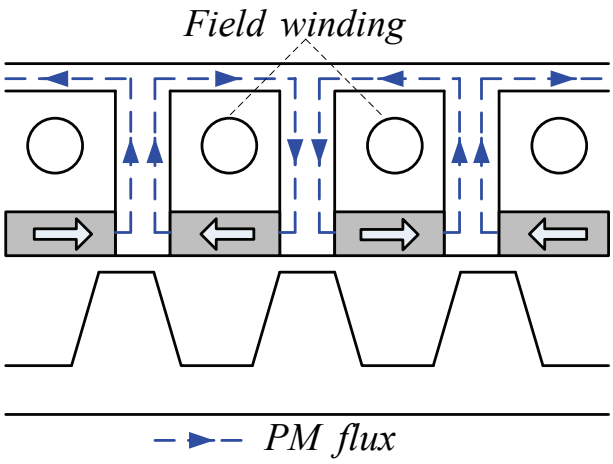

(a) PM-flux ($i_f = 0$)

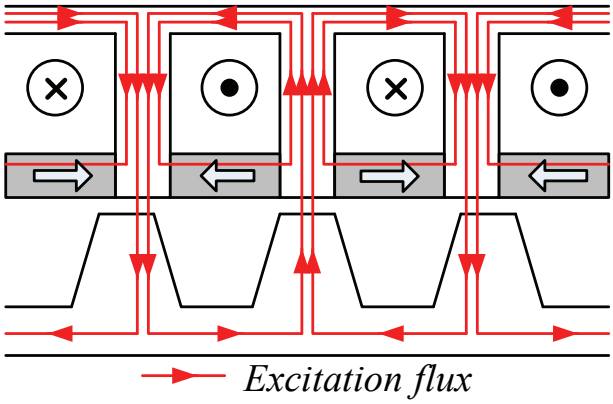

(b) Field excitation flux ($i_f > 0$)

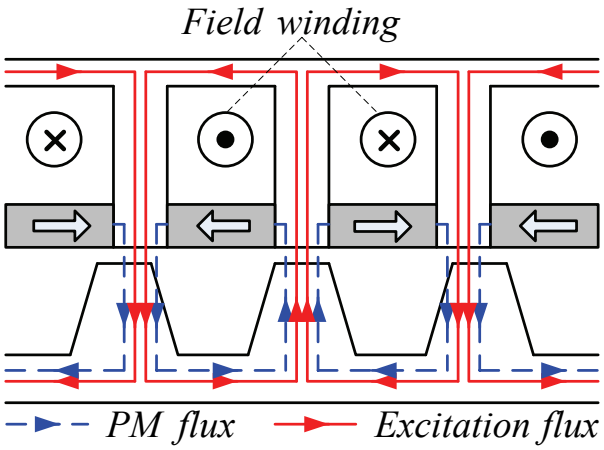

(c) Net enhancing flux-linkage

Fig. 4.3. Flux-linkage adjustability of the prototype HEPMM.

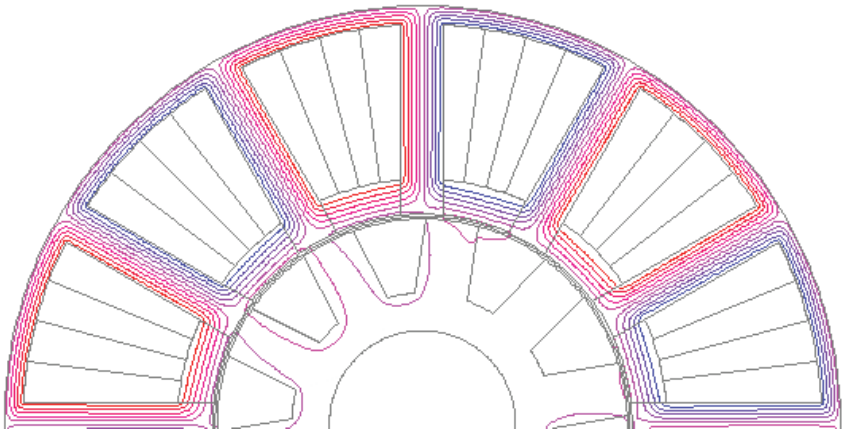

(a) Only PM-flux (i_f = 0)

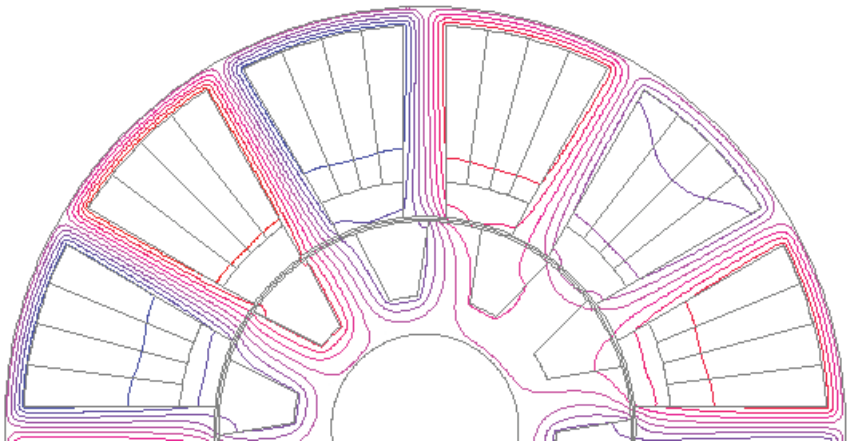

(b) Only field excitation flux (i_f > 0)

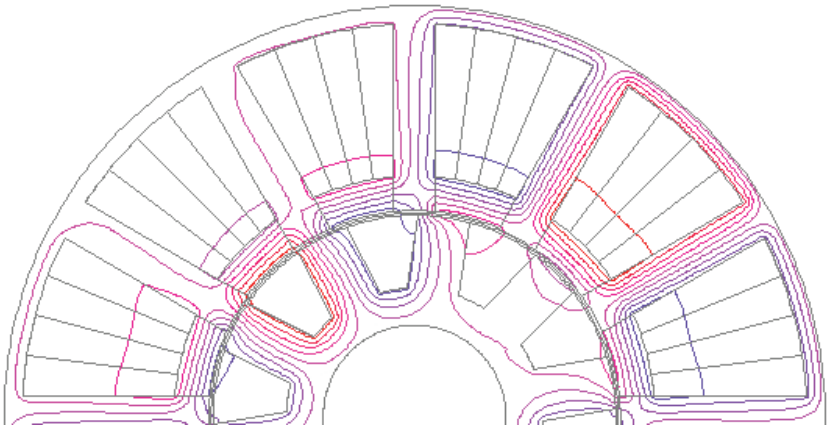

(c) Total enhancing flux-linkage (PM, i_f > 0)

Fig. 4.4. Flux-distributions of the prototype HEPMM.

In steady-state, the simplified voltage equations of the HEPMM in the synchronous reference frame are given in the matrix form by (4.1).

$$\begin{bmatrix} v_d \\ v_q \\ v_f \end{bmatrix} = \begin{bmatrix} R_s & -\omega_e L_q & 0 \\ \omega_e L_d & R_s & \omega_e L_{mf} \\ 0 & 0 & R_f \end{bmatrix} \begin{bmatrix} i_d \\ i_q \\ i_f \end{bmatrix} + \begin{bmatrix} 0 \\ \omega \psi_{pm} \\ 0 \end{bmatrix} \tag{4.1}$$

The flux-linkages are expressed as,

$$\begin{bmatrix} \psi_d \\ \psi_q \\ \psi_f \end{bmatrix} = \begin{bmatrix} L_d & 0 & L_{mf} \\ 0 & L_q & 0 \\ L_{mf} & 0 & L_f \end{bmatrix} \begin{bmatrix} i_d \\ i_q \\ i_f \end{bmatrix} + \begin{bmatrix} \psi_{pm} \\ 0 \\ 0 \end{bmatrix}. \tag{4.2}$$

where v_d, v_q, i_d, i_q are d-, q-axis voltages and currents, v_f, i_f are field excitation voltage and current, L_d, L_q, are d-axis and q-axis inductances, L_{mf}, L_f are the mutual and self-inductances of field winding, R_s, R_f are armature and field resistances, ψ_d, ψ_q, ψ_{pm} are d-axis, q-axis and PM flux-linkages, and ω_e is the electrical rotor speed.

The electromagnetic torque is given by (4.3).

$$T_e = \frac{3}{2} P\left(\psi_d i_q - \psi_q i_d\right) \tag{4.3}$$

By instituting of the d-axis and q-axis flux-linkages as given in (4.2) into (4.3), the torque can be represent by (4.4).

$$T_e = \frac{3}{2} P\left[\left(\psi_{pm} + L_{mf} i_f\right) i_q + \left(L_d - L_q\right) i_d i_q\right]. \tag{4.4}$$

Based on the unity saliency of the prototype machine [AFI15] in which the d-axis and q-axis inductances are approximately equal ($L_d = L_q$), the torque equation can be expressed as,

$$T_e = \frac{3}{2} P\left(\psi_{pm} + L_{mf} i_f\right) i_q . \tag{4.5}$$

4.3 Flux-weakening Control Methods

In this section, three flux-weakening control methods, which are classified based on the utilisation of weakening currents, i.e. utilising field excitation current only, utilising armature current only, and optimisation method, will be explained as follows:

4.3.1 Flux-weakening control method utilising field excitation current (Method-I)

According to the outstanding feature of the HEPMM in which the flux-linkage can effectively be enhanced/weakened through field winding, it is possible to utilise the modification of field excitation current to extend the operating speed range in flux-weakening region. Hence, the flux-weakening control based on the utilisation of field excitation current is shown in Fig.4.4. It is obvious that the maximum field excitation current is initially employed in order to enhance the maximum torque, and it will be adjusted in flux-weakening region by the modified field excitation current (Δi_f) as given by (4.6). It is determined based on the voltage error regulation method [KWO07] in which the different voltages between the input and output of the voltage limitation block are utilised. In this modified part, the α-β axis voltages are converted to the *d*-*q* axes by the Park's transformation.

$$\Delta i_f = \alpha \sqrt{\frac{\omega_c}{s+\omega_c}(v_d^* - v_{dm}^*)^2 + \frac{\omega_c}{s+\omega_c}(v_q^* - v_{qm}^*)^2} \tag{4.6}$$

Therefore, the modified field excitation reference current is given as,

$$i_f^* = i_{f,\max} - \Delta i_f . \tag{4.7}$$

where α is the constant gain, ω_c is the bandwidth of the low-pass filter (LPF), s is the integral operator, * denotes a reference value, v_d, v_q are *d*- and *q*-axis voltages, v_{dm}, v_{qm} are *d*- and *q*-axis output voltages of over-modulation block, and $i_{f,\max}$ is the maximum field excitation current.

The gain α directly influences the dynamic performance and steady-state torque, a larger gain exhibits a faster dynamic response, but a lower torque per ampere ratio [KWO06]. The α gain can be determined by (4.8), which has been introduced in [LEV08]. However, since the bandwidth of flux-weakening control loop is typically quite low compared to the bandwidth of the *d*-*q* axis current control loops, the bandwidth of

low-pass filter is also low. In this thesis, the bandwidth of low-pass filter is set at 10 Hz, while $\alpha = 1.5$.

$$\alpha = \frac{\ln 9}{t_{rfw}\omega_e L_d}. \tag{4.8}$$

where t_{rfw} is the flux-weakening control loop rise time, which is 100-450 ms [LEV08].

All reference currents are shown in Table 4.1, in which the q-axis current can be maintained at the maximum armature current (I_m) in the whole operating speed range due to zero d-axis current.

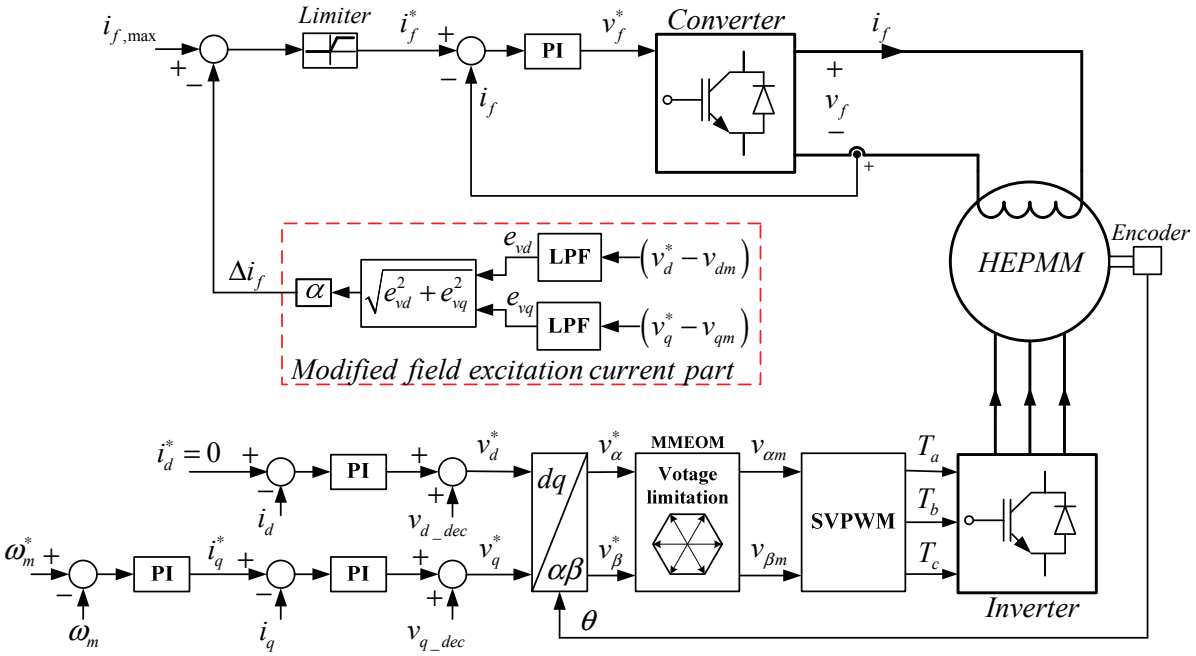

Fig. 4.4. Flux-weakening control strategy utilising field excitation current (Method-I).

Table 4.1. Operating conditions with utilising field excitation current.

Reference currents	Constant-torque region	Flux-weakening region
i_d^*	0	
i_q^*	I_m	
i_f^*	$i_{f,\max}$	$i_{f,\max} - \Delta i_f$

It should be noted that the HEPMM's torque equation is a function of both field excitation flux ($L_{mf}i_f$) and the q-axis current as given by (4.5), which is different from the conventional machine. Therefore, in Method-I, the torque generation in the flux-weakening region would be gradually decreased in proportion to the decreasing of field

excitation current.

4.3.2 Flux-weakening control method utilising armature current (Method-II)

Fig.4.5 shows the flux-weakening control of the HEPMM based on the utilisation of armature current as mentioned in [KWO07], [LIU12], while the field excitation current is maintained at its maximum value in the whole operating speed range in order to achieve the maximum enhanced torque. Hence, only the *d*-axis current is utilised to weaken the flux-linkage while the voltage and current are beyond the constraints. However, the higher increasing speed results in the lower *q*-axis voltage due to the modified *d*-axis current. As a result, in order to extend the speed range in case the *q*-axis voltage reaches to zero, the *q*-axis current reference needs to be modified instead. All reference currents are expressed in Table 4.2.

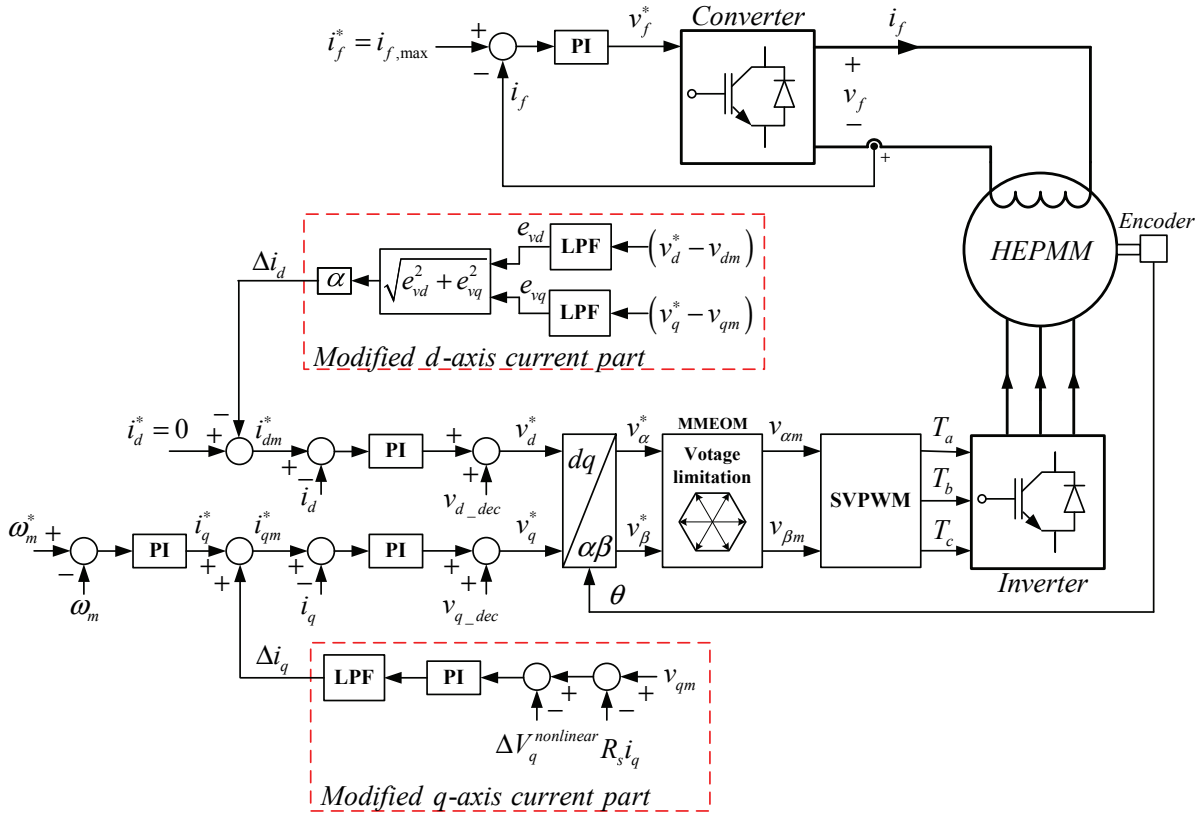

Fig. 4.5. Flux-weakening control strategy utilising armature current (Method-II).

Table 4.2 Operating conditions with utilising armature current.

Reference currents	Constant-torque region	Flux-weakening region
i_{dm}^*	0	$i_d^* - \Delta i_d$
i_{qm}^*	$i_{qm}^* = i_q^* = I_m$	$\min\left(i_q^*, \sqrt{I_m^2 - i_d^2}\right) + \Delta i_q$
i_f^*	$i_{f,max}$	

1) Modification of the *d*-axis reference current

It is well known that for extending a speed range under the current and voltage limits, the *d*-axis reference current needs to be adjusted to weaken the flux-linkage. In this method, the *d*-axis reference current is automatically modified tracking the MTPA trajectory. Thus, the modified *d*-axis current (Δi_d) is given by (4.9) [KWO07], [LIU12]. It is also based on the voltage error regulation method, which has been explained in (4.6).

$$\Delta i_d = \alpha \sqrt{\frac{\omega_c}{s+\omega_c}(v_d^* - v_{dm}^*)^2 + \frac{\omega_c}{s+\omega_c}(v_q^* - v_{qm}^*)^2} \ . \tag{4.9}$$

Therefore, the modified *d*-axis reference current is given as,

$$i_{dm}^* = i_d^* - \Delta i_d \ . \tag{4.10}$$

where i_{dm}^*, i_{qm}^* are the *d*-axis and *q*-axis modified reference currents.

2) Modification of the *q*-axis reference current

When the machine operates under the infinite constant power speed ratio characteristic with $L_d I_m > \psi_{pm}$ [KWO07], [LIU12] in which the *q*-axis voltage is controlled toward zero by the *d*-axis current, and hence, the higher speed range cannot be achieved. Under this condition, the *q*-axis current would be modified instead following the maximum torque per voltage (MTPV) trajectory, which means the *d*-axis voltage will be controlled while the *q*-axis voltage is still maintained at zero. The modified *q*-axis current (Δi_q) is given by (4.11) [LIU12]. Indeed, it will be activated corresponding to the negative value of the *q*-axis voltage. Since the PI regulator is utilised with the compensation of both voltage loss of inverter and resistance voltage drop, a good dynamic response of this method can be achieved.

$$\Delta i_q = \min\left(0, \left(k_p + \frac{k_i}{s}\right) \times \frac{\omega_c}{s+\omega_c}\left(v_q^* - \Delta V_q^{nonlinear} - R_s i_q\right)\right) \tag{4.11}$$

where k_p, k_i are the regulator gains, and $\Delta V_q^{nonlinear}$ is the estimated q-axis nonlinear voltage loss of inverter. Consequently, the modified q-axis reference current can be given as,

$$i_{qm}^* = \min\left(i_q^*, \sqrt{I_m^2 - i_d^2}\right) + \Delta i_q . \tag{4.12}$$

3) Estimation of q-axis voltage loss of inverter

The estimated voltage loss of inverter has been analyzed in [KIM06], which is also mentioned in chapter 2. It is determined by utilising the ideal characteristic of switching power devices provided by the manufacturers, the dead time, and the measured DC-link voltage. The static gain of voltage loss (A_p), which is defined in literature as the intermediate parameter, is given as,

$$A_p = \frac{\left(V_{dc} - V_{ce} + V_d\right)\left(t_d + t_{on} - t_{off}\right)}{3T_s} + \frac{V_{ceo} + V_{do}}{6} \tag{4.13}$$

where V_{dc} is the measured DC-link voltage, V_{ce} and V_d are the voltages drop of switching power devices, t_d is the dead time, t_{on} and t_{off} are the total turn-on and turn-off transition times, V_{ceo} and V_{do} are the threshold voltages of switching power devices, and T_s is the sampling period. Based on the Park's transformation, the estimated q-axis nonlinear voltage loss of inverter can be given by (4.14).

$$\begin{aligned} \Delta V_q^{nonlinear} = -2A_P \Bigg(& sign(i_a)\sin\theta_e + sign(i_b)\sin\left(\theta_e - \frac{2\pi}{3}\right) \\ & + sign(i_c)\sin\left(\theta_e + \frac{2\pi}{3}\right)\Bigg) + \frac{r_{ce} + r_d}{2} i_q \end{aligned} \tag{4.14}$$

where $i_{a,b,c}$ denote the phase currents, *sign* is the signum function to define the current direction, and r_{ce} and r_d are the resistances of switching power devices.

However, since the maximum field excitation current is employed in whole operating region, the efficiency might be deteriorated in flux-weakening operation due to unnecessary copper loss of field winding. As a result, the utilisation of all currents should be optimised.

4.3.3 Optimisation Method (Method-III)

Employing the maximum field excitation current for all operating regions might cause a low efficiency in the flux-weakening region due to a redundant copper loss of field winding. Therefore, in order to achieve the higher efficiency of the HEPMM, the utilisation of both armature and field excitation currents will be verified under the same condition in terms of torque and speed.

4.3.3.1 Maximum Efficiency Condition

Based on the relation of torque and mechanical speed, hence, the mechanical output power can be estimated by (4.15).

$$P_m = T_e \omega_m = \frac{3}{2}\left(\psi_d i_q - \psi_q i_d\right)\omega_e \tag{4.15}$$

According to the assumption of the balanced impedance and sinusoidal flux distribution, the electrical input power is given by (4.16) in which the power consumption of field winding is considered.

$$P_e = \frac{3}{2}\left(v_d i_d - v_q i_q\right) + v_f i_f \tag{4.16}$$

From the *d*-axis and *q*-axis voltage equations in (4.1), the electrical input power can be rearranged as (4.17) in which the copper losses, i.e. armature winding and field winding copper losses, and mechanical power are separated.

$$P_e = \underbrace{\frac{3}{2}\left(R_s i_d^2 + R_s i_q^2 + \frac{2}{3}R_f i_f^2\right)}_{Copper\ losses} + \underbrace{\frac{3}{2}\left(\psi_d i_q - \psi_q i_d\right)\omega_e}_{Machanical\ power} \tag{4.17}$$

In this research, the maximum efficiency is determined depending on the variation of field excitation current, which is compared to the method that the field excitation current is maintained at its maximum value. Both methods are investigated under the same condition in terms of torque and speed. Hence, only the influence of copper loss is considered whereas the other losses, for instance, the core loss and the mechanical loss can be neglected. The copper losses, i.e. armature and field windings, are calculated by utilizing the measured currents and resistances, for which the temperature rise is not considered. Therefore, based on the utilisation of the mechanical output power (P_m) and the electrical input power (P_e), accounting for the power consumption of the field

winding, the HEPMM's efficiency can be expressed by (4.18).

$$\eta = \frac{P_m}{P_e} = \frac{\left(\psi_d i_q - \psi_q i_d\right)\omega_e}{\left(R_s i_d^2 + R_s i_q^2 + \frac{2}{3} R_f i_f^2\right) + \left(\psi_d i_q - \psi_q i_d\right)\omega_e} \tag{4.18}$$

However, in experiments, since the mechanical output power is calculated by the measured load torque and the measured speed, the whole losses have been considered.

In order to determine the maximum efficiency condition of the HEPMMs, the differentiation of the efficiency (η) with respect to the amplitude of armature current (I_a) is considered. In equation (4.18), the *d*-axis and *q*-axis currents are replaced by the armature current in the form of amplitude and angle (θ_i), as defined in Fig.4.6. It is noted that since the *d*-axis and *q*-axis currents are defined by the variation of the angle, whole operating conditions can be considered.

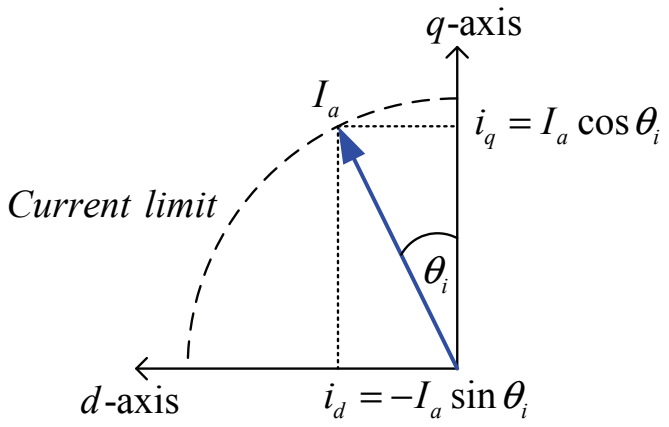

Fig. 4.6. Projection of armature current.

The differentiation of the efficiency is expressed as,

$$\frac{\partial \eta}{\partial I_a} = 0, \text{ where } I_a = \sqrt{i_d^2 + i_q^2},$$

$$\frac{\left[\begin{array}{l}\left(R_s I_a^2 + \frac{2}{3} R_f i_f^2 + \psi_d I_a \omega_e \cos\theta_i + \psi_q I_a \omega_e \sin\theta_i\right)\left(\psi_d \omega_e \cos\theta_i + \psi_q \omega_e \sin\theta_i\right) \\ -\left(\psi_d I_a \omega_e \cos\theta_i + \psi_q I_a \omega_e \sin\theta_i\right)\left(2R_s I_a + \psi_d \omega_e \cos\theta_i + \psi_q \omega_e \sin\theta_i\right)\end{array}\right]}{\left(R_s I_a^2 + \frac{2}{3} R_f i_f^2 + \psi_d I_a \omega_e \cos\theta_i + \psi_q I_a \omega_e \sin\theta_i\right)^2} = 0$$

In the above equation, it can be rewritten as,

$$\frac{\left(-R_s I_a^2+\frac{2}{3}R_f i_f^2\right)\left(\psi_d \omega_e \cos\theta_i+\psi_q \omega_e \sin\theta_i\right)}{\left(R_s I_a^2+\frac{2}{3}R_f i_f^2+\psi_d I_a \omega_e \cos\theta_i+\psi_q I_a \omega_e \sin\theta_i\right)^2}=0$$

Hence,

$$\left(-R_s I_a^2+\frac{2}{3}R_f i_f^2\right)\left(\psi_d \omega_e \cos\theta_i+\psi_q \omega_e \sin\theta_i\right)=0$$

Consequently, the maximum efficiency can be achieved whilst the copper loss of armature winding and the copper loss of field winding are equal, as expressed by (4.19).

$$\frac{3}{2}R_s I_a^2 = R_f i_f^2 . \tag{4.19}$$

Since both the armature winding and field winding of the prototype machine are located on the same place of the stator, the temperature rises of two windings are assumed to be identical. Furthermore, the same coil types of those windings are used for this machine. As a result, the resistance ratio between armature winding and field winding can be approximately remained constant even operating in the flux-weakening region. Therefore, the winding resistances can be easily replaced by their turn numbers, rather than utilising the resistances. Since the turn ratio of the prototype machine is 1/3 (N_s = 184, N_f = 552), where N_s and N_f are the turns number of armature winding and field winding respectively, the optimal field excitation current with respect to the maximum efficiency condition can be given by (4.20).

$$i_{f,opt}=\sqrt{\frac{3}{2}\left(\frac{N_s}{N_f}\right)I_a}=\frac{I_a}{\sqrt{2}}=\sqrt{\frac{i_d^2+i_q^2}{2}} . \tag{4.20}$$

4.3.3.2 Optimisation flux-weakening control method (Method-III)

The optimisation flux-weakening control method, which is defined as Method-III, utilises both the field excitation and *d*-axis currents in order to extend the operating speed range and maximise the efficiency, as shown in Fig.4.7. In this method, the optimal field excitation reference current is employed as shown in (4.20). In the constant-torque region, the optimal field excitation reference current remains at its maximum value because the prototype machine has been optimised for achieving the highest efficiency when the maximum armature current is employed. In the flux-weakening region, both of the field excitation and the *d*-axis currents are utilised to weaken the flux-linkage. Meanwhile, the *q*-axis current is controlled with regard to the requirement of the speed and load-torque. In this method, the modification of both *d*-axis and *q*-axis currents are based on the same principle of Method-II, as shown in Fig.4.6.

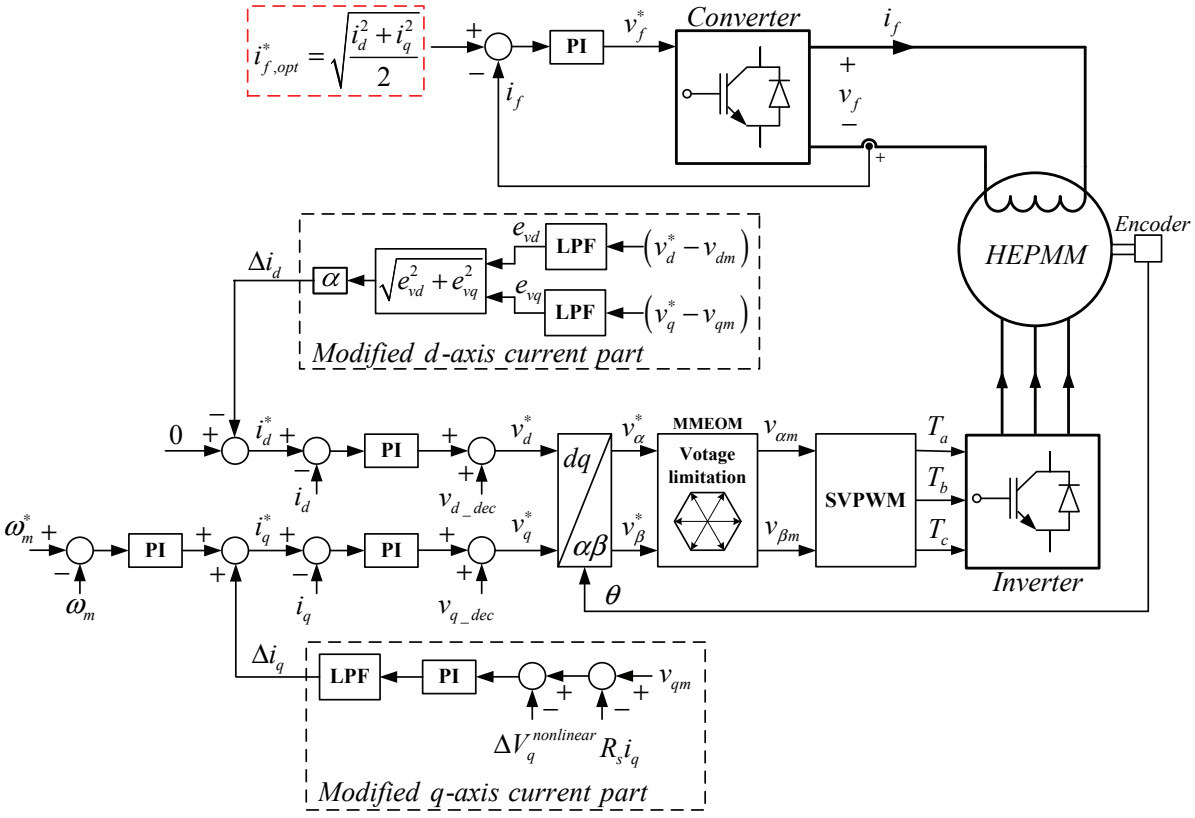

Fig. 4.7. Optimisation flux-weakening control strategy (Method-III).

As a consequence, the requirement the *d*-axis and *q*-axis currents would be reduced compared with the Method-II. Since the optimal field excitation current utilises only the *d*-axis and *q*-axis currents, it is simple to implement and robust to the machine parameter variation. The current references of the optimisation flux-weakening control method are given in Table 4.3.

Table 4.3. Operating conditions with utilising optimisation method.

Reference currents	Constant-torque region	Flux-weakening region
i_{dm}^*	0	$i_d^* - \Delta i_d$
i_{qm}^*	$i_{qm}^* = i_q^* = I_m$	$\min\left(i_q^*, \sqrt{I_m^2 - i_d^2}\right) + \Delta i_q$
i_f^*	$i_{f,opt} = \sqrt{\frac{i_d^2 + i_q^2}{2}}$	

4.4 Experimental Verification

4.4.1 Experimental Setup

The field orientation control algorithm is implemented on a dSPACE platform in order to verify the performance of the proposed method experimentally. A 1.5 kW wound field type DC motor is utilised to adjust the load-torque. Other experimental equipment has introduced in Chapter 2. In order to increase the utilisation of DC-link voltage in flux-weakening region [KWO06], the minimum magnitude error over-modulation (MMEOM) is applied. The setup parameters are defined in Table 4.4.

Table 4.4. Experimental setup

Maximum motor test speed	1200 rpm
Maximum absolute field excitation current	5.6 A
Maximum armature current	7.92 A
DC link voltage	40 V
DC supply voltage of the converter	30 V
Switching frequency of the inverter	10 kHz
Switching frequency of the converter	5 kHz

4.4.2 Experimental Results

Fig.4.8 shows the measured results of all flux-weakening control methods. The measured torque and output power against speed are shown in Figs.4.8(a) and (b), respectively. It is obvious that all control methods can achieve the same torque and output power in the constant-torque region due to the same enhanced field excitation currents as illustrated in Fig.4.9(a). In the flux-weakening region, the torque and output power of Method-I is significantly deteriorated and the operating speed range is also limited as only the field excitation current is controlled. Meanwhile, Method-II and Method-III can provide higher torque and power. The *d*-axis and *q*-axis currents of all control methods are shown in Fig.4.9(b). It is obvious that Method-II utilises only the *d*-axis current to weaken the flux-linkage in which the field excitation current maintains at its maximum value (5.6 A) in all operating regions, while Method-III utilises both field excitation and *d*-axis currents. Compared to Method-II, the requirement of the *d*-axis current is decreased in Method-III. Consequently, higher *q*-axis current can be utilised under the current-limit as shown in Fig.4.9(b).

Fig.4.10 shows the measured copper loss and efficiency of all flux-weakening control methods. The field winding copper loss is shown in Fig.4.10(a). Obviously, Method-I exhibits the lowest copper loss of field winding compared with other methods regarding to the field excitation current control. In Method-II, the field winding copper loss is kept at 94 W throughout the operating regions, while it can be greatly reduced in the flux-weakening region for Method-III as a result of the optimal field excitation and *d*-axis armature currents as illustrated in Fig.4.9(a). Likewise, the armature winding copper loss of all flux-weakening control methods are shown in Fig.4.10(b). These are calculated based on the employing of *d*-axis and *q*-axis currents as shown in Fig.4.9(b). As a result, the total copper losses for all operating regions which consist of the field winding and the armature winding copper losses are depicted in Fig.4.10(c). Although the total copper losses of Method-I can be remarkably reduced in the flux-weakening region than Method-II and Method-III corresponding to the modification of field excitation current, the operating speed range is limited. However, based on the utilisation of the optimal field excitation and *d*-axis armature currents, Method-III can achieve higher efficiency in flux-weakening region than Method-II, and wider speed region compared to Method-I, Fig.4.11.

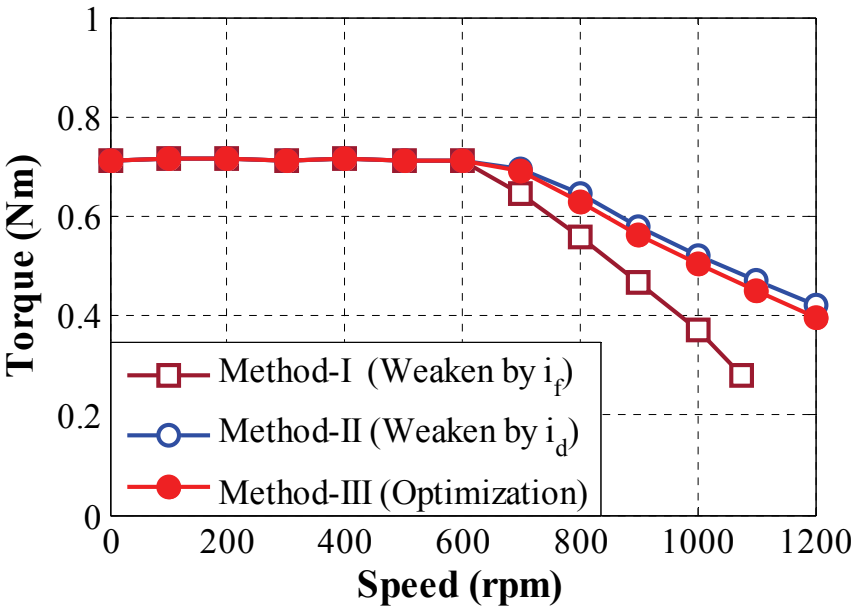

(a) Torque

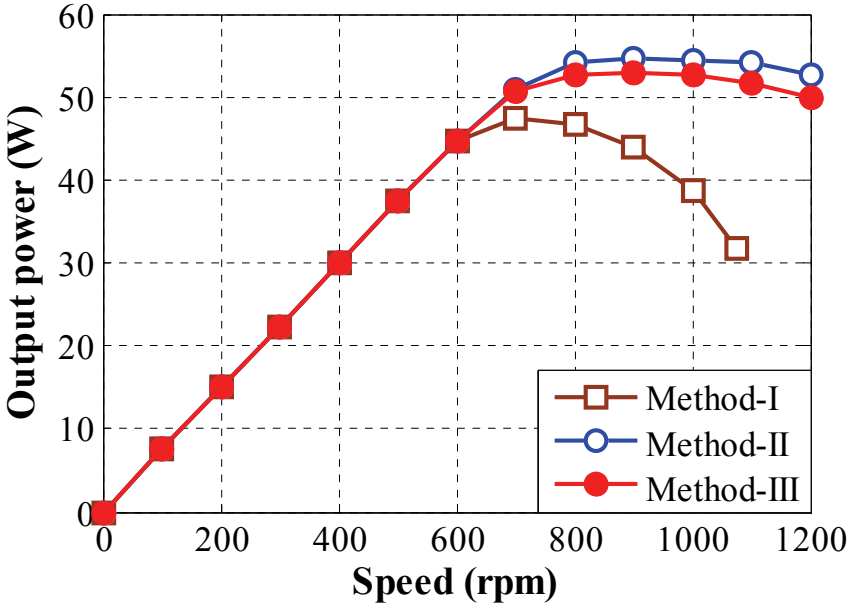

(b) Mechanical output power

Fig. 4.8. Measured torque and output against speed

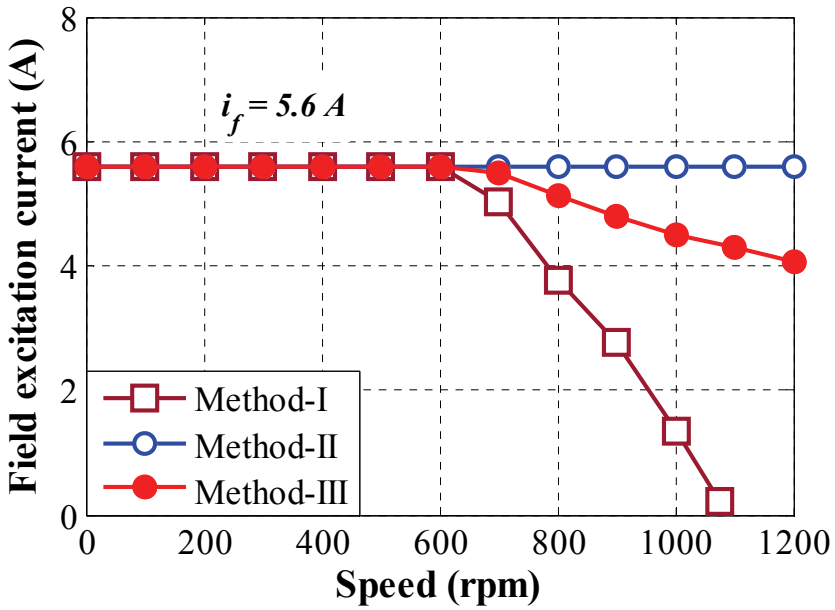

(a) Field excitation current

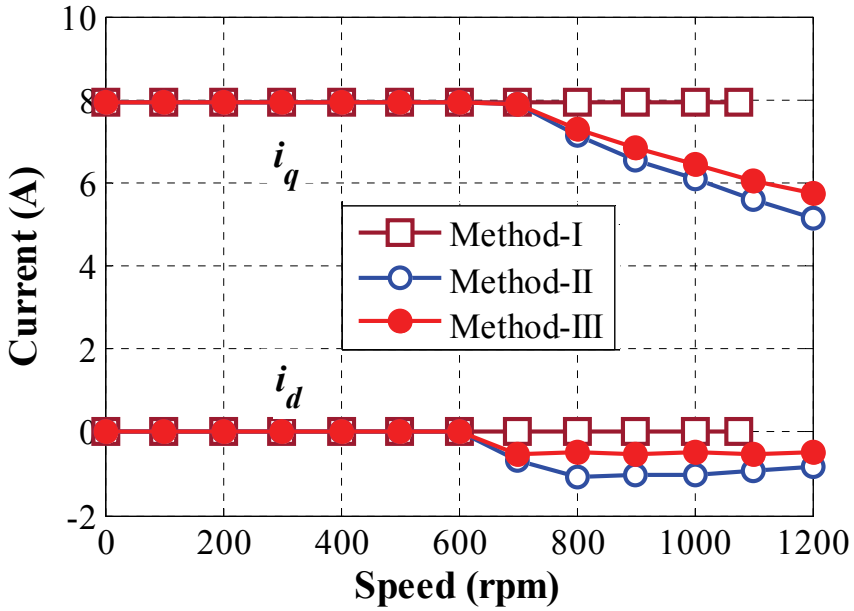

(b) *d*-axis and *q*-axis currents

Fig. 4.9. Measured currents against speed

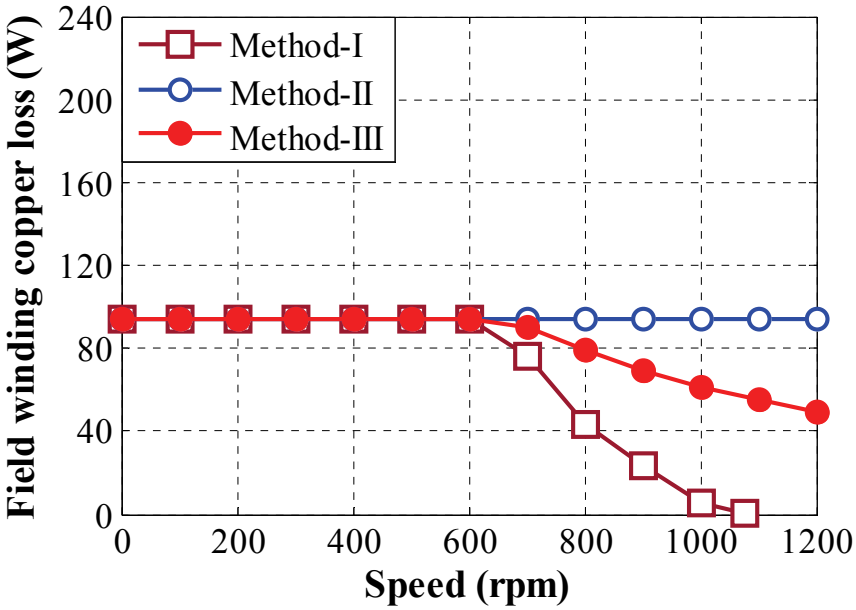

(a) Field winding copper loss

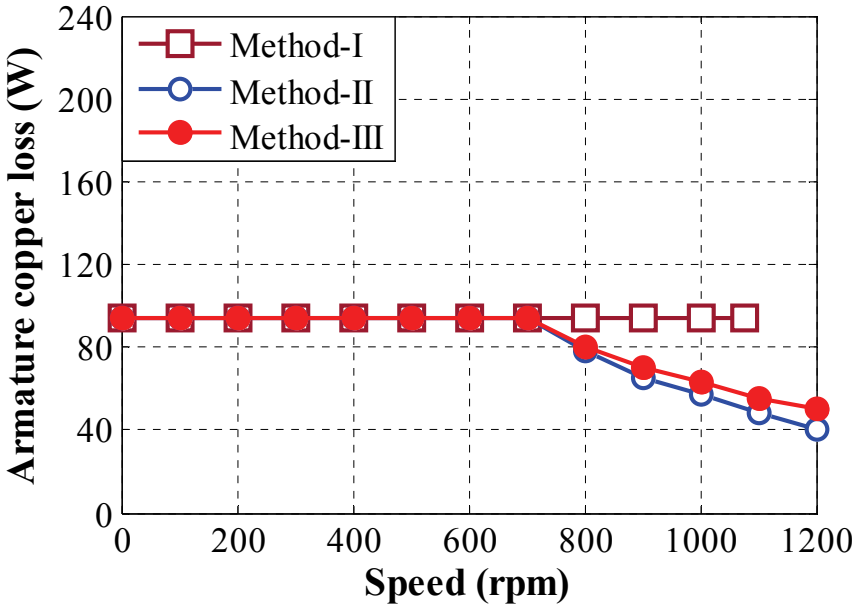

(b) Armature winding copper loss

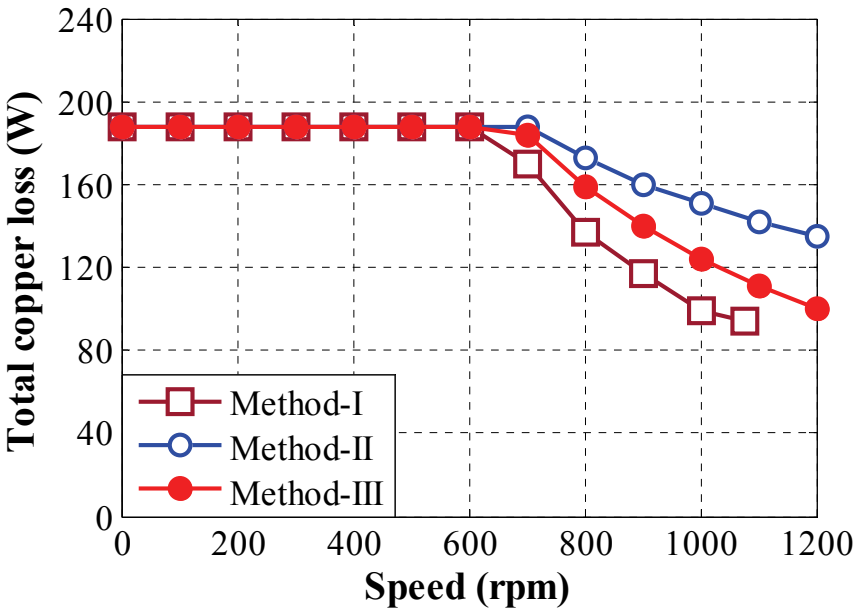

(c) Total copper loss.

Fig. 4.10. Measured copper losses against speed

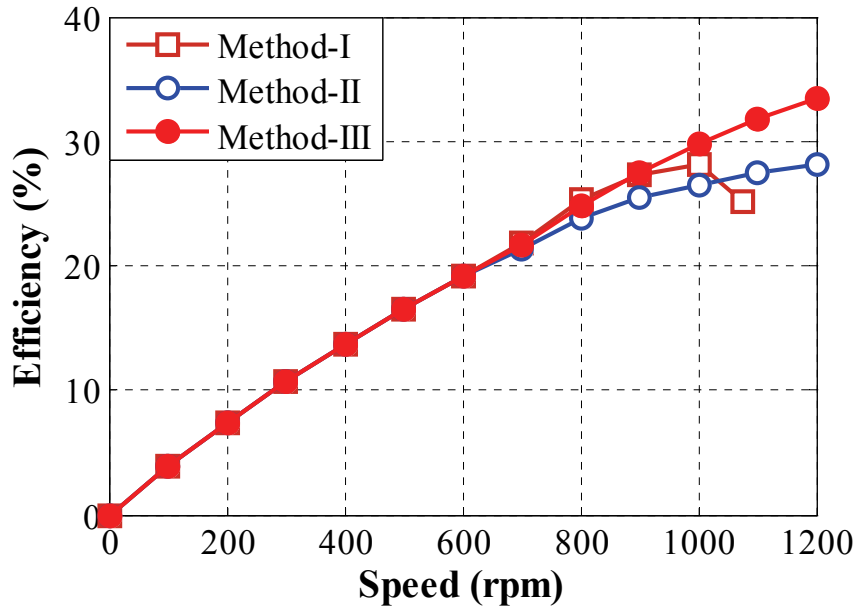

(b) Efficiency.

Fig. 4.11. Efficiency against speed.

Fig.4.12 shows the effectiveness of Method-III in the dynamic response since it exhibits a desirable flux-weakening performance in terms of high efficiency and wide operating speed range. The machine is operated at 1.0 second as a unit step by setting the reference speed at 1000 rpm, Fig.4.12(a). After around 5.0 seconds, the speed can track with its reference. The dynamic response of the optimal field excitation current, the *d*-axis current, and the *q*-axis current are shown in Fig.4.12(b). It is obvious that the optimal field excitation current is calculated as the same value as the maximum field exitation current in the constant-torque region corresponding to the results under steady-state condition, Fig.4.9(a), and it is gradually modified following the *d*-axis and *q*-axis currents in flux-weakening region. In Fig.4.12(c), the minimization tracking of copper losses in both field and armature windings can be achieved. The copper losses in two windings are similar in all operating regions, which is consistent to the principle of Method-III. The total copper loss in Method-III can be considerably reduced in the flux-weakening region compared to Method-II, as shown in Fig.4.12(d). It is noted that since Method-I exhibits low torque in flux-weakening region and the operating speed range is visibly constrained, it will not be mentioned in the dynamic response.

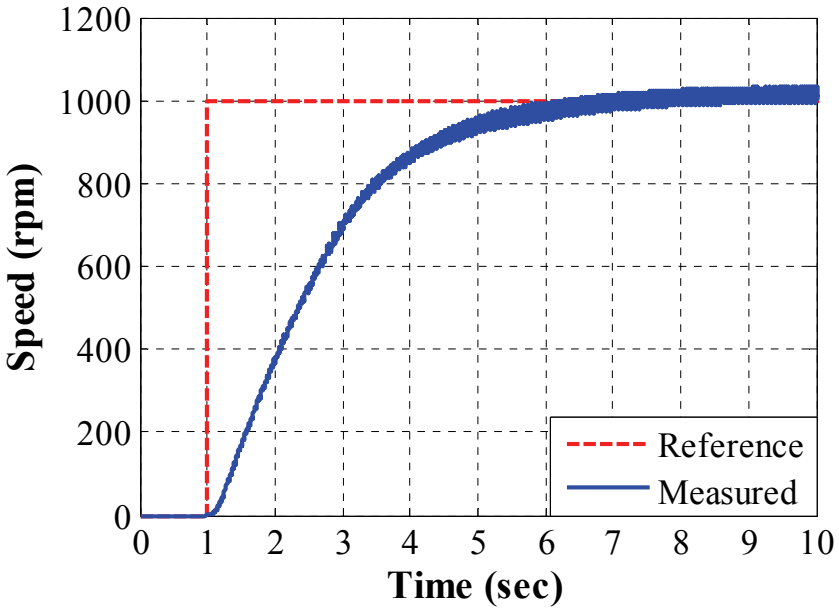

(a) Speed

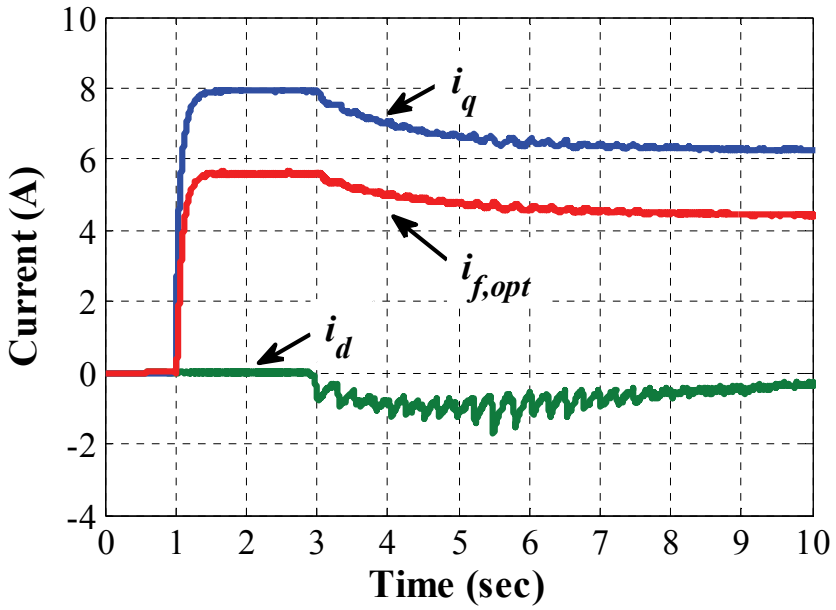

(b) *d*-axis current, *q*-axis current, and optimal field excitation current

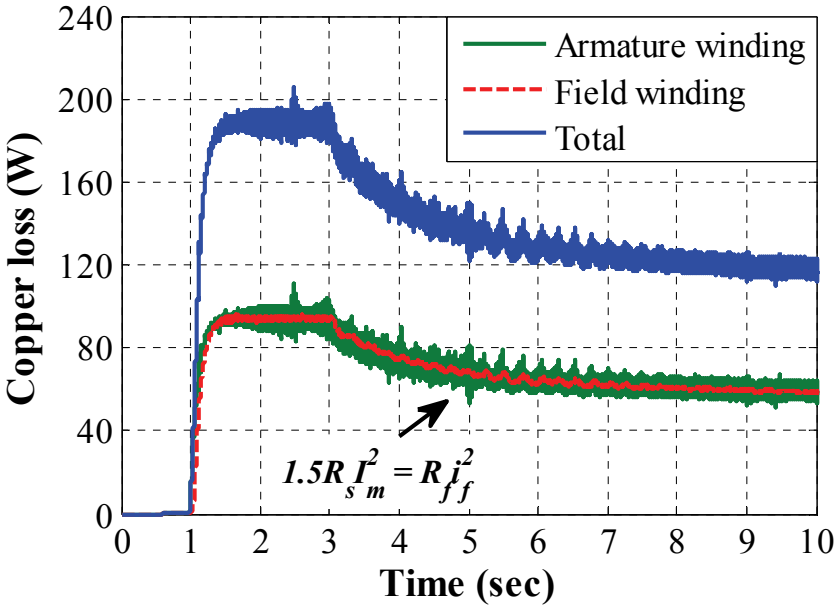

(c) Copper loss minimization tracking.

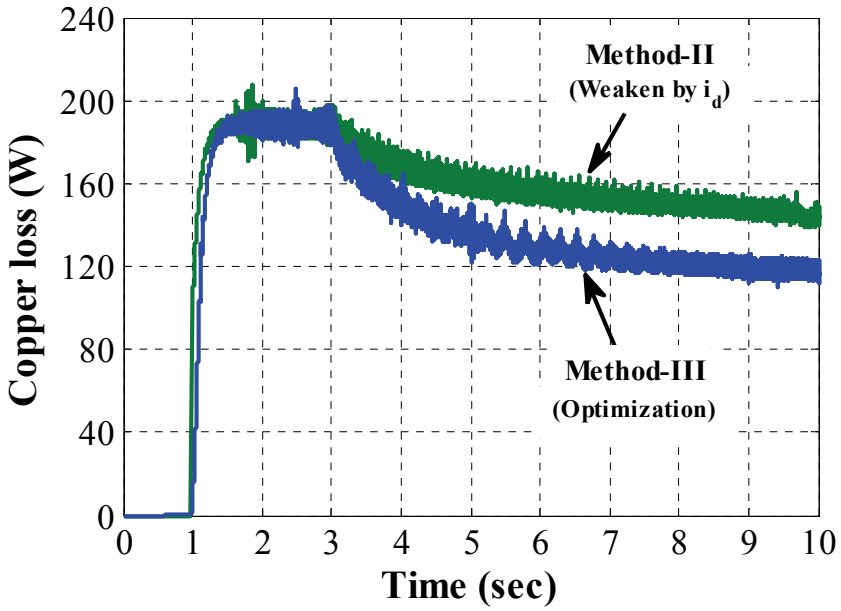

(d) Copper losses

Fig. 4.12. Dynamic responses of the Method-III.

4.5 Summary

Three practical flux-weakening control strategies for the HEPMMs have been presented in this chapter. Those methods can be categorised based on the utilisation of weakening currents: (1) utilising field excitation current only, (2) utilising armature current only, and (3) optimisation method. All flux-weakening control methods have been compared in terms of the torque, operating speed range, and efficiency in both the constant-torque and flux-weakening regions. Based on the experimental results, the optimisation method (Method-III) exhibits a wider operating speed range than Method-I utilising field excitation current alone and higher efficiency in flux-weakening region than Method-II utilising armature current only. Furthermore, Method-III is simple to implement and robust to the variation of machine parameters. It can be easily applied to other hybrid-excited machines as well.

CHAPTER 5

EFFICIENCY IMPROVEMENT OF HYBRID-EXCITED PERMANENT MAGNET MACHINES UTILISING OPTIMAL FIELD EXCITATION CURRENT CONTROL

In this chapter, the efficiency improvement for the hybrid-excited PM machine is proposed. It is based on the optimisation method, which has presented in Chapter 4. The prototype HEPMM (Machine-II) is utilised to verify the effectiveness of the proposed control strategy. Since the maximum field excitation current is commonly employed to increase the maximum torque via enhancing the flux-linkage, the field excitation current might exceed the specification of the machine when operating under low torque condition. As a result, the efficiency is deteriorated due to the copper loss of field winding. Hence, the field excitation current needs to be optimised in order to improve the efficiency. This chapter proposes a new efficiency improvement control strategy that can be effectively utilised in all operating modes. The optimal field excitation current is determined as a function of *d*-axis and *q*-axis currents regardless of the machine parameter variation. It is simple to implement and robust to the machine parameter variation. The effectiveness of the proposed method is verified by experimental results.

5.1 Introduction

To further improve the efficiency of PMSMs, loss minimization control methods have been proposed [CHE03], [KHA11], [LEE09]. In order to minimise the copper loss in the constant-torque and low-torque operation regions, the optimizing armature current based on the maximum torque per ampere (MTPA) technique is utilised [KHA11], [LEE09], whilst in the flux-weakening region, the adaptive current controller method is employed to limit the *d*-axis current ripple [CHE03]. However, since only the PM is used as an excitation source for such machines, the viable control for improving efficiency is limited. In [ZHU11], the searching efficiency improvement is proposed in which the *d*-axis current can be adjusted to track the optimal efficiency. However, the current oscillation cannot be avoided and a slow dynamic response occurs due to intensive calculation.

The hybrid-excited permanent magnet machines (HEPMMs), Fig.5.1 [AFI15], exhibit a capability to adjust the flux-linkage. Therefore, these machines can provide more control functions for the improvement of efficiency. The HEPMMs commonly consist of two excitation sources, i.e. permanent magnets (PMs) and field windings. Owing to adjustable field excitation flux, the HEPMM exhibits the potential to optimise the air-gap flux in both enhancing and weakening characteristics. Consequently, high torque, wide speed operation range, and high efficiency can be achieved [CHE11a], [OWE10], which makes this machine more attractive.

For the operation of the HEPMMs, the maximum field excitation current is usually employed to produce the maximum torque in the constant torque region. However, the efficiency would be deteriorated when the field excitation current is higher than the requirement of the machine in low load-torque or even in flux-weakening region. The copper loss minimization can be achieved on the condition that the copper loss ratio between field winding and armature winding is optimised [SHI07]. In [AMA09], the maximum efficiency can be obtained based on the selection of the specific value of the field excitation current. Further, the methods based on Extended Lagrange multipliers optimisation, which can improve the efficiency, have also been introduced in [HUA12], [MBA12], [NGU14], [SHI07]. Such methods generate the optimal reference currents by the analytical expressions to achieve the maximum efficiency. However, they are not only complicated, but also highly sensitive to the machine parameters, such as the armature winding and the field winding resistances. Based on the maximum torque, the self-optimizing method which is independent to the machine parameters is presented in [WAN13]. However, this method still encounters with the fluctuation of the field excitation current.

In this chapter, a new control strategy based on the optimal field excitation current is presented to improve the efficiency of HEPMM. The maximum efficiency condition is analyzed based on the differentiation method. The optimal field excitation current can be expressed as a function of d- and q-axes currents regardless of machine parameter variation. Thus, it is simple to implement and robust to the machine parameter variation. The proposed method can be practically utilised in all operation modes. The effectiveness of the proposed control strategy is validated experimentally.

5.2 Efficiency Improvement Control Strategy

The proposed control block diagram is presented in Fig.5.2. It is based on the vector control in which the *d*-axis and *q*-axis currents are separately controlled in terms of the flux-linkage and given torque, respectively. The field excitation reference current is set as a function of the *d*-axis and the *q*-axis currents corresponding to the maximum efficiency condition as shown by (4.19), in chapter 4. In order to achieve the tracking performance of the field excitation current, the DC-DC converter operating with the current feedback control is utilised. In Fig.5.1, the operating modes, i.e. low-torque operation mode, constant-torque mode, and flux-weakening mode, are defined in order to verify the effectiveness of the proposed method. Since the field excitation current is employed to enhance the flux-linkage and to improve the efficiency as proposed, the *d*-axis current is utilised to weaken the flux-linkage in flux-weakening operation.

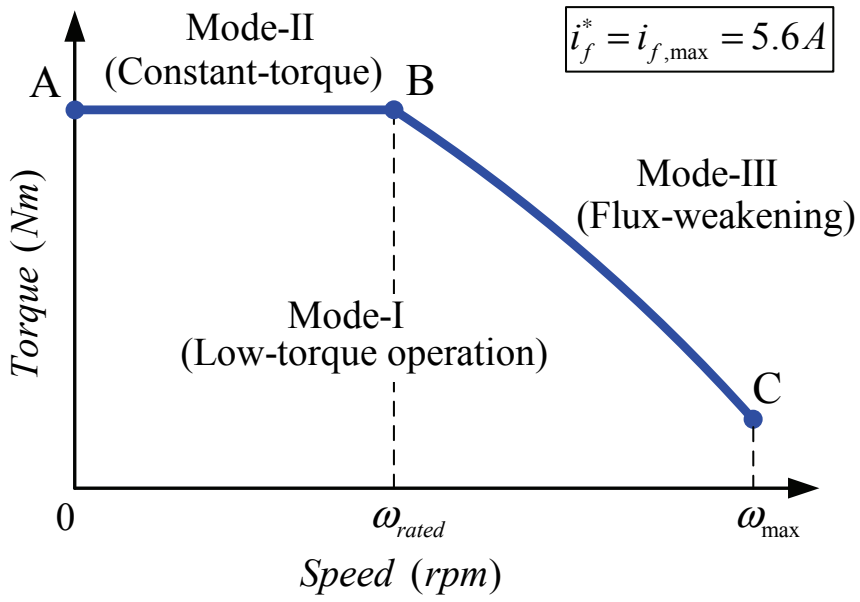

Fig. 5.1. Definition of operating modes.

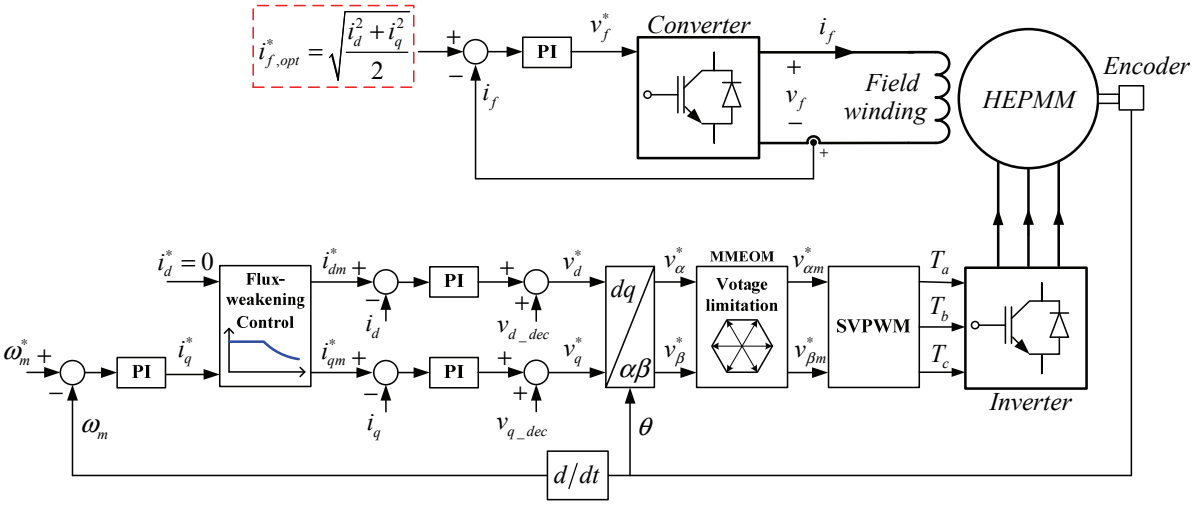

Fig. 5.2. Efficiency improvement control block diagram of a three-phase HEPMMs.

Table 5.1. Proposed operating conditions.

Reference currents	**MODE-I** (Low-torque operation)	**MODE-II** (Constant-torque)	**MODE-III** (Flux-weakening)
i_{dm}^*	0	0	$i_d^* - \Delta i_d$
i_{qm}^*	$i_{qm}^* = i_q^* = f(T_L)$	$i_{qm}^* = i_q^* = I_m$	$\min\left(i_q^*, \sqrt{I_m^2 - i_d^2}\right) + \Delta i_q$
i_f^*	$i_{f,opt} = \sqrt{\frac{i_d^2 + i_q^2}{2}}$		

5.2.1 Low torque operation mode

When the machine operates in Mode-I, which is indicated as low-torque operation in Fig.5.1, the command voltage remains inside the voltage limit. Hence, the flux-weakening control is not activated even when the machine is operated in high speed region. In this mode, the *d*-axis reference current is set at zero due to a unity saliency ratio of the validated machine, whilst the *q*-axis reference current is provided by the speed regulator corresponding to a variation of the load torque, Table 5.1. Due to the machine topology where the PM usage is intently reduced, the maximum field excitation current reference is commonly employed to provide the maximum torque via the enhanced flux-linkage. However, it might exceed the requirement of the machine when it operates at the low load-torque condition. As a result, the HEPMM's efficiency would be deteriorated due to the copper loss of field winding. Accordingly, the maximum efficiency condition can be achieved in case the copper losses of the armature winding and the field winding are equal, as mentioned in (4.18). Therefore, by inserting the *d*-axis and *q*-axis currents of

the low-torque operation mode into (4.19), the optimal field excitation reference current can be given as,

$$i_{f,opt}^{*} = \sqrt{\frac{i_d^2 + i_q^2}{2}} = \frac{i_q}{\sqrt{2}}. \tag{5.1}$$

It is noticed that, since the unnecessary copper loss of field winding can be further eliminated in the lower torque operation in which the requirement of field excitation current is reduced based on the proposed method, the higher efficiency improvement can be achieved.

5.2.2 Constant torque operation mode

The constant-torque mode (Mode-II), the machine is operated between point A and point B, Fig.5.1. Since the maximum field excitation current is initially employed, the maximum torque can be achieved with the maximum *q*-axis current. Meanwhile, the *d*-axis reference current is set at zero because it does not contribute to the torque generation due to non-saliency of the prototype machine. These reference currents are shown in Table 5.1. Thus, based on the maximum efficiency condition as shown in (4.19), the optimal field excitation reference current for this mode can be given by (5.2).

$$i_{f,opt}^{*} = \sqrt{\frac{i_d^2 + i_q^2}{2}} = \frac{I_m}{\sqrt{2}} \tag{5.2}$$

5.2.3 Flux-weakening operation mode

When the machine operates beyond point B in Fig.5.1, the flux-weakening mode (Mode-III) is activated. In this mode, the required speed is higher than the rated speed while the armature current remains at its maximum. Consequently, the command voltage would exceed the voltage limit of inverter. Therefore, to achieve the flux-weakening performance under the current and voltage limits, the *d*-axis and the *q*-axis reference currents need to be modified [KWO06], [KWO07], [LIU12], as follows:

1) Modification of the d-axis reference current

When the command voltage exceeds the voltage limit, the d-axis reference current is automatically modified to provide a wide speed range. In this research, based on the voltage error regulation method, the modification current of the *d*-axis (Δi_d) is given by (3) [KWO07]. It utilises the difference between the command and output voltages of the limitation block, Fig.5.2, in which the α-β axes voltages are converted to the *d*-*q* axes by the Park's transformation.

$$\Delta i_d = \alpha \sqrt{\frac{\omega_c}{s+\omega_c}(v_d^* - v_{dm}^*)^2 + \frac{\omega_c}{s+\omega_c}(v_q^* - v_{qm}^*)^2} \tag{5.3}$$

where α is the constant gain, ω_c is the bandwidth of the first-order low-pass filter. Therefore, the modification of the *d*-axis reference current is given as,

$$i_{dm}^* = i_d^* - \Delta i_d \,. \tag{5.4}$$

where i_{dm}^*, i_{qm}^* are the *d*-axis and *q*-axis modified reference currents.

2) Modification of the *q*-axis reference current

In flux-weakening operation, since *d*-axis current opposes the flux-linkage produced by PMs and the field excitation flux, *q*-axis voltage is decreased. At the certain point, the *q*-axis voltage would be zero when it operates under the infinite constant power speed ratio characteristic with $L_d I_m > \psi_{pm}$ [KWO07], [LIU12]. As a consequence, the speed range might not be increasingly extended. Accordingly, in order to extend the speed range under this condition, the *q*-axis current should be decreased to track the maximum torque per voltage (MTPV), which is the voltage limit trajectory provided by the actual inverter system. In case of HEPMM, the center of the voltage limit ellipse is at $-\left(\psi_{pm} + L_{mf} i_f\right)/L_d$ as aforementioned in (3.9), Chapter 3. Then, the modification current of the *q*-axis (Δi_q) is expressed by (5.5) [KWO07]. It is activated corresponding to the negative value of the *q*-axis voltage.

$$\Delta i_q = \frac{\beta}{s} \omega_e v_q^* \tag{5.5}$$

where β is the constant gain, and *s* is the integral operator. The modification of the *q*-axis reference current is given as,

$$i_{qm}^* = \min\left(i_q^*, \sqrt{I_m^2 - i_d^2}\right) + \Delta i_q \,. \tag{5.6}$$

The reference currents in both *d*-axis and *q*-axis are modified without the requirement of machine parameters. Therefore, the flux-weakening performance can be achieved by the proposed method. The reference currents for whole operating modes are presented in Table 5.1. It is clearly seen that since the optimal field excitation current of the proposed method is determined as a function of only *d*-axis and *q*-axis currents for all operating modes, it is simple to implement experimentally

5.3 Experimental Verification

5.3.1 Experimental setup

The field orientation control algorithm is implemented on a dSPACE platform in order to verify the performance of the proposed method experimentally. A 1.5 kW wound field type DC motor, of which the rated speed is 1,600 rpm, is utilised to adjust the load-torque. It is implemented with an external resistance load to dissipate the generated power. The test rig is shown in Chapter 2. The three-phase voltage source inverter is employed based on the SVPWM switching technique to operate the HEPMM. The minimum magnitude error over-modulation (MMEOM) is applied for increasing the utilization of the DC-link voltage, [KWO06]. The field excitation current is regulated by the step-down (buck type) DC-DC converter. The setup parameters are given in Table 5.2.

Table 5.2. Experimental setup

Maximum motor test speed	1200 rpm
DC-link voltage	40 V
Maximum armature current (peak)	7.92 A
Switching frequency of the inverter	10 kHz
DC supply voltage of the converter	30 V
Maximum field excitation current	5.6 A
Switching frequency of the converter	10 kHz

5.3.2 Experimental results

Fig.5.3 shows the measured results of the prototype machine against the field

excitation current operating in Mode-I, the low torque operation mode. The load torque of 0.3 Nm and 0.5 Nm are applied with the controlled speed at 500 rpm. In Fig.5.3(a), it is obvious that the efficiency can be significantly changed with the variation of the field excitation current. The maximum efficiency points for both load torques exist. Fig.5.3(b) shows the *q*-axis current against the field excitation current. At the same given torque, when the flux-linkage is further enhanced due to the increasing of field excitation current, the *q*-axis current should be decreased. Likewise, the total copper loss, which has considered the copper losses of armature winding and field winding, is shown in Fig.5.3(c). Fig.5.3(d) shows the copper loss curves of field winding and armature winding in either load torque. The intersection of both copper loss curves exhibits the maximum efficiency as shown in Fig.5.3(a). The field excitation current is the optimal condition when both copper losses are equal. For instance, at 0.3 Nm the optimal current is around 3.6 A.

Fig.5.4 shows the *d*-axis and *q*-axis currents operating in the constant-torque mode (Mode-II) and flux-weakening mode (Mode-III). The proposed method based on the optimal field excitation current is compared with the method that utilises only maximum field excitation current, with a fixed value at 5.6 A. In Mode-II, since the prototype machine has been optimised to achieve the highest efficiency corresponding to the maximum current, the optimal field excitation current is the same as the maximum field excitation current as shown in Fig.5.5. Consequently, both methods provide the same *d*-axis and *q*-axis currents, Fig.5.4(a). In Mode-III, in order to extend the speed range, the *d*-axis and *q*-axis currents are modified according to the flux-weakening control. In this mode, since the field excitation current is reduced according to the optimal condition, Fig.5.5, the enhanced flux-linkage is decreased. As a result, higher *q*-axis current of the proposed method is employed compared with the method that utilises only the maximum field excitation current. The current trajectory is shown in Fig.5.4(b).

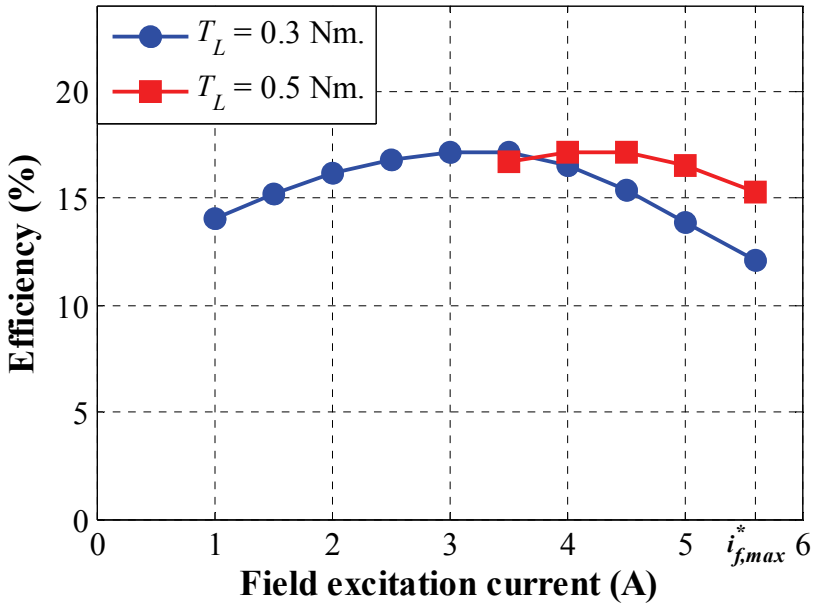

(a) Efficiency

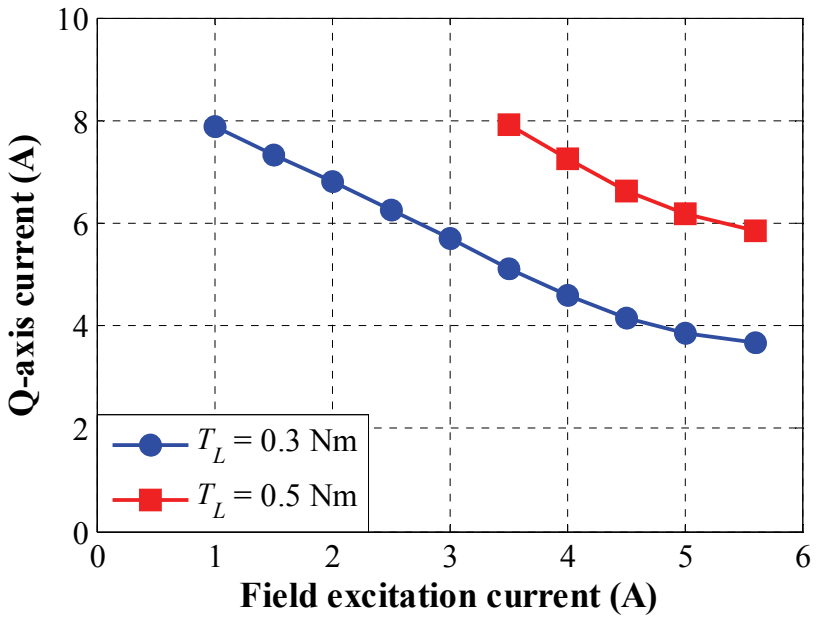

(b) q-axis current

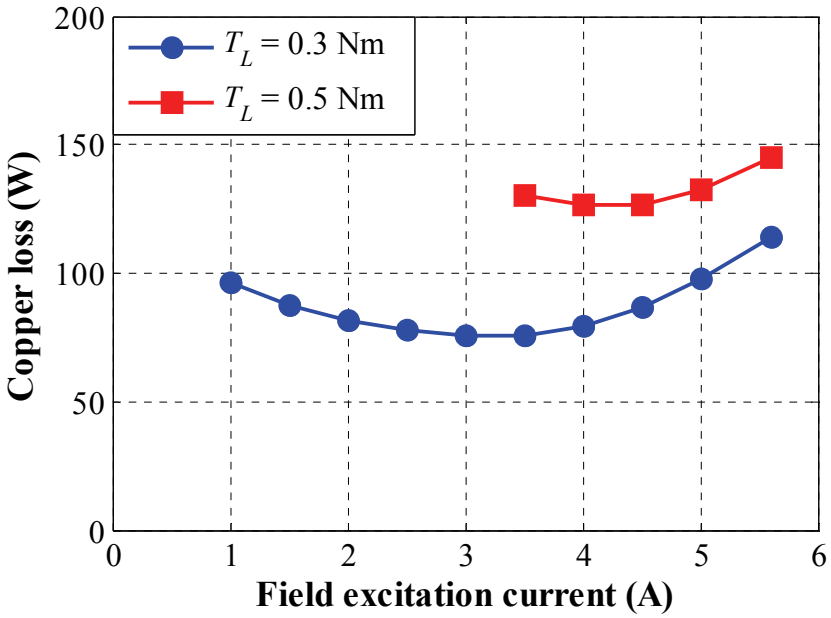

(c) Total copper loss

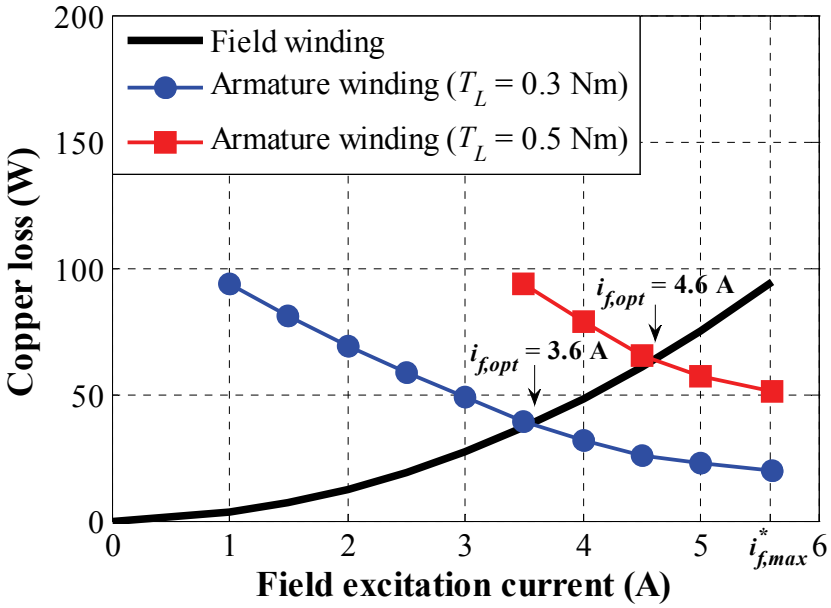

(d) Maximum efficiency operation points

Fig. 5.3. Measured results versus the field excitation current operating in Mode-I with load-torque of 0.3 Nm and 0.5 Nm.

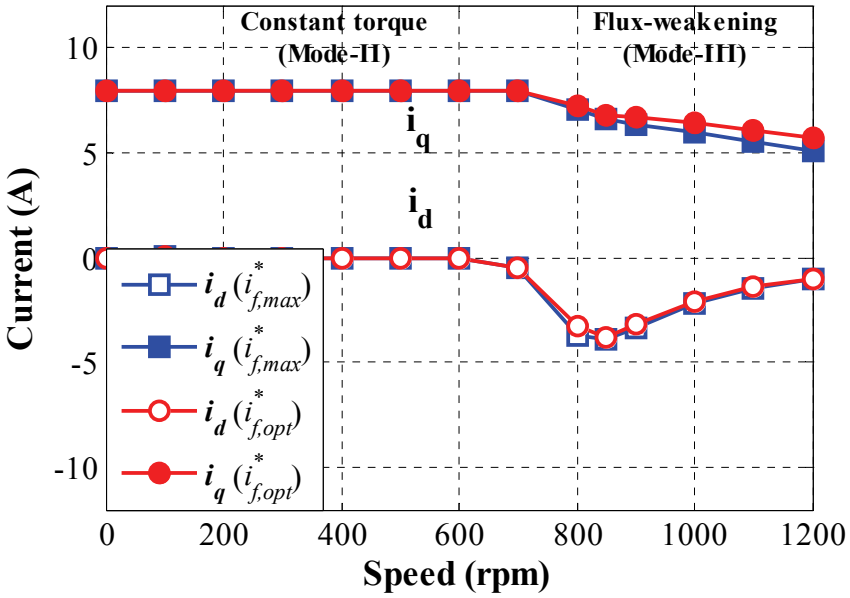

(a) *d*-axis and *q*-axis currents

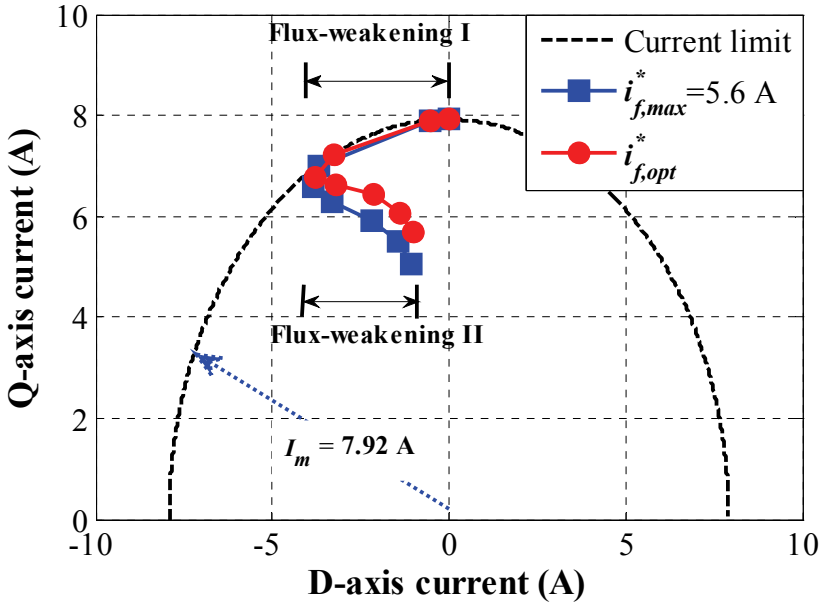

(b) Current trajectory

Fig. 5.4. Measured currents in the constant-torque and the flux-weakening operation modes (Mode-II and Mode-III).

Fig.5.5 shows the optimal field excitation current in whole operating modes along with the *d*-axis and *q*-axis currents, as shown in Fig.5.3(b) and Fig.5.4(a). Hence, the total copper loss of the proposed method can be significantly reduced compared with the method that utilises only the maximum field excitation current, as shown in Fig.5.6.

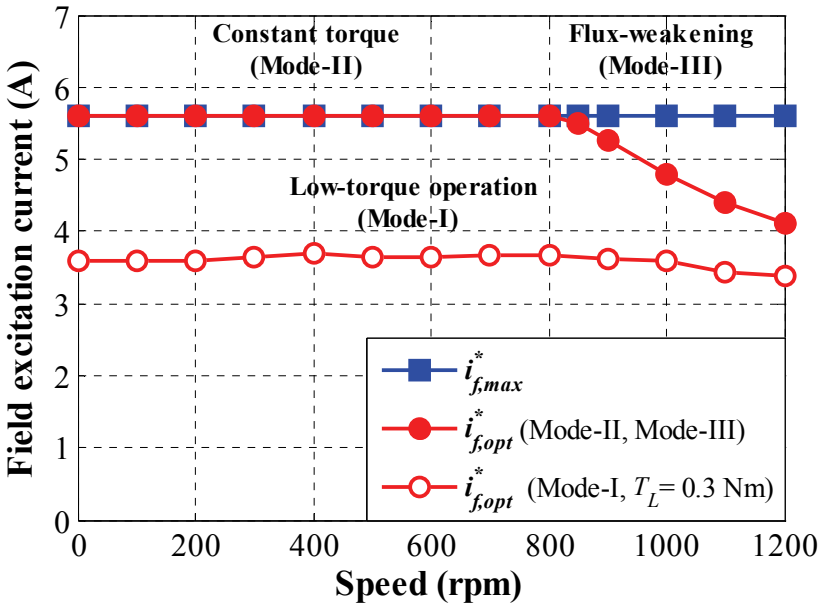

Fig. 5.5. Optimal field excitation current.

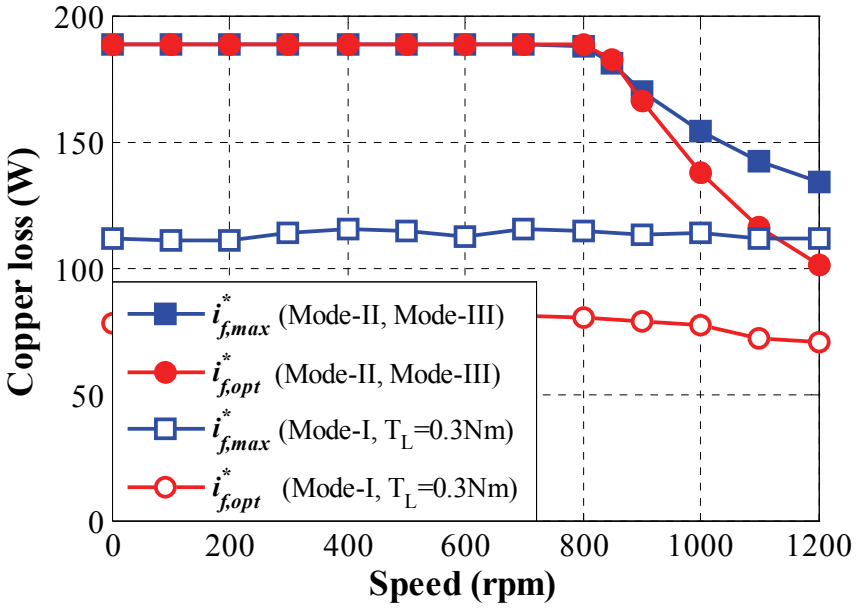

Fig. 5.6. Measured total copper loss.

Fig.5.7 demonstrates the effectiveness of the proposed method in terms of the efficiency improvement for all operating modes compared with the method that utilises only maximum field excitation current. Since the optimal field excitation current at 0.3 Nm is lower than 0.5 Nm, Fig.5.3(d), the dispensable copper loss of field winding is further eliminated, resulting in higher efficiency. In Mode-I, the lower the torque the higher the efficiency improvement can be achieved, as shown in Fig.5.7(a). In addition, when the machine operates in Mode-II, in which the efficiency of the prototype machine has been maximised, while in Mode-III, the efficiency of the proposed method can be significantly improved as shown in Fig.5.7(b). It is obvious that the proposed method exhibits the improved performance and can be applied to any speed and torque operation.

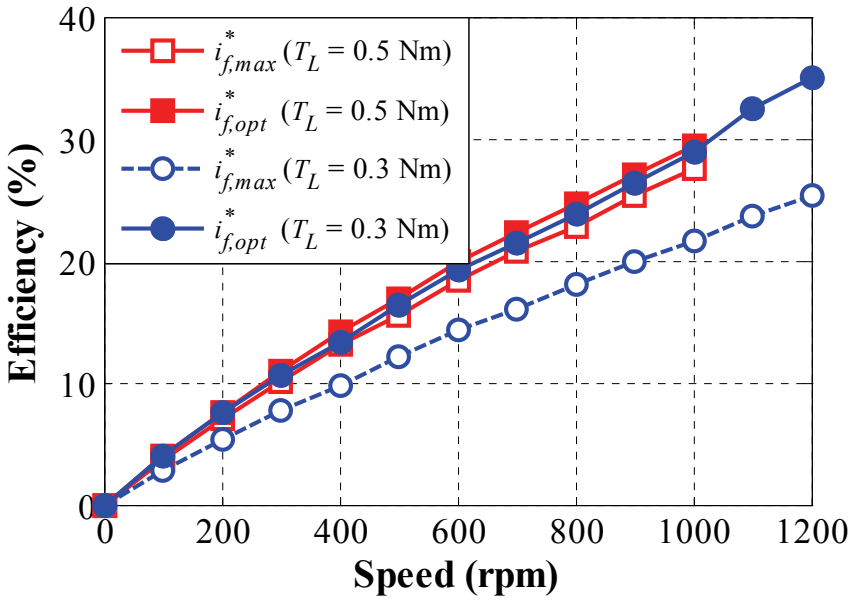

(a) Low-torque operation (Mode-I)

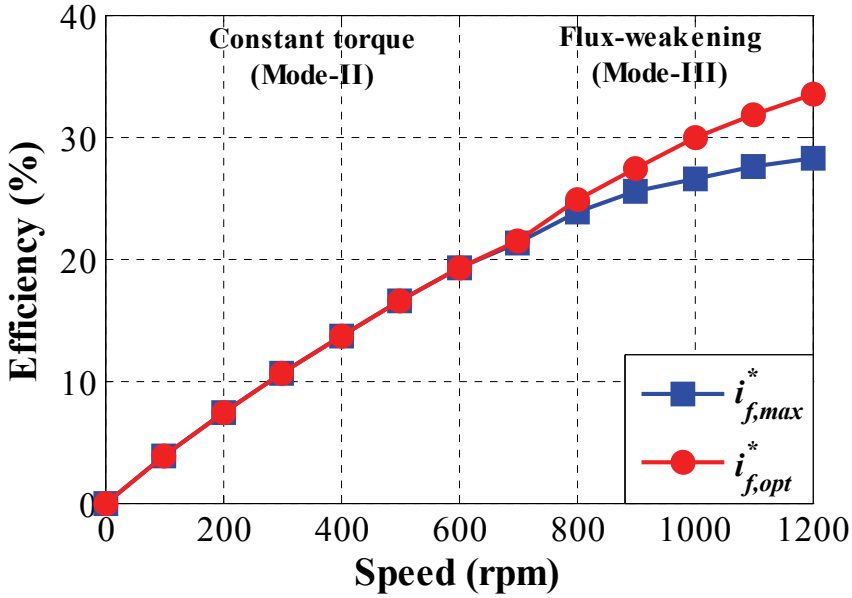

(b) Constant-torque and flux-weakening (Mode-II and Mode-III)

Fig. 5.7. Efficiency improvement.

Fig.5.8 shows the transient response results of the efficiency improvement method when the load-torque is varied from 0.3 Nm to 0.5 Nm. The load-torque of 0.3 Nm is firstly applied, as shown in Fig.5.8(a), in order to compare the efficiency improvement between the method that utilises the maximum field excitation current only and the optimisation method. Then, the load torque will be changed to 0.5 Nm at around 17.0 s of the experimental time. The field excitation current is initially set at it maximum value, Fig.5.8(b), while the speed is controlled at 500 rpm in the whole operating regions. The *d*-axis and *q*-axis currents are shown in Fig.5.8(c). It is noted that the optimisation method is activated at approximately 8.0 s. Since the field excitation current is reduced according to the optimisation method, the efficiency in both given load-torque conditions can be effectively improved compared to the method that utilises only the maximum field excitation current, Fig.5.8(d), corresponding to the efficiency in Fig.5.3(a). In addition, the optimised field excitation current also exhibits a good response. The machine speed and DC-link voltage are shown in Fig.5.8(e) and (f), respectively. It is obvious that, both of speed and DC-link voltage can be maintained at their references under the utilization of the optimised field excitation current during the change of load-torque, which confirms the good dynamic performance of the proposed method.

It is noted that although the measured torque provided by the torque transducer shows the transient spikes at around 5.0 s and 22.0 s in Fig.5.8(a), the *d-q* axis currents and the machine speed can still track their references without the impact of those transient spikes. However, the torque transducer, which has been mentioned in Chapter 2, provides the maximum torque at 10 Nm, but the prototype machine is designed as a low power machine which also generates a low torque. As a result, the transient spikes of the torque signal would be a noise from measurement.

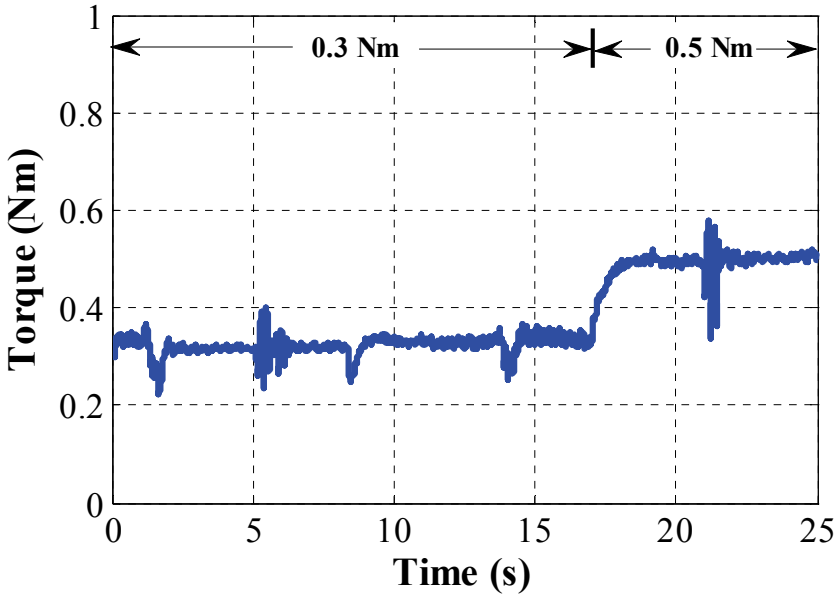

(a) Torque

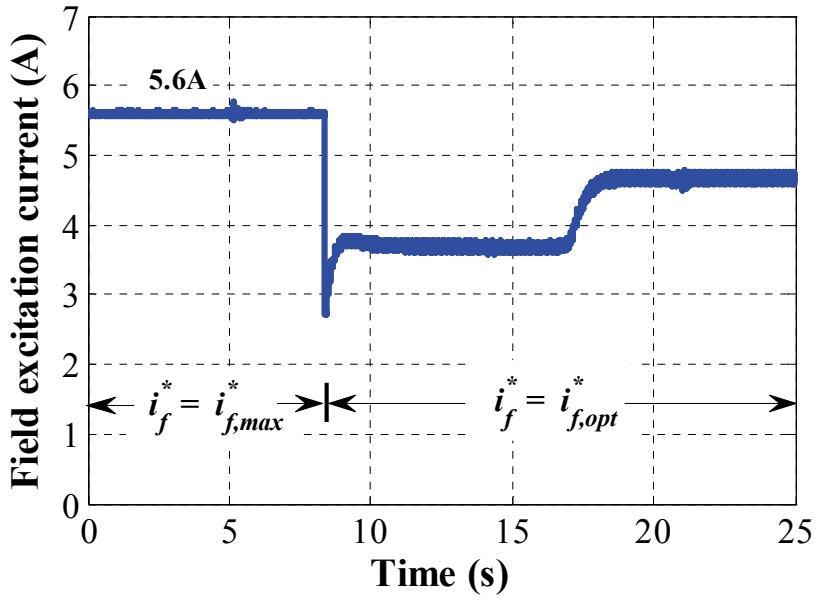

(b) Field excitation current

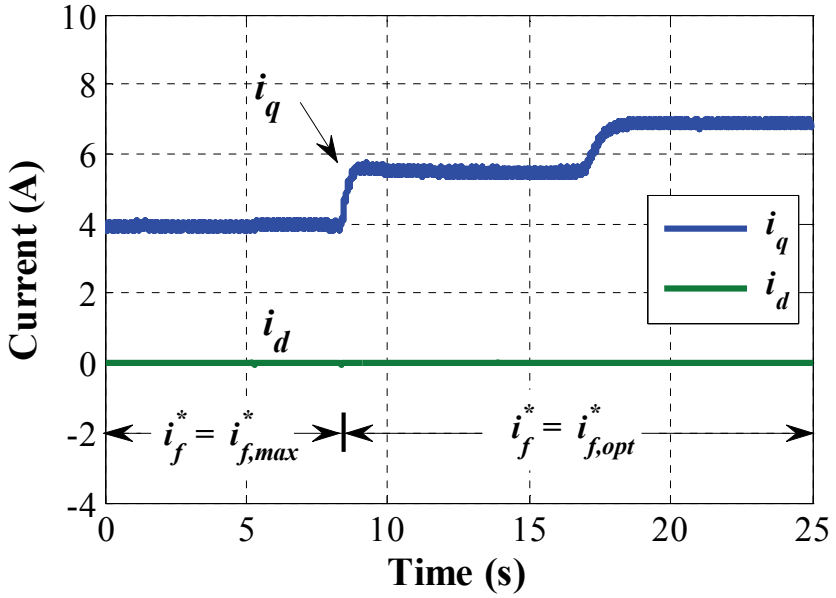

(c) *d*-axis and *q*-axis currents

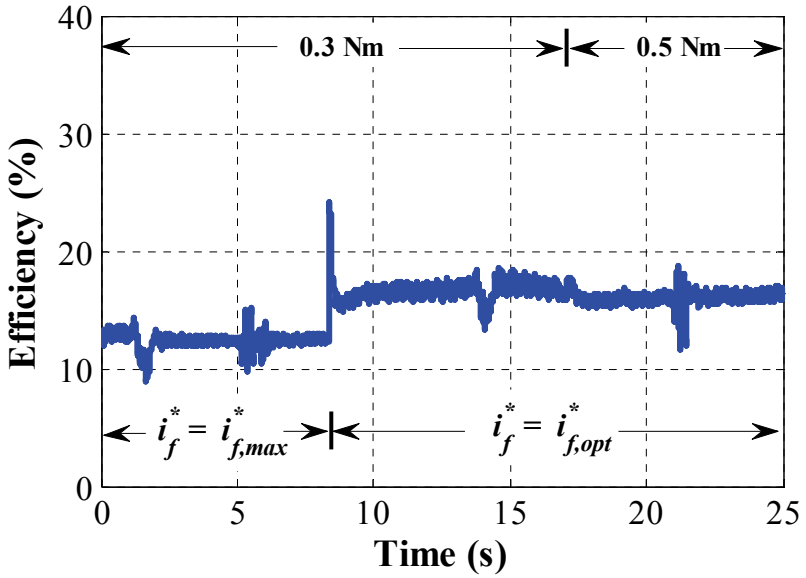

(d) Efficiency

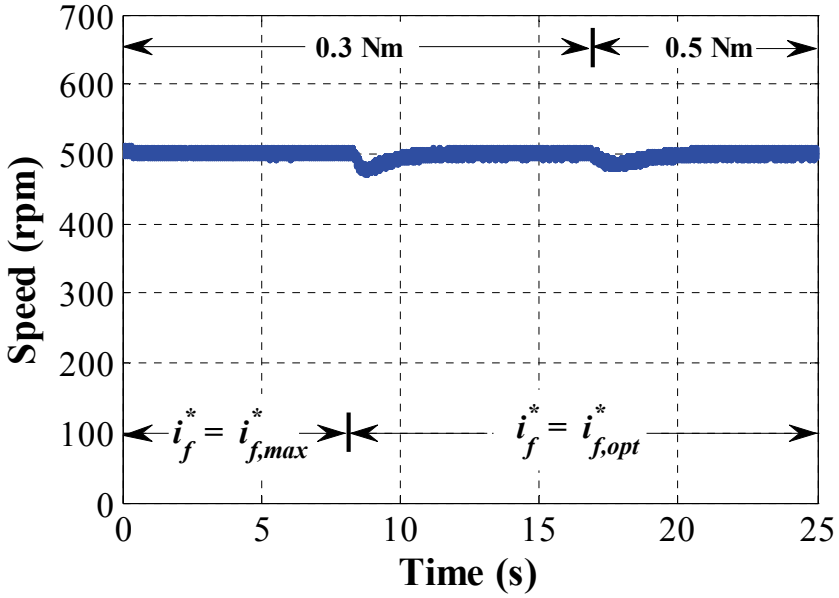

(e) Speed

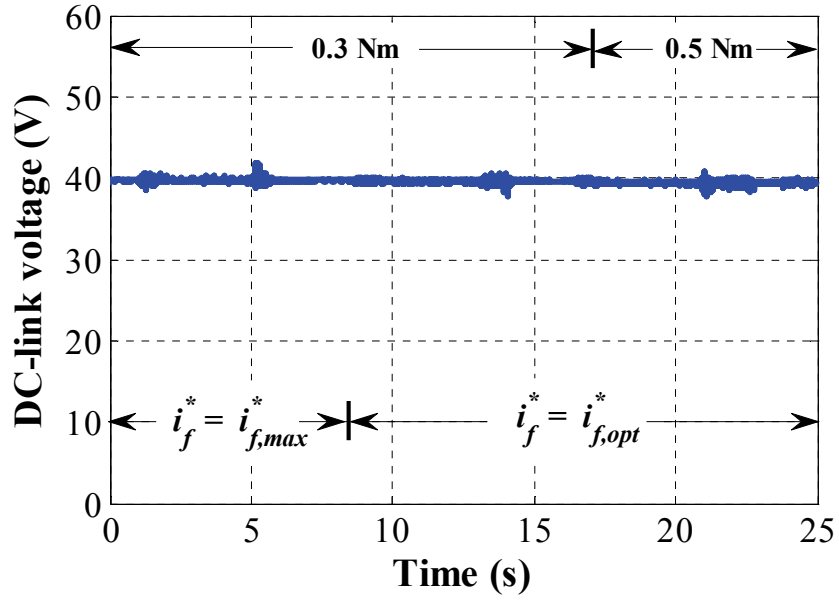

(f) DC-link voltage

Fig. 5.8. Transient response results of the efficiency improvement method under load-torque of 0.3 Nm and 0.5 Nm.

5.4 Efficiency Map

Based on the novel feature of this machine topology in which the PM usage is reduced, the flux-linkage is mainly controlled by the field excitation flux. Hence, the maximum field excitation current is commonly employed in order to enhance the maximum torque. However, the efficiency of the proposed method can be significantly improved in all operating modes as illustrated in Fig.5.7. Alternatively, the measured efficiency maps of the flux-weakening control strategies, as presented in Chapter 4, for all operating regions are illustrated and compared, as follows:

(1) The method that utilises the field excitation current only (Method-I, chapter 4), which the field excitation current is still fixed at its maximum current (i_f = 5.6 A) when the machine operates under low-torque operation.

(2) The method that utilises the armature current only (Method-II, chapter 4), while the field excitation current is maintained at its maximum current (i_f = 5.6 A) under low-torque operation.

(3) The proposed method in which the optimised field excitation current is utilised for all operating regions (Method-III, Chapter 4). Those methods are presented in Fig.5.9(a), (b), and (c), respectively.

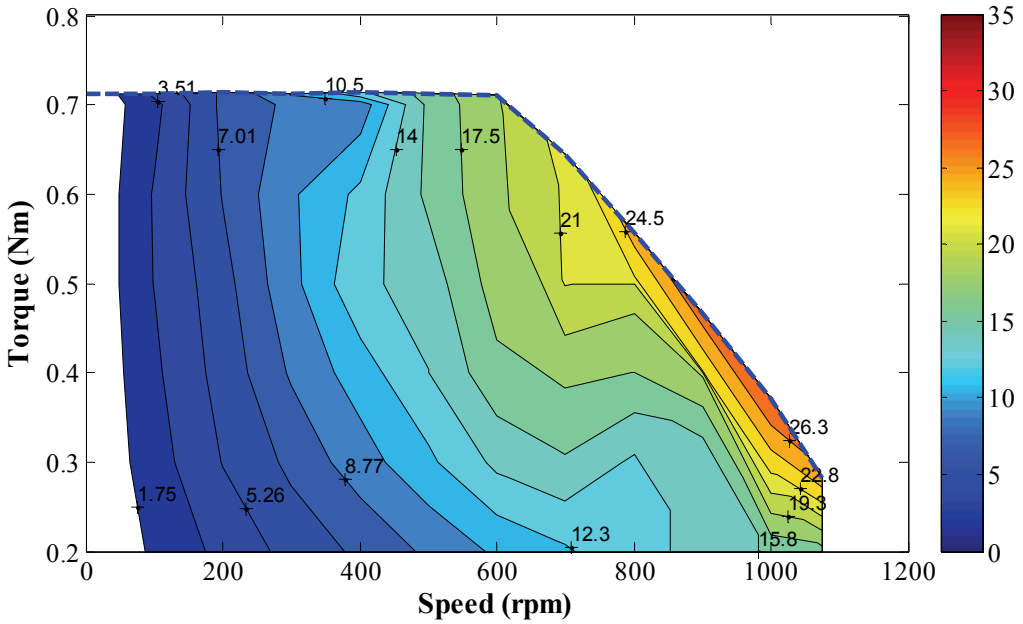

(a) Utilising field excitation current only (Method-I, Chapter 4)

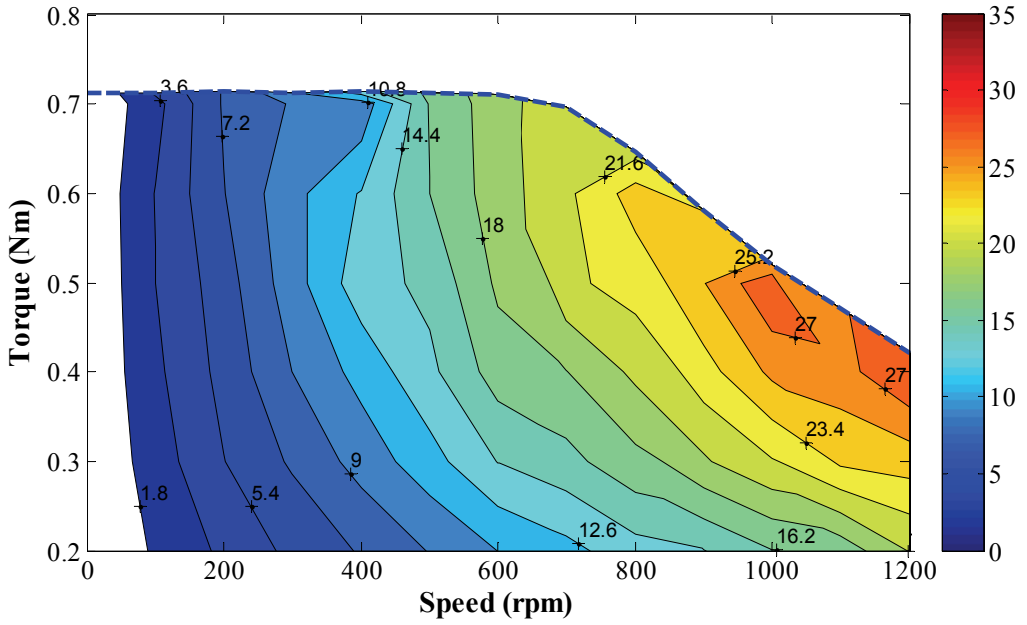

(b) Utilising armature current only (Method-II, Chapter 4)

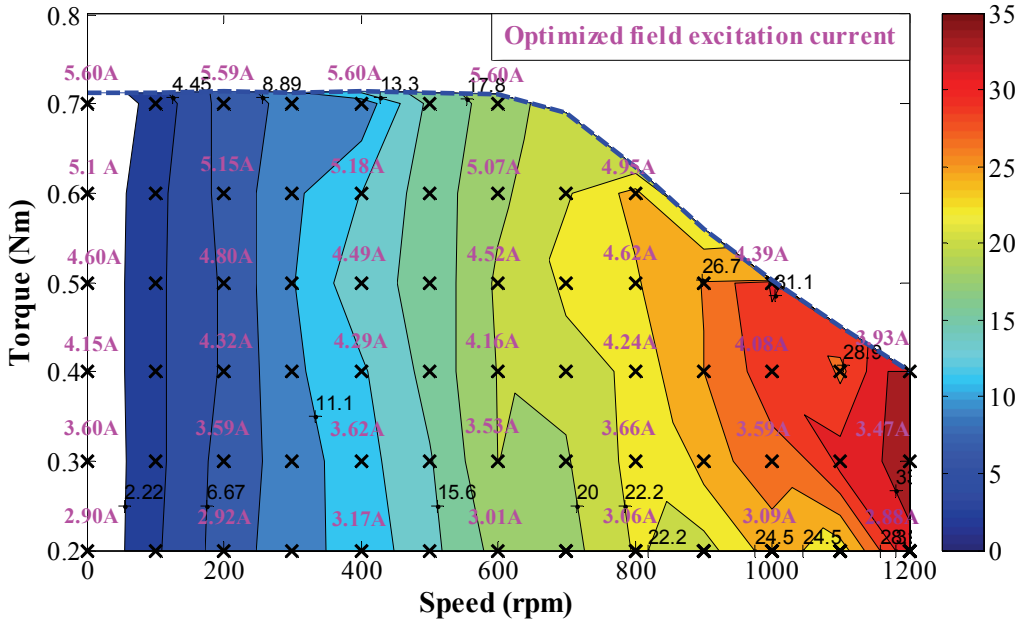

(c) Utilising optimisation method (Method-III, Chapter 4)

Fig. 5.9. Efficiency map versus speed.

The efficiency is calculated by the measured mechanical output power and measured electrical input power in which the total losses, such as core losses and mechanical loss, have been considered. In the proposed method, the optimal field excitation current is determined based on the equal field winding and armature winding copper losses. Consequently, the total copper loss is minimised. Therefore, the proposed method can provide higher efficiency in all operating regions compared with the method that utilises the maximum field excitation current under the low-torque operation of both flux-weakening control methods, i.e. utilising field excitation current only (Method-I, Chapter 4) and utilising armature current only (Method-II, Chapter 4).

It should be note that in Fig.5.7 to Fig.5.9, the efficiency is low because the prototype machine is a low power machine and power consumption of the field winding is considered. Also, a low DC-link voltage is applied to limit the testing speed range which is imposed by the test rig. However, the proposed method has demonstrated the effectiveness in terms of the efficiency improvement for all operating modes.

5.5 Summary

A new efficiency improvement control strategy based on the optimal field excitation current for the hybrid-excited permanent magnet machines has been presented in this chapter. The proposed method has demonstrated the effectiveness of enhanced performance in terms of the efficiency for all operating modes. It is worth mentioning that only the turn ratio of field winding to armature winding is required instead of their resistances to determine the optimal field excitation current. Therefore, regardless of machine parameter variation, the optimal field excitation current can be expressed as a function of *d*-axis and *q*-axis currents with respect to the maximum efficiency condition. Consequently, the proposed method is simple to implement experimentally and robust to the machine parameter variation, and can be conveniently applied to other hybrid-excited machines.

CHAPTER 6

MAXIMUM EFFICIENCY TRACKING OF HYBRID-EXCITED PERMANENT MAGNET MACHINES UTILISING FIELD EXCITATION CURRENT CONTROL

In this chapter, the maximum efficiency tracking (MET) method for the control of HEPMMs is proposed in order to minimise the field excitation flux by searching for an appropriate field excitation reference current. The field excitation current is automatically modified with a small value of tracking step size over every time interval, while its direction and magnitude are determined by the comparison of the current and previous efficiency values. Consequently, the proposed method can be easily applied to other hybrid-excited machines without the requirement of machine parameters and even the turn-ratio between the field winding and the armature winding, as required in the efficiency improvement method presented in chapter 5. The effectiveness of the proposed method is verified by experimental results.

6.1 Introduction

In order to enhance the operating performance of the PMSM in terms of energy saving, cooling system capability, and even environmental pollution control, the efficiency improvement in variable speed drives has become an increasingly important issue [ABU06], [SOU95]. As a result, a large amount of literature has been presented, which mainly focuses on efficiency improvement, copper loss minimization, adaptive control, as well as optimisation methods [ABU06], [CAV05], [CHE03], [LI15], [MOR94a], [NI15], [SOU95], [ZHU11]. However, since the excitation flux source of such machines is only based on the PM, the viable control for improving efficiency is limited, as introduced in chapter 5.

The HEPMMs have the capability to adjust the flux-linkage via the field winding [AFI15], [WAN12], and these machines also provide the potential to optimise the flux-linkage in both enhancing and weakening characteristics based on the optimisation of both armature and field excitation currents, as mentioned in Chapters 4 and 5. Therefore, these machines can provide more control means for the improvement of efficiency. For

that reason, high torque, wide speed operation range, and maximum efficiency can be achieved [CHE11], [OWE10], [POT15], which are the attractive points of the HEPMMs.

The field excitation current is basically employed at its maximum value in order to produce the maximum torque of the HEPMMs. When it is operated under a low load-torque condition or even in a flux-weakening region, the field excitation current is higher than the requirement of the machine. Consequently, the efficiency deteriorates due to the over requirement of copper loss, which is mainly from the field winding copper loss. In order to minimise the copper loss of the HEPMM, the ratio between the field winding and the armature winding is optimised [SHI07]. In [AMA09], the specific value of the field excitation current is selected to achieve the maximum efficiency under any torque and speed condition. Likewise, the optimised reference currents, i.e. *d*-axis, *q*-axis, and field excitation currents, are determined based on the Extended Lagrange multipliers optimisation for improving the maximum efficiency of the HEPMM and have been presented in [HUA12], [MBA12], [NGU14], [SHI07], [WAN13]. However, since those optimised current references are in the format of analytical expressions, they involve a heavy computational burden and are also machine parameters dependent. The efficiency improvement of the HEPMM (Machine-II) has already been presented in chapter 5, in which the field excitation and armature currents are optimised for all operating regions. Nevertheless, it is based on the utilization of the armature and field windings turn ratio, and the coil-type of both windings are assumed to be the same.

The maximum efficiency tracking (MET) method is presented in this chapter. It compares the efficiency between the current and previous values to define the direction of the modified field excitation reference current, which can be easily applied to other hybrid-excited machines. Experimental results are performed under dynamic condition to validate the effectiveness of the proposed method.

6.2 Proposed Control Strategy

To achieve the maximum efficiency of the HEPMM under the same given torque and speed, the utilization of the field excitation current is investigated, the proposed method ($i_{f,MET}$), by comparing it with a method where the field excitation current is maintained at its maximum value ($i_{f,max}$). Under this condition, only the copper loss directly influences the efficiency, while the other losses, e.g. core loss and mechanical loss, are negligible, as introduced in Chapter 5. Accordingly, the efficiency is improved when the appropriate field excitation current is utilised, Fig.6.1. Based on the mechanical output power (P_m), which is calculated by the measured (T_m) torque and speed (ω_m) in rad/s, while the core loss and mechanical loss of both methods are assumed to be equal under the same torque and speed condition, therefore, the HEPMM's efficiency (η) can be given by equation (6.1). It is utilised for the analysis of efficiency improvement by the field excitation current. Therefore, in this chapter, the maximum efficiency tracking method is proposed as follows:

$$\eta = \frac{P_m}{P_e} = \frac{\left(\psi_{pm} + L_{mf} i_f\right) i_q \omega_e}{\underbrace{\left(R_s i_d^2 + R_s i_q^2 + \frac{2}{3} R_f i_f^2\right)}_{Copper\ losses} + \underbrace{\left(\psi_{pm} + L_{mf} i_f\right) i_q \omega_e}_{Mechanical\ power}} \tag{6.1}$$

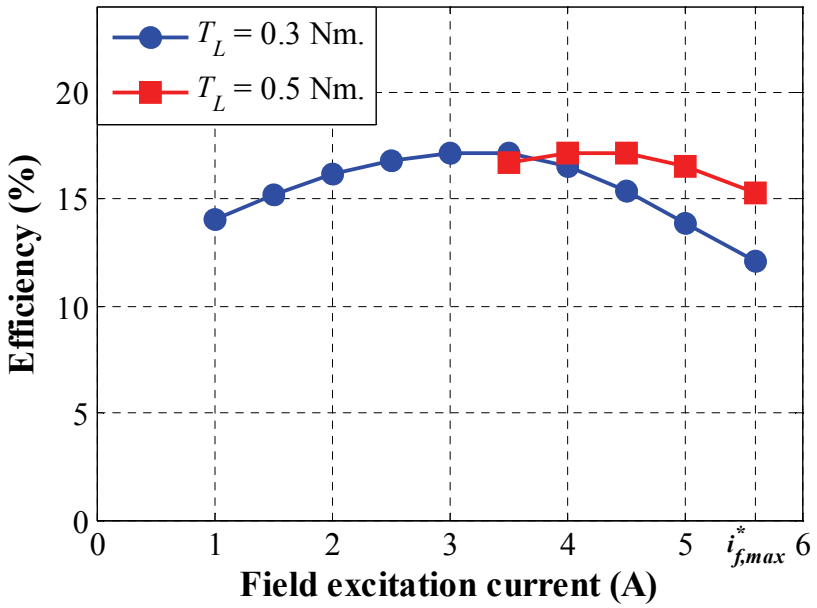

Fig. 6.1. Efficiency against field excitation current with load-torque at 0.3 Nm and 0.5 Nm.

6.2.1 Maximum Efficiency Tracking Method

Fig.6.2 shows the control block diagram of the maximum efficiency tracking (MET) method for the HEPMMs. The proposed method is based on the principle of field orientation control, in which the *d*-axis and *q*-axis currents are independently controlled according to the rotor position [BOL08]. With regard to the maximum torque per ampere (MTPA) trajectory [KIM13], [ZHU02], the *d*-axis reference current is defined to be zero due to the non-saliency of the prototype machine ($L_d = L_q$). Meanwhile, the *q*-axis reference current is provided by the speed regulator which corresponds to the variation of the load-torque. Based on the operating principle of the HEPMM, the field excitation current is utilised to enhance the flux-linkage of the PMs. The field excitation current is commonly employed at its maximum value to achieve the maximum torque of such a machine [POT15]. However, when the machine is operated at some points in a low torque condition, the requirement of the machine's flux-linkage is decreased corresponding to the torque equation as given by (4.3), in Chapter 4. Indeed, since the flux-linkage of such a machine can be directly modified by the field excitation current control, the copper loss of the field winding could be minimised in case the appropriate field excitation current is employed at any given torque and speed conditions. Consequently, the efficiency can be improved.

The MET algorithm of the HEPMM is illustrated in Fig.6.3, where all operating points are expressed on the efficiency curve against the field excitation current. It is observed that, at point A, the maximum field excitation current ($i_{f,max}$) is initially employed in order to enhance the maximum torque of such a machine as aforementioned. At this point of operation, the efficiency might be low due to the over requirement of the field excitation current. Therefore, based on the proposed method, the field excitation reference current is modified by the tracking step size (Δi_f) during the time interval T_P until the maximum efficiency operating point is achieved. The direction of the modified field excitation reference current is defined based on the comparison of the efficiency between the current and previous values, as shown in Fig.6.4. It should be noted that, since efficiency is commonly calculated based on measured currents and voltages rather than Utilising the estimated PM flux-linkage and inductances, the influence of those signal noises cannot be avoided and thus the performance of the proposed method may be deteriorating. Therefore, the window moving average efficiency (η_{avg}) is also presented in

this chapter. It is determined under dynamic condition and takes the average value during the tracking time interval before sending it to the decision process.

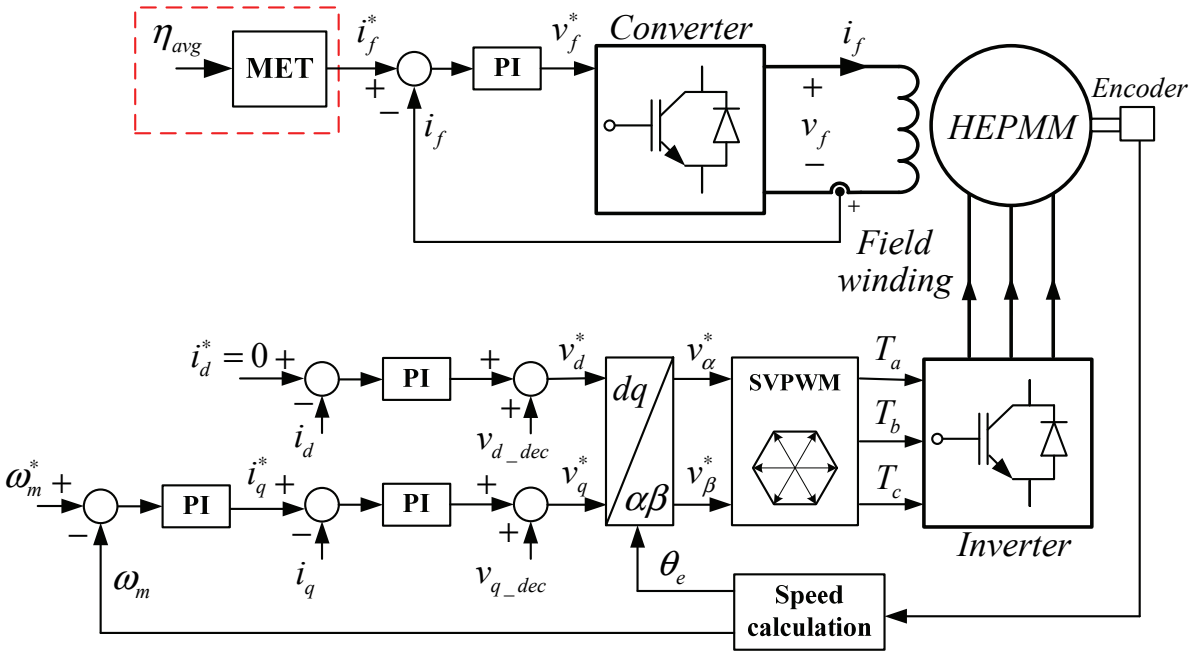

Fig. 6.2. Maximum efficiency tracking control block diagram of the HEPMM.

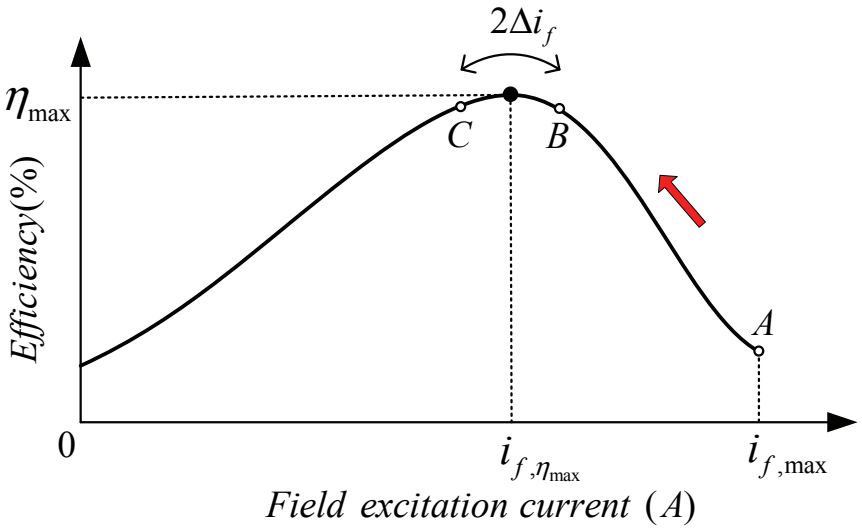

Fig. 6.3. Maximum efficiency tracking.

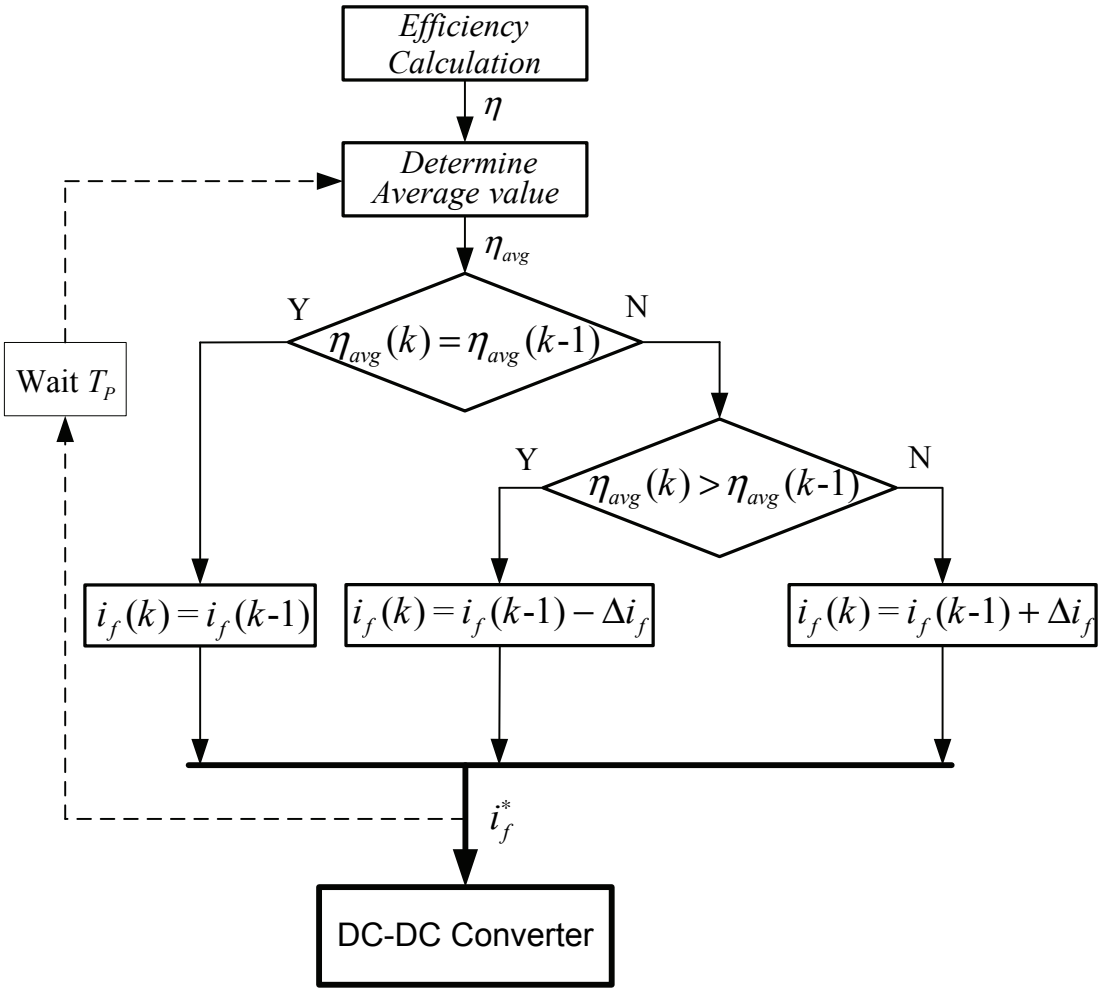

Fig. 6.4. Flowchart of the MET.

In Fig.6.4, when the current value of the average efficiency is greater than its previous value (η_{avg}(k) > η_{avg}(k-1)), the field excitation reference current is subtracted by the tracking step size (i_f(k) = i_f(k) - Δi_f). In contract, it will be added by the tracking step size. Meanwhile, when the previous and current values of the average efficiency are equal within the tracking time interval, the field excitation reference current remains the same as its previous value. Based on the MET algorithm, the field excitation reference current is oscillated around the maximum efficiency point, which is between points B and C as shown in Fig.6.3. However, since the proposed method use only the average efficiency for comparison to determine the direction of the field excitation current adjustment for achieving the maximum efficiency, it can be applied to other hybrid machines even if there is a difference in topology and turn ratio between the armature and field windings.

6.2.2 Window Moving Average Efficiency

The fixed window moving average technique [DES13] is utilised to determine the average efficiency during the MET operation. There are 100 calculation points for each tracking time interval that is executed every 5.0 ms. The efficiency rate is firstly divided by 100, which provides the total calculation point. Then, it is added to the previous efficiency until the last counting point is reached, i.e. *n* is counted to 100, as illustrated by the bold-lines shown in Fig.6.5(a). As a result, the average efficiency during a tracking time interval is given and held by the zero-order-hold (ZOH) function until the next tracking interval time is reached, as illustrated in Fig.6.5(b).

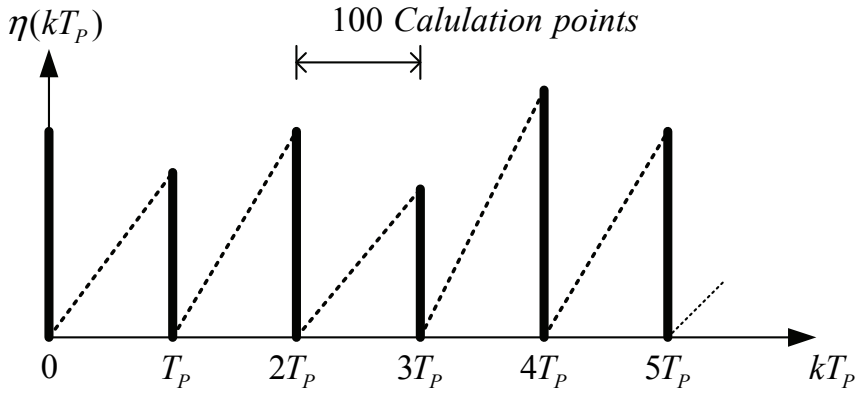

(a) Efficiency against tracking interval time

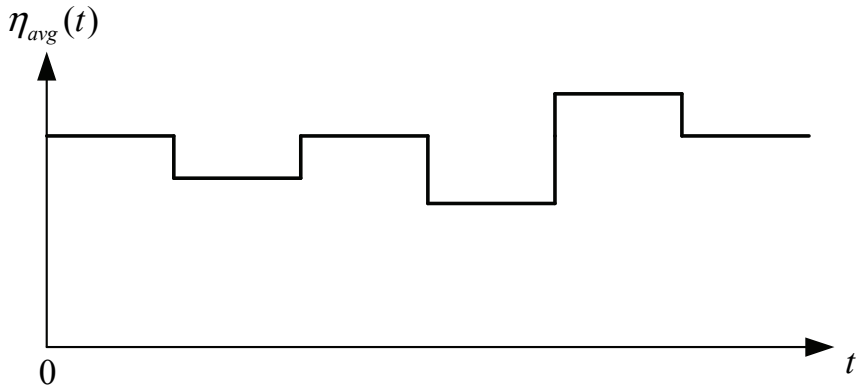

(b) Average efficiency with ZOH function

Fig. 6.5. Window moving average efficiency.

Hence, the average efficiency over any tracking interval time $\eta(kT_P)$, as illustrated by the bold-lines shown in Fig.6.5(a), can be given as,

$$\eta(kT_P) = \frac{\sum_{n=1}^{100} \eta(t)}{100} \tag{6.2}$$

where k is a count number of tracking interval time, n is a count number of the calculation point, and t is time.

The average efficiency (η_{avg}) can be presented as a function of time, which consists of the unit-step function and average efficiency in any tracking time interval, as given by (6.3).

$$\eta_{avg}(t) = \sum_{k=0}^{\infty} \eta_{avg}(kT_P)\left[u(t-kT_P) - u(t-(k-1)T_P\right] \tag{6.3}$$

where u denotes a unit-step function.

It is noted that, since the average efficiency is determined over every specific time range with N samples (N = 100 for this research), it is named as the window moving average, as introduced in [DES13]. The influence of signal noises that might reduce the performance of the proposed method can be eliminated. The measured efficiency is illustrated in Fig.6.6.

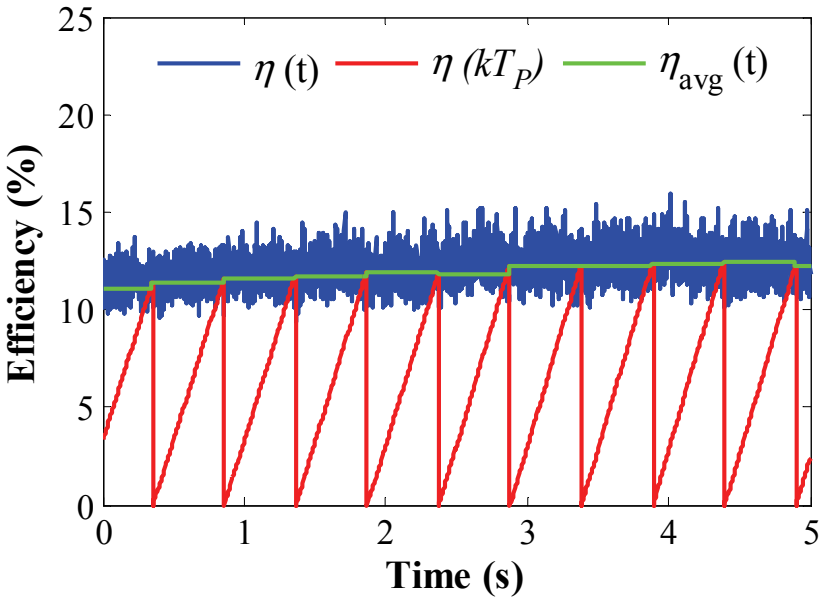

Fig. 6.6. Measured average efficiency.

6.2.3 Field Excitation Current Control

Figs.6.7(a) and (b) show the basic circuit and field excitation current control of the step down (buck-type) DC-DC converter, which is utilised to regulate the field excitation current by tracking the maximum efficiency point at any given torque and speed. The field voltage (v_f) is automatically adjusted corresponding to the field excitation current feedback control. The switching pulse signals, which are used to trigger the power switch devices, are generated proportional to the regulated duty cycle (D). Meanwhile, the proportional and integral (PI) regulators are employed in order to improve the tracking accuracy of the field excitation current. In addition, although the field winding resistance might change due to temperature rise, the field excitation current can still track its reference value.

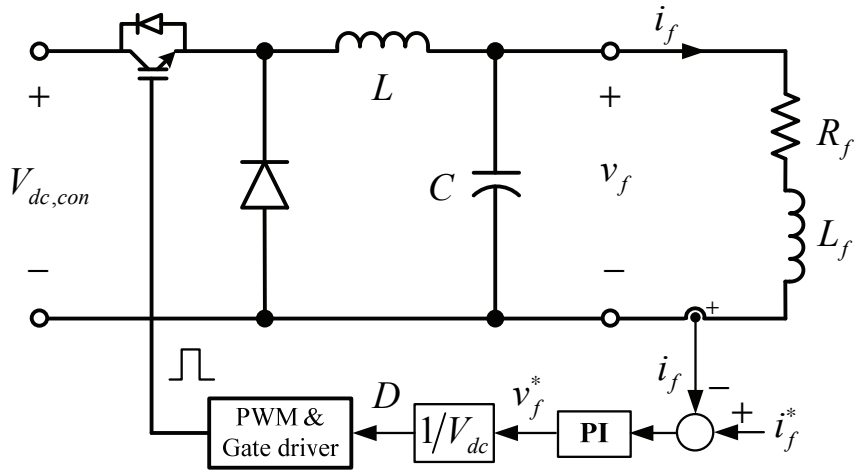

(a) Step down (buck type) DC-DC converter

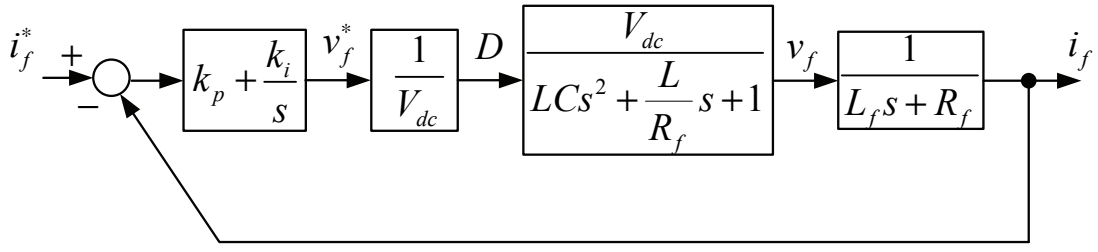

(b) Field excitation current feedback control

Fig. 6.7. Step down DC-DC converter with current feedback control.

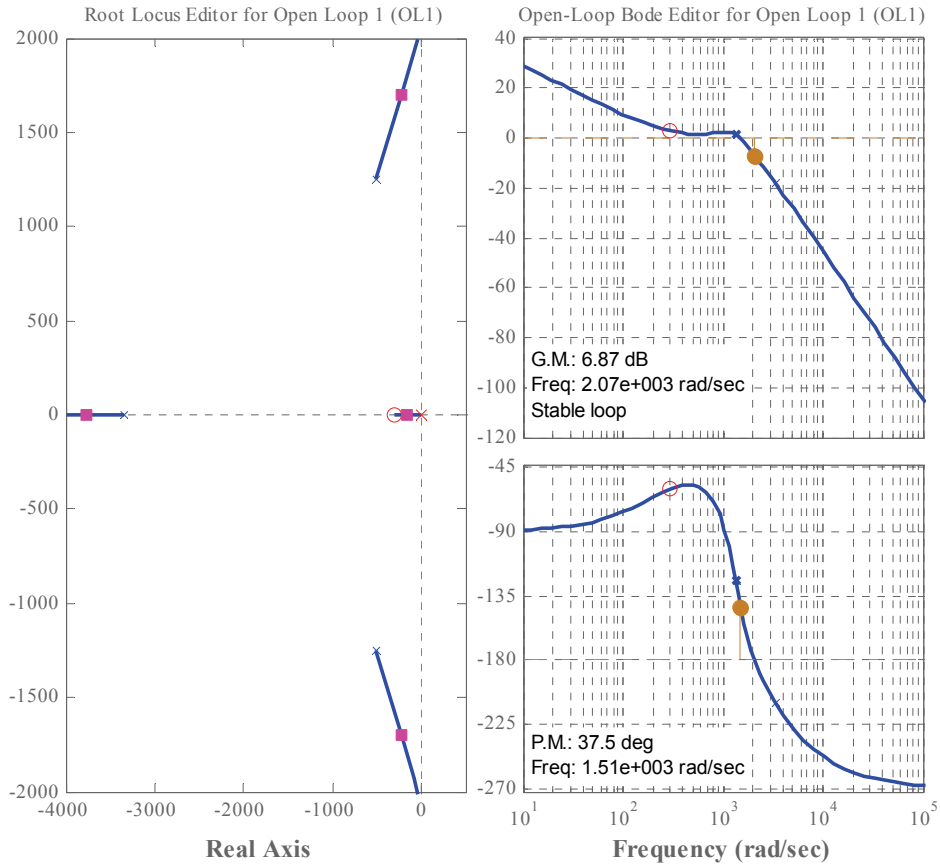

(a) Root locus and bode diagram design based on open loop transfer function.

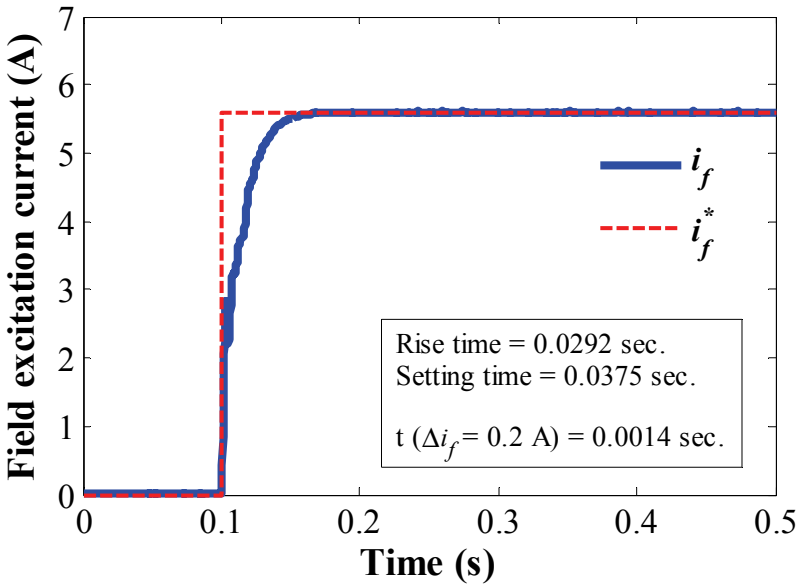

(b) Measured step response

Fig. 6.8. Field excitation current controller design.

Fig.6.8(a) shows the root-locus and bode-diagram of the field excitation current controller design (k_p = 1.0, k_i = 300). It is observed that, since all poles and zeros are located in the left hand-side of the root-locus, the system is stable which also corresponds to the bode diagram. In Fig.6.8(b), the field excitation current exhibits a good tracking accuracy and fast response, in which the rising-time and setting-time are 29.2 ms and 37.5 ms, respectively. In addition, it is also sufficient for the modification of the tracking step size (Δi_f), which takes only 1.4 ms, less than the tracking time interval (T_P). Hence, the field excitation current control can be efficiently modified according to the MET algorithm.

6.3 Experimental Verification of Efficiency Improvement

6.3.1 Experimental setup

The MET algorithm demonstrated is based on the field orientation control, which is implemented on a dSPACE platform. A 1.5 kW wound field type DC motor is utilised as a generator to regulate the load-torque, while an external resistance is used to dissipate the generated power. The space vector pulse width modulation (SVPWM) technique with the minimum magnitude error over-modulation (MMEOM), as described in chapter 2, is applied to the three-phase voltage source inverter (VSI). To verify the effectiveness of the proposed method, the DC-link voltage and the testing speed are set at 40 V and 500 rpm, respectively. Meanwhile, other setup parameters are given in Table 6.1.

Table 6.1. Experimental setup

Motor test speed	500 rpm
DC-link voltage	40 V
DC supply voltage of the converter	30 V
Maximum armature current	7.92 A
Maximum field excitation current	5.6 A
Switching frequency of the inverter	10 kHz
Switching frequency of the converter	10 kHz
Tracking time interval (T_P)	0.5 s
Tracking step size (Δi_f)	0.2 A

Based on the proposed method, the tracking time interval (T_p) and tracking step size (Δi_f) need to be properly defined. If T_p is settled as a small value, the operating point can become unstable. In contrast, a too big value might reduce the tracking speed [FEM05].

Meanwhile, Δi_f is preferred to be set at a small value in order to avoid the oscillation in the field excitation current, but it will affect the tracking response. Indeed, since the efficiency is mainly utilised to achieve the maximum efficiency, which is calculated by the output power and copper losses (R_f = 3.0 Ω and R_s = 1.0 Ω as shown in Table 2.2).

Based on the MET algorithm and the experimental setup, the window moving average efficiency and the field excitation reference current modification implemented in Matlab/Simulink are illustrated in Fig.6.9(a) and (b), respectively.

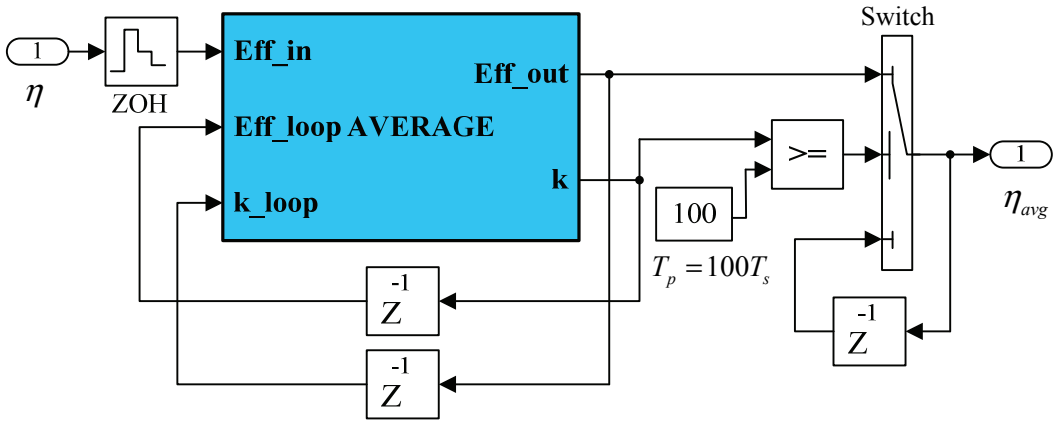


```
function [Eff_out,k] = AVERAGE(Eff_in,k_loop,Eff_loop)

if k_loop >= 100;
    k = 0;
    Eff_out = 0;
else
    k=k_loop+1;
    Eff_out = Eff_in/100+Eff_loop;
end
```

(a) Window moving average efficiency part

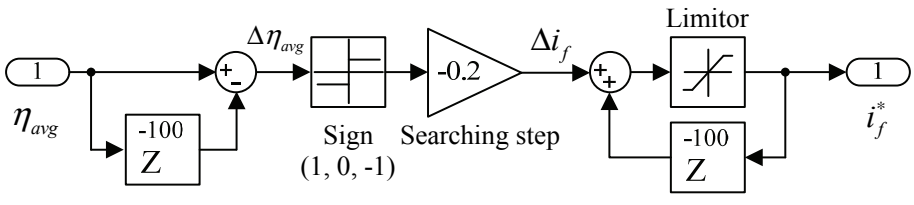

(b) Field excitation reference current modification part

Fig. 6.9. MET algorithm in Matlab/Simulink model.

6.3.2 Experimental results

In order to verify the performance of the proposed method in terms of the efficiency improvement, two field excitation current control methods are compared as follows:

(1) Utilising the maximum field excitation current for all operating regions ($i_{f,max}$).

(2) Utilising the modified field excitation current based on the MET method ($i_{f,MET}$).

Figs.6.10 - 6.11 show the experimental results of both control methods. In order to demonstrate the effectiveness of the proposed method, the prototype machine is started with the load-torque at 0.3 Nm, then changed to 0.5 Nm at around 15.0 s of the experimental time, as shown in Fig.6.10(a). Meanwhile, the speed is controlled at 500 rpm across the whole operating region. In Fig.6.10(b), the field excitation current for both methods are initially employed at its maximum value (5.6 A). Under this condition, the copper loss and efficiency of both methods are equal due to the same armature and field excitation currents, as illustrated in Figs.6.10(c) and (d), respectively. Afterwards, the MET is activated at approximately 4.0 s, where the field excitation current of the proposed method starts tracking for maximum efficiency. The load-torque is maintained at 0.3 Nm. Based on the MET algorithm, the field excitation current ($i_{f,MET}$) is modified, decreasing from 5.6 A to around 3.6 A, as illustrated in Fig.6.10(b). Therefore, the total copper loss of the proposed method is significantly reduced compared to the method which utilised the maximum field excitation current for all operating regions ($i_{f,max}$), as shown in Fig.6.10(c). As a result, the efficiency can be significantly increased from approximately 12% to 20% (increasing ~66.7%) under the given torque and speed condition, as shown in Fig.6.10(d).

Likewise, when the load-torque is changed from 0.3 Nm to 0.5 Nm at around 15.0 s, the field excitation current of the proposed method ($i_{f,MET}$) is modified from 3.6 A to around 4.6 A corresponding to the requirement of the flux-linkage, as illustrated in Fig.6.10(b). Under this condition, the efficiency can be increased by ~16.5% compared to the method which utilises the maximum field excitation current for all operating regions ($i_{f,max}$). It should be noted that the operation in the lower load-torque exhibits the higher capability to improve the efficiency which is proportional to the elimination of the

redundant field winding copper loss.

Fig.6.10(e) shows the *q*-axis and *d*-axis currents of both field excitation current control methods, i.e. $i_{f,max}$ and $i_{f,MET}$. The *d*-axis current of both methods remain at zero due to the non-saliency of the prototype machine, while the *q*-axis currents with the same values corresponding to the load torque at 0.3 Nm are initially utilised. After the activation of the MET, the field excitation current of the proposed method decreases compared to the method which uses the maximum field excitation current for all operating regions ($i_{f,max}$) under the same condition. Therefore, the utilization of the *q*-axis current is increased, as shown in Fig.6.10(e). It is also the same trend as the load-torque at 0.5 Nm. However, due to the winding turn ratio of the prototype machine, in which the field winding resistance is greater than the armature winding resistance, the total copper loss is mainly influenced by the field excitation current rather than the armature current. It means that the decrease of the field winding copper loss that relates to $i_{f,MET}$ is larger than the increase of the armature winding copper loss produced by the *q*-axis current.

Fig. 6.10(f) shows the output power of both field excitation current control methods related to the load-torque as shown in Fig.6.10(a). It is obvious that the machine speed and DC-link voltage of both methods can be constantly maintained at their references during the modification of the field excitation current, even though the load-torque is changed, which confirms the good dynamic performance of the proposed method, as shown in Figs. 6.11(a) and (b).

Since 2 efficiency improvement control strategies, i.e. the optimisation method ($i_{f,opt}$) and the maximum efficiency tracking ($i_{f,MET}$), have been proposed in this thesis, the performance of both methods in terms of efficiency are compared as shown in Fig.6.12. It is observed that although both methods can improve the efficiency in steady-state condition, the optimisation method ($i_{f,opt}$), which is a function of *d*-*q* axis currents, exhibits better dynamic response than the maximum efficiency tracking method ($i_{f,MET}$). It is noted that, the efficiency is calculated without the consideration of temperature rise and iron loss. However, those methods are based on the assumption of the same iron loss and mechanical loss since the same given torque and speed condition is considered.

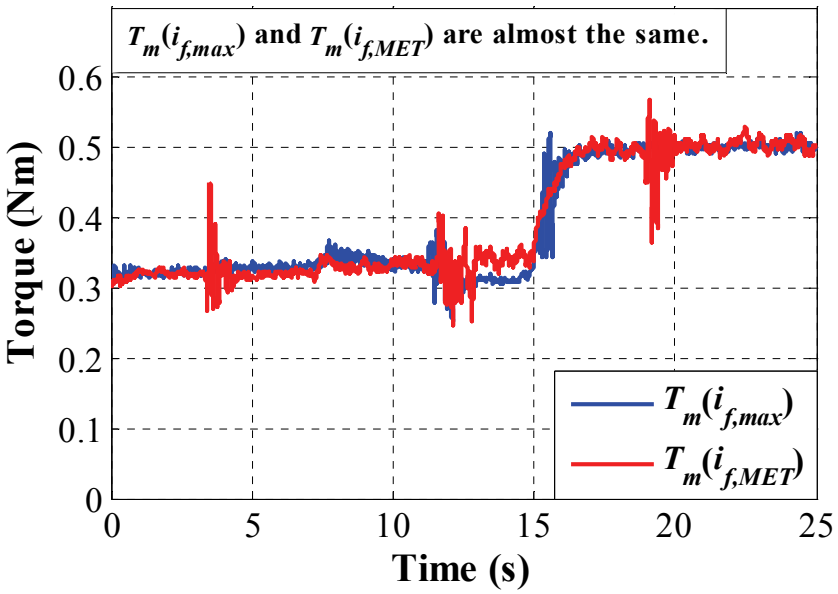

(a) Measured torque

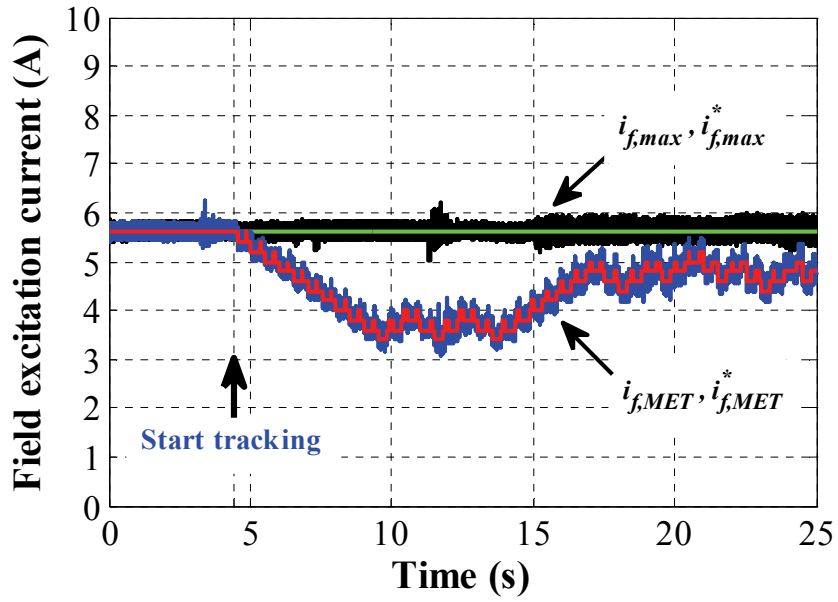

(b) Field excitation current control

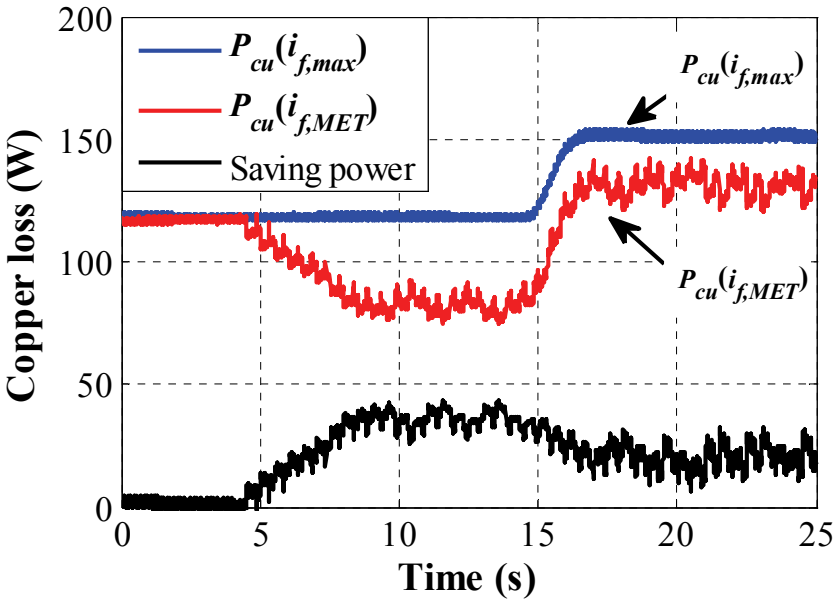

(c) Total copper loss

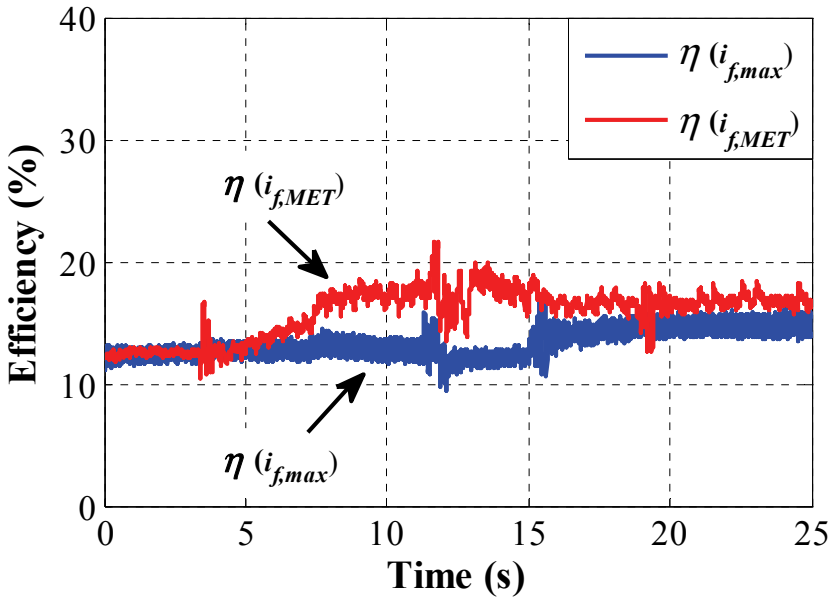

(d) Efficiency

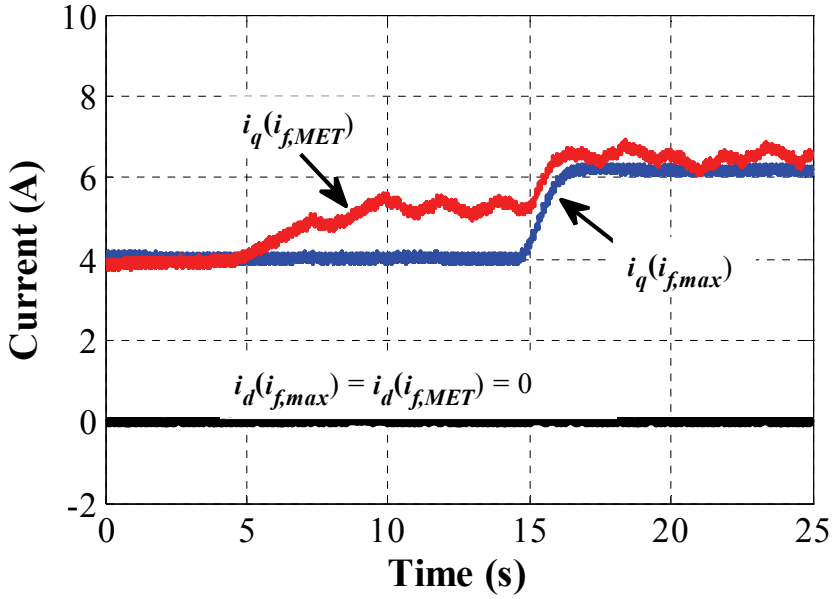

(e) *d*-axis and *q*-axis currents

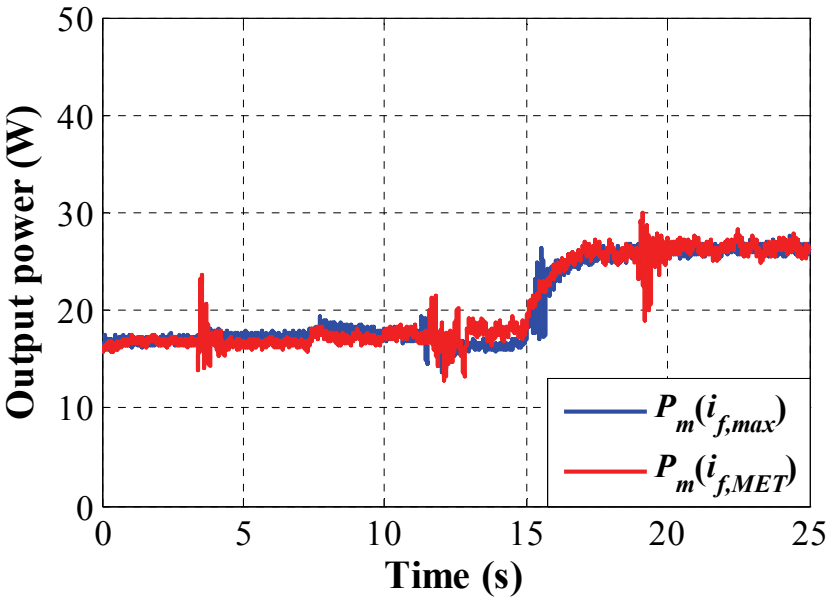

(f) Output power

Fig. 6.10. Experimental results of the proposed method ($i_{f,\mathrm{MET}}$) compared to the method which utilised the maximum field excitation current for all operating regions ($i_{f,\mathrm{max}}$).

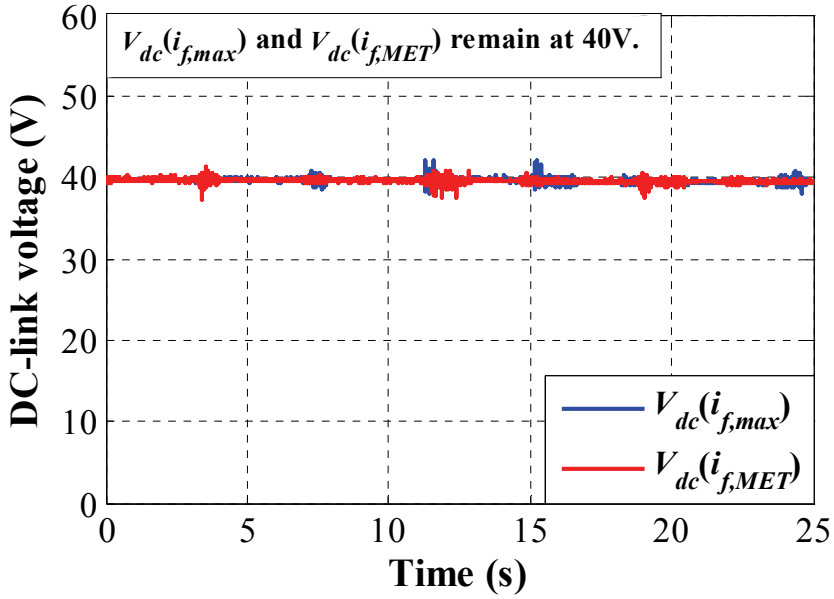

(a) DC-link voltage

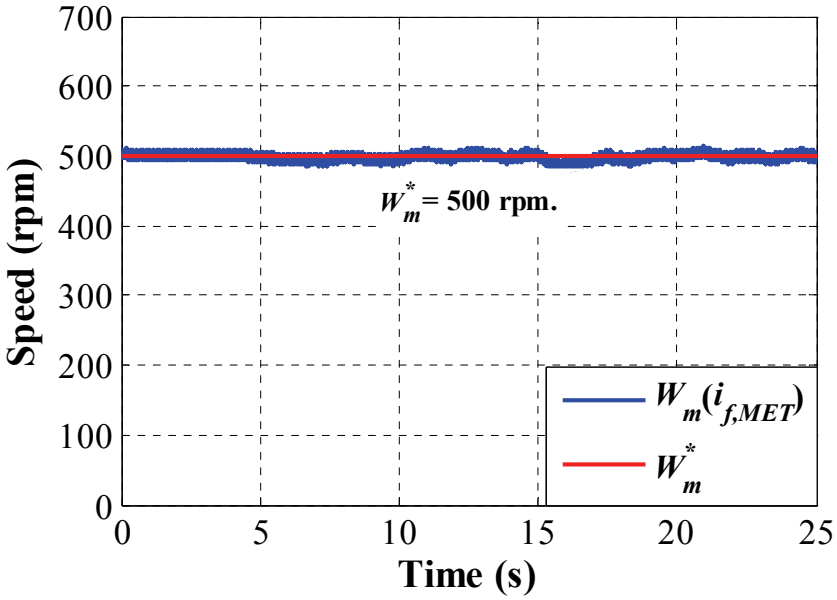

(b) Speed

Fig. 6.11. DC-link voltage and speed.

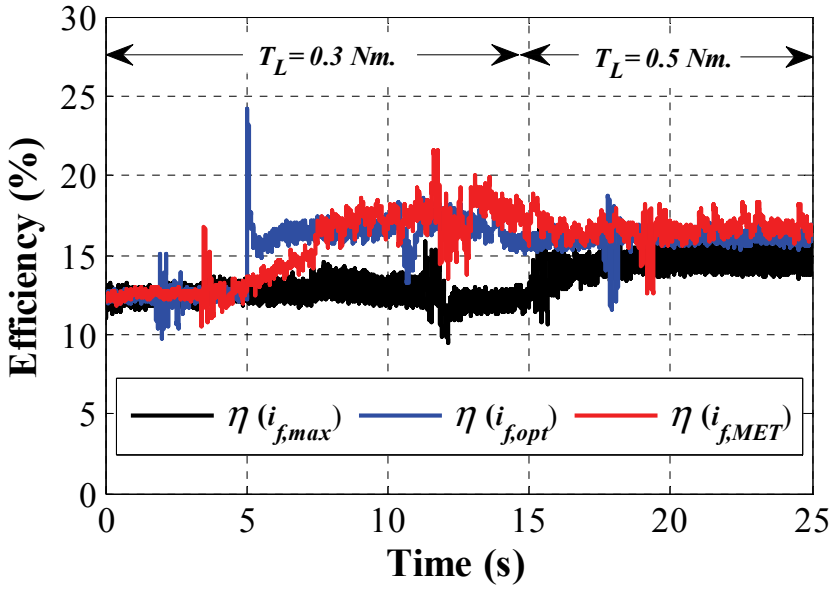

Fig. 6.12. Comparison of the efficiency improvement control strategies.

6.4 Summary

This chapter has proposed the maximum efficiency tracking method for the HEPMM (Machine-II) based on searching for the optimal field excitation current under the given torque and speed conditions. The experimental results have shown that the efficiency of the HEPMM can be improved based on the proposed method compared with the method which utilised the maximum field excitation current for all operating regions. Likewise, the proposed method is verified under dynamic conditions, when the load-torque is changed, to confirm the effectiveness of the field excitation current control and the window moving average. Since the direction of the modified field excitation reference current is defined based on the comparison of the current and previous efficiency values, the proposed method can be applied to other hybrid-excited machines.

CHAPTER 7

FAULT PROTECTION CAPABILITY OF HYBRID-EXCITED PERMANENT MAGNET MACHINES UTILISING FIELD EXCITATION CURRENT CONTROL

In this chapter, the fault protection capability of a novel hybrid-excited permanent magnet (PM) machine is examined to illustrate its great capability to prevent the dangerous overvoltage issue from the uncontrolled generator fault (UCGF) at high speed operation. PM flux of the novel hybrid-excited PM machine is inherently short-circuited when the field excitation current is not fed into the excitation windings. Therefore, when the machine UCGF is detected in the high speed region, the DC-link overvoltage issue can be effectively reduced by instantly changing the field excitation current to be zero. Since only the field excitation current is utilised to protect the machine and inverter switches from the UCGF, it is simple to implement and the concept of proposed control strategy can also be applied to other hybrid-excited PM machines. Finally, the proposed control strategy is verified by both simulation and experimental results on the hybrid-excited PM machine.

7.1 Introduction

Permanent magnet (PM) machines are attractive for many applications due to their advantages, for example, high power density, high efficiency, and wide operating speed range [CHE11], [ZHU07]. Since these machines are widely considered for some safe-critical applications such as aerospace and automotive industry, the system reliability has become an increasingly important issue [CHE97], [EST08], [ZHU09]. For this reason, a large amount of literature have been presented related to the fault impacts, detections, and fault tolerances for the machines [ABO09], [CHE97], [ELR11], [ERR12], [HAN06], [LIU10], [WEL04].

Among the various machine fault types, the uncontrolled generator fault (UCGF) at high speed in a PM machine [CHO13], [HAN06], [JAH99], [LIA05], [PEL11], [WEL04] is one of the most serious scenarios that can damage the machine and inverter switches and will be particularly discussed in this chapter. The UCGF is emerged when

the flux-weakening control is unexpectedly disappeared, which usually happens when the switching signals are suddenly removed or the encoder is damaged [CHO13], [HAN06], [JAH99], [LIA05], [PEL11], [WEL04]. It would be a serious problem if the machine operates at high speed, since the back-emf in each phase winding which is usually several times higher than the rated supply voltage will immediately become a voltage source to deliver the regenerated energy charging the DC-link capacitor. Under this condition, in case the DC-link capacitor cannot absorb this energy, high voltage in the DC-link might explode the capacitor, inverter switches, and even demagnetise the PMs [CHO13], [SUN07]. Although the UCGF has been presented in [CHO13], [HAN06], [JAH99], [LIA05], [PEL11], [WEL04], these researches focus mostly on the optimisation of the machine parameters such as the saliency ratio, PM per-unit flux, and rotor moment of inertia.

For the prototype hybrid-excited PM machine developed in [AFI15], the field winding acts as a major excitation source compared to the PMs. Consequently, under the UCGF condition, the flux-linkage and back-emf could be entirely reduced when the field excitation current is controlled towards zero ($i_f^* = 0$), while remaining the excitation current at the maximum could cause a large regenerated overcurrent.

Therefore, the fault protection capability of the HEPMM will be examined in this chapter. Based on the hybrid-excited PM machine, the field excitation current control strategy is proposed, which can effectively remove the dangerous overvoltage from the UCGF. Due to that only the field excitation current is utilised to protect the machine and inverter switches against the UCGF, it is easy and simple to implement. Finally, the proposed control strategy is verified by both simulation and experimental results on the hybrid-excited PM machine.

7.2 Machine Topology and Operating Principle

7.2.1 HEPMM Topology (Machine-II)

The three-phase 12-stator slot/10-rotor pole HEPMM is shown in Fig.1 [AFI15], where the PMs are placed between the contiguous slot openings of the stator teeth. Each phase winding consists of four armature coils connected in series. The twelve dc coils are also connected in series to form a single winding. Since the back-emf of the prototype machine is nearly zero when the field excitation current is not employed (i_f^*=0), this machine exhibits a fault protection capability based on the control of field excitation current. The parameters of the prototype machine and dimensions have been described in Chapter 2, while the operating principle of this machine has clearly been illustrated in Chapter 4. It is noted that since such a machine has no magnets or excitation coils on the rotor, robust rotor structure and high speed operation can be provided for this topology.

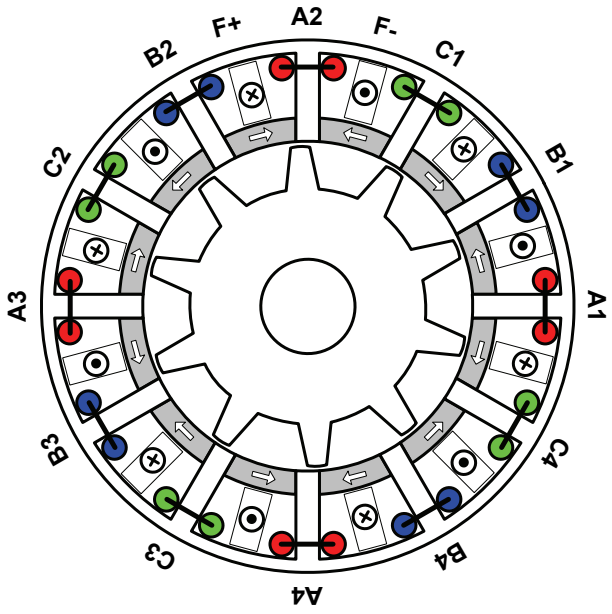

Fig. 7.1. Cross-section of the prototype HEPMM.

7.2.2 Flux Regulation Capability and Back-emf

The phase flux-linkage and back-emf against the rotor position of the prototype machine at various specific field excitation currents and at 400 rpm are shown in Figs.7.2(a) and (b), respectively. It can be observed that the amplitude of phase flux-linkage can be enhanced with the increase of the field excitation current, also as shown in Fig. 7.3. When the field excitation current is zero (i_f^*= 0), the amplitude of phase flux-linkage is only approximately 0.98 mWb, while the back-emf is almost zero. Obviously, the higher field excitation current can produce the larger phase flux-linkage and back-emf and vice versa.

It should be noted that the HEPMM can provide a high torque in the constant-torque region [AFI15], and it also offers more freedom for the flux-weakening currents, i.e. field excitation and *d*-axis currents, for extending speed range in the flux-weakening region. Moreover, when the worse-scenarios arise, such as inverter short-circuit at high speed, the back-emf of the hybrid-excited PM machine can be significantly diminished by adopting i_f = 0. Thus, the potential damages of the machine and inverter can be prevented. As a result, the HEPMMs exhibit significant advantages in terms of fault protection capability compared to the conventional PM machines.

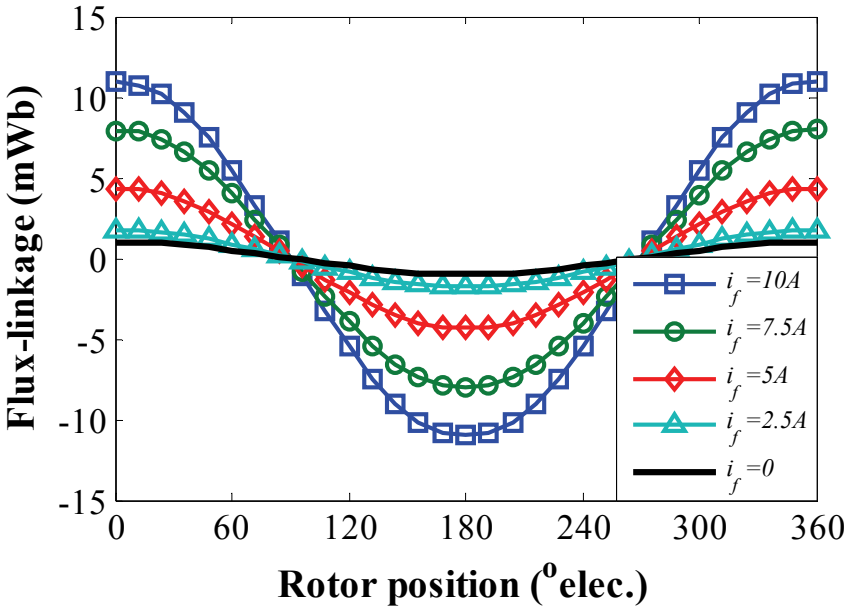

(a) Flux-linkage

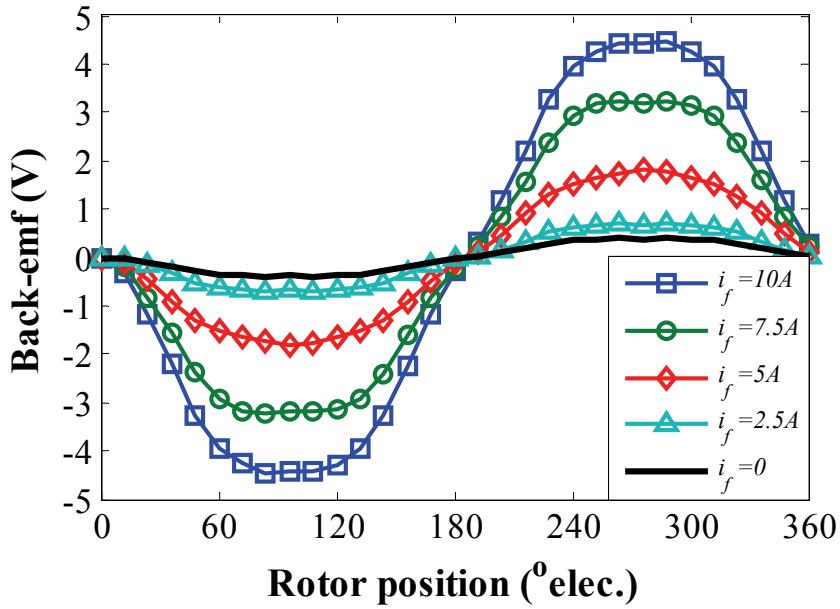

(b) Back-emf

Fig. 7.2. Open-circuit characteristics of phase A for the prototype machine corresponding to the specific values of field excitation current.

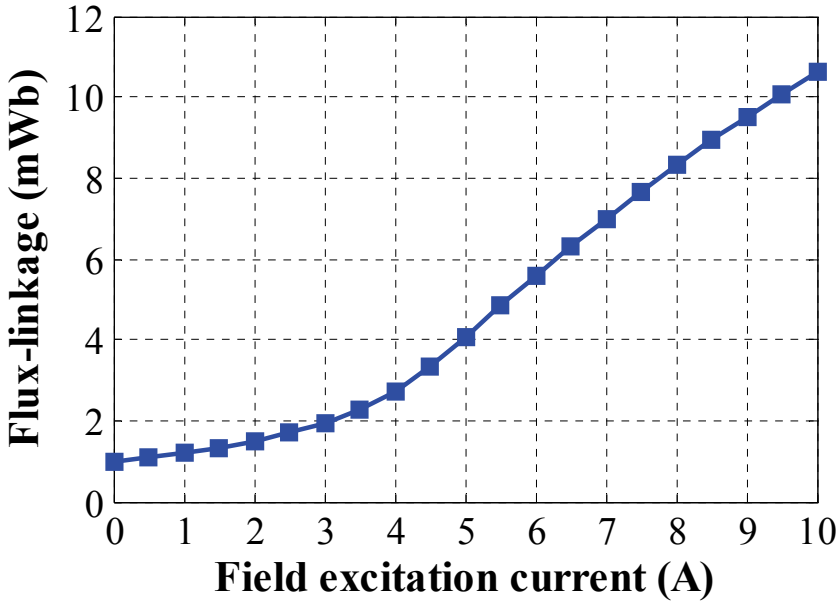

Fig. 7.3. Phase A flux-linkage amplitude with field excitation current.

7.3 Fault Protection Operation

7.3.1 Uncontrolled Generation Fault

In order to extend the operating speed range within the current and voltage constraints, the flux-weakening control technique is required. In this operation, the amplitude of back-emf would be greatly increased in proportional to the machine speed. However, when the flux-weakening control is unexpectedly disappeared, the back-emf in each phase would instantaneously become a large voltage source, which delivers the regenerated current (i_{regen}) back to the DC-link through the free-wheeling diodes of the inverter switches, as shown in Fig.7.4. This fault has been defined as uncontrolled generator fault (UCGF) presented in [CHO13], [HAN06], [JAH99], [LIA05], [PEL11], [WEL04], which is usually emerged from, e.g., the removal switching signals of inverter switches and the damage of the processing unit or speed encoder. Furthermore, it would be serious if the DC-link capacitor cannot absorb the abruptly regenerative energy. Consequently, the explosion of both capacitor and inverter switches might be unpredictably emerged as caused by the dangerous overvoltage.

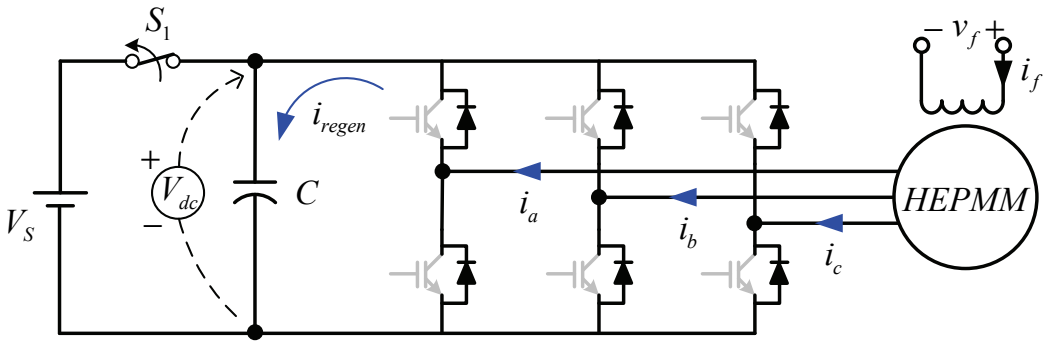

Fig. 7.4. Uncontrolled generator fault (all gate-signals are removed).

In this research, the switch (S_1) is simultaneously controlled to protect the main dc power supply (V_s) whereas the fault is emerged and detected. The DC-link voltage (V_{dc}) is measured between anode and cathode terminals of the capacitor as shown in Fig.7.4. It is noted that since the other overvoltage protections, such as the braking resistance, is not considered in this circuit, the impact of the UCGF can be evaluated considering only the regenerative energy that produced by the machine.

7.3.2 Proposed Fault Protection Control Strategy

As aforementioned in section 7.2, the HEPMM has the excellent feature of flux-regulation capability by adjusting the field excitation winding. As a consequence, the field winding would be possibly utilised to eliminate the regenerated energy caused by the UCGF, particularly at the high speed flux-weakening operation.

The fault protection control strategy for the HEPMM is shown in Fig.7.5. In normal operation, as defined in Fig.7.5(a), the maximum field excitation current ($i_{f,max}$) is employed in whole operating regions in order to achieve the maximum torque. The *d*-axis current is utilised to weaken the flux-linkage in flux-weakening operation, while the *q*-axis current is determined according to the speed and load-torque as shown in Fig.7.5(b). In the UCGF, the DC-link capacitor is rapidly charged by the regenerated current that results in the serious overvoltage, and thus, the DC-link voltage is utilised to activate the fault operation. Practically, when the DC-link voltage is greater than or equal to the pre-set maximum DC-link voltage ($V_{dc} \geq V_{dc,max}$), the field excitation current is controlled to be zero to protect the drive system ($i_f^* = 0$). As a result, the overvoltage issued could be solved for the HEPMM with the proposed control strategy.

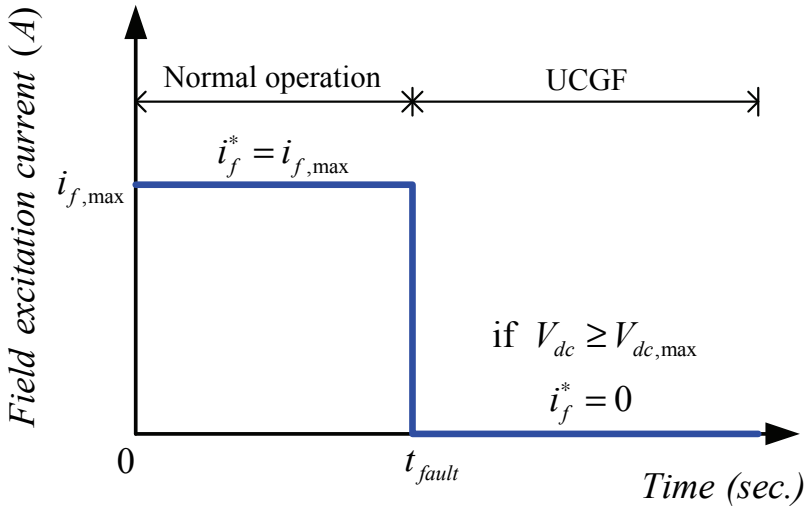

(a) Field excitation current control

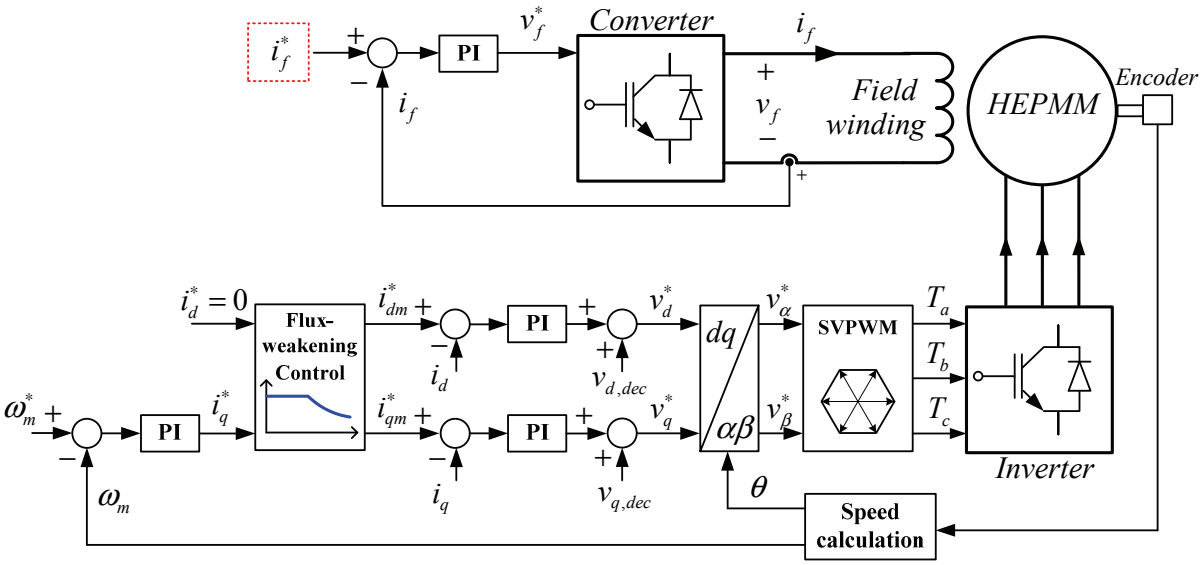

(b) Control block diagram of the HEPMM

Fig. 7.5. Fault protection control strategy.

7.4 Verification of Fault Protection Capability

The effectiveness of the fault protection control method is verified by both simulations and experiments in this research. These will be explained sequentially as follows.

Table 7.1. Fault protection verification setup

Motor reference speed	2700 rpm
DC-link voltage (V_{dc})	24 V
Pre-set maximum DC-link voltage ($V_{dc,max}$)	25 V
Maximum armature current	7.92 A
Maximum field excitation current ($i_{f,max}$)	10 A

7.4.1 Simulation Results

The Simulink@MATLAB is utilised in order to simulate the UCGF condition and verify the fault protection control. In the simulation, the DC-link voltage is set to 24 V, as shown in Table 7.1, while the machine speed is controlled at 2,700 rpm. In addition, the maximum field excitation current is employed at 10 A to enhance the maximum flux-linkage, the impact of the regenerated energy, under the fault condition, will be clearly

demonstrated. In order to detect the UCGF condition, the maximum DC-link voltage ($V_{dc,max}$) is set to 25 V. Other setting parameters are presented in Table 7.1.

Figs.7.6 – 7.7 show the simulation results of the fault protection control capability based on the operation principle of the HEPMM. Two field excitation current control strategies under the UCGF are illustrated and compared, i.e.,

(1) Maximum field excitation current in whole regions (i_f^*= 10 A) to simulate the conventional PM machines in which the excitation cannot be changed when UCGF happens.

(2) Maximum field excitation current in normal operation, and zero field excitation current when UCGF detected (i_f^*= 0).

In normal operation mode, Fig.7.6(a), the HEPMM is operated in the flux-weakening region with the speed at 2,700 rpm. Meanwhile, the maximum field excitation current is used to enhance the torque output, as shown in Fig.7.6(b). The amplitudes of line back-emfs of both strategies are at the same level closely to the level of DC-link voltage due to the same speed and flux-linkage, as shown in Fig.7.6(c) before the UCGF.

The UCGF is set to emerge at 2.0 s of the simulation time. In the UCGF mode, the machine speeds for both strategies are significantly decreased, Fig.7.6(a). For the control strategy utilising the maximum field excitation current in the whole region (i_f^*= 10 A), the DC-link voltage is rapidly increased by around 22 V (~88.0%), as shown in Fig.8(c). Under this condition, the DC-link capacitor is quickly charged by the regenerated current from the machine, which corresponds to the *d*- and *q*-axes current variations as shown in Fig.7.7(a).

Based on the proposed fault protection control method, when the DC-link voltage is greater than or equal to 25 V, as defined in Table 7.1, the UCGF can be detected. Therefore, the field excitation current is then controlled to be zero (i_f^*= 0), as shown in Fig.7.6(b). Then, the line back-emf can be visibly decreased, as shown in Fig.7.6(d), compared to the results of the strategy that utilises the maximum field excitation current in whole regions in Fig. 7.6(c). Consequently, the regenerated current of the HEPMM can be mostly reduced corresponding to the *d*-axis and *q*-axis currents as shown in Fig.7.7(b) and (c), respectively. In addition, the effectiveness of the proposed fault protection control method can be clearly proved by the power storage of the capacitor, as shown in Fig.7.7(d). It is seen that, although a peak of the regeneration power is approximate 110

W after the UCGF, it can be quickly reduced based on zero field excitation current (i_f^*= 0) compared to the maximum field excitation current strategy (i_f^*= 10 A).

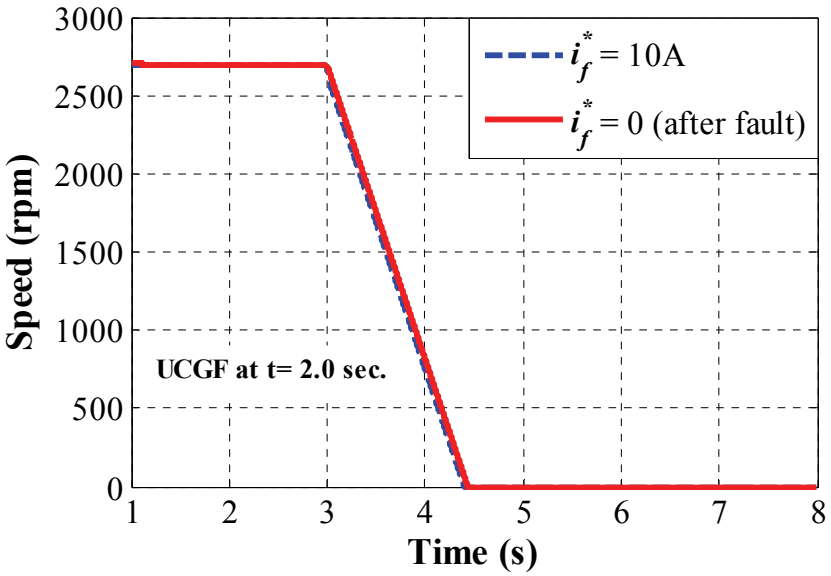

(a) Speed

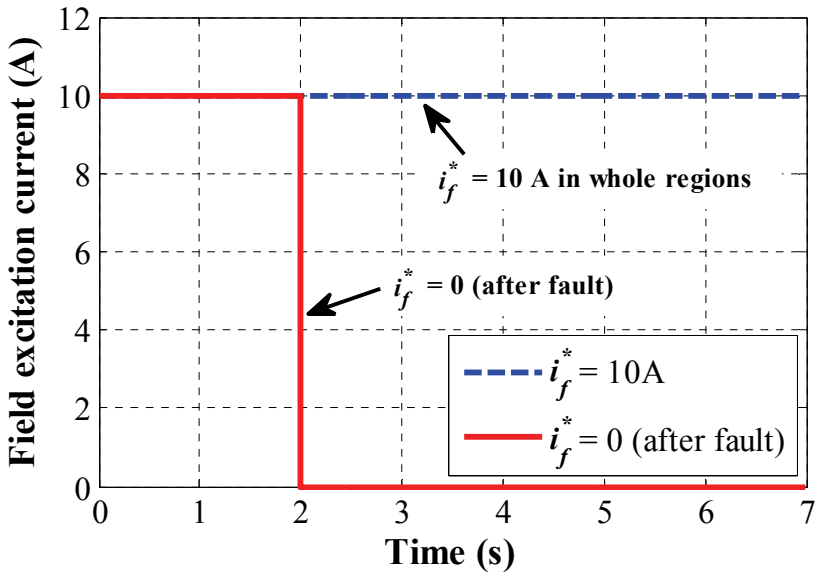

(b) Field excitation current control

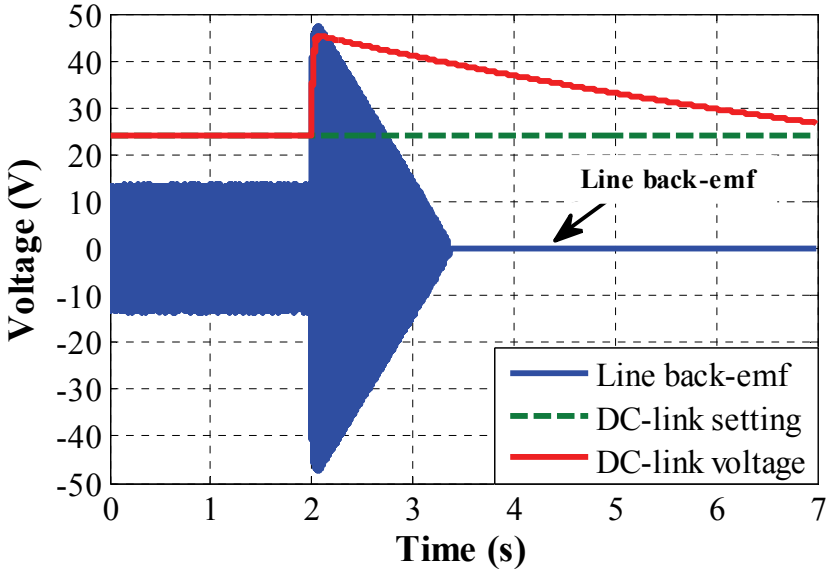

(c) Line back-emf (i_f^* = 10 A)

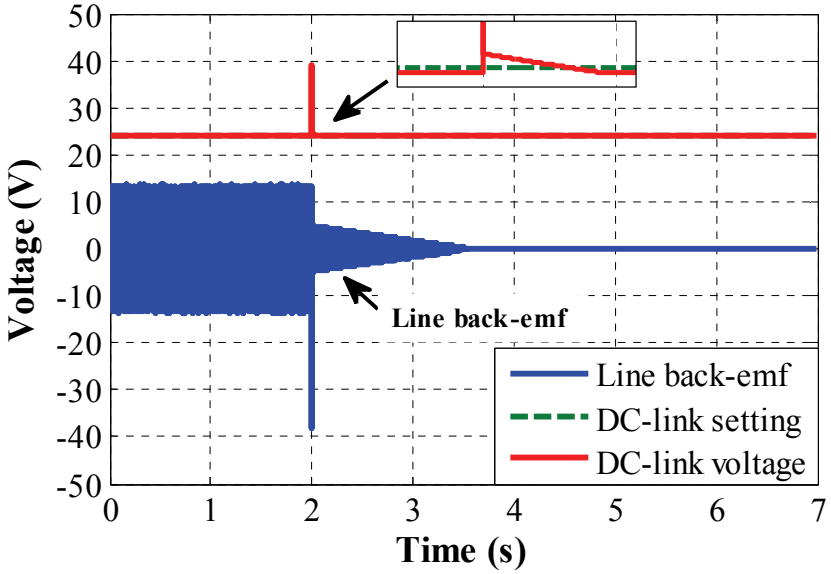

(d) Line back-emf (i_f^* = 0 after UCGF)

Fig. 7.6. Simulation results of the proposed fault protection method (i_f^* = 0) compared to the method that utilising the maximum field excitation current for all regions (i_f^* = 10 A).

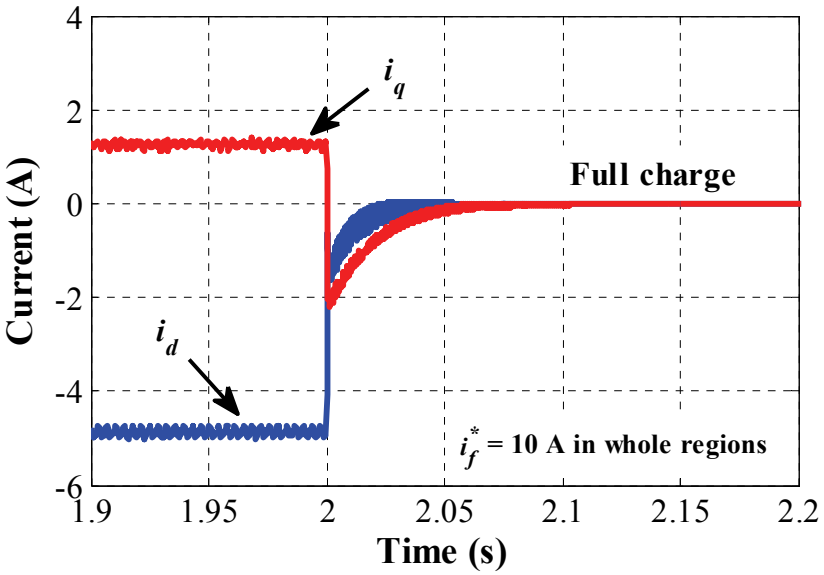

(a) *d*- and *q*-axis currents (i_f^*= 10 A)

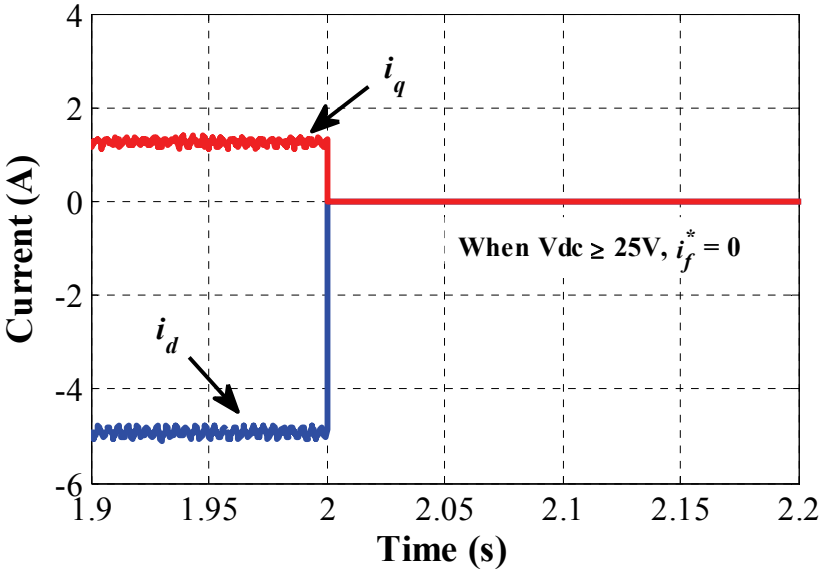

(b) *d*- and *q*-axis currents (i_f^*= 0 after UCGF)

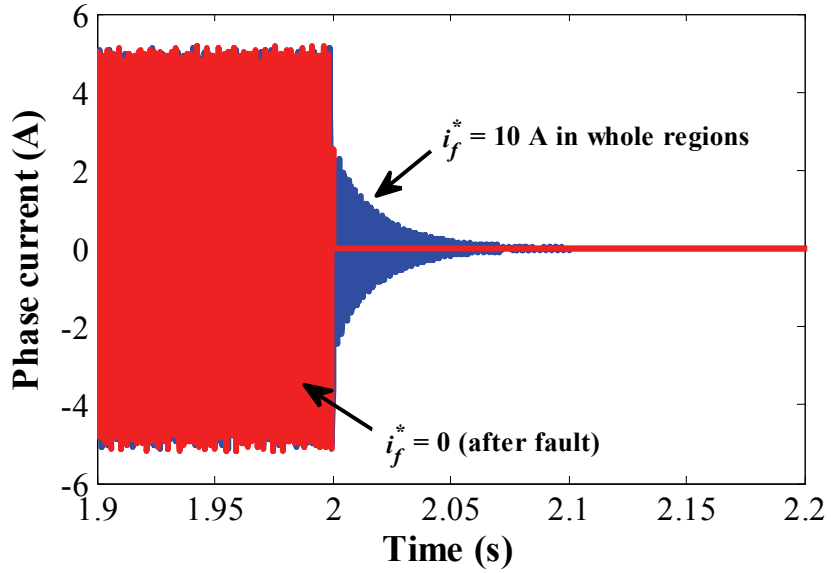

(c) Armature current

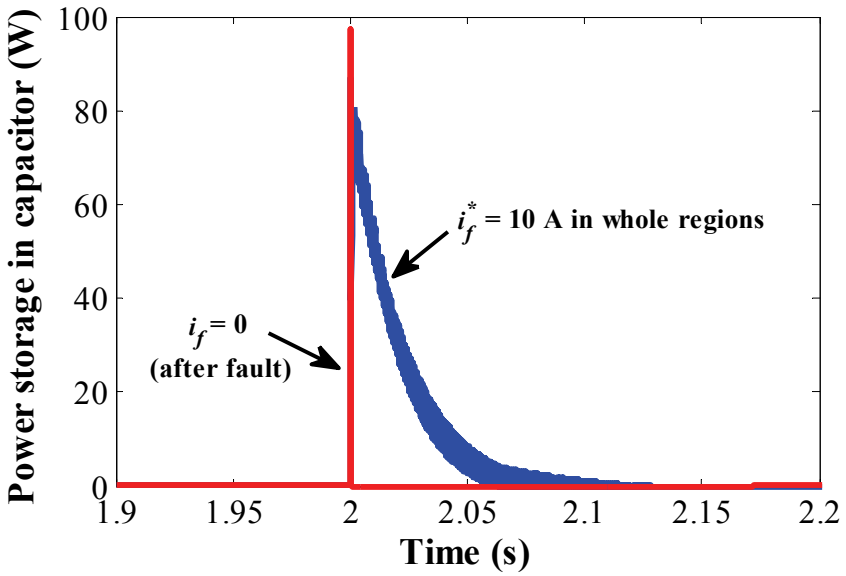

(d) Power storage in capacitor

Fig. 7.7. Simulation results, currents and power storage in capacitor, of the proposed fault protection method (i_f^* = 0) compared to the method that utilising the maximum field excitation current in whole regions (i_f^* = 10 A).

7.4.2 Experimental results

The prototype HEPMM, as shown in Fig.7.1, is controlled based on the vector control. It is implemented on a dSPACE platform. The prototype machine is connected to a 1.5 kW wound field type DC motor, which is utilised to regulate the load-torque through an external resistance, for dissipating the generated power. The three-phase voltage source inverter (VSI) is utilised based on the SVPWM switching technique, while the field excitation current is regulated by the step-down DC-DC converter, as mentioned in Chapter 2. The experimental setup parameters are defined in Table 7.1.

Since the UCGF is one of the most dangerous faults that can rapidly regenerate the energy back to the inverter caused the overvoltage, especially in flux-weakening operation, it is considered in this thesis in order to verify the fault protection capability of the prototype HEPMM. The UCGF is usually emerged from, e.g., the removal switching signals of inverter switches and the damage of the processing unit or speed encoder. Therefore, in order to generate the UCGF in the experiment, all switching gate-signals are suddenly removed.

Figs.7.8 and 7.9 show the measured results of the fault protection control for the HEPMM, which utilises zero field excitation current (i_f^*= 0) after the UCGF is detected, compared to the method that utilising the maximum field excitation current in whole regions (i_f^*= 10 A). The measured speed and field excitation current are shown in Figs.7.8(a) and (b), respectively. It is noted that those results exhibit the same trends as the simulation results. In the normal operation mode, both control strategies are controlled in the flux-weakening region at 2,700 rpm, whereas the maximum field excitation current is utilised. The UCGF happens at 2.0 second of the experimental time. Under the UCGF condition, since the flux-density of the method utilising i_f^*= 10 A is higher than the method utilising i_f^*= 0 due to the field excitation flux resulting in the higher core loss [LEE11], the speed of the method utilising i_f^*= 10 A falls more quickly than the method utilising i_f^*= 0, as illustrated in Fig.7.8(a).

It is obvious that, for the control strategy utilising the maximum field excitation current in the whole region (i_f^*= 10 A), the measured DC-link voltage is speedily increased by around 19 V (~79.16%), as shown in Fig.7.8(c). Meanwhile, the overvoltage in the DC-link capacitor can be eliminated based on the proposed method (i_f^*= 0). Likewise, the effectiveness of the fault protection capability of the HEPMM can be

clearly proved by the comparison of measured line voltage, (V_{ab}), as shown in Fig.7.8(d). The regenerated current and power storage in the capacitor are shown in Figs.7.9(a) and (b), respectively.

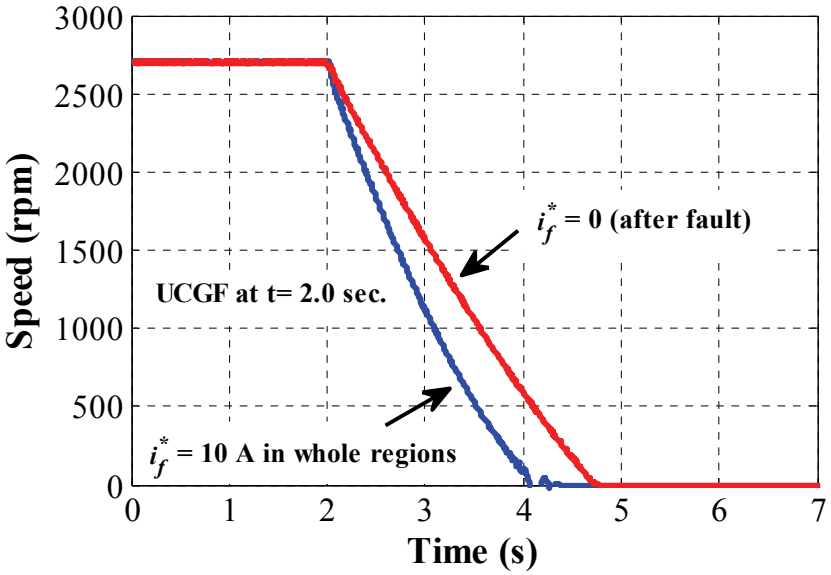

(a) Speed

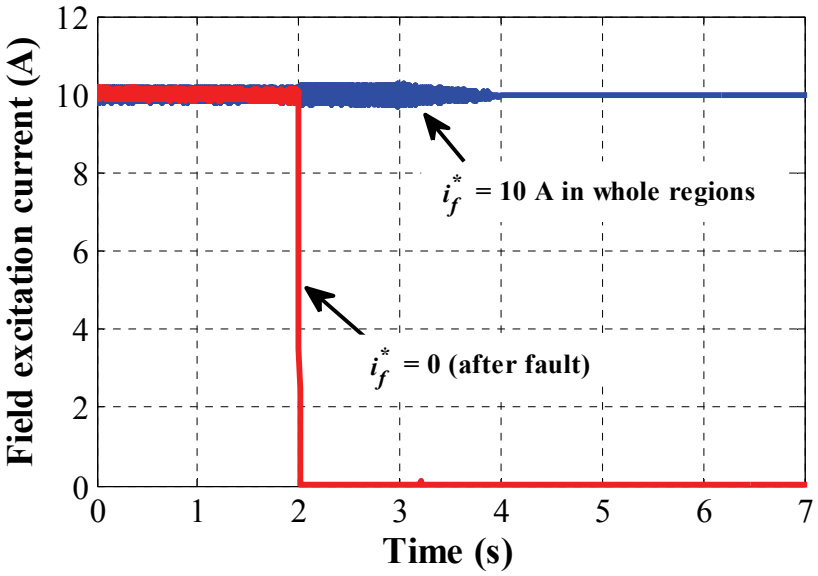

(b) Field excitation current control

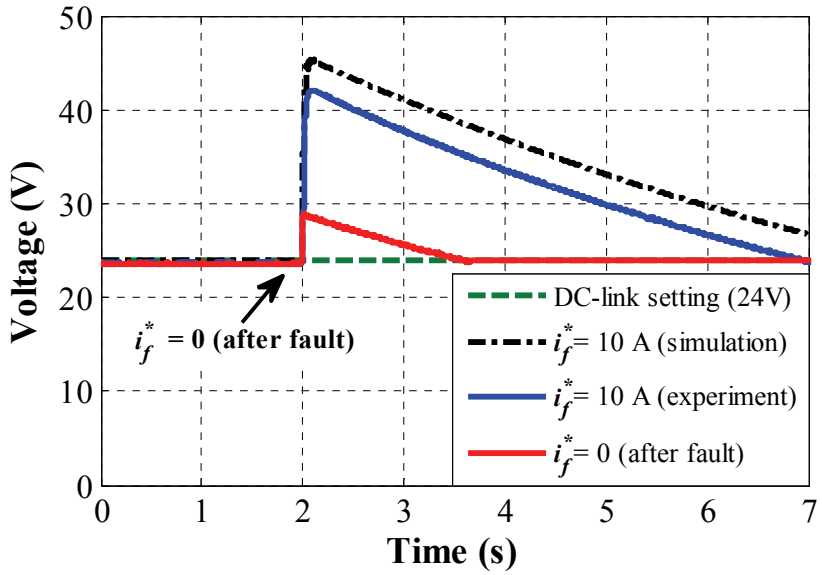

(c) DC-link voltage

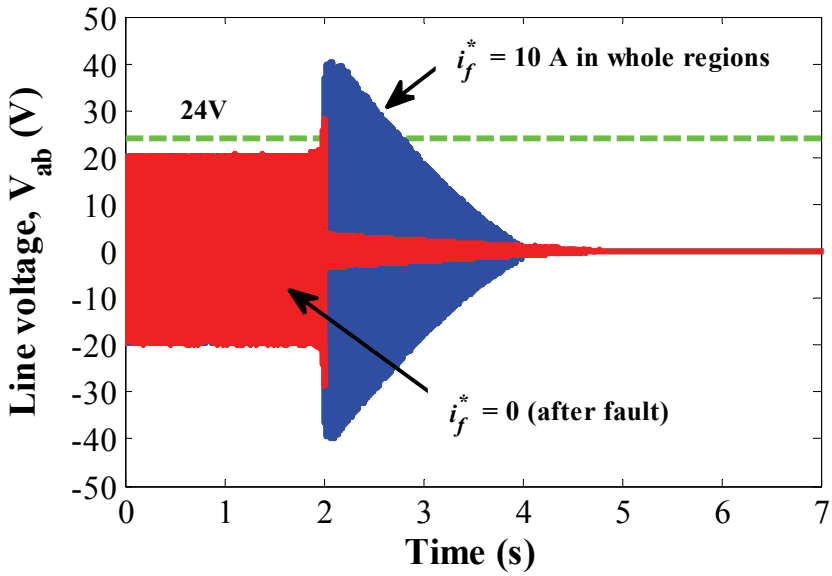

(d) Line voltage

Fig. 7.8. Experimental results of the proposed fault protection method (i_f^*= 0) compared to the method utilising the maximum field excitation current in whole regions (i_f^*= 10 A).

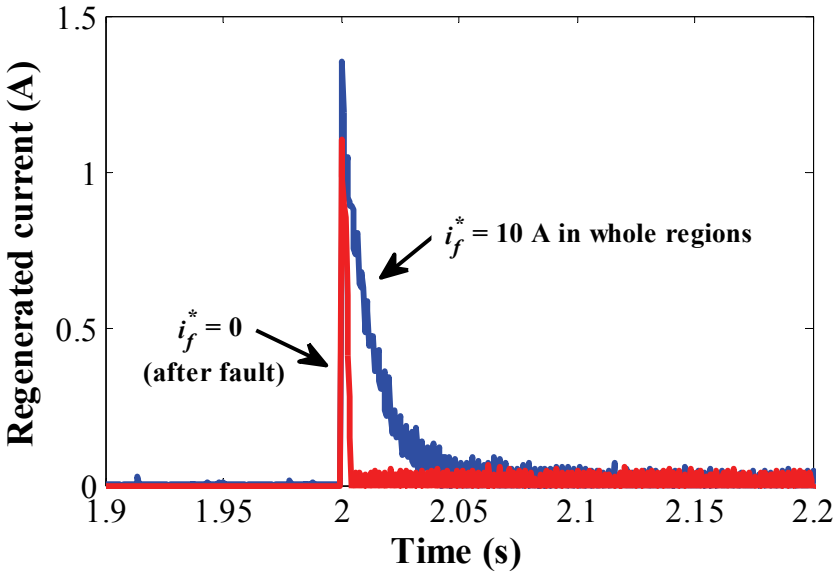

(a) Regenerated current

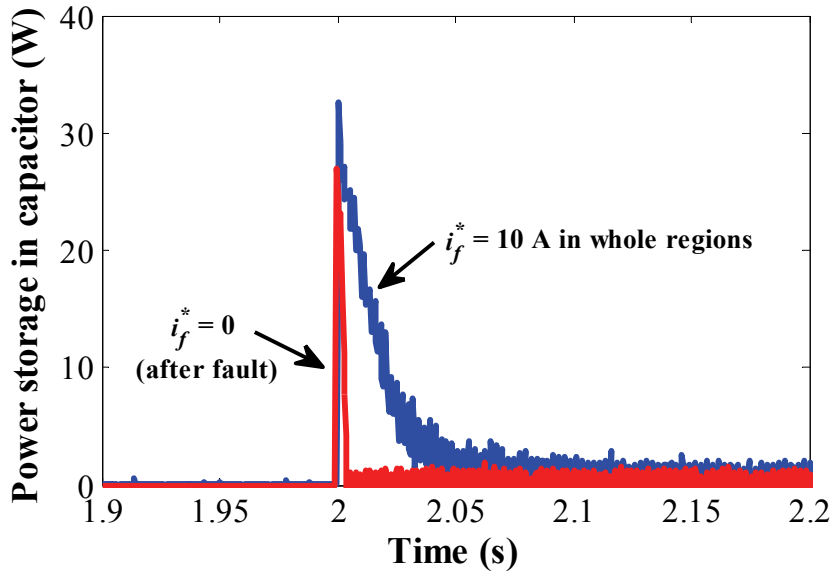

(b) Measured power storage in capacitor

Fig. 7.9. Measured regenerated current and power storage in capacitor of the proposed fault protection method (i_f^* = 0) compared to the method that utilising the maximum field excitation current in whole regions (i_f^* = 10 A).

It should be noted that, based on the utilization of zero field excitation current (i_f^*= 0) after the fault is detected, the line voltage can be greatly reduced compared to the method that utilising the maximum field excitation current in whole regions (i_f^*= 10 A). Therefore, the experimental results agree well with the simulation results and the operation principle of the HEPMM in which the regenerated back-emf can be effectively adjusted by the field excitation current.

7.5 Summary

This chapter examined the fault protection capability of the hybrid-excited permanent magnet machine (HEPMM) based on the field excitation current control strategy under the UCGF conditions. The results have shown that the amplitude of back-emf can be efficiently reduced by utilising zero field excitation current control (i_f^*= 0) when the UCGF fault happens. The proposed fault protection control strategy for the HEPMM is simple to implement as only the field excitation current control is utilised, and can be also applied to other hybrid-excited PM machines. Finally, the simulation and experimental results confirmed the effectiveness of the fault protection control strategy on the hybrid PM machine.

CHAPTER 8

GENERAL CONCLUSIONS AND FUTURE WORK

This thesis has presented various novel control strategies developed for hybrid-excited permanent magnet machines, including the flux-enhancing/weakening control, efficiency improvement, and fault protection capability.

8.1. Flux enhancing/weakening control strategy

8.1.1 HESFPMM with iron flux-bridge (Machine-I)

The special magnetic circuit of this machine topology can effectively reduce the flux-linkage by partially short-circuiting the PM flux via the iron bridge. However, in the prototype HESFPMM (Machine-I), the flux-linkage still exists when the field excitation current is zero, due to the large reluctance of iron bridges. Hence, the negative field excitation current can be utilised to weaken the flux-linkage, while the positive field excitation current can enhance the flux-linkage effectively.

Based on the experiments carried out, the output torque can be effectively enhanced by the positive field excitation current, but the ability to further reduce the air-gap flux with the negative field excitation current is limited due to the high reluctance of the saturated iron flux bridges when the field excitation flux and the PM flux are in the same direction. When the negative field excitation current is increased, the output torque is reduced, since the torque is directly related to the field excitation flux. Hence, in order to achieve the good performance of this machine in terms of high torque and wide speed range, a new control strategy for the HESFPMM has been presented. In the constant torque region, the positive field excitation current is utilised to enhance the torque, and is gradually modified when the speed exceeds the rated speed of enhanced torque until the field excitation current is zero. In the flux-weakening region, the *d*-axis current is utilised, whilst the field excitation current is controlled towards zero rather than negative in the flux-weakening mode. It has been demonstrated experimentally that the proposed method exhibits a smooth transition between flux-enhancing and flux-weakening operations via utilising the field excitation current control, good robustness against machine parameters based on the voltage error regulation method, extended speed range, and higher efficiency

in the flux-weakening region, compared to the conventional methods using only the field excitation current control as represented in Fig.8.1.

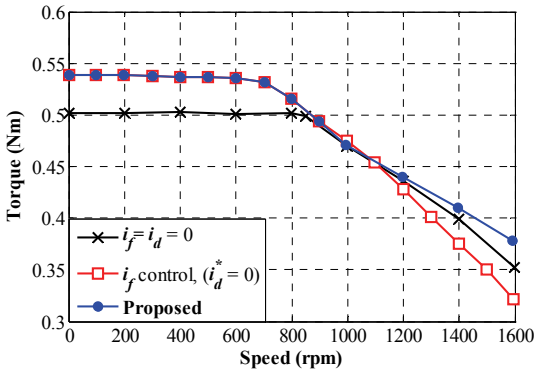

(a) Measured torque

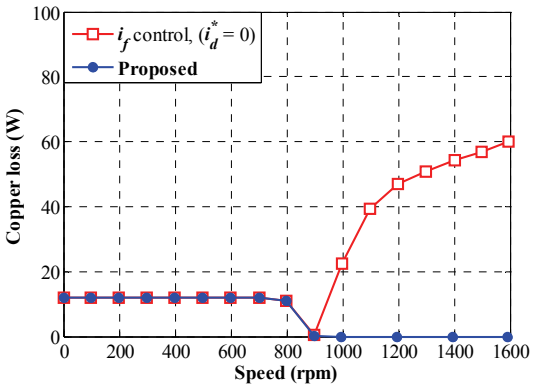

(b) Copper loss of field winding

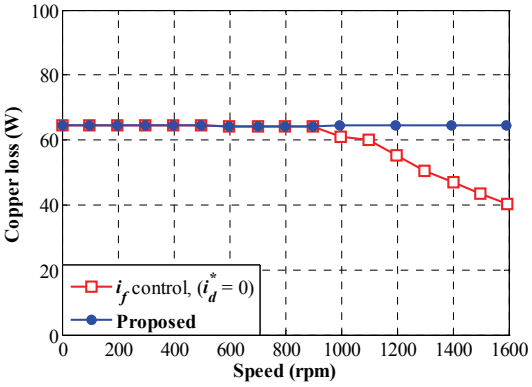

(c) Copper loss of armature winding

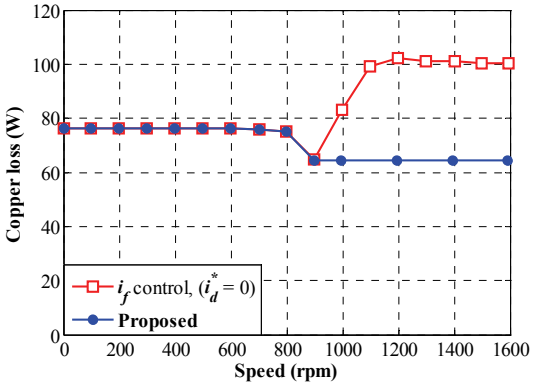

(d) Total copper loss

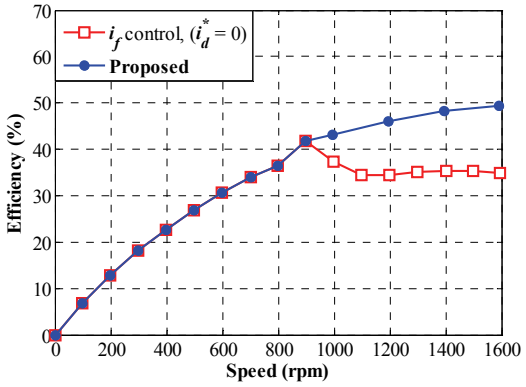

(e) Efficiency

Fig. 8.1. Experimental results of Chapter 3.

8.1.2 HEPMM (Machine-II)

Only the positive field excitation current is utilised to modify the flux-linkage of this machine in both flux-enhancing and flux-weakening operations. The field excitation flux is also a major excitation source compared with the PMs. For this machine, three controllable currents, i.e. *d*-axis, *q*-axis, and field excitation currents, are available, in which the appropriate settings for these currents need to be developed and verified. Three flux-weakening control methods for the HEPMM, namely utilising field excitation current alone (Method-I), utilising armature current alone (Method-II), and optimisation method (Method-III), have been compared and investigated in terms of the torque, operating speed range, and efficiency in both the constant-torque and flux-weakening regions.

It has been proven experimentally that the maximum efficiency of the HEPMM can be achieved when the copper loss in the armature winding and the copper loss in the field winding are equal. Indeed, since both the armature winding and the field winding of the prototype HEPMM (Machine-II) are located in the same place in the stator, the rise in temperature in the two windings are assumed to be identical. Furthermore, the same coil types are used in both windings in this machine. As a result, the resistance ratio between the armature winding and the field winding can remain approximately constant in all operating regions. For this reason, the winding resistances can easily be replaced by their turn numbers, rather than utilising resistances, their optimal ratio is defined as the optimisation method. The optimised field excitation current is found to be a function of *d*-axis and *q*-axis currents, which is simple to implement and robust in terms of the machine parameter variation.

It has been observed that all three methods can achieve the same torque in the constant-torque region due to the enhanced field excitation currents, whilst the optimisation method (Method-III) exhibits a wider operating speed range and higher efficiency in the flux-weakening region compared to other methods as shown in Fig. 8.2. Furthermore, it can also be easily applied to other hybrid-excited machines.

The comparison of control strategies for the hybrid-excited permanent magnet machines is illustrated in Table 8.1. It is obvious that the optimisation method exhibits a higher performance than other methods in terms of high torque, wide speed range, and high efficiency.

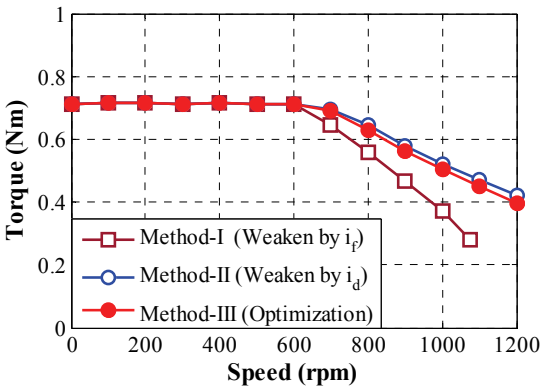

(b) Measured torque

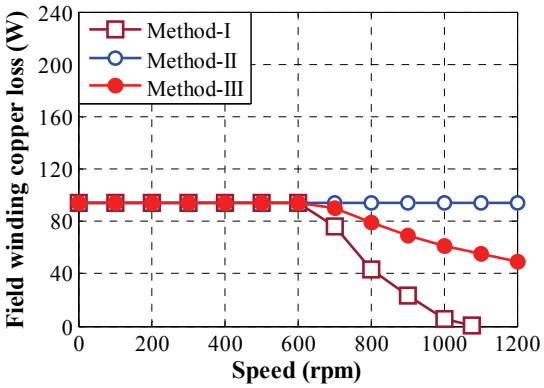

(b) Copper loss of field winding

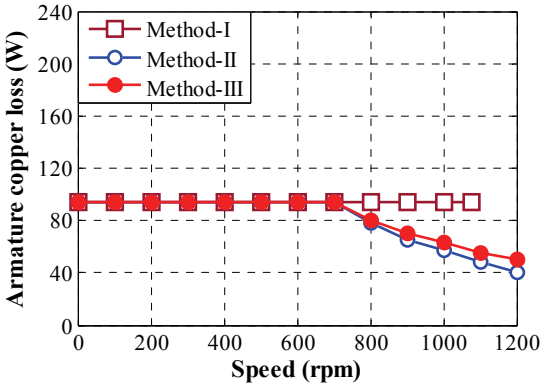

(c) Copper loss of armature winding

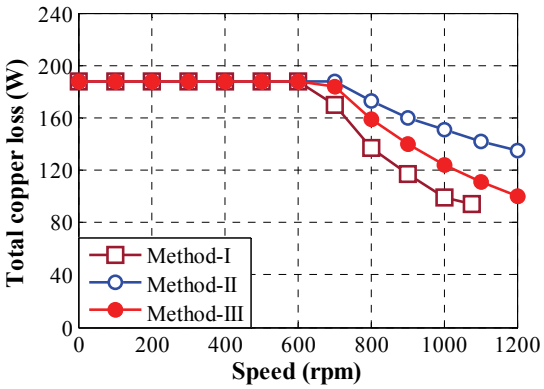

(d) Total copper loss

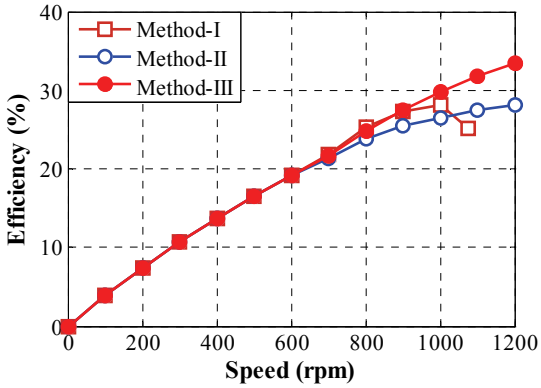

(f) Efficiency

Fig. 8.2. Experimental results of Chapter 4.

Table 8.1. Comparison of flux-weakening control strategies

Machine	Chapter	Performance	i_f control, $i_d = 0$.	i_f =max, i_d control.	Optimisation i_f & i_d, i_q control.
HESFPMM (Machine-I) (± i_f)	3	Torque	Low	-	High
		Speed range	Limited	-	No limit
		Copper loss of armature winding	High	-	Low
		Copper loss of field winding	High	-	High
		Total copper loss	High	-	Low
		Efficiency	Low	-	High
HEPMM (Machine-II) (+ i_f)	4,5	Torque	Low	Highest	High
		Speed range	Limited	No limit	No limit
		Copper loss of armature winding	High	Lowest	Low
		Copper loss of field winding	Lowest	High	Low
		Total copper loss	Lowest	High	Low
		Efficiency	Low	Low	Highest
	7	Fault protection capability (i_f= 0)	Applicable		

Table 8.2. Comparison of efficiency improvement

Machine	Chapter	Topic	Optimisation	MET
HEPMM (Machine-II)	5,6	Efficiency improvement	Yes	Yes
		Machine parameters	Required	Not required
		Current ripple of i_f	Low	High
		Dynamic response	Fast	Slow
		Implementation	Simple	Simple

8.2. Efficiency improvement

8.2.1 Optimisation method

Since the maximum field excitation current is commonly employed to increase the maximum torque via enhancing the flux-linkage, the field excitation current might exceed the specification of the machine when operating under low torque conditions. As a result, the efficiency is deteriorated due to large copper loss in the field winding. The efficiency improvement of the HEPMMs by utilising field excitation current control has therefore been experimentally investigated and compared to the method that utilises the maximum field excitation current. The proposed method is based on the optimisation condition, which has been discussed in the previous section. The proposed method can provide higher efficiency in all operating regions compared with the method that utilises the maximum field excitation current. The proposed method enables improvements in efficiency as presented in the efficiency map under low load torque operation. In addition, the proposed method exhibits a good dynamic response, and can be conveniently applied to other hybrid-excited machines.

8.2.2 Maximum efficiency tracking

This is based on the same verified conditions for the efficiency improvement as presented in section 8.2.1. The maximum efficiency tracking (MET) method for the HEPMMs is proposed to minimise the field excitation flux, under any given speed and torque conditions, by searching for an appropriate field excitation reference current. The field excitation current is automatically modified by using a small value of tracking step size over every time interval, whilst its direction is determined based on the comparison of the current and previous efficiency values. The window moving average is utilised to improve the accuracy of the MET algorithm.

It has been found that the efficiency of the HEPMM can be improved via this proposed method compared with the method of utilising the maximum field excitation current for all operating regions. The proposed method can be applied to other hybrid-excited machines without the requirement for machine parameters, or even the turn ratio between the field winding and the armature winding, as required in the method presented in section 8.2.1. Furthermore, the comparison of both efficiency improvement control strategies is illustrated in Table 8.2.

8.3. Fault protection capability

Since the PM flux of the HEPMM (Machine-II) is inherently short-circuited when the field excitation current is not fed into the excitation windings, the open-circuit back-emf is almost zero. For this reason, this machine exhibits some fault protection capability, which can be utilised to prevent dangerous excess voltage issues from uncontrolled generator faults (UCGF) at high speed operation. A novel method of fault protection for the HEPMM is thus proposed and verified experimentally, based on the utilisation of field excitation current control. The fault is monitored by the DC-link voltage, which makes it simple. The results have shown that the amplitude of back-emf can be efficiently reduced (~79.16%) by using zero field excitation current control ($i_f = 0$) when the UCGF fault happens. The proposed fault protection control strategy for the HEPMM is simple to implement as only the field excitation current control is utilised. It can be also applied to other hybrid-excited PM machines.

8.4. Future work

In the HESFPMM (Machine-I), the flux-weakening performance is limited when the negative field excitation current is employed, which is caused by the high reluctance of the saturated iron flux bridges. It might be possible, therefore, to extend the operating speed range of this machine's topology by modifying the thickness of iron flux-bridges to avoid the saturation problem, which can directly improve the circulated field excitation flux in the stator back-iron. As a result, high torque at low speed and a wide speed range can be achieved by utilising only the field excitation current control.

Fault protection capability control in other HEPMM topologies which employ a large volume of PM, the open-circuit back-emf cannot be zero when $i_f = 0$. It might be possible to utilise both the *d*-axis current and the field excitation current in order to reduce the back-emf of these machines during faults. It should be noted that this method cannot be used for the UCGF, since the inverter would not be controlled if all switching gate-signals were removed, thus damage to the processing unit may occur. It would, however, be effective with single-phase open-circuit faults and DC power supply short-circuit faults at high speed operation, which could also deliver the regenerated current back to the DC-link that causes the excess voltage issue, since the back-emf of the HEPMM can be controlled by the armature current.

REFERENCES

[ABO09] M. T. Abolhassani and H. A. Toliyat, "Fault tolerant permanent magnet motor drives for electric vehicles," in *Proc. IEEE Int. Electric Machines & Drives Conf. (IEMDC)*, Miami, Florida, 3-6 May 2009, pp. 1146-1152.

[ABU06] J. A. Abu-Qahouq, H. Mao, H. J. Al-Atrash and I. Batarseh, "Maximum efficiency point tracking (MEPT) method and digital time control implementation," *IEEE Trans. Power Electron.*, vol. 21, no. 5, pp. 1273-1281, Sep. 2006.

[ABU12] H. Abu-Rub, A. Iqbal, and J. Guzinski, *High performance control of AC drives*, John Wiley & Sons, 2012.

[AFI15] I. A. A. Afinowi, Z. Q. Zhu, Y. Guan, J. C. Mipo, and P. Farah, "Hybrid-excited doubly salient synchronous machine with permanent magnets between adjacent salient stator poles," *IEEE Trans. Magn*., vol. 51, no. 10, pp.1-9, Oct. 2015.

[AFI16] I. A. A. Afinowi, Z. Q. Zhu, K. Y. Guan, J. Mipo, and P. Farah "A novel brushless AC doubly salient stator slot permanent magnet machine," *IEEE Trans. Energy Convers*., vol. 31, no. 1, pp. 283–292, Mar. 2016.

[AMA09] Y. Amara, L. Vido, M. Gabsi, E. Hoang, A. Hamid Ben Ahmed, and M. Lecrivain, "Hybrid excitation synchronous machines: energy-efficient solution for vehicles propulsion," *IEEE Trans. Veh. Technol*., vol. 58, pp. 2137-2149, 2009.

[BIA06] N. Bianchi, S. Bolognani, and P. Frare, "Design criteria for high-efficiency SPM synchronous motors," *IEEE Trans. Energy Convers.*, vol. 21, no. 2, pp. 396–404, Jun. 2006.

[BOL00] S. Bolognani, M. Zordan, and M. Zigliotto, "Experimental fault-tolerant control of a PMSM drive," *IEEE Trans. Ind. Electron*., vol. 47, no. 5, pp. 1134-1141, Oct. 2000.

[BOL08] I. Boldea, "Control issues in adjustable-speed drives," *IEEE Ind. Electron. Mag*., vol. 2, no. 3, pp. 32–50, Sep. 2008.

[CAV05] C. Cavallaro, A. O. Di Tommaso, R. Miceli, A. Raciti, G. R. Galluzzo, and M. Trapanese, "Efficiency enhancement of permanent-magnet synchronous motor drives by online loss minimization approaches," *IEEE Trans. Ind. Electron*., vol. 52, No.4, pp. 1153-1160, Aug. 2005.

[CHE03] J. J. Chen, and K. P. Chin, "Minimum copper loss flux-weakening control of surface mounted permanent magnet synchronous motors," *IEEE Trans. Power Electron.*, vol. 18, no.4, pp. 929-936, 2003.

[CHE10] B.Cheng and T.R. Tesch, "Torque feedforward control technique for permanent-magnet synchronous motors," *IEEE Trans. Ind. Electron*., vol. 57, no. 3, pp. 969-974, Mar. 2010.

[CHE11] J. T. Chen, Z. Q. Zhu, S. Iwasaki, and R. Deodhar, "A novel E-core switched-flux PM brushless AC machine," *IEEE Trans. Ind. Appl*., vol.47, no.3, pp.1273-1282, 2011.

[CHE11a] J. T. Chen, Z. Q. Zhu, S. Iwasaki, and R. Deodhar, "A novel hybrid-excited switched-flux brushless AC machine for EV/HEV applications," *IEEE Trans. Veh. Technol*., vol. 60, no. 4, pp. 1365-1373, May. 2011.

[CHE11b] M. Cheng, W. Hua, J. Zhang, and W. Zhao, "Overview of stator permanent magnet brushless machines," *IEEE Trans. Ind. Electron*., vol. 58, no. 11, pp. 5087-5101. Nov. 2011.

[CHE97] Y.S. Chen, Z. Q. Zhu, and D. Howe, Fault analysis of pm of brushless ac under field-weakening operation, *Proc. 32th Universities Power Engineering Conference (UPEC)*, Manchester, UK, 10-12 Sept. 1997, pp. 41-44.

[CHE99] Y. S. Chen, Z. Q. Zhu, and D. Howe, "Influence of inaccuracies in machine parameters on field-weakening performance of PM brushless AC drives," *in Proc. IEEE Int. Conf. Electr. Mach. Drives*, Seattle, Washington, 9-12 May 1999, pp. 691-693.

[CHE99a] Y. S. Chen, "Motor topologies and control strategies for permanent magnet brushless AC drives", PhD Thesis, University of Sheffield, 1999.

[CHO13] G. Choi, T. M. Jahns, "Interior permanent magnet synchronous machine rotor demagnetization characteristics under fault conditions," *IEEE Energy*

Conversion Congress and Exposition (ECCE), Denver, Colorado, 15-19 Sept. *2013*, pp. 2500-2507.

[CHU14] W. Q. Chu, Z.Q. Zhu, and J. T. Chen, "Simplified analytical optimization and comparison of torque densities between electrically excited and permanent-magnet machines," *IEEE Trans. Ind. Electron*., vol. 61, no.9, pp. 5000-5011, Sep. 2014.

[CON10] A. Consoli, G. Scarcella, G. Sceba, and A. Testa, "Steady-state and transient operation of IPMSMs under maximum-torque-per-ampere control," *IEEE Trans. Ind. Appl*., vol. 46, no. 1, pp.121-129, Jan./Feb. 2010.

[DES13] R. Destro, L. Matakus, W. Komatsu, and N. R. N. Ama, "Implementation aspects of adaptive window moving average filter applied to PLLs - Comparative study," *in Proc. IEEE Brazilian Power Electronics*, Gramado, Brazil, 27-31 Oct. 2013, pp. 730-736.

[DHA90] W. Hua, M. Cheng, Z. Q. Zhu, and D. Howe, "Analysis of current-regulated voltage-source inverters for permanent magnet synchronous motor drives in normal and extended speed ranges," *IEEE Trans. Energy Convers.*, vol. 5, no. 1, pp. 137–144, Mar. 1990.

[DSP10] dSPACE, *Hardware installation and configuration reference*, Release 6.6, May 2010.

[ELR11] A. M. El-Refaie, "Fault-tolerant permanent magnet machines: a review," *IET Elect. Power Appl*., vol. 5, no. 1, pp. 59–74, Jan. 2011.

[ERR12] R. R. Errabelli and P. Mutschler, "Fault-tolerant voltage source inverter for permanent magnet drives," *IEEE Trans. Power Electron*., vol. 27, no. 2, pp. 500–508, Feb. 2012.

[EST08] J. O. Estima and A. J. M. Cardoso, "Performance analysis of permanent magnet synchronous motor drives under inverter fault conditions", in *Proc. 18th Int. Conf. Elect. Machines (ICEM)*, Vilamoura, Protugal, 6-9 Sep. 2008, pp. 1-6,

[FAI13] Fairchild Semiconductor Corporation, *IGBT FGH40N60SMDF*, Nov. 2013.

[FEM05] N. Femia, G. Petrone, G. Spagnuolo, and M. Vitelli, "Optimization of perturb and observe maximum power point tracking method," *IEEE Trans. Power Electron.*, vol. 20, no. 4, pp. 963-973, 2005.

[FIN13] Finder, *44 Series - Miniature PCB relays DPDT (series 44.62)*, 2013.

[GAN11] Z. Gan, C. Ming, H. Wei, and D. Jianning, "Analysis of the oversaturated effect in hybrid excited flux-switching machines," *IEEE Trans. Magn.*, vol. 47, no.10, pp. 2827-2830, 2011.

[GAU14] B. Gaussens, E. Hoang, M. Lecrivain, P. Manfe, and M. Gabsi, "A hybrid-excited flux-switching machine for high-speed DC-alternator applications," *IEEE Trans. Ind. Electron*., vol. 61, no.6, pp. 2976-2989, 2014.

[HAN06] S. H. Han, T. M. Jahns, M. Aydin, M. K. Guven, and W. L. Soong, "Impact of maximum back-emf limits on the performance characteristics of interior permanent magnet synchronous machines," in *Rec. of 2006 IEEE Industry Applications Society Annual Meeting*, Tampa, Florida, 8-12 Oct. 2006, vol. 4, pp. 1962-1969.

[HAV99] A. M. Hava, S.K. Sul, R. J. Kerkman, and T. A. Lipo, "Dynamic over-modulation characteristics of triangle intersection PWM methods," *IEEE Trans. Ind. Appl*., vol. 35, no. 4, pp. 896–907, 1999.

[HEN10] Hengstler GmbH, *Incremental Encoder RI 58-D / RI 58TD*, Jul. 2010.

[HOA07] E. Hoang, M. Lecrivain, and M. Gabsi, "A new structure of a switching flux synchronous polyphased machine with hybrid excitation," *European Conference on Power Electronics and Applications*, Aalborg, Denmark, 2-5 Sept. 2007, pp. 1-8.

[HOA97] E. Hoang, A. H. Ben-Ahmed, and J. Lucidarme, "Switching flux permanent magnet polyphased synchronous machines," *in Proc. 7th Eur. Conf. Power Electron. Appl*., Trondheim, Norway, 8-10 Sept. 1997, pp. 903–908.

[HOL94] J. Holtz, "Pulsewidth modulation for electronic power conversion," *in Proc. IEEE*, vol. 82, no. 8, pp. 1194–1214, Augt. 1994.

[HON80] V. B. Honsinger, “Permanent magnet machine asynchronous operation,” *IEEE Trans. Power App. Syst*., vol. PAS-99, no. 4, pp. 1503-1509, Apr. 1980.

[HON82] V. B. Honsinger, “The fields and parameters of interior type ac permanent-magnet machines,” *IEEE Trans. Power, Appl. Syst*., vol. PAS-101, pp. M67-876, 1982.

[HUA08] W. Hua, M. Cheng, Z. Q. Zhu, and D. Howe, “Analysis and optimization of back emf waveform of a flux-switching permanent magnet motor,” *IEEE Trans. Energy Convers.*, vol. 23, no. 3, pp. 727–733, Sep. 2008.

[HUA12] M. Huang, H. Lin, H. Yunkai, P. Jin, and Y. K. Guo, “Fuzzy control for flux weakening of hybrid exciting synchronous motor based on particle swarm optimization algorithm,” *IEEE Trans. Magn*., vol. 48, no. 11, pp. 2989–2992, 2012.

[HUA15] W. Hua, G. Zhang and M. Cheng, “Flux-regulation theories and principles of hybrid-excited flux-switching machines,” *IEEE Trans. Ind. Electron*., vol. 62, no. 9, pp. 5359-5369, Sep. 2015.

[HUA16] L. R. Huang, Z. Q. Zhu, and W. Q. Chu, “Optimization of electrically excited machine for electrical vehicle applications considering load condition,” *The 8th International Conference on Power Electronics, Machines and Drives (PEMD 2016),* Glasgow, UK, 19-21 April 2016, pp.1-6.

[ICF14] A. S. Icfanuti, L. N. Tutelea, F. J. H. Kalluf, and I. Boldea, “A novel design of stator ferrite PM single phase doubly salient small motor: FEM characterization and controlled dynamics”, *Int. Conf. Optimization of Electrical and Electronic Equipment (OPTIM)*, Bran, Romania, 22-24 May 2014, pp. 284-290.

[INA00] K. Inagaki, A. Chiba, M. A. Rahman, and T. Fukao, “Performance characteristics of inset-type permanent magnet bearingless motor drives,” i*n Proc. PESWM*, Singapore, 23-27 Jan. 2000, pp. 202-207.

[INT05] International Rectifier, *Integrated Power Hybrid IC for Appliance Motor Drive Applications IRAMY20UP60B*, Jul. 2005.

[JAH99] T. M. Jahns and V. Caliskan, “Uncontrolled generator operation of interior PM synchronous machines following high speed inverter shutdown,” *IEEE Trans. Ind. Appl*., vol. 35, no. 6, pp. 1347–1357, Nov./Dec. 1999.

[JUN99] J. Jung, and K. Nam, “A dynamic decoupling control scheme for high-speed operation of induction motors”, *IEEE Trans. Ind*., vol. 46, no. 1, pp. 100-110, 1999.

[KEF10] L. Kefsi, Y. Touzani, M. Gabsi, “Hybrid excitation synchronous motor control with a new flux weakening strategy,” *IEEE Vehicle Power and Propulsion Conference (VPPC)*, Lille, France, 1-3 Sept. 2010, pp. 1-5.

[KHA11] M. Khan, M. Uddin, and M. A. Rahman, “A new loss minimization control of interior permanent magnet motor drives operating with a wavelet based speed controller,” *in Proc. IEEE Ind. Appl. Soc. Annu. Meeting*, Orlando, Florida, 9-13 Oct. 2011, pp. 1-8.

[KIM06] H. W. Kim, M. J. Youn, K. Y. Cho, and H. S. Kim, “Nonlinearity estimation and compensation of PWM VSI for PMSM under resistance and flux linkage uncertainty,” *IEEE Trans. Cont. Sys. Tech*., vol. 14, no. 4, pp. 589-601, Jul. 2006.

[KIM11] K. H. Kim, “Simple online fault detecting scheme for short-circuited turn in a PMSM through current harmonic monitoring,” *IEEE Trans. Ind. Electron*., vol. 58, no. 6, pp. 2565-2568, Jun. 2011.

[KIM13] S. Kim, Y. D. Yoon, S. K. Sul, and K. Ide, “Maximum Torque per Ampere (MTPA) Control of an IPM Machine Based on Signal Injection Considering Inductance Saturation,” *IEEE Trans. Power Electron.*, vol. 28, no. 1, pp. 488-497, Jan. 2013.

[KIM97] J. M. Kim, and S.K. Sul, “Speed control of interior permanent magnet synchronous motor drive for the flux weakening operation,” *IEEE Trans. Ind. Appl*., vol. 33, no. 1, pp. 43–48, 1997.

[KUR04] K. Kurihara and M. A. Rahman, “High-efficiency line-start interior permanent-magnet synchronous motors,” *IEEE Trans. Ind. Appl*., vol. 40, no. 3, pp. 789-796, May/Jun. 2004.

[KWO06] T. S. Kwon and S.K. Sul, "Novel antiwindup of a current regulator of a surface-mounted permanent-magnet motor for flux-weakening control," *IEEE Trans. Ind. Appl*., vol. 42, no. 5, pp. 1293-1300, 2006.

[KWO07] T. S. Kwon and S. K. Sul, "A novel flux weakening algorithm for surface mounted permanent magnet synchronous machines with infinite constant power speed ratio," *Int. Conf. Elect. Mach. Systems*, Seoul, Korea, 8-11 Oct. 2007, pp. 440–445.

[KWO08] T. S. Kwon, G. Y. Choi, M. S. Kwak, and S. K. Sul, "Novel flux-weakening control of an IPMSM for quasi-six-step operation," *IEEE Trans. Ind. Appl*., vol. 44, no. 6, pp. 1722-1731, 2008.

[LEE09] J. Lee, K. Nan, S. Choi, and S. Kwon, "Loss-minimizing control of PMSM with the use of polynomial approximations," *IEEE Trans. Power Electron.*, vol. 24, no. 4, pp. 1071-1082, 2009.

[LEE11] J.-P. Lee, S.-C. Han, Y.-H. Han, and T.-H. Sung, "Loss characteristics of SFES with amorphous core for PMSM," *IEEE Trans. Appl. Supercond*., vol. 21, no. 3, pt. 2, pp. 1489–1492, 2011.

[LEE14] B. S. Lee, N. Pothi, M. M. J. Al-Ani, and Z. Q. Zhu, "Experimental study of torque and flux weakening performance of alternative switched flux pm machines," *7th IET Int. Conf.on Power Electronics, Machines and Drives (PEMD),* Manchester, UK, 8-10 April 2014, pp. 1-6.

[LEM12] LEM, *Voltage Transducer LV 25-P*, Nov. 2012.

[LEM14] LEM, *Current Transducer LA 25-P*, Nov. 2014.

[LEV08] V. R. Jevremovic , D. P. Marcetic, "Closed-loop flux weakening for permanent magnet synchronous motors", *4th IET Int. Conf.on Power Electronics, Machines and Drives (PEMD),* York, UK, 2-4 April 2008, pp. 717-721.

[LI15] G. S. Li, J. F. Xie, and L. Y. Xu, "Maximum efficiency control method of permanent magnet synchronous motor based on three-dimensional table," in *Proc. International Conference on Advanced Mechatronic Systems (ICAMechS)*, Beijing, China, 22-24 Aug. 2015, pp. 392-396.

[LIA05] C. Z. Liaw, W. L. Soong, B. A. Welchko, and N. Ertugrul, "Uncontrolled generation in interior permanent-magnet machines," *IEEE Trans. Ind. Appl*., vol. 41, no. 4, pp. 945–954, Jul./Aug. 2005.

[LIN12] P. Y. Lin and Y. S. Lai, "Voltage control technique for the extension of DC-link voltage utilization of finite-speed SPMSM drives," *IEEE Trans. Ind. Electron*., vol. 59, no. 9, pp. 3392-3402, Sep. 2012.

[LIU10] C. Liu, K. T. Chau, and W. Li, "Comparison of fault-tolerant operations for permanent-magnet hybrid brushless motor drive," *IEEE Trans. Magn*., vol. 46, no. 6, pp. 1378–1381, Jun. 2010.

[LIU12] H. Liu, Z. Q. Zhu, E. Mohamed, Y. Fu, and X. Qi, "Flux-weakening control of nonsalient pole PMSM having winding inductance, accounting for resistive voltage drop and inverter nonlinearities," *IEEE Trans. Power Electron.*, vol. 27, no. 2, pp. 942-952, Feb. 2012.

[MAC91] S. R. Macminn, and T. M. Jahns, "Control techniques for improved high-speed performance of interior PM synchronous motor drives," *IEEE Trans. Ind. Appl*., vol. 27, no. 5, pp. 997–1004, Sep./Oct.1991.

[MAG14] Magtrol, *In-Line Torque Transducers TM 301 – TM 308*, Feb. 2014.

[MAR98] D. S. Maric, S. Hiti, C. C. Stancu, and J. M. Nagashima, "Two improved flux weakening schemes for surface mounted permanent magnet synchronous machine drives employing space vector modulation," *in Proc. IEEE IECON'98*, Aachen, Germany, 31 Aug. - 4 Sep. 1998, pp. 508-512.

[MBA12] R. Mbayed, G. Salloum, L. Vido, E. Monmason, and M. Gabsi, "Hybrid excitation synchronous machine control in electric vehicle application with copper losses minimization," *6th IET Int. Conf.on Power Electronics, Machines and Drives (PEMD)*, Bristol, UK, 27-29 Mar. 2012, pp. 22-27.

[MER54] F. W. Merrill, "Permanent magnet excited synchronous motors," *AIEE Trans*., vol. 73, no. 2, pp. 1754–1760, Jan. 1954.

[MOC91] H. Mochikawa, T. Hirose, and T. Umemoto, "Overmodulation of voltage source PWM inverter," *in Conf. Rec. JIEE-IAS Conf.* 1991, pp. 466-471.

[MOR90] S. Morimoto, Y. Takeda, T. Hirasa, and K. Taniguchi, "Expansion of operating limits for permanent magnet motor by current vector control

considering inverter capacity," *IEEE Trans. Ind. Appl*., vol. 26, no. 5, pp. 866-871, Sep./Oct. 1990.

[MOR94] S. Morimoto, M. Sanada, and Y. Takeda, "Wide-speed operation of interior permanent magnet synchronous motors with high-performance current regulator," *IEEE Trans. Ind. Appl*., vol. 30, no. 4, pp. 920–926, 1994.

[MOR94a] S. Morimoto, Y. Tong, Y. Takeda, and T. Hirasa, "Loss minimization control of permanent magnet synchronous motor drives," *IEEE Trans. Ind. Electron*., vol. 41, no.5, pp. 511-517, Oct. 1994.

[NGU14] C. D. Nguyen and W. Hofmann, "Self-tuning adaptive copper-losses minimization control of externally excited synchronous motors," *Int. Conf. Electrical Machine (ICEM)*, Berlin, Germany, 2-5 Sept. 2014, pp. 897–902.

[NI15] R. Ni, D. Xu, G. Wang, L. Ding, G. Zhang, and L. Qu, "Maximum efficiency per ampere control of permanent-magnet synchronous Machines," *IEEE Trans. Ind. Electron*., vol. 62, no.4, pp. 2135-2143, April 2015.

[OH13] H. Oh, K. Y. Song, K. Y. Cho, and H. W. Kim, "Initial rotor position detecting algorithm of PM synchronous motor using incremental encoder," *IEEE Energy Conversion Congress and Exposition (ECCE) Asia*, Melbourne, Australia, 3-6 June *2013*, pp. 681-686.

[ONG97] C. M. Ong, *Dynamic simulation of electric machinery*, Prentice Hall, 1997.

[OWE09] R. L. Owen, Z. Q. Zhu, and G. W. Jewell, "Hybrid excited flux-switching permanent magnet machines," *Proc.13th Eur. Conf. Power Electron, Appl. (EPE'09)*, Barcelona, Spain, 8-10 Sept. 2009, pp. 1–10.

[OWE10] R. L. Owen, Z. Q. Zhu, and G. W. Jewell, "Hybrid-excited flux-switching permanent-magnet machines with iron flux bridges," *IEEE Trans. Magn*., vol.46, no.6, pp.1726-1729, 2010.

[PAN05] C. Pan and J. Liaw, "A robust field-weakening control strategy for surface mounted permanent-magnet motor drives," *IEEE Trans. Energy Convers.*, vol. 20, no. 4, pp. 701–709, Dec. 2005.

[PEL11] G. Pellegrino, A. Vagati, and P. Guglielmi, “Design tradeoffs between constant power speed range, uncontrolled generator operation, and rated current of IPM motor drives,” *IEEE Trans. Ind. Appl*., vol. 47, no. 5, pp. 1995–2003, Sep./Oct. 2011.

[POT15] N. Pothi, Z. Q. Zhu, I. A. A. Afinowi, B. Lee, and Y. Ren, “A new control strategy for hybrid-excited switched-flux permanent magnet machines,” *IET Electr. Power Appl*., vol. 9, no. 9, pp. 612–619, 2015.

[RAH80] M.A. Rahman, “Permanent magnet synchronous motors-A review of the state of design art,” *Proceedings of International Conference on Electric Machines (ICEM)*, Sep. 1980, pp. 312-319.

[RAH87] M.A. Rahman, “Analytical models for exterior type permanent magnet synchronous motors”, *IEEE Trans. Magn.*, vol. 23, no. 5, pp. 3625-3627, Sept. 1987.

[REF05] EL-Refaie, A.M.; Jahns, T.M., "Optimal flux weakening in surface PM machines using fractional-slot concentrated windings," *IEEE Trans. Ind. Appl*., vol.41, no.3, pp. 790-800, May-June 2005.

[RIB04] R. L. A. Riberio, C. B. Jacobina, E. R. C. da Silva, and A. M. N. Lima, “Fault-tolerant voltage-fed PWM inverter AC motor drive systems,” *IEEE Trans. Ind*. *Electron.*, vol. 51, no. 2, pp. 439-446, Apr. 2004.

[SEB86] T. Sebastian, G.R. Slemon, and M.A. Rahman, “Modeling of permanent magnet synchronous motors,” *IEEE Trans. Magn*., vol. 22, no. 5, pp. 1069–1071, Sep. 1986.

[SEO98] J. K. Seok, J. S. Kim, and S. K. Sul, “Overmodulation strategy for high-performance torque control,” *IEEE Trans. Power Electron.*, vol. 13, no.4, pp. 786-792, 1998.

[SHI07] S. Shinnaka and T. Sagawa, “New optimal current control methods for energy-efficient and wide speed-range operation of hybrid-field synchronous motor,” *IEEE Trans. Ind. Electron*., vol. 54, no.5, pp. 2443-2450, 2007.

[SON96] J.-H. Song, J.-M. Kim, and S.-K. Sul, "A new robust SPMSM control to parameter variations in flux weakening region," *in Proc. IEEE IECON*, Taipei, Taiwan, 5-10 Aug. 1996, vol. 2, pp. 1193-1198.

[SOO94] W. L. Soong, and T. J. E. Miller, "Field-weakening performance of brushless synchronous AC motor drives," *IET Electr. Appl*., vol. 141, no. 6, pp. 331–340, 1994.

[SOU95] G. C. D. Sousa, B. K. Bose, and J. G. Cleland, "Fuzzy logic based on-line efficiency optimization control of an indirect vector-controlled induction motor drive," *IEEE Trans. Ind. Electron*., vol. 42, no. 2, pp. 192-198, April 1995.

[SUL11] S. K. Sul, *Control of electric machine and drive systems*, John Wiley & Sons, 2011.

[SUN07] T. Sun, S. H. Lee, and J. P. Hong, "Faults analysis and simulation for interior permanent magnet synchronous motor using Simulink@MATLAB", in *Proc. Int. Conf. on Elect. Mach. & Syst. (ICEMS)*, Seoul, Korea, 8-11 Oct., 2007, pp. 900-905.

[SUN15] T. Sun, J. Wang, and X. Chen, "Maximum Torque Per Ampere (MTPA) control for interior permanent magnet synchronous machine drives based on virtual signal injection," *IEEE Trans. Power Electron*., vol. 30 no. 9, pp. 5036-5045, Sep. 2015.

[THO08] A. Thomas, Z. Q. Zhu, G. W. Jewell, and D. Howe, "Flux-switching PM brushless machines with alternative stator and rotor pole combinations", in *Proc. Int. Conf. on Elect. Mach. & Syst. (ICEMS)*, Wuhan, China, 17-20 Oct. 2008, pp. 2986-2991.

[TUR10] M. Tursini, E. Chiricozzi, and R. Petrella, "Feedforward flux-weakening control of surface-mounted permanent magnet synchronous motors accounting for resistive voltage drop," *IEEE Trans. Ind. Electron*., vol. 57, no.1, pp. 440-448, Jan. 2010.

[TUR16] T. Turker, U. Buyukkeles, and A. F. Bakan, "Robust current and torque controls for PMSM driven satellite reaction wheel," *IEEE Trans. Ind. Electron*., vol. 63, no.6, pp. 3906-3914, June 2016.

[VAN88] H. W. Van Der Broeck, H. C. Skudelny, and G. V. Stanke, "Analysis and realization of a pulsewidth modulator based on voltage space vectors," *IEEE Trans. Ind. Appl*., vol. 24, no. 1, pp. 142–150, Jan./Feb. 1988.

[VAS03] P. Vas, *Sensorless vector and direct torque control*, Oxford University Press, 2003.

[WAL07] O. Wallmark, L. Harnefors, and O. Carlson, "Control algorithms for a fault-tolerant PMSM drive," *IEEE Trans. Ind. Electron*., vol. 54, no. 4, pp. 1973-1980, Aug. 2007.

[WAN12] Y. Wang, and Z. Q. Deng, "Hybrid excitation topologies and control strategies of stator permanent magnet machines for DC power system," *IEEE Trans. Ind. Electron*., vol. 59, no.12, pp. 4601-4616, Dec. 2012.

[WAN13] W. Wang, and Z. Zhang, "Maximum torque control of hybrid excitation synchronous machine drives based on field current self-optimizing method," *in Proc. 39th Annu. IECON*, Vienna, Austria, 10-13 Nov. 2013, pp. 2977-2982.

[WEI09] H. Wei, C. Ming, and Z. Gan, "A novel hybrid excitation flux-switching motor for hybrid vehicles," *IEEE Trans. Magn*., vol. 45, no.10, pp. 4728-4731, 2009.

[WEI11] H. Wei, Z. Gan, C. Ming, and D. Jianning, "Electromagnetic performance analysis of hybrid-excited flux-switching machines by a nonlinear magnetic network model," *IEEE Trans. Magn.*, vol. 47, no.10, pp. 3216-3219, 2011.

[WEL02] B. A. Welchko, T. M. Janhns, and S. Hiti, "IPM synchronous machine drive response to a single-phase open circuit fault," *IEEE Trans. Power Electron*., vol. 17, no. 5, pp. 764-771, Sep. 2002.

[WEL03] B. Welchko, T. Jahns, W. Soong, and J. Nagashima, "IPM synchronous machine drive response to symmetrical and asymmetrical short circuit faults," *IEEE Trans. Energy Convers*., vol. 18, no. 2, pp. 291–298, Jun. 2003.

[WEL04] B. A. Welchko, T. A. Lipo, T. M. Jahn, and S. E. Schulz, "Fault tolerant three-phase AC motor drive topologies: A comparison of features, cost,

and limitations," *IEEE Trans. Power Electron*., vol. 19 no. 4, pp. 1108-1116, Jul. 2004.

[WU15] Z. Z. Wu, Z. Q. Zhu, and J. T. Shi, "Novel doubly salient permanent magnet machines with partitioned stator and iron pieces rotor," *IEEE Trans. Magn*., vol.51, no.5, pp.1-12, May 2015.

[YAM10] K. Yamazaki, K. Ando, K. Nishika, K. Shima, T. Fukami, and K. Shirai, "Assist effects of additional permanent magnets in salient-pole synchronous generators", in *XIX International Conference on Electrical Machines* (*ICEM*), Rome, Italy, 6-8 Sept. 2010, pp. 1-6.

[YOO07] Y. D. Yoon and S. K. Sul, "New flux weakening control for surface mounted permanent magnet synchronous machine using gradient descent method," *in Proc. 7th Int. Conf. Power Electron*., Daegu, Korea, 22-26 Oct. 2007, pp. 1208-1212.

[YOO07a] Y. D. Yoon, W. J. Lee, and S. K. Sul, "New flux weakening control for high saliency interior permanent magnet synchronous machine without any tables," *in Proc. IEEE Eur. Conf. Power Electron. Appl*., Aalborg, Denmark, 2-5 Sept. 2007, pp. 1-7.

[YU12] W. Yu and D. Zhiquan, "Comparison of hybrid excitation topologies for flux-switching machines," *IEEE Trans. Magn.*, vol. 48, no.9, pp. 2518-2527, 2012.

[YU12a] W. Yu and D. Zhiquan, "Hybrid excitation topologies and control strategies of stator permanent magnet machines for DC power system," *IEEE Trans. Ind. Electron*., vol. 59, no.12, pp. 4601-4616, 2012.

[ZHA10] Q. Zhang, S. Huang, and G. Xie, "Design and experimental verification of hybrid excitation machine with isolated magnetic paths," *IEEE Trans. Energy Convers*., vol. 25, no. 4, pp. 993–1000, Dec. 2010.

[ZHA16] J. Zhao, M. Lin, and D. Xu, "Minimum-copper-loss control of hybrid excited axial field flux-switching machine," *IET Electr. Appl*., vol. 10, no. 2, pp. 82–90, 2016.

[ZHU00] Z. Q. Zhu, Y. S. Chen, and D. Howe, "On-line optimal field weakening control of permanent magnet brushless AC drives," *IEEE Trans. Ind. Appl*., vol. 36, no. 6, pp. 1661–1668, Nov./Dec. 2000.

[ZHU02] Z. Q. Zhu, Y. S. Chen, D. Howe, and P. Farah, "Iron loss in permanent-magnet brushless AC machines under maximum torque per ampere and flux weakening control," *IEEE Trans. Magn*., vol. 38, no. 5, pp.3285-3287, Sep. 2002.

[ZHU05] Z.Q. Zhu, Y. Pang, D. Howe, S. Iwasaki, R. Deodhar, and A. Pride, "Analysis of electromagnetic performance of flux-switching permanent magnet machines by non-linear adaptive lumped parameter magnetic circuit model," *IEEE Trans. Magn*., vol. 41, no. 11, pp. 4277–4287, Nov. 2005.

[ZHU07] Z. Q. Zhu and D. Howe, "Electrical machines and drives for electric, hybrid, and fuel cell vehicles," *Proc. IEEE*, vol. 95, no. 4, pp. 746–765, Apr. 2007.

[ZHU08] Z. Q. Zhu, J. T. Chen, D. Howe, S. Iwasaki, and R. Deodhar, "Analysis of a novel multi-tooth flux switching permanent magnet brushless ac machines for high torque direct drives," *IEEE Trans. Magn*., vol.44, no.11, pp.4313-4316, 2008.

[ZHU09] Z. Q. Zhu, K. Utaikaifa, K. Hoang, Y. Liu, and D. Howe, "Direct torque control of three-phase PM brushless AC motor with one phase open circuit fault," in *Proc. IEEE Int. Conf. Elect. Mach. Drives*, Miami, Florida, 3-6 May 2009, pp. 1408–1415.

[ZHU10] H. Zhu, X. Xiao, and Y. Li, "PI type dynamic decoupling control scheme for PMSM high speed operation," *IEEE Applied Power Electronics Conference and Exposition (APEC)*, Palm Springs, California, 21-25 Feb. 2010, pp. 1736-1739.

[ZHU11] Z. Q. Zhu and L. M. Gong, "Improved sensorless operation of permanent magnet brushless ac motors based on online optimal efficiency control," *in Proc. IEEE Int. Elect. Mach. Drive. Conf., Niagara Falls*, Canada, 15-18 May 2011, pp. 1591-1596.

[ZHU12] Z. Q. Zhu, M. M. J. Al-Ani, X. Liu, M. Hasegawa, A. Pride, and R. Deodhar, "Comparative study of torque-speed characteristics of alternate switched-flux permanent magnet machine topologies," *6th IET Int. Conf. on Power Electronics, Machines and Drives (PEMD),* Manchester, UK, 8-10 April 2014, pp. 1-6.

[ZHU12a] Z. Q. Zhu, and Z. Azar, "Torque speed characteristics of switched flux permanent magnet machines," *The international Journal for Computation and Mathematics in Electrical and Electronic Engineering* (*COMPEL)*, 2012.

APPENDIX A

OPTIMAL CONDITION OF THE MTPA TRAJECTORY

In order to achieve the maximum torque in the constant torque region, the optimal currents, i.e. *d*-axis and *q*-axis currents, are determined based on the differentiation of torque equation of the PMSMs, as illustrated by the red-line for the maximum torque per ampere (MTPA) in Fig.A.1. Indeed, it has been demonstrated in [CHE99a].

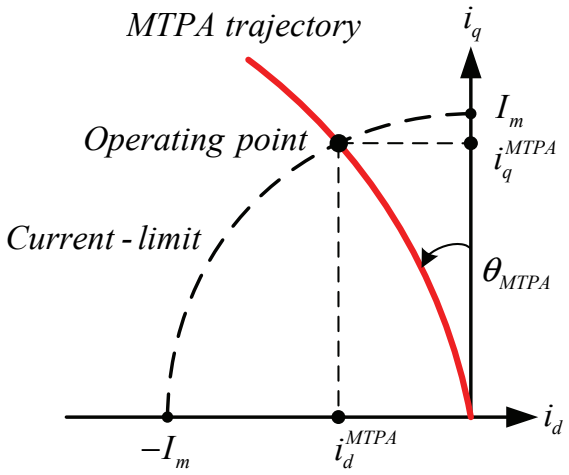

Fig. A.1 MTPA trajectory.

The torque equation of the PMSM can be expressed by (A.1).

$$T_e = \frac{3}{2} P\left[\psi_{pm} i_q - \left(L_q - L_d\right) i_d i_q\right] \tag{A.1}$$

The *d*-axis and *q*-axis currents based on Fig.A.1 are given by,

$$i_d^{MTPA} = -I_m \sin\theta_{MTPA} \tag{A.2}$$

$$i_q^{MTPA} = I_m \cos\theta_{MTPA}. \tag{A.3}$$

By substituting the currents from (A.2) and (A.3) into (A.1), the torque can be given as,

$$T_e = \frac{3}{2} P\left[\psi_{pm} I_m \cos\theta_{MTPA} + \left(L_q - L_d\right) I_m^2 \sin\theta_{MTPA} \cos\theta_{MTPA}\right] \tag{A.4}$$

The differentiation of the torque to the optimal current angle is expressed as,

$$\frac{\partial T_e}{\partial \theta_{MTPA}} = 0, \quad \text{where} \quad 2\sin\theta_{MTPA}\cos\theta_{MTPA} = 1 - 2\sin^2\theta_{MTPA}$$

$$-\psi_{pm} I_m \sin\theta_{MTPA} + \left(L_q - L_d\right) I_m^2 \left(1 - 2\sin^2\theta_{MTPA}\right) = 0$$

$$2\left(L_q - L_d\right) I_m^2 \sin^2\theta_{MTPA} + \psi_{pm} I_m \sin\theta_{MTPA} - \left(L_q - L_d\right) I_m^2 = 0$$

Therefore,

$$\sin\theta_{MTPA} = \frac{-\psi_{pm} I_m \pm \sqrt{\psi^2{}_{pm} I^2{}_m - 8\left(L_q - L_d\right)^2 I^4{}_m}}{4\left(L_q - L_d\right) I_m^2}$$

Based on the scenarios of *d*-axis and *q*-axis inductances conditions it can be summarized as,

$$\sin\theta_{MTPA} = \begin{cases} -\dfrac{\psi_{pm}}{4\left(L_d - L_q\right) I_m} + \sqrt{\dfrac{\psi_{pm}^2}{16\left(L_d - L_q\right)^2 I_m^2} + \dfrac{1}{2}} & ;\ L_d > L_q \\ 0 & ;\ L_d = L_q \\ -\dfrac{\psi_{pm}}{4\left(L_d - L_q\right) I_m} - \sqrt{\dfrac{\psi_{pm}^2}{16\left(L_d - L_q\right)^2 I_m^2} + \dfrac{1}{2}} & ;\ L_d < L_q \end{cases} \tag{A.5}$$

Substituting the currents from (A.5) into (A.2) with the consideration of current relation $\left(I_m^2 = i_d^2 + i_q^2\right)$, the optimal *d*-axis current can be given as a function *q*-axis current by (A.6).

$$i_d^{MTPA} = \begin{cases} \dfrac{\psi_{pm}}{2\left(L_d - L_q\right)} - \sqrt{\dfrac{\psi_{pm}^2}{4\left(L_d - L_q\right)} + i_q^2} & ;\ L_d < L_q \\ 0 & ;\ L_d = L_q \\ \dfrac{\psi_{pm}}{2\left(L_d - L_q\right)} + \sqrt{\dfrac{\psi_{pm}^2}{4\left(L_d - L_q\right)} + i_q^2} & ;\ L_d > L_q \end{cases} \tag{A.6}$$

APPENDIX B

DETERMINING ROTOR POSITION ALIGNMENT

The incremental encoder is employed to provide the rotor position information, which is utilised in the Park's transformation and the control system based on the vector control. However, it is necessary to align the zero position of the encoder to the *d*-axis, as shown in Fig.B.1. The rotor position alignment is determined as introduced in [OH13].

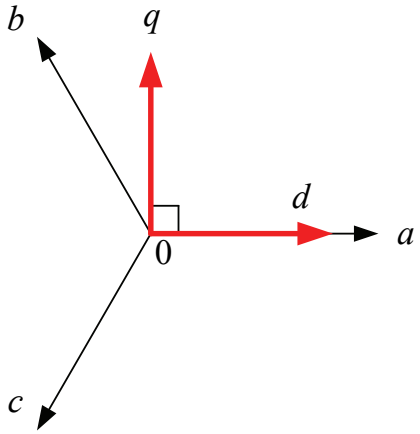

Fig. B.1 Rotor position alignment.

By adjusting the offset angle with the positive direction, the appropriate rotor position can be obtained when the negative direction of phase-A back-emf waveform matches with the zero electrical rotor position, as shown in Fig.B.2.

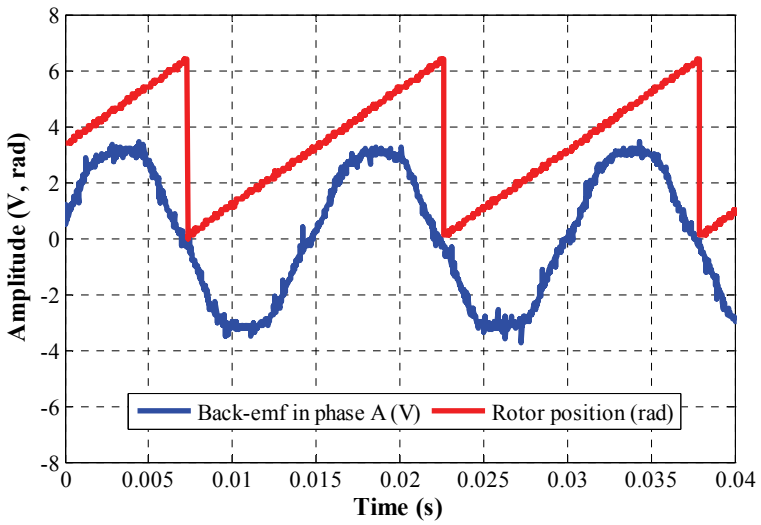

Fig. B.2 Measured rotor position alignment.

PUBLICATIONS

Journal papers in print:

[1] **N. Pothi**, Z. Q. Zhu, I. A. A. Afinowi, B. Lee, and Y. Ren, "A new control strategy for hybrid-excited switched-flux permanent magnet machines," *IET Electr. Power Appl*., vol. 9, no. 9, pp. 612–619, 2015.

Conference papers in print:

[1] **N. Pothi** and Z. Q. Zhu, "A new control strategy for hybrid-excited switched-flux permanent magnet machines without the requirement of machine parameters," in *Proc. 7th IET Int. Conf. Power Electron., Mach. Drives (PEMD)*, Manchester, UK, 8-10 April 2014, pp. 1-6.

[2] B. S. Lee, **N. Pothi**, M. M. J. Al-Ani, and Z. Q. Zhu, "Experimental study of torque and flux weakening performance of alternative switched flux PM machines," in *Proc. 7th IET Int. Conf. Power Electron., Mach. Drives (PEMD)*, Manchester, UK, 8-10 April 2014, pp. 1-6.

Papers in draft:

[1] N. Pothi, Z. Q. Zhu, and Y. Ren, "Flux-weakening control of hybrid-excited permanent magnet machines," drafted and to be submitted.

[2] N. Pothi, Z. Q. Zhu, and Y. Ren, "Efficiency improvement of hybrid-excited permanent magnet machines utilising optimal field excitation current control," drafted and to be submitted.

[3] Z. Q. Zhu, N. Pothi, and P. L. Xu, "Fault protection capability of hybrid-excited permanent magnet machines utilising field excitation current control," drafted and to be submitted.